

Dissertation  
submitted to the  
Combined Faculty of Natural Sciences and Mathematics  
of the Ruperto Carola University  
Heidelberg, Germany  
for the degree of  
Doctor of Natural Sciences

Presented by  
Lena Maetani Appel, M.Sc.  
born in: Summit, New Jersey, USA  
Oral Examination: May 13, 2020



Dynamics of the T cell response to solid tumors under anti-CD40 treatment

Referees:

Prof. Dr. Thomas Höfer

Prof. Dr. Ursula Kummer



<b>Zusammenfassung</b>	<b>V</b>
<b>Summary</b>	<b>IX</b>
<b>1. Introduction</b>	<b>1</b>
<b>2. Analysis of proliferating cells and modeling techniques</b>	<b>11</b>
2.1. Analyzing dye dilution measurements . . . . .	11
2.1.1. Introduction . . . . .	11
2.1.2. A mixture model for the analysis of cell proliferation measurements	13
2.1.3. Accounting for overlapping peaks in the model . . . . .	19
2.2. Estimating errors . . . . .	20
2.3. Estimating proliferation dynamics from cell division profiles . . . . .	21
2.3.1. Properties of the cell proliferation ODE model . . . . .	22
2.3.2. Estimation of the proliferation dynamic from cell division profiles with an ODE model . . . . .	23
2.3.3. Mean number of divisions as a summary statistic of the cell division profiles . . . . .	24
<b>3. T cell dynamics in a melanoma mouse model</b>	<b>25</b>
3.1. Results of the melanoma mouse experiments . . . . .	26
3.1.1. Experimental setup . . . . .	26
3.1.2. Changes induced by the anti-CD40 treatment and common features of the experiments . . . . .	28
3.2. Mathematical model describing the T cell dynamics in a melanoma mouse model . . . . .	33
3.2.1. Basic model structure construction . . . . .	34
3.2.2. Alternative models . . . . .	38

3.2.3.	Model selection for the identification of treatment induced changes	45
3.2.4.	Best minimal model for the time-resolved experiment . . . . .	47
3.2.5.	Best minimal model for the proliferation-resolved experiment . . .	52
3.3.	Comparison of the results obtained from the melanoma mouse model ex- periments . . . . .	57
3.3.1.	Adaptations of the model and differences between the experiments	57
3.3.2.	Comparison of the parameter estimates . . . . .	58
3.3.3.	Concluding remarks on the results of the melanoma mouse model .	62
<b>4.</b>	<b>T cell dynamics in a pancreatic ductal adenocarcinoma mouse model</b>	<b>63</b>
4.1.	Results of the pancreatic ductal adenocarcinoma mouse experiments . . .	64
4.1.1.	Experimental setup . . . . .	64
4.1.2.	Changes induced by the anti-CD40 treatment and common features of the experiments . . . . .	65
4.2.	Mathematical model describing the T cell dynamics in a pancreatic cancer mouse model . . . . .	71
4.2.1.	Basic model structure construction . . . . .	71
4.2.2.	Alternative models . . . . .	73
4.2.3.	Model selection for the identification of the treatment induced changes in the second experiment . . . . .	78
4.2.4.	Model selection for the identification of the treatment induced changes in the third experiment . . . . .	83
4.3.	Review of the results of the pancreatic ductal adenocarcinoma experiments	88
4.3.1.	Challenges when fitting the sparse data of the PDAC experiments	88
4.3.2.	Comparison of the results of the PDAC and melanoma experiments	89
<b>5.</b>	<b>Discussion</b>	<b>95</b>
	<b>Bibliography</b>	<b>105</b>
	<b>Acknowledgments</b>	<b>123</b>
<b>A.</b>	<b>Supplementary information to the solution of ordinary differential equations for birth models</b>	<b>125</b>
<b>B.</b>	<b>Supplementary information to the melanoma experiments and models</b>	<b>131</b>
<b>C.</b>	<b>Supplementary information to the pancreatic ductal adenocarcinoma experi- ments and models</b>	<b>143</b>

---

## Zusammenfassung

---

Immunmodulatorische Ansätze in der Krebstherapie, die sich die T-Zell-Antwort des Patienten zunutze machen, haben sich als eine vielversprechende Behandlungsoption erwiesen. Allerdings zeigt die Unvorhersehbarkeit des Therapieergebnisses, dass die Wirkungsweise und die Faktoren, die den Erfolg einer Immuntherapie bestimmen, nicht ausreichend verstanden sind. Durch die datengetriebene Entwicklung eines mathematischen Modells zur Beschreibung der T-Zell-Antwort auf einen Tumor, wollen wir in dieser Arbeit einen Einblick in die zugrunde liegenden Mechanismen gewinnen. Das Augenmerk liegt hierbei auch auf dem Einfluss einer immuntherapeutischen Intervention auf diese Dynamik. Zu diesem Zweck werden Daten aus einem Mausmodell für das Melanom und das Pankreaskarzinom verwendet. Das Melanom ist dafür bekannt, gut auf Immuntherapien anzusprechen und stellt somit eine Art Prüfstand für neue Therapieansätze dar; das Pankreaskarzinom hingegen ist eine Krebsart für die dringend neue therapeutische Ansätze benötigt werden. Die in dieser Arbeit untersuchte Behandlungsmethode mit einem agonistischen Antikörper gegen CD40 zeigte bereits vielversprechende Ergebnisse in präklinischen Studien zum Pankreaskarzinom und wird außerdem in klinischen Studien der Phase I für verschiedene Tumorindikationen verwendet. Allerdings herrscht keine klare Meinung darüber, wie diese Intervention genau die T-Zell-Antwort beeinflusst. Diese Dynamik wurde bisher auch nicht mit der Hilfe von datengetriebenen mathematischen Modellen untersucht.

Zunächst entwickeln wir eine akkurate Analyseverfahren für *in vivo* Proliferationsmessungen, da sich unser Modellierungsansatz stark auf diese Daten stützt. In diesem Zusammenhang werden Zellen zu Beginn einer Messung gefärbt, z.B. mit CFSE, und die Anzahl der darauffolgenden Teilungen kann durch die sich halbierende Farbstoffintensität nachvollzogen werden. Die hieraus folgenden Intensitätsverteilungen sind bei Daten aus *in vitro* Messungen klar unterscheidbar und die meisten aktuellen Modellierungsansätze wurden für diesen Fall optimiert. Hierbei reicht es oftmals aus, die Daten durch parametrische Verteilungen zu beschreiben. Allerdings stammen unsere Daten aus *in vivo* Messungen, sodass die Analyse durch stark überlappende Intensitätsverteilungen

von Zellen erschwert wird und wir herkömmliche Ansätze nur bedingt anwenden können. Aus diesem Grund entwickeln wir eine Analysemethode, die die datenspezifische Intensitätsverteilung berücksichtigt, indem sie den Daten inhärente Informationen wie die Hintergrundhelligkeit und die Verteilung der Farbstoffintensität ungeteilter Zellen verwendet. Des Weiteren ermöglicht sie die flexible Kombination von Proben, um robuste Optimierungsergebnisse zu erhalten und wird erfolgreich mit sechs Datensätzen getestet, die von unseren Kooperationspartnern zur Verfügung gestellt wurden. Dadurch können wir den prozentualen Anteil der Zellen in verschiedenen Generationen verlässlich bestimmen, auch wenn die Verteilungen stark überlappen.

Als nächstes konstruieren und validieren wir ein mathematisches Modell, das die T-Zell-Antwort auf ein Melanom in Mäusen beschreibt, die mit anti-CD40 oder einer Isotypkontrolle behandelt wurden. Dabei wird das Modell durch die Daten aus zwei Mausmodell-Experimenten motiviert, welche von unseren Kooperationspartnern durchgeführt wurden. Die Messungen werden zu verschiedenen Zeitpunkten nach dem Transfer naiver T-Zellen durchgeführt und liefern absolute Zellzahlen sowie sich ergänzende Informationen zur Zellproliferation, die durch die neu beschriebene Methode analysiert werden. Anhand der Datensätze werden verschiedene plausible mathematische Modellalternativen getestet und der wahrscheinlichste Mechanismus identifiziert. Unsere Untersuchungen zeigen, dass sich die Proliferation der T-Zellen im Wächterlymphknoten im Laufe der Zeit abschwächt und weisen auf einen Teilungsstopp nach vier bis sechs Generationen hin. Im Tumor ist ein Stopp nach einigen Teilungen ebenfalls wahrscheinlich, aber er variiert stärker zwischen den Experimenten: In einem Fall teilen sie sich insgesamt sechs Mal und im anderen Fall teilen sich die Zellen zweimal nach Eintritt in den Tumor. Die Proliferation im Tumor ist schneller als im Lymphknoten und stellt somit einen Kontrast zum abrupten Teilungsstopp dar. In einem nächsten Schritt bestimmen wir Mechanismen, die durch die anti-CD40 Behandlung verändert werden. Dabei finden wir eine verstärkte Aktivierung naiver T-Zellen – ein Effekt, der im Einklang mit der Literatur steht – und zusätzlich eine verzögerte Auswanderung aus dem Wächterlymphknoten.

Schließlich untersuchen wir die gemessene T-Zell-Dynamik in einem Mausmodell für Pankreaskarzinom und zeigen, dass sie durch ein ähnliches mathematisches Modell beschrieben werden kann. Dieses Modell bestätigt einen Teilungsstopp der T-Zellen im Tumor und in den Wächterlymphknoten. Aber bis zu diesem Stopp, der nach insgesamt sechs Teilungen einsetzt, ist die Proliferation schneller als im Melanommodell. Das ist besonders im Wächterlymphknoten ausgeprägt, da sich die Teilungsaktivität im Laufe der Zeit nicht abschwächt. Dem gegenüber steht die Tatsache, dass sowohl das Modell als auch die Daten auf ein allgemein erhöhtes Sterben der T-Zellen im Pankreaskarzinom-Mausmodell hindeuten – ein Phänomen, das in unseren Untersuchungen zum Melanommodell auf den Tumor beschränkt zu sein scheint. Außerdem stellen wir fest, dass die Teilungsrate durch die anti-CD40 Behandlung erhöht wird und finden zusätzlich Hinweise auf eine verstärkte Aktivierungsrate. Dies wirft die Frage auf, ob anti-CD40 auch die Proliferation bereits aktivierter T-Zellen beeinflusst. Da die Migrationsrate durch die Daten nicht gut bestimmbar ist, können wir keine Aussage darüber treffen, ob die Behandlung die Auswanderung der Zellen aus dem Lymphknoten verzögert.

Insgesamt stellen wir in dieser Arbeit eine Möglichkeit vor, *in vivo* Fluoreszenzmessungen sich teilender Zellen zu analysieren. Darüber hinaus bestimmen wir Eigenschaften der naiven T-Zell-Antwort auf zwei unterschiedliche Tumortypen und untersuchen die Auswirkungen einer anti-CD40 Behandlung auf diese Dynamik. Diese mechanistischen Erkenntnisse können dazu beitragen, die Art und Weise zu verbessern, in der anti-CD40 bei der Behandlung von Krebs eingesetzt wird.



Immunomodulatory approaches harnessing the patient's T cell response against cancer have established themselves as a promising treatment option. Nevertheless, the poor predictability of a patient's response shows our limited understanding of the factors that determine whether immunotherapy works. To gain an insight into the underlying mechanisms we develop a data-driven mathematical model of T cells responding to tumors under an immunotherapeutic intervention. To this end, we analyze data obtained from a murine model for melanoma, which is a responsive tumor with respect to immunotherapy and thus, a suitable testbed for new treatment options. In addition, we study the T cell response in a murine model of pancreatic ductal adenocarcinoma—in the clinical setting a tumor for which new therapeutic approaches are urgently needed. The treatment with an agonistic antibody against CD40, which is investigated in this thesis, shows promising results in preclinical studies with pancreatic cancer and is applied in clinical phase I studies for several tumor indications. Still, it is not well understood how this intervention shapes the T cell response and a data-driven modeling approach has not been attempted yet.

First, we develop a method for the accurate analysis of dye dilution measurements of dividing cells *in vivo*, since our modeling approach strongly relies on proliferation data. For these measurements cells are initially stained with a fluorescent dye, such as CFSE, and their proliferative activity can be traced due to a halving of the dye intensity with every division. The resulting dye intensity peaks are usually clearly separated if the data are obtained from *in vitro* measurements and most analyzing approaches have been optimized for this case. In these methods it often suffices to use parametric distributions to describe the data. However, our data stems from *in vivo* experiments and has strongly overlapping peaks, such that its analysis is difficult with these approaches. For this reason, we develop a method where data-inherent information like the background intensity and the distribution of the dye intensities of undivided cells is used to account for the data specific shape of the peaks. It furthermore allows for the flexible combination of samples to obtain robust optimization results and is successfully tested with six data

sets provided by collaboration partners. In this way, we can reliably discern the relative fractions of cells in different generations, even if the peaks are strongly overlapping.

Secondly, we introduce and validate a data-driven mathematical model describing the anti-tumor T cell response. The model is devised with data obtained from two murine melanoma experiments performed by our collaboration partners, in which also the effect of anti-CD40 has been investigated. The measurements are conducted at various time points post naive T cell transfer and provide absolute cell counts, as well as complementary information on cell proliferation, which we analyze with our newly described method. Overall, these two data sets enable us to test various plausible mathematical model alternatives and to identify the most likely mechanism. In the draining lymph node our investigation reveals that the proliferation of T cells is attenuated over time and provides evidence of a division stop after four to six generations. In the tumor a cessation of proliferation is likely, but varies more between the experiments: We find a total of six or more divisions in one case and in the other case two further divisions after the cells enter the tumor. The proliferation in the tumor is faster than in the draining lymph node and stands in contrast to this abrupt division stop. Subsequently, we determine mechanisms which are changed by the treatment with anti-CD40. We find evidence for an enhanced activation of the naive T cells, which has been suggested previously. In addition, we identify a delayed egress from the draining lymph node due to the treatment.

Thirdly, a similar mathematical model can explain the measured T cell dynamic in a murine pancreatic cancer model. In this model, we also confirm a division stop, both in the tumor and the draining lymph node. However, in contrast to the melanoma setting we find a faster proliferation before it ceases after six divisions. The difference of the proliferative activity is particularly pronounced in the draining lymph node, where it is not attenuated over time. Interestingly, for the pancreatic tumor both the model and the data point to an increased overall death of T cells, which in the melanoma setting was mainly confined to the tumor. Furthermore, we determine that the anti-CD40 treatment increases the proliferation rate and also find evidence for an enhanced activation. This raises the question whether the treatment is affecting the proliferation of already activated T cells, too. As the egress rate is not well constrained by the data, we cannot determine whether the drug slows egress also in this tumor model.

Overall, in this work we introduce a method to analyze in vivo cell proliferation dye measurements. We also reveal properties of the naive T cell response to two different tumor types and the effects of anti-CD40 treatment on these dynamics. These mechanistic insights may help improve the way in which anti-CD40 is applied in the treatment of cancer.

# CHAPTER 1

---

## Introduction

---

Until quite recently cancer therapy held very few options: either surgery, radiotherapy or chemotherapy and in most cases a combination of these. While this is still true for many cancers, over the last three decades a promising approach harnessing the body's own immune system to combat malignancies has established itself as a further and promising treatment option. Still, both the scope and the mode of action are not well understood, which is reflected in the unpredictability of the patient's response to the treatment. Yet, with the intensive research conducted in the field, it doesn't seem overly optimistic to expect substantial progress in the near future.

First therapeutic approaches along these lines were conducted in the late 1980ies by treating metastatic melanoma with the patient's own immune cells [1]. In the early 90ies Honjo and Allison recognized the potential of immunomodulating biomolecules as a therapeutic option against cancer. The latter two were awarded with the nobel prize in 2018, creating widespread attention to cancer immunotherapy. Nowadays there is a multitude of immune-therapeutic options, which can be categorized as: 1) cell based therapies, where selected immune cells are infused into the patient; 2) monoclonal antibody based therapies; 3) vaccination approaches; 4) modulation of the immunosuppressive tumor metabolism and environment; 5) immunostimulatory cytokines [2]. In this thesis we focus on a member of the group of monoclonal antibody based therapies, which offer a plethora of different options for modulating the response of immune cells and most prominently of T cells.

Monoclonal antibodies can be divided into two groups: antibodies specifically targeting the tumor and antibodies which directly interact with immune cell receptors. The latter can again be subdivided into agonistic antibodies, which stimulate the immune response, and antagonistic antibodies, which inhibit the downregulation of immune cell activity.

The last subgroup comprises the immune checkpoint blockades targeting CTLA-4 and PD-1, which were FDA approved in 2011 and 2014 for melanoma and subsequently for

a range of different tumors and have brought substantial progress in cancer therapy.

In contrast, agonistic antibodies frequently target members of the tumor necrosis factor-receptor (TNFR) family, where one of the best studied receptors is CD40. This receptor has been known for some time as a potential treatment option and is expected to be a good augmentation to other cancer therapeutic approaches [3], like the established immune checkpoint blockades [4].

**The role of CD8+ T cells** Many immunotherapeutic agents, like CD40 and the checkpoint blockades, are investigated with respect to their effect on the T cell compartment [5, 6, 7].

T cells are an integral part of the adaptive immune response, which has the ability to specifically recognize and remember antigens and combat the associated pathogens. To this end, each T cell expresses many copies of the same T cell receptor on their cell surface, which recognizes a certain antigen with a high specificity. There are only a few T cell clones with the same receptor [8], equipping the human organism with a repertoire of more than  $10^7$  different T cell receptors at any given time.

T cells, which have not encountered their antigen yet (so-called naive T cells) circulate through the body via the blood and lymphatic system. They sample antigen presenting cells (APCs), most prominently dendritic cells, in the quest of the antigen which is recognized by their T cell receptor. In the course of an adaptive immune response, antigen presenting cells are activated at the site of inflammation, where they also ingest antigens, and subsequently migrate to a local lymphoid tissue—in most cases the draining lymph node. There they present the antigen and activate naive T cells with the corresponding T cell receptor. The activation, the subsequent differentiation and proliferation of a naive T cell after its initial antigen encounter is often referred to as priming. There are two important functional subclasses of T cells: CD4+ and CD8+ T cells. Upon activation CD4+ T cells orchestrate the immune response by interacting with different immune cells, mostly with those of the myelomonocytic lineage. In contrast, primed CD8+ T cells directly kill infected cells presenting the specific antigen—and with this also tumor cells, if the antigen is specific to these. Antigens, which are unique to the tumor, are called tumor specific antigens or neoantigens and if they are relatively restricted to the tumor, they are referred to as tumor associated antigens.

Hence, the focus on CD8+ T cells in immunotherapy can be explained by the fact that these cells are known to be direct mediators of antitumor activity due to their ability to kill targeted tumor cells [9]. In addition, the fact that properties of the CD8+ T cell response are related to prognostic markers in the immune therapy of cancer, like the composition of CD8+ T cell subsets [10, 7], their infiltration of the tumor [11, 12] and the distribution of their clone sizes [13], underlines their importance for the success of the therapy. Furthermore, the success of the checkpoint blockades, which are reported to enhance CD8+ T cell immunity, contributed to the interest and continued research on the role of CD8+ T cells in the tumor context [7, 6].

---

## Treatment of tumor with anti-CD40 monoclonal antibodies and checkpoint blockades

**The importance of the constant region of monoclonal antibodies** In immunotherapy monoclonal (and therefore identical) therapeutic antibodies with a certain specificity are widely used and can be produced in large quantities. They consist of a target antigen-specific variable domain and a constant region with varying IgG isotypes. Depending on the type of Fc $\gamma$  receptors on the recipient's immune cells with which the IgG isotype interacts, the triggered immune response can be the opposite [14, 15]. If it interacts with activatory Fc $\gamma$  receptors, the cross-linking can induce antibody dependent-cellular cytotoxicity (ADCC) and the targeted cells are killed subsequently. This effect is needed if the antibody is targeting tumor associated antigens like CD20 (rituximab) and HER2 (trastuzumab). If, on the other hand, an immunostimulatory pathway should be targeted, it is reported to be beneficial, if the constant region binds to an inhibitory Fc $\gamma$  receptor [16, 17]. Since this interaction does not require intracellular signaling, it is assumed that the agonistic effect is mediated via cross-linking of immune cells [18]. Apparently there are also various monoclonal antibodies, which do not require any interaction with Fc $\gamma$  receptors. These are thought to either “only” block immune checkpoints or assemble the targeted immunestimulatory receptors on the cell surface by a specific configuration of their hinge region [19, 15].

In our mouse model experiment, which is presented in chapter 3 & 4, we use two agonistic anti-CD40 antibodies called clone 3/23 mIgG1 (mouse IgG1) and the commercially available FGK45. Both depend on cross-linking via inhibitory Fc $\gamma$  receptors [20, 18]. 3/23 mIgG1 is a chimeric version of the commercially available clone 3/23 developed in the group of Prof. Glennie (University of Southampton), where the rat IgG part has been changed to a mouse IgG, making it more potent with respect to the T cell response [18]. Unfortunately, a direct comparison to FGK45 is not available, but personal communication suggests that the agonistic effect is similar. It is still important to keep in mind that although both antibodies apparently interact with the same Fc $\gamma$  receptor [18, 21], the difference in the IgG of FGK45 with a rat IgG2a and clone 3/23 with a mouse IgG1 can lead to a difference in the cross-linking behaviour, which in turn can modulate the immune response differently.

**Immune checkpoint blockades** A multitude of receptors tightly regulate the activation of the immune system via “checkpoint” receptors. These are usually found on activated T cells and are thought to be a control against an excessive immune response and essential for maintaining central and peripheral tolerance to avoid autoimmune responses [22, 23]. But through the continued exposure to antigen in a tumor environment and by cancer cells utilizing this immune suppressive mechanism [24, 25] T cells are brought into an exhausted state. This state is marked by the dysfunction of T cells, which in the best case can be reversed by the inhibition of these immune checkpoints and leads to tumor rejection: Most prominently this has been shown with blockades of the surface proteins “cytotoxic T-lymphocyte-associated protein 4” (CTLA-4) and “programmed cell death protein 1” (PD-1) [23, 10, 7]. Anti-CTLA-4 was the first checkpoint inhibitor to be

approved by the FDA in 2011 and improved the long-term survival rates of unresectable metastatic melanoma from 10% to 20 – 30% [26, 27, 28]. Shortly after, in 2014, the first anti-PD-1 was approved for various solid tumors and Hodgkin’s lymphoma. The treatment via PD-1 blockade has good clinical responses with a 5-year survival rate in melanoma of 34 – 41% [29], and less severe adverse events compared to an anti-CTLA-4 treatment [30]. A combination of both therapies is reported to have an increased overall survival rate over each monotherapy [31].

Still, the responses between different tumor types, as well as the individual responses of patients with the same tumor are varying strongly, such that there is an ongoing debate about predictive markers for treatment success with immune checkpoint blockades. In the recent years a variety of factors contributing to a successful treatment have been discussed. On the one hand the (induced) immunogenicity of the tumor is thought to be important [32, 33], as well as mutations which make the tumor cells resistant to the attacks from immune cells [34]. On the other hand various characteristics of the immune and especially T cell repertoire responding to the tumor are reported to be predictive, as has been discussed above.

Many predictive features, like the infiltration of the tumor by a responding immune cell repertoire, are closely linked to the tumor microenvironment. If it is packed with immunosuppressive cells and has a dense extra cellular matrix, neither immune cells nor drugs can infiltrate or access the tumor cells [35]. These tumors were defined to be immunologically cold by Sharma and Allison [36] as opposed to T cell infiltrated tumors, which are referred to as hot tumors.

These findings in turn raise the question how immunotherapeutic strategies should be adapted for tumors, which do not respond to immune checkpoint blockades. One of the considered additional treatment options is to target CD40 [4].

**The effect of CD40 on CD8+ T cells** CD40 is expressed most prominently on antigen presenting cells, like B cells and dendritic cells, but also on myeloid cells and non-immune cells including fibroblasts and endothelial cells. The activation of CD40 by its ligand CD40L, which is expressed mainly on CD4+ T cells, is generally associated with enhanced cell survival, inflammatory responses and cytokine production [37]. The widespread expression of CD40 on different immune cells suggests that it has a broad role in the immune system [5].

The CD40/CD40L axis is in particular important during the initiation of an adaptive immune response (Fig. 1.2 station 2)). Although dendritic cells can activate CD8+ T cells in some infections without any further help, in most cases they need the support from CD4+ T cells [38]. This requires an interaction between dendritic cells, CD4+ and CD8+ T cells. CD4+ T cells express CD40L upon recognizing the antigen-MHC II complex and costimulatory ligands (B7) on dendritic cells, see Fig. 1.1a. In consequence, CD40L binds to CD40 on the dendritic cells and the latter are subsequently stimulated to express further stimulatory receptors (4-1BB ligand and B7). These in turn bind to receptors on CD8+ T cells (4-1BB and CD28) and enhance their activation, see Fig. 1.1b and ref. [39].

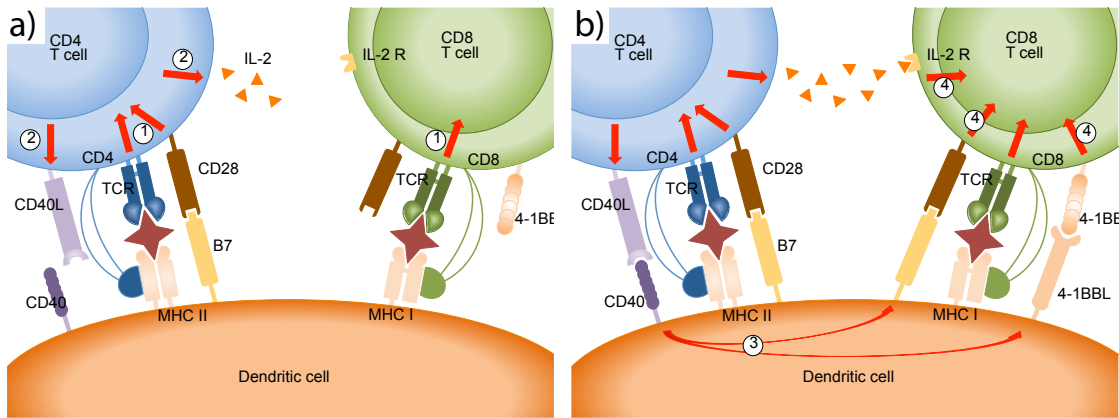


**Figure 1.1.:** CD40 dependent CD8 T cell stimulation mediated by dendritic cells. a) CD4 T cell is activated by a dendritic cell presenting an antigen-MHCII complex and a costimulatory ligand. It upregulates CD40L. b) CD40 binding to CD40L increases the expression of B7 and 4-1BB-L on dendritic cells. This binds to CD28 and 4-1BB on CD8 T cells providing additional stimulation. (adapted from ref. [38])

Indeed, many studies have shown that CD40 plays a major role for CD8 T cells, especially through this interaction, in the course of which APCs are licensed [40, 41, 42, 43] and can thus support the priming of CD8+ T cells [44, 45, 46, 47]. It also has been shown that CD40 activation can substitute CD4+ T cells in the activation of a CD8+ T cell mediated immune response [44]. Other studies report a crucial role of CD40 in CD8+ T cell memory formation [48, 49, 50].

**CD40 therapy in the clinical setting** The immunomodulatory ability of CD40 is employed in the treatment of autoimmune diseases [37] as well as cancer. The latter comprises two rationales [51]: On the one hand, CD40 is targeted on CD40 expressing tumors triggering cell mediated killing or transducing a pro apoptotic signal to induce their death. On the other hand agonistic anti-CD40 antibodies are applied to stimulate the immune cells. In this thesis we will focus on the latter mechanism in the CD8+ T cell context.

As early as 2007 first clinical trials with an agonistic anti-CD40 antibody (CP-870,893) showed objective partial response rates of 27% in melanoma patients [52]. CP-870,893 activates without depending on cross-linking with Fc $\gamma$  receptors, which is the likely reason for its potency [19], but can cause severe adverse events. In the following, a second generation of anti-CD40 antibodies with a constant domain binding to inhibitory Fc $\gamma$  receptors were introduced (Chi Lob 7/4, ABBV-428, APX005M, SEA-CD40) in the hope of lessening side effects, while increasing the therapeutic potency [53]. Many of these antibodies (APX005M, SEA-CD40, but also CP-870,893) are in ongoing or recently completed phase I clinical trials for various solid tumors, amongst them melanoma and pancreatic ductal adenocarcinoma. They are mostly combined with other cancer therapeutic agents (checkpoint blockades and vaccination strategies), but are also used as monotherapies, see [clinicaltrials.gov:#NCT02482168](https://clinicaltrials.gov/#NCT02482168), [#NCT03123783](https://clinicaltrials.gov/#NCT03123783), [#NCT02376699](https://clinicaltrials.gov/#NCT02376699),

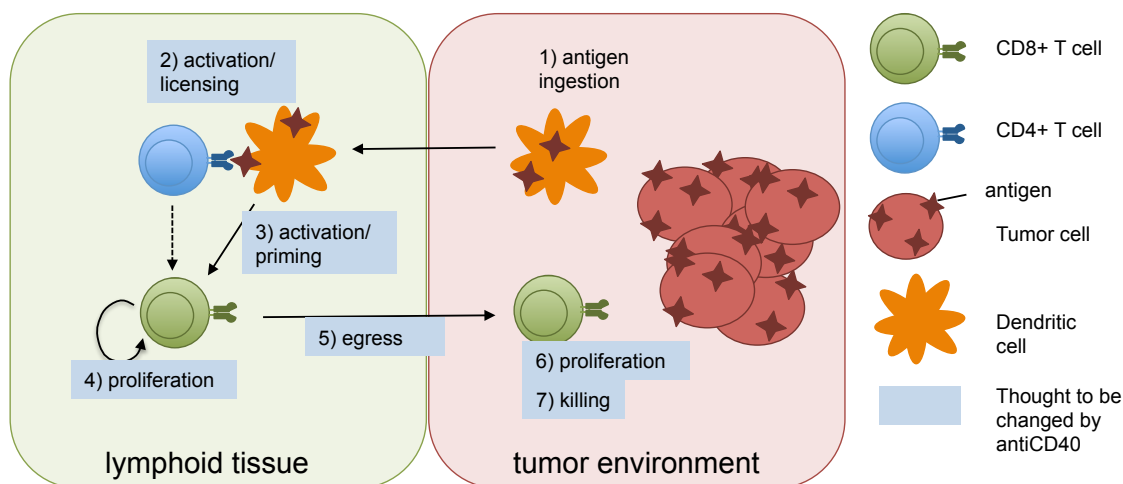


**Figure 1.2.:** T cell response to tumor. The role of the CD40-CD40L axis in station 2) and 3) is well established, see Fig. 1.1. There are multiple ways in which anti-CD40 treatment is thought to directly or indirectly affect the T cell response (blue boxes).

#NCT01103635 and #NCT03597282 and refs. [54, 55] .

In the light of the many attempts to apply anti-CD40 in a clinical setting for a variety of tumors with different co-therapeutic agents, it is pressing to better understand the effects of an anti-CD40 treatment. For this reason the effect of anti-CD40 has been investigated in various mouse models highlighting different mechanisms of action.

**CD40 treatments effects on CD8+ T cells in murine tumor models** Many murine tumor model studies agree that agonistic CD40 therapy generates protective tumor immunity. While some studies claim that anti-CD40 mainly acts on myeloid cells and macrophages [56, 57], others confirm the beneficial effect of anti-CD40 treatment on CD8+ T cells [47, 58, 59]—by enhancing activation and avoiding peripheral tolerance of T cells [60, 61, 62] and by inducing proliferation and the infiltration of tumors [63, 64]. However, most studies agree that the general effect of a anti-CD40 monotherapy on the tumor is subtle and that full potential can only be achieved if it is combined with other therapies, like immune checkpoint blockades, radiotherapy or chemotherapy [57, 63, 60, 64, 65]. For example, Byrne and Vonderheide suggest in ref. [63], that the chemotherapy releases the necessary antigens to support the CD40-mediated priming and activation of T cells, that this combination also has a positive effect on the macrophage, myeloid and dendritic cell compartment and that it supports the recruitment and expansion of T cells, the consequences of which can be observed in the tumor environment. Indeed, the many ways in which anti-CD40 is thought to act (see Fig. 1.2) raises the hope that an anti-CD40 treatment can turn an immunologically cold tumor into a hot one by acting on various immune cells and modifying the tumor microenvironment [4, 63].

Obviously, although anti-CD40 treatment has been investigated in many studies, the

---

exact effect on CD8+ T cells in a tumor context remains unclear (e.g. priming new T cells VS only boosting preexisting responses) [4]. Indeed, a mechanistic and time resolved understanding of the effects on naive T cells has not been the focus in the field, perhaps also because the effects of a monotherapy are subtle. With quantitative methods like mathematical modeling on the other hand, it is possible to highlight small changes of the measured and fitted T cell dynamics, which is done in this thesis. A more thorough understanding of the individual treatment effect can contribute to develop well-founded therapeutic strategies including an anti-CD40 therapy in a meaningful way.

### **Treatment success in different cancer types: The special role of melanoma**

**Melanoma as a model for immune responses to cancer** Melanoma was a rare skin cancer in the 50ies, but incidences have risen annually by 4 - 6% among the fair-skinned populations [66], an increase higher than for almost any other tumor [67]. Although treatable when in early stages, the median survival for metastized tumors is low. Even after the introduction of immunotherapy, especially the immune checkpoint blockades, around 50% of the patients do not respond to a treatment [68, 69].

And yet melanoma is in principle a “hot” tumor and relatively responsive to immunotherapy. This is probably due to 1) the high immune cell infiltrate, especially with CD8 T cells, which are thought to mediate the immune response to tumor to a large degree [70] 2) the high immunogenicity/ mutational load [71, 72] and 3) the relatively small stromal tumor microenvironment [73]. As a consequence, a large part of the advances and understanding gained in the field of tumor immunotherapy are first described in the context of malignant melanoma [74].

But even in a well studied tumor like melanoma the conditions for a successful immunotherapy and optimal support of the immune response are still unpredictable [72] and thus, better therapeutic approaches are needed. These do not necessary need to be new targets, but already an informed combination and timing strategy could change the efficacy substantially [75]. If these are once established in melanoma, it can be expected that lessons learned in this tumor model can be transferred to other tumor types as well.

To this end, in this thesis we employ the frequently used syngeneic B16 melanoma cell line in C57/BL6 mice and study its treatment with anti-CD40. It is well established in preclinical studies and used as a subcutaneous melanoma model to investigate the treatment of human melanoma [76] due to its highly invasive nature and its characterization to be “difficult to treat” [77, 78]. In order to study the T cell response to this tumor a B16 cell line expressing ovalbumin, B16/OVA, is applied together with so-called OT-I CD8+ T cells recognizing an ovalbumin derived antigen.

**The need for new therapies for pancreatic ductal adenocarcinoma** Pancreatic ductal adenocarcinoma (PDAC) stands in stark contrast to melanoma, being a tumor with low T cell infiltration and a dense extracellular matrix including various immunosuppressive cells [73]. In consequence, it is a cancer with an exceptionally poor prognosis having a 5 year survival rate of only 7-9% [79, 80]. Further reasons for the dismal prognosis are a late diagnosis and spread of metastasis at early stages leading to 80% of the patients having

already acquired unresectable tumors at the time of presentation. Most therapeutic options show little to no effect, including immune checkpoint blockades [81, 82, 83]. To reverse this phenotypically cold tumor into a tumor with a high T cell infiltrate and a less hostile and more permeable tumor microenvironment is a main goal for the research on combinatoric therapies with anti-CD40 [4]. Indeed, there is reason to believe that PDAC is a case for immune therapy, as it has an intermediate mutational load [71] and as it has been shown that PDAC are not void of infiltrating T cells, which furthermore respond to their autologous tumor [84].

In this thesis, to mimic the characteristics of the PDAC and to study the effect of an anti-CD40 treatment in a mouse model, our collaboration partners developed a murine PDAC cell line which has a similar histopathology to the human PDAC. Similarly to the melanoma cell line, it expresses a tumor specific antigen (ovalbumin), which was achieved by retroviral transfer.

### **Mathematical modeling in immuno-oncology**

Mathematical modeling in support of preclinical and clinical studies in oncology has co-evolved with the advances in this field and aims at resolving various research questions. Initial efforts often focused on describing tumor growth. The generalization of Gompertzian tumor growth [85] predicting the growth pattern from early tumor size measurements, was a first remarkable milestone. With the wake of immunotherapy in oncology in the 90ies many efforts focused on describing the interaction between tumor and immune cells in order to provide an insight into possible mechanisms governing the dynamics of the different players. It started with two to three component predator-prey like models, where the immune cells (very often T cells) are the predator and the tumor is the prey [86, 87, 88, 89]. Depending on the correctness of the assumptions, these models can explain the influences of the players on the observed phenomena in a general way, but may not be very useful for research relevant questions due to strong simplifications. The complexity of most mechanistic modeling approaches grew rapidly with the discovery of more cells and cytokines contributing to the immune surveillance and editing of the tumor. But in this case, most mechanistic modeling attempts suffer from the lack of data to inform these complex models. Hence, parameters are estimated from published data and assumptions with respect to the interactions are taken from the literature [89, 90, 91, 92] and many studies focus on investigating the emergent theoretical properties of the model, by conducting sensitivity and stability analysis [93, 94, 95, 96]. But the validity of the predictions and analysis in all these models depend strongly on the model assumptions and the chosen parameters from publications, as only little data is used to calibrate the model. Thus, the choice of the involved cell types can often be challenged by new findings and furthermore, in these models it is difficult to account for the fact that parameters from different publications are depending on their experimental setups and might not be compatible. Still, these models reveal interesting emergent properties of the observed system, which can give valuable hints about the underlying mechanism of an observed phenomenon.

On the other hand, there are classical “fit for purpose” [97] modeling approaches in

---

immuno-oncology like pharmacokinetic/pharmacodynamic (PK/PD) models, which are concerned with optimal dosing schedules by predicting the distribution, uptake and degradation of a medication [98]. These can partially replace dose selection trials [99], as has been done in the case of pembrolizumab [100, 101], a PD-1 checkpoint inhibitor. All in all, these are pragmatic and very helpful approaches, which provide informative predictions, but rely strongly on prior knowledge about the system and provide a limited new insight into the mechanisms of action of the investigated treatment.

A third option are data driven models, which aim at describing small and measurable aspects of an interaction mechanistically. This requires a cooperation in close coordination between experimentators and modelers, since the data that can be provided and the required information in order to calibrate the model must be well matched. Especially in the field of quantitative immunology, there are many data driven models studying the T cell division kinetics in acute infection settings [102, 103, 104], the T cell differentiation [105] and T cell responses to vaccines [106]. Importantly the mechanisms regulating T cell death, quiescence and proliferation has been successfully described with cellular machines (cyton model) and the concept of a so-called division destiny, which is the predestined number of divisions an activated lymphocyte does post activation [107, 108, 109, 110]. Many studies succeeded in assessing the T cell proliferation dynamics by analyzing cell proliferation dye measurements [111, 112]—often with a mixture model approach [113, 114]. Furthermore, stochastic dynamic models have been successfully applied to understand the underlying mechanisms producing robust T cell responses on a population level in acute infection settings [115] and the composition of the T cell ages has been investigated thoroughly by combing T cell fate mapping and mathematical modeling [116]. In addition, T cell activation and interaction with tumor cells at the level of molecular pathways is also studied with mathematical models, such that the emerging behavior can be explained [117, 118].

Thus, by focusing on the studied system and uniting or, if possible, ignoring negligible other influences, one can obtain mechanistic insights into the dynamics in question. These detailed studies can then eventually inform more complex models. To our knowledge the naive T cell response under an anti-CD40 treatment in a tumor context has not been studied so far, but would provide a valuable contribution to inform combination strategies with immune checkpoint blockades. Since we focus on the CD8<sup>+</sup> T cell response, we confine ourselves to investigate the effects of anti-CD40 on the stations 3) - 6) in Fig. 1.2.

### **Aims of this thesis**

In this thesis we strive to understand the effect of the immunomodulatory antibody anti-CD40 on the early T cell response to melanoma and pancreatic ductal adenocarcinoma.

Importantly, since the success and informative value of a model depends crucially on the type of data, the experiments were planned in close collaboration with Lena Kranz and Mustafa Diken at TRON (Translational Oncology at the University Medical Center of the Johannes Gutenberg University) in Mainz, Germany and Isabel Poschke at the dkfz (German Cancer Research Center) in Heidelberg, Germany, who also conducted the experiments.

The ability to distinguish different model mechanisms and parameters, furthermore, critically depends on the preprocessing of the data. Hence, the first chapter is dedicated to the introduction of a mixture model using data inherent information, which we developed for analyzing noisy *in vivo* measurements of cell proliferation dyes. This is applied to the T cell measurements in murine melanoma and pancreatic ductal adenocarcinoma experiments such that we obtain data which can be used in the second and third chapter. In the second chapter we establish a data driven model with the results of the melanoma experiment, which reveals dynamical properties of the T cell response to tumor, while ruling out other model options. In addition, a model selection successfully points out anti-CD40 treatment effects in this model framework. The same model successfully describes results of the pancreatic ductal adenocarcinoma experiment, where comparable findings with respect to the dynamics and anti-CD40 treatment effect could be identified.

With this mechanistic data driven modeling approach, we not only provide insights into the early T cell response in a tumor setting and the subtle effects of an anti-CD40 treatment on this dynamics, but can also point at the underlying differences between the two tumor models.

---

## Analysis of proliferating cells and modeling techniques

---

This chapter mainly discusses methods which have been employed in this PhD project to deduce the number of cell divisions from dye intensity measurements and to subsequently obtain the proliferation dynamics via modeling.

In the first part a mixture model is developed for the analysis of the cell dye measurements, such that the proportion of cells, which have undergone different numbers of divisions, i.e. are in different generations, can be distinguished. The second and third part are focusing on the modeling of cell proliferation and the fit of these models to the frequencies of cells in each generation, which are obtained from the first part.

### 2.1. Analyzing dye dilution measurements

#### 2.1.1. Introduction

If the proliferative process of cells cannot be observed directly, proliferation monitoring and analysis is usually conducted with either the help of molecules which are taken up during DNA synthesis by proliferating cells (e.g. Bromodeoxyuridine, in short BrdU) or with cell dyes, which are diluted with each cell division [111]. For the latter approach cells are dyed at the beginning of the experiment and the dye intensity halves with every division, such that the number of divisions after the dye has been applied can be deduced. Frequently used fluorescent dyes are carboxyfluorescein succinimidyl ester (CFSE), CellTrace<sup>TM</sup> Violet (CTV) and Cell Proliferation Dye eFluor<sup>TM</sup> 450 (CPD). The fluorescent intensity of the cells is measured with flow cytometry. In the following we will only speak of CFSE, which has been applied in all experiments discussed in this thesis, but the analysis works analogously for all dyes. As the dye intensity is halved with each division, the distribution of the CFSE intensities of cells (CFSE profile) under optimal conditions consists of equidistant proliferation peaks on a log scale, which can

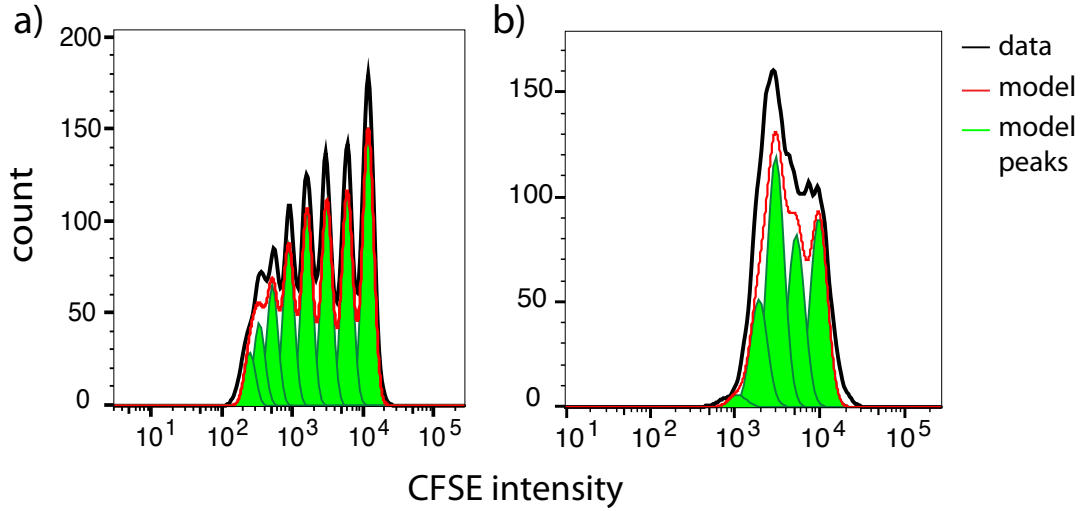


**Figure 2.1.:** Two exemplary CFSE profiles *in vivo* with mixture models fitted to the data with the program FlowJo<sup>TM</sup> (v10) a) Distinct proliferation peaks are fitted well. b) Without a clear undivided peak the fit needs time intensive manual adjustments of the model parameters to achieve a mediocre fit, even if the shape of the peak is informed from other well distinguishable CFSE profiles. Experimental data: Lena Kranz and Mustafa Diken.

be clearly distinguished from each other (Fig.2.1a).

These CFSE profiles are usually analyzed by separating the individual peaks with vertical lines (gating) or by fitting a mixture model to this profile.

However, when analyzing the CFSE profiles two limitations have to be taken into consideration. First, the applicable dye concentration is limited due to cytotoxicity. Thus, the number of distinguishable generations is limited, because the peaks overlap increasingly as their CFSE intensity decreases, due to the contribution of the autofluorescence of cells. Secondly, the peaks often overlap already in early generations due to the variability in the brightness of the initially dyed undivided cells. This becomes more pronounced in *in vivo* experiments (Fig. 2.1b). Thus, methods, that have been optimized for the analysis of *in vitro* data cannot be used for the data obtained and analyzed in this thesis.

For instance, the widely used software FlowJo<sup>TM</sup>, which assists the evaluation of flow cytometry measurements, contains a module for fitting and analyzing CFSE profiles with a mixture model consisting of lognormal distributions [119]. A strong overlap of the CFSE profile peaks, the approximation of single cell peaks with a parametric distribution and/or not accounting for the autofluorescence, made it difficult to obtain a reasonable fit to the data. Adjustments of the mixture model parameters by hand were needed and resulted in a fit, which nevertheless does not describe the data correctly (Fig. 2.1b), although the program performs well when peaks are clearly distinguishable (Fig. 2.1a).

Indeed, in other approaches using mixture models to fit *in vitro* CFSE profiles, we can see that it is sufficient to approximate the autofluorescence and the undivided cell

intensity distribution with lognormal distributions [113] or leave out the contribution of the autofluorescence [114], to obtain reasonable fits to the data.

Additionally, in these studies the CFSE profile fitting procedures are integrated into label-structured cell proliferation models. In this way, CFSE profiles are directly used as observables at successive time points to inform the models. This modeling approach also exploits the fact that time resolved measurements are easily available for *in vitro* experiments, such that the dynamics of the label loss and the proliferation dynamics can be better substantiated with data. For our model, however, which describes the dynamics of cell proliferation and absolute cell numbers in different organs simultaneously, it is useful to separate the CFSE profile fitting and obtain the proliferative information independently.

In the following, we will present a method that exploits data-inherent information for the analysis of CFSE profiles and for obtaining the frequencies of cells in each generation. To this end, it uses information on the undivided cell intensity and auto-fluorescent intensity distributions without having to assume a parametrized distribution. It, furthermore, flexibly accounts for the variability of the CFSE intensities in different groups of samples.

### 2.1.2. A mixture model for the analysis of cell proliferation measurements

A mixture model consisting of proliferation peaks and a fitting procedure are developed, with which overlapping peaks in the CFSE profile can be distinguished. Thus, the information on the number of cells in each generation can be obtained. This was written and implemented with the programming language R [120].

Section A provides an overview of the algorithm applied to single samples and substantiates the fitting procedure. A more detailed step-wise explanation of the algorithm is given in the section B. Section C explains how the results from B are brought together to finalize the optimization.

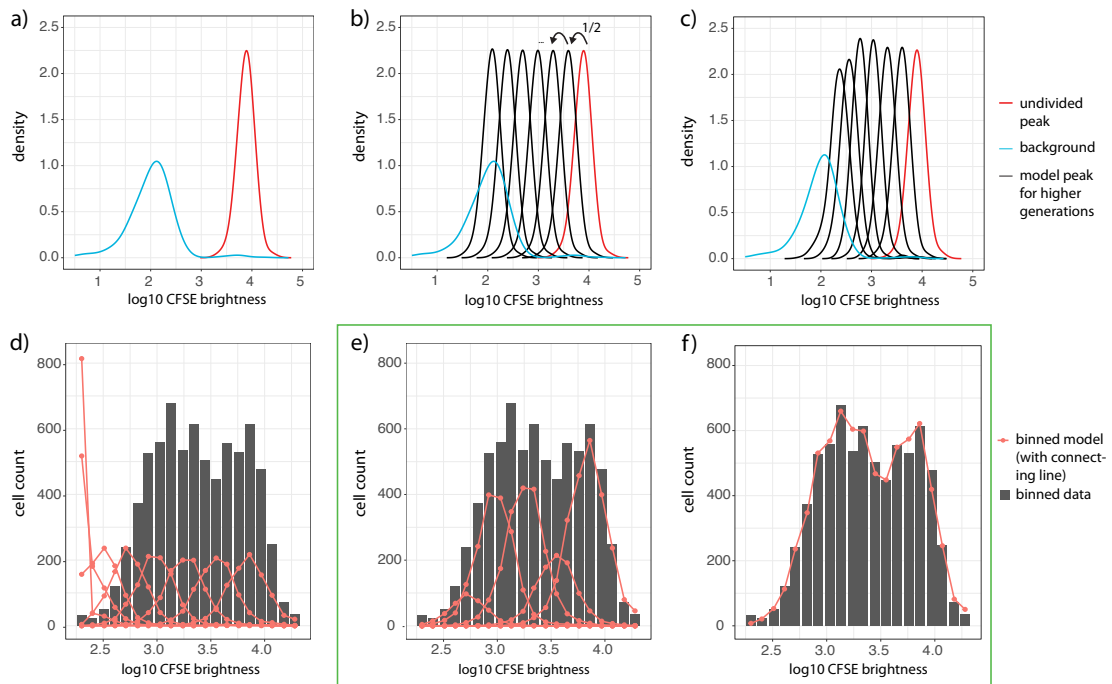


**Figure 2.2.:** Workflow to fit CFSE data a) An undivided cell peak (red) and a peak of unstained cells (blue), which are both obtained from the data, are used to inform our algorithm. b) The undivided cell peak is used as a model peak for undivided cells. Its fluorescence intensities are divided by factors of two—to mimic the intensity which is halved in every division—in order to obtain model peaks of higher generations. c) By sampling CFSE intensities from the unstained cells (blue) and adding them to the intensities of the model peaks in b) we account for the contribution of autofluorescence to the peaks. Dimmer peaks broaden. d) Binned model peaks with equal weights (red points, connected by lines) and binned data (grey bars), to which the model needs to be fitted. Green box: Fitted model after optimizing the weights of the peaks and finding the correct position on the x-Axis, i.e. the correct CFSE brightness for the undivided cells: e) Binned model peaks. f) Summed peaks from e). Experimental data: Lena Kranz and Mustafa Diken.

**A: Algorithm overview for a single sample and rationale**

**Data preparation:** The sample data are pre-processed by binning the CFSE intensities and we obtain a histogram (Fig. 2.2d, grey bars).

**Model creation:** First, the CFSE intensities of an undivided cell peak in the data is taken, which is used as an “undivided model peak”, i.e. a model peak for undivided cells. We shift this peak to some position  $p$  on the CFSE intensity axis, which we assume to be close to the undivided cell peak of the sample (Fig.2.2a, red). We will come back to the details of shifting the peak when the optimization is discussed.

Second, the undivided model peak intensities are divided by  $2^n$  ( $n = 0, 1, 2, \dots$ ), such that we obtain model peaks of the 0, 1, 2, ...th generation, which are equidistant on a log scale (Fig. 2.2b, red and black).

Third, we add CFSE intensities sampled from an autofluorescence peak to each peak in the data (Fig. 2.2a-c, blue), i.e. the two peaks are convoluted in a discrete manner. As a result the peaks of higher generations of our mixture model are broadening (Fig. 2.2c, broadening is more obvious with binned model peaks, see Fig. 2.4). The autofluorescence peak is part of the mixture model as well (Fig. 2.2c, blue).

Finally, this multi-peak model (Fig. 2.2c, all peaks) is binned with the same boundaries as the CFSE intensities of the sample (Fig. 2.2d, red points, connected by lines), such that the difference between the model and the data can be calculated for each bin and combined to obtain a chi-square statistic.

**Optimization:** Two types of variables of the mixture model need to be optimized to obtain a good fit to the data (Fig. 2.2 e & f): First, the absolute CFSE intensity of the model peaks, meaning the position  $p$  of the undivided model peak on the CFSE intensity axis, and second, the relative weights of the peaks.

The optimal position of the undivided model peak is determined by a step-wise increase of possible positions  $p$ . After setting a position the model is created as described above and the weights of the model peaks are optimized using a general purpose optimizer *optim*, [120]. Finally, the result for each position  $p$  (optimized weights for each peak and corresponding minimized chi-square statistic) is saved for this sample.

**Reason for separately optimizing the undivided model peak position in a discrete manner** It proves to be expedient to separately optimize the mixture model for different undivided model peak positions in appropriate intervals and choose the optimal position in a second step. The range, in which undivided model peak positions are tested, can be guessed by examining the profile to be fitted.

This procedure enables us to determine the optimal offset, i.e. undivided model peak position, not only for each sample specifically, but flexibly for combinations of samples by summing their chi-square statistic for each offset. Thus, depending on the sample combination, we obtain different best offsets. In this way samples can be combined, which are expected to have the same offset, e.g. samples measured on the same day and from the same organ. In principle, these samples are best fitted simultaneously to obtain a common best fit and corresponding offset. Unfortunately, this does not always work. Samples, where we expect the offset to be the same, can sometimes still differ in their

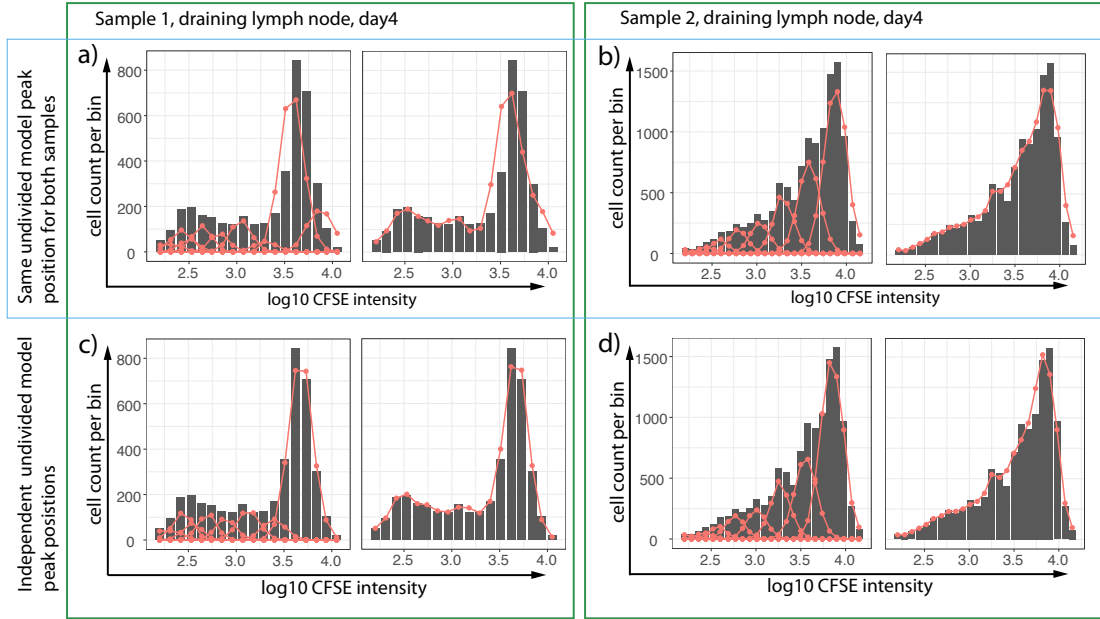


**Figure 2.3.:** Exemplary model fit (red dots with connecting line) to CFSE profiles from samples (grey bars), which were treated in the same way experimentally, but where the same undivided model peak position cannot be assumed: Both samples from two different mice are recovered from the draining lymph node and analyzed 4 days post CFSE staining and transfer. a) & b) The undivided model peak position resulting from a joint optimization of both samples is used for the model fits. This position is determined by adding the chi-square statistic of both samples for each undivided model peak position and taking the position which is minimizing this sum. c) & d) The undivided model peak position which minimizes the chi-square statistic for each sample individually is used for the model fits. We can see that in c) & d) the model fit looks better, especially for Sample 1.

undivided cell peak position, such that different offsets need to be taken. We encounter such a case in the third Melanoma experiment discussed in section 3.1. The OT-I T cell samples of different mice, which were taken from the same organ and on the same day post staining, need a different zero peak position. If the samples are fitted simultaneously, the CFSE profile cannot be described correctly, see Fig. 2.3. In other cases a whole group, where we expected the offset to be the same, has no clear undivided cell peak, such that we need to combine it with another group of samples to find a common plausible offset.

## B: Detailed description of the algorithm applied to each sample

**Step 1: Pre-processing of the CFSE intensities of the sample** The logarithm of the CFSE intensities of each cell is taken and the cell intensities are binned, such that we obtain a histogram. The number of bins  $k_{tot}$  is determined by Doane's formula [121]

$$k_{tot} = 1 + \log_2(m) + \log_2(1 + |g1|/\sigma). \quad (2.1)$$

Here  $\sigma = \sqrt{(6 * (m - 2)) / ((m + 1) * (m + 3))}$ ,  $m$  is the number of cells in the sample and  $g_1$  is the skewness of the distribution. As this frequently proved to be too few bins, especially for small  $m$ , we added the option to multiply this by a factor, which was between one and two for the samples analyzed in this thesis. The bins with their boundaries will be referred to as  $b_k = (b_{k,lower}, b_{k,upper})$ , where  $k = 1, 2, \dots, k_{tot}$ .

A maximum bin width  $\max(b_{k,upper} - b_{k,lower}) \leq 2/3 \cdot \log_{10}(2)$  is set, which ensured that the bin width is not larger than  $2/3$  of the distance between two peaks. The factor of  $2/3$  can be changed easily in our algorithm, but for the samples used in this thesis, it was an appropriate choice. The number of cells per bin  $b_k$  will be denoted with  $a_k$ .

Samples with  $m \leq 15$  are excluded from the analysis.

### Step 2: Choice of the tested positions

- The CFSE intensities of an undivided sample in the data are taken and these are introduced to the algorithm as a vector  $\vec{x}_0$ , which is now the undivided model peak (Fig. 2.2a, red peak). If this cannot be obtained from the data, this peak is sampled from a lognormal distribution, which has also been applied in similar studies ([113, 119]).
- A plausible area for the position of the undivided model peak is determined by comparing its original position  $p$  and the assumed position of the undivided cells of the sample  $p_{sample}$ . As we only need a rough estimation of both positions  $p$  and  $p_{sample}$ , these can be guessed by examining the profiles. Then  $\Delta p = \log_{10}(p_{sample}/p)$  is calculated, which is the shift needed on a  $\log_{10}$  scale to get from  $p$  to  $p_{sample}$ .
- For our data the appropriate distance between each tested offset, i.e. undivided model peak position, turned out to be 0.015 on a  $\log_{10}$  scale. This is a  $1/20$ th part of the distance between peaks and is sufficiently dense to find a good fit to our samples. To this end we determine offset factors  $q_j = 10^{0.015j + \Delta p}$ , with  $j = -10, -9, \dots, 9, 10$ . Multiplying  $q_j$  with the CFSE intensities of the undivided model peak will result in this peak's position being shifted by increments of 0.015 for increasing  $j$ s on a  $\log_{10}$  scale around  $\log_{10}(p_{sample})$ .

The following steps 3 and 4 are performed for each  $j$

### Step 3: Creation of the model peaks and pre-processing

- The undivided model peak intensities,  $\vec{x}_0$ , are multiplied with  $q_j$ .
- By dividing each entry of the vector  $\vec{x}_0$  by  $2^n$ , one obtains multiple vectors  $\vec{x}_n$  representing the brightness of cells having divided  $n = (0, 1, 2, \dots, n_{tot})$  times (Fig. 2.2b, black peaks). In our samples we mostly chose  $n_{tot} = 10$ . Although the model fit is relatively robust with respect to the choice of  $n_{tot}$ , in an extreme case, where the initial CFSE intensity was particularly bright, increasing this number was necessary to fit the data. Each of these strings

will be referred to as different model peaks and each entry corresponds to the CFSE intensity of cells in different generations.

- To each entry of the model peaks  $\vec{x}_0 \dots \vec{x}_{n,tot}$  an autofluorescence (Fig. 2.2a-c, blue peak) intensity is sampled and added (Fig. 2.2c, black peaks). The autofluorescence peak is taken from undyed cells, which ideally are of the same cell type as the dyed cells and taken from the same sample.
- The autofluorescence peak is included into the multi-peak model. We now have model peaks  $\vec{x}_n$  with  $n = 0, \dots, n_{tot} + 1$ , i.e.  $n_{tot} + 2$  model peaks. For convenience we will rename these to  $\vec{x}_l$ , with  $l = 1, \dots, l_{tot}$ ,  $l_{tot} = n_{tot} + 2$  and  $l = n + 1$ .
- The log of the intensities of all model peaks is taken.
- The kernel density estimate for each model peak is calculated and we obtain a smooth function.
- The proportion of each model peak which falls into the bin boundaries of  $b_k$  is calculated by numerical integration. One obtains a matrix  $C' = (c'_{k,l})$ , where the columns represent different peaks and the rows contain the proportions of cells in bin  $b_k$ . Proportions of the model peak outside the binned area are mapped into the first and last bin respectively. As the distribution of cells for low CFSE intensities becomes sparse in the  $\log_{10}$  space, the proportion of cells falling into  $b_1$  are calculated without smoothing and integrating and are entered directly into the first row of  $C'$ , i.e.  $c'_{k=1,l}$ .
- Finally each column, which represent a model peak, of  $C'$  is multiplied with the total cell number found in the CFSE profile and we obtain  $C$ .

**Step 4: Fitting of the peak weights** We introduce the weights  $\vec{\vartheta}$  with entries  $(\vartheta_1, \vartheta_2, \dots, \vartheta_{l,tot})$  for each model peak. The quantity of interest predicted by the model is the number of cells per bin  $b_k$  and will be referred to as  $d_k$ . This will be fitted to the binned CFSE intensities of the sample, namely  $a_k$ .  $d_k$  is calculated by

$$d_k(\vec{\vartheta}) = \sum_l c_{k,l} \vartheta_l, \quad (2.2)$$

where the weighted sum of the peaks is taken for every bin.

- $\vec{\vartheta}$  is optimized by minimizing the chi-square statistic

$$\arg \min_{\vec{\vartheta}} \chi^2 = \arg \min_{\vec{\vartheta}} \sum_k \frac{(a_k - d_k(\vec{\vartheta}))^2}{d_k(\vec{\vartheta})} = \hat{\vartheta}. \quad (2.3)$$

Here it turns out to be quicker to first optimize all  $\vec{\vartheta}$  simultaneously, although they are dependent as they should sum to one. In a second fit

this dependency is accounted for by only optimizing  $(\vartheta_1, \vartheta_2, \dots, \vartheta_{n-1})$ , such that  $\vec{\vartheta} = \left( \vartheta_1, \vartheta_2, \dots, \vartheta_{l-1}, 1 - \left( \sum_{i=1}^{l-1} \vartheta_i \right) \right)$ , which sometimes improved the fit slightly.

- Thus, for each offset  $q_j$ , we obtain the minimum chi-square estimate  $\hat{\vartheta}_j$  and a corresponding minimized chi-square statistic  $\chi_j^2$ .

**Step 5: Save the result for this sample** The set of optimized weights  $\hat{\vartheta}_j$  with corresponding  $\chi_j^2$  for each tested offset  $q_j$  is saved for this sample.

### C: Finding the optimal offset factor $q_j$

For a single sample the optimal offset factor  $q_j$  can be determined by comparing the minimized  $\chi_j^2$  and choosing the  $q_j$  belonging to the smallest  $\chi_j^2$ . For a group of samples  $G$  the optimal offset  $q_j$  can be calculated easily: The  $\chi_j^2$  is summed over all samples in the group  $G$  for each  $j$ , i.e.  $\chi_{j,G}^2 = \sum_{g \in G} \chi_{j,g}^2$ , and the offset  $q_j$  corresponding to the minimal  $\chi_{j,G}^2$  is taken.

In the following chapters the group of samples, where we expected the offset to be the same, are samples taken on the same day after CFSE application and from the same organ in the mouse. As some organs had only highly proliferated cells and no clear undivided cell peak, we combine these with other organs of the same day, where we find enough undivided cells. In some rare cases, samples of the same day and same organ differ strongly, such that we take the individual offsets for these samples.

The resulting distribution of normalized weights  $\vec{\vartheta} = (\vartheta_1, \vartheta_2, \dots, \vartheta_{l,tot})$  plotted against the corresponding number of divisions will be referred to as the cell division profile.

### 2.1.3. Accounting for overlapping peaks in the model

As discussed in the introduction the model peaks for higher generations overlap stronger such that the weights for these peaks become hard to identify. Thus, we introduce a threshold for the overlap between peaks of neighbouring generations  $(n, n+1)$ , with  $n = (0, 1, \dots)$ , above which the weights of these peaks are merged.

To this end, we first calculate the model peaks for each sample using its optimal undivided model peak position  $q_j$  and its corresponding background, but with equal weights for each peak. They are binned (Fig. 2.4) and for each two neighbouring peaks  $(n, n+1)$  the overlap  $o$  is calculated from the fraction of cells shared in these bins. Then, for each  $(n, n+1)$  the mean  $\langle o \rangle$  and standard deviation  $sd_o$  of the overlap is calculated for all the samples from the same time point and organ. If  $(\langle o \rangle + sd_o) > 0.66$  for  $(n, n+1)$ , we merged the weights of all peaks  $\geq n$  for each of these samples and will refer to them as generation  $n+$ .  $sd_o$  is added to  $\langle o \rangle$ , as the overlap varies strongly in some cases. Like this we obtain a conservative estimate for our threshold. An overview over the generations merged in each experiment is found in Tab. 3.2 in section 3.1.2 and in Tab. 4.2 in section 4.1.2, where the analyzed data from our experiments are described.

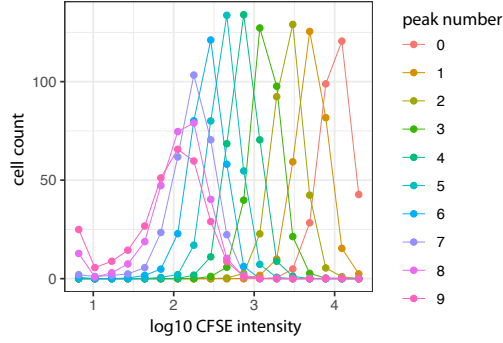


**Figure 2.4.:** Example of equally weighted binned model peaks and the corresponding number of cells per bin (points) connected by a line to guide the eye.

## 2.2. Estimating errors

The changing number of cells over time is modeled with the help of ordinary differential equations, where the cells in different compartments are the states  $\vec{x}(t)$  and the rates are given by a set of parameters  $\vec{\Theta}$ . We obtain a set of differential equations

$$\dot{\vec{x}}(\vec{\Theta}, t) = f(\vec{x}(\vec{\Theta}, t), \vec{\Theta}). \quad (2.4)$$

From the solutions of the differential equation one can calculate the quantities of interest with the observation function  $\vec{y}(t)$ , which can be compared to experimentally measured observables ( $y_i$ ):

$$\vec{y}(\vec{\Theta}, t) = g(\vec{x}(\vec{\Theta}, t), \vec{\Theta}) \quad (2.5)$$

To determine how well the model fits a given set of data, a likelihood function  $L(\vec{\Theta}|\vec{y})$  is introduced. For a given set of parameters  $\vec{\Theta}$  and data  $\vec{y}$  this likelihood function is equal to the probability density function  $p(\vec{y}|\vec{\Theta})$  to measure these data given the parameter set  $\vec{\Theta}$  and the model.

If the measurements are independently normally distributed it takes the form:

$$L(\vec{\Theta}) = \prod_i \left( \frac{1}{\sqrt{2\pi\sigma_i^2}} \exp\left(-\frac{(y_i - y_i(\vec{\Theta}))^2}{2\sigma_i^2}\right) \right). \quad (2.6)$$

However there are cases where the errors  $\sigma_i$  are not known or the errors estimated from the data cannot be trusted, which would lead to a biased fit to the data. A possibility to fit the data in these cases is the estimation of the errors, where they become a function of the model parameters:  $\sigma_i = \sigma_i(\vec{\Theta})$ .

Calculating the negative loglikelihood  $l(\vec{\Theta}) = -\log(L(\vec{\Theta}))$  we thus obtain:

$$l(\vec{\Theta}) = \text{const.} + \frac{1}{2} \sum_{i=1} \left( 2\log(\sigma_i(\vec{\Theta})) + \left( \frac{y_i - y_i(\vec{\Theta})}{\sigma_i(\vec{\Theta})} \right)^2 \right). \quad (2.7)$$

The maximum likelihood estimate  $\hat{\Theta}$  is the parameter vector minimizing the negative loglikelihood function and provides the best fit given the model and the data.

## 2.3. Estimating proliferation dynamics from cell division profiles

### Introduction

The process of proliferation in a simple birth model can be described with the following ordinary differential equation (ODE)

$$\begin{aligned} \dot{G}_0(t) &= -kG_0(t) \\ \dot{G}_1(t) &= 2kG_0(t) - kG_1(t) \\ \dot{G}_2(t) &= 2kG_1(t) - kG_2(t), \\ &\dots \end{aligned} \quad (2.8)$$

where  $k$  is the proliferation rate and  $G_i$  are the number of cells in the  $i$ th generation. This intuitive modeling approach and its implicated results are used because of its comparative simplicity [122, 123, 124]. A solution of this ODE with time dependent rates is discussed in the first part (section 2.3.1).

Still, it is important to keep in mind, that this way we implicitly introduce an exponentially distributed waiting time for each division, although cells have a finite minimal interdivision time [125]. Indeed, *in vitro* measurements of interdivision times show smaller coefficients of variation (CV) than an exponential distribution [126]. Although *in vivo* interdivision times are assumed to have a larger CV due a heterogeneous environment, it is unlikely to exceed the CV of an exponential distribution. In consequence we often see the distribution resulting from the solution of the ODE to have a higher variance than the cell division profile obtained from the data, which worsens the fit. This problem will be discussed in the second part (section 2.3.2) and an alternative to using the frequencies of the cell division profile as observables will be discussed in the third part (section 2.3.3), which circumvents this issue. It is worthwhile mentioning that deBoer and Perelson even argue in ref. [125] that fits of the ODE model to the cell proliferation data, lead to an overestimation of the average interdivision time, because the exponential waiting time leads to a division cascade of cells dividing without intermission, which needs to be slowed down.

In general, in order to include more realistic interdivision times, one can introduce a Smith-Martin like model with a fixed delay in the cell cycle [127, 128, 129, 130], one

can include cell age dependent rates [111, 113, 131] or introduce other (not exponential) distributions for the division times [131, 132, 107]. If one wants to stay within the formalism of ODEs, it is possible to introduce multiple compartments for one state with the same transition rate leading to consecutive exponential waiting times, such that the effective interdivision time would be gamma-distributed. The choice of the modeling approach strongly depends on the type of data—e.g. do we only consider means or also higher moments—and more importantly, the level of detailed information one hopes to obtain from the data. Our *in vivo* experiments have multiple sources of noise and the focus will therefore lie on understanding which proliferation dynamics are in principle able to describe the data in different organs rather than an accurate estimate of interdivision time distributions. As we find reasonable fits with our simple modeling approach, we thus do not consider more complicated modeling options in our later models, and we have to keep the limitations of this approach in mind.

### 2.3.1. Properties of the cell proliferation ODE model

It is easy to see that the solution of (2.8) results in Poisson distributed frequencies of cells in different generations [122]

$$\frac{G_n(t)}{G_{tot}(t)} = \frac{(2kt)^n}{n!} e^{-2kt}, \quad (2.9)$$

where  $G_{tot}$  is the total cell number.

The models in the following sections required time dependent proliferation rates  $k(t)$  and we try to understand the influence of the exact form of  $k(t)$  on the CFSE profile in order to make informed choices for our rate.

Solving (2.8), with a time-dependent proliferation rate  $k(t)$ , we can show (see suppl. section A.1), that the number of cells in each generation  $G_n(t)$  is defined by

$$G_n(t) = \frac{2^n G_0}{n!} K(t)^n e^{-K(t)}, \quad (2.10)$$

where  $K(t) := \int_0^t k(t') dt'$ . The total number of cells is  $G_{tot}(t) = G_0 e^{K(t)}$ , which is the solution to  $\dot{G}_{tot}(t) = k(t)G(t)$  and can be solved analogously to the first part in suppl. section A.1. Thus, the frequency of cells in each generation is given by

$$\frac{G_n(t)}{G_{tot}(t)} = \frac{(2K(t))^n}{n!} e^{-2K(t)} = \frac{\lambda^n}{n!} e^{-\lambda}, \quad (2.11)$$

with  $\lambda = 2K(t)$ . We see that the frequencies of cells in different generations are again Poisson distributed and only dependent on the integral  $K(t)$  of the proliferation rate  $k(t)$ .

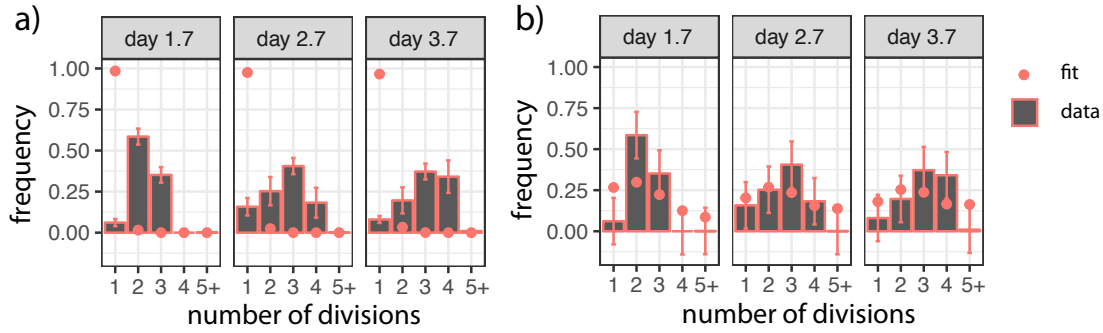


**Figure 2.5.:** Model fits to cell division profiles with and without error estimation. The bars indicate the frequency of cells in each generation (cell division profile) and the points are representing the solution of the ODE, which has been fitted to the data. a) The last generations with small errors dominate the model fit. b) Reasonable fit, where the errors were estimated, but the discrepancy between the solution of the ODE and the data becomes obvious. Experimental data: Lena Kranz and Mustafa Diken.

### 2.3.2. Estimation of the proliferation dynamic from cell division profiles with an ODE model

Two limitations have to be taken into consideration, if we want to leverage the information contained in the cell division profiles, i.e. the percentages of cells in each generation, by fitting them directly with our ODE model.

First, the shape of the cell division profile, especially at early time points, deviates from a Poisson distribution due to less variable (non-exponential) interdivision times as discussed in the introduction. For example, we can often observe an abrupt decrease of frequencies in higher generations. This is likely a consequence of the finite interdivision time of each cell [111] resulting in a lack of cells beyond the maximum number of divisions which a cell can do in a given time.

An extreme case of this characteristic is observed in the first melanoma experiment introduced in section 3.1, which is analyzed as described in section 2.1. Due to the abrupt decrease of frequencies in higher generations with additionally very small errors (last generation  $<sd> = 0.002$ ), this leads to a model fit dominated by the last generations (see Fig. 2.5a). On the other hand, similarly extreme cell division profiles are not observed in other experiments in section 3.1, which casts doubts on the correctness of the small errors. We can thus fit the cell division profile while estimating errors as mentioned in section 2.2: Although the model fit looks better than in Fig. 2.5a, one sees now the discrepancy between the shape of the cell divisions profile and the fit. The model prediction exhibits a flatter profile with a higher variance (Fig. 2.5b). As a consequence, when using the cell division profiles directly for the fit, there is a possibility that trying to fit different aspects of the exact shape leads to more local minima of the likelihood.

Second, it is problematic that our observables, i.e. the different generations of the CFSE profile, are not independent. If they are all used for fitting, the information gained from

fitting these observables is overestimated. Thus, when fitting the profiles directly at least one generation is omitted, which would be completely dependent from the frequencies in the other generations. In cases where 2 or more generations only make up  $\leq 2\%$  of the total frequencies, we omitted these generations.

To circumvent these problems, for cases where a fit to the cell division profile is not necessary, we introduce and use a summary statistic as an observable instead. This is discussed in the next section.

### 2.3.3. Mean number of divisions as a summary statistic of the cell division profiles

In order to omit the necessity to describe the exact shape of the data with our model and circumvent the problems mentioned in the section before, the mean number of divisions can be calculated and used as an observable. We define this as the sum of cell frequencies weighted with the number of divisions they have done. It is

$$\text{MDiv}_{n+} = \frac{x_1 + x_2 \cdot 2 + \dots x_{n-1} \cdot (n-1)}{\sum_{i=1}^{n-1} x_i}, \quad (2.12)$$

where  $x_i$  is the number of cells in generation  $i$ . The last generation  $n+$  which is the sum of all cells larger than  $n-1$  is omitted, as one would have to guess a weighting factor, which is not known for the data. Instead the fraction of  $n+$  cells is used directly as an observable.

Furthermore the 0th generation is omitted from the normalization of the mean number of divisions and is used directly as an observable as well. This turns out to be useful, because the 0th generation contains information on the activation rate/ time-to-first-division, which is distinct from the proliferation rate.

---

## T cell dynamics in a melanoma mouse model

---

In this chapter it is our aim to both qualitatively and quantitatively understand the initial dynamics of T cells upon tumor encounter and the effects of an agonistic anti-CD40 treatment on this dynamics through mathematical modeling. To this end three similar experiments with Melanoma mouse models and adoptively transferred T cells (OT-I T cells) recognizing the tumor have been conducted. The first is the most extensive experiment, where we have four measurement time points. It is referred to as Exp. 1 or the “time-resolved” experiment and a mathematical model is developed to describe its OT-I T cell dynamics. The analysis of this experiment leaves the need to confirm differences observed between the data from the treatment and control experiments and to give more precise answers regarding the proliferation and activation rate estimates: The second experiment, referred to as Exp. 2 or the replicate experiment, is a limited repetition and is used to confirm the subtle differences observed between the data of anti-CD40 treated and control mice. But it is not used for a model fit as it contains only two measurement time points with few cells for the CFSE analysis and no additional measurements of the proliferation dynamics to inform our model. We aim to answer the questions regarding the activation and proliferation dynamics with a second follow-up study. In Exp. 3 or the “proliferation-resolved” experiment, the proliferation of OT-I T cells is assessed in more detail with an additional cell proliferation dye. This data is not only compared to the original study, but a slightly adapted model is fitted to the data, such that conclusions drawn from the results of the first fit can be tested and refined.

The chapter is structured as follows. Section 3.1 highlights common differences between the treatment and control data and furthermore, discusses differences between the results of the three experiments. The presented cell division profiles have been analyzed with the methods introduced in the previous chapter (see section 2.1). In section 3.2 the developed mathematical model and its fit to the data is discussed: We first introduce the basic model structure for Exp. 1 and Exp. 3. Second, we discuss alternative model

structures, which have been considered to fit the data. Third, by fitting the basic model structure to the treatment and control data simultaneously and conducting a model selection, we determine mechanisms which need to be different between the two settings and thus, can assumed to be influenced by the anti-CD40 treatment.

Finally, we present and discuss the best model fit to each experimental data set. In section 3.3 the results for both experiments are compared.

All experiments in this chapter have been conducted by Lena Kranz and Mustafa Diken at TRON (Translational Oncology at the University Medical Center of the Johannes Gutenberg University) in Mainz, Germany. The experiments and the analysis of the flow cytometry data were jointly discussed in order to obtain adequate data for modeling.

## 3.1. Results of the melanoma mouse experiments

### 3.1.1. Experimental setup

In all three experiments the tumor grown from the well established Melanoma cell line B16-OVA expressing ovalbumin (OVA) as a model antigen was inoculated subcutaneously into mice. This tumor site has the advantage that the tumors could be monitored and measured at all time points during the experiment. After 14 or 21 days, when the tumor had a size between  $87 \pm 11 \text{mm}^3$ ,  $38 \pm 5 \text{mm}^3$  and  $350 \text{mm}^3 \pm 62 \text{mm}^3$  respectively, the mice were divided into a control and a treatment group of equal sizes, such that 3-5 mice could be sacrificed on each read out day in each group (see Fig. 3.1). On the day, on which the mice were grouped and which is referred to as day 0, 5 million CFSE-dyed OT-I T cells recognizing an OVA derived peptide (SIINFEKL) have been injected. Together with the OT-I T cell transfer one group received an isotype control (RatIG2a) and the other group was treated with  $500 \mu\text{l}$  of an agonistic anti-CD40 antibody (FGK45). A large number of transferred cells was necessary in order to recover enough OT-I T cells in different organs for a sound statistical analysis. By varying the time between tumor inoculation and cell transfer (14 days, 21 days and 21 days) our collaboration partners tried to achieve similar tumor sizes for all experiments on the day of cell transfer, but still they remained significantly different.

Samples from the blood, the tumor and the draining lymph node (where the whole organ can be used as a sample) were read out on day 2, 3, 4 & 7, day 2 & 4 and day 3 & 4 post OT-I cell transfer, respectively (see Fig. 3.1). In these samples the OT-I T cells and endogenous T cells were identified and analyzed with flow cytometry. Their number was extrapolated to the sample and eventually to the whole organ via true count beads. In this context, the mice were all assumed to have  $1500 \mu\text{l}$  of blood. The proliferation information is obtained from the measurements of the CFSE intensity in all experiments and additionally BrdU in the third experiment, which was given i.p. 14h prior to the measurement.

The CFSE measurement quantifies how often cells have divided. BrdU, on the other hand, is only incorporated by dividing cells, such that we can additionally check whether cells in different generations are having varying fractions of dividing cells

### 3.1. Results of the melanoma mouse experiments

**Table 3.1.:** Exact times, when samples were taken

Exp.	“Day 2”	“Day 3”	“Day 4”	“Day 7”
1	40h/ 1.7d	64h/ 2.7d	88h/ 3.7d	160h/ 6.7d
2	40h/ 1.7d	- -	86h/ 3.6d	- -
3	- -	66h/ 2.75d	90h/ 3.75d	- -

at the time point of measurement.

The exact times when the samples were taken vary, such that, when referring to the data taken on day X, this implies slightly different times for different experiments, see Tab. 3.1. In figures and fits we only use the exact times.

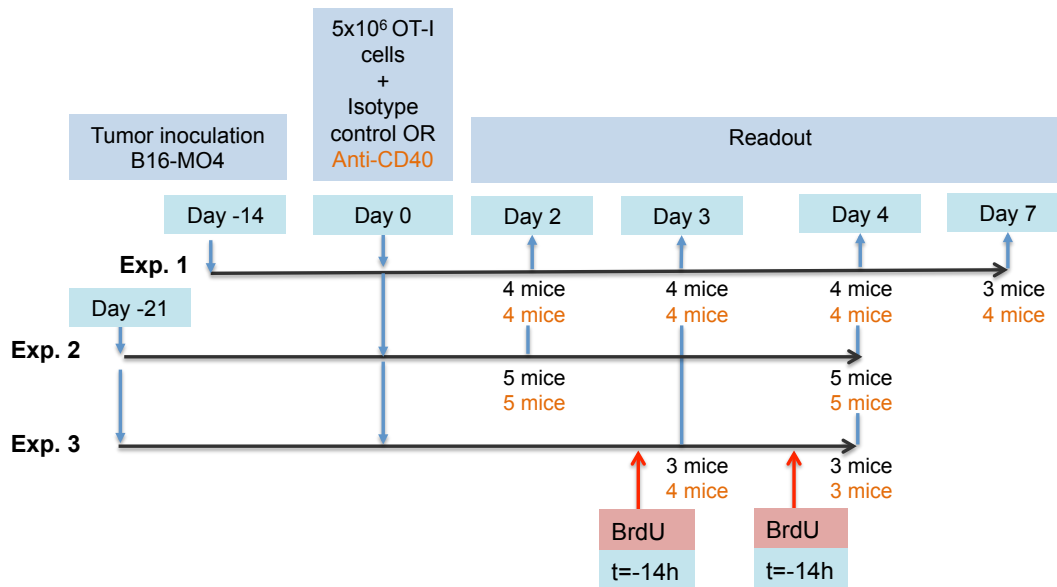


**Figure 3.1.:** Overview over the three murine melanoma experiments. The number of available mice at different time points in the control (black) and treatment (orange) groups are indicated. Experiments conducted by Lena Kranz and Mustafa Diken.

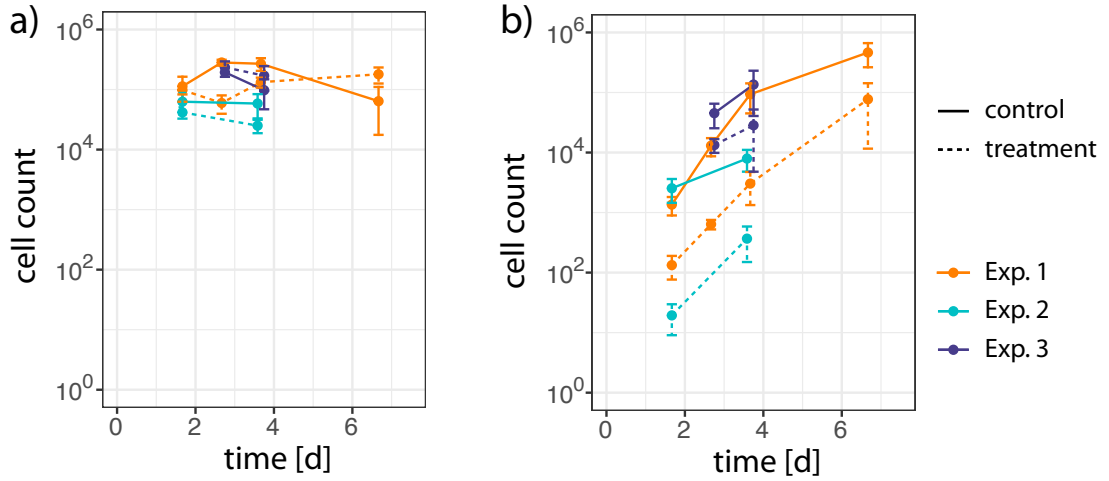


**Figure 3.2.:** Absolute OT-I T cell numbers measured for the treatment (dashed) and control (solid) in the a) draining lymph node and b) tumor in Exp. 1 (orange), Exp. 2 (light blue) and Exp. 3 (purple). Experimental data: Lena Kranz and Mustafa Diken.

### 3.1.2. Changes induced by the anti-CD40 treatment and common features of the experiments

Despite the biological variability of the experiments, it is possible to distinguish common tendencies in the data obtained from treated mice.

**Absolute cell numbers** An unexpected difference between the treatment and control is, that the absolute OT-I T cell numbers in the tumor are lower for the treatment setting (Fig. 3.2b). Intriguingly, especially in the first experiment we can see that the anti-CD40 treatment has an effect on the tumor growth (significant differences in tumor sizes on day 1.7 and 3.7) and is hinting towards a contained tumor growth in the follow-up studies (Fig. 3.3b). The smaller numbers of OT-I T cells in the tumor is not only a consequence of the smaller tumors, but indeed the T cells are less densely populating the tumor in the anti-CD40 treated mice (suppl. Fig. B.1). For the absolute cell numbers in the draining lymph node we cannot discern a shared tendency induced by the treatment between the experiments (Fig. 3.2a).

**Cell division profiles and information on the proliferation dynamics** The CFSE intensity measurement is analyzed as described in the previous chapter (section 2.1). The generations which are merged according to the criteria in section 2.1.3 are found in tab. 3.2. As discussed in section 2.1 we only use CFSE samples for analysis with more than 15 cells and here, we only show data where a minimum of three samples is available. This data is also used for the model fitting in section 3.2.

The cell division profiles do not change in Exp. 1 and Exp. 3 after day 2.7/2.75 in the draining lymph node and thus the proliferation of the OT-I T cells seems to be

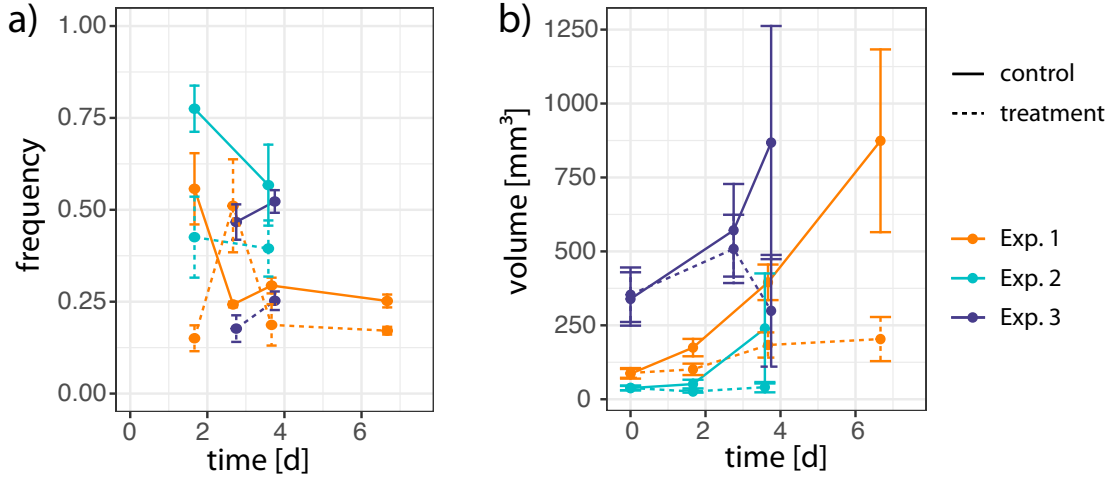


**Figure 3.3.:** a) Fraction of undivided OT-I T cells in the draining lymph node derived from the CFSE measurements and b) tumor sizes in Exp. 1 (orange), Exp. 2 (light blue) and Exp. 3 (purple) for the treatment (dashed) and control (solid). Experimental data: Lena Kranz and Mustafa Diken.

attenuated over time in this organ (Figs. 3.4 and 3.6). Another explanation would be, that with higher generations the proliferation stops or the egress from the draining lymph node increases. But the decrease of the BrdU+ fraction from day 2.75 to day 3.75 in Exp. 3 hints at a decreasing proliferation in the draining lymph node over time (Fig. 3.7). Contrasted to our observation in the draining lymph node, it seems that the division in the tumor is ongoing (Figs. 3.4 - 3.6 and Fig. 3.7). Again, it is not clear from the cell division profiles whether this is due to a continued proliferation in the tumor or due to a preferential migration of proliferated cells from the draining lymph node. However the increasing fraction of BrdU+ cells in the tumor as opposed to the draining lymph node hints at a steady or even increasing proliferation over time. Regarding the cell division profiles, there is a marked difference between the first experiment and the third. The sudden decrease of cells in higher generations in the draining lymph node and the peaked fraction of cells in generation 4 in the tumor in Exp. 1 (Fig. 3.4) are at odds with the cell division profiles in Exp. 3. Exp. 2 seems to have an intermediate characteristic. As the tumor sizes are consistently smaller in the first and second experiment, this might be part of the explanation.

The lack of BrdU+ cells in the undivided generation and the increased fraction of BrdU+ cells with higher generations (Fig. 3.6) can be understood with the following consideration: The availability of BrdU is reported to be short in [133], i.e.  $\ll 14h$ . If the  $S$ ,  $G_2$  and  $M$  phase together are distinctly shorter than  $14h$  (which is very likely for activated T cells, see [125, 126, 102]), then all cells in  $S$  phase at the time point of BrdU availability, will have divided by the time they are measured. In consequence, the fraction of BrdU+ cells at the time point of measurement depends on the number of cells

**Table 3.2.:** Generations, of which the weights from the CFSE intensity data analysis (section 2.1), can be trusted

Exp.	Day 2		Day 3		Day 4		Day 7	
	dLN	tumor	dLN	tumor	dLN	tumor	dLN	tumor
1	0-5	0-5	0-5	0-5	0-4	0-4	0-4	0-4
2	0-5*	0-5*	-	-	0-4	0-4	-	-
3	-	-	0-5	0-4	0-4	0-4	-	-

\*Here the weights could be measured for 0-6, but for simplicity and comparability it is reduced to 0-5

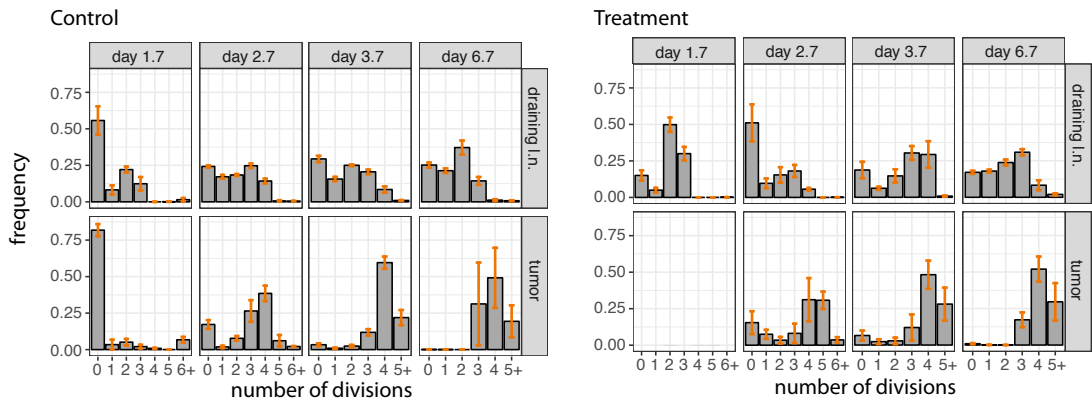


**Figure 3.4.:** Cell division profiles of OT-I T cells derived from the CFSE measurement data of Exp. 1 for control (left) and treatment (right) and for the draining lymph node (upper panel) and tumor (lower panel). Experimental data: Lena Kranz and Mustafa Diken.

in  $S$  phase in the previous generation 14hrs ago. So, if the previous generation has more cells, which is the case for higher generations, it receives a comparatively high number of BrdU+ cells until the time point of measurement. And the undivided generation is left by all its BrdU+ cells and obviously receives none from a lower generation.

**Fraction of undivided cells** If cells are governed by a common proliferation rate, we expect more or less Poisson distributed frequencies in the cell division profile, (see section 2.3.1). If we bear this in mind, the remarkably high undivided cell fraction (Fig. 3.4 - 3.6) hints at a distinct time-to-first-division. We take a closer look at the dynamics of the undivided cells in the draining lymph node, where the activation of naive cells is supposed to take place (Fig. 3.3a). Here, we see that the fraction is lower for the anti-CD40 treatment setting, which hints at an increased activation rate due to the treatment. This would be in line with the reports describing CD40 to support the priming of T cells [44, 45, 46, 47]. All the more it is surprising to see the elevated fraction of undivided cells on the third day for the treatment setting in the first experiment (Fig. 3.3a), which

### 3.1. Results of the melanoma mouse experiments

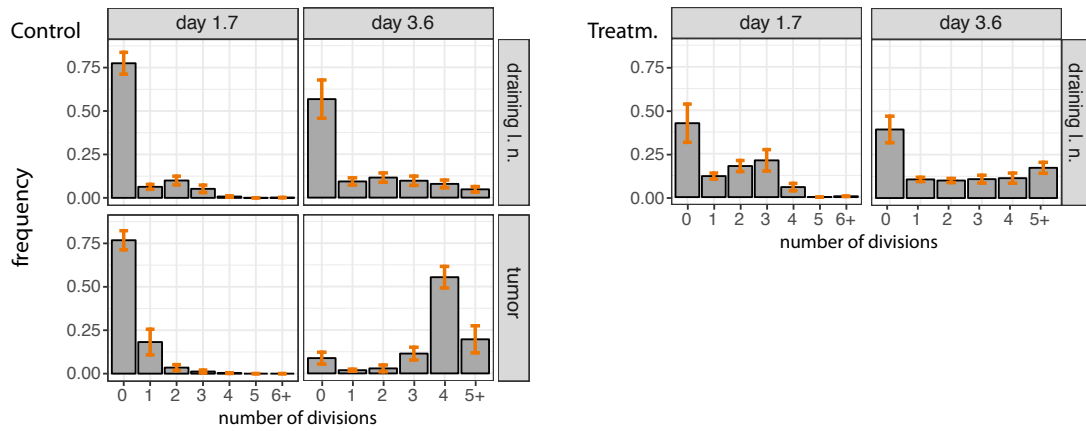


**Figure 3.5.:** Cell division profiles of OT-I T cells derived from the CFSE measurement data of Exp. 2 for control (left) and treatment (right) and for the draining lymph node (upper panel) and tumor (lower panel). Experimental data: Lena Kranz and Mustafa Diken.

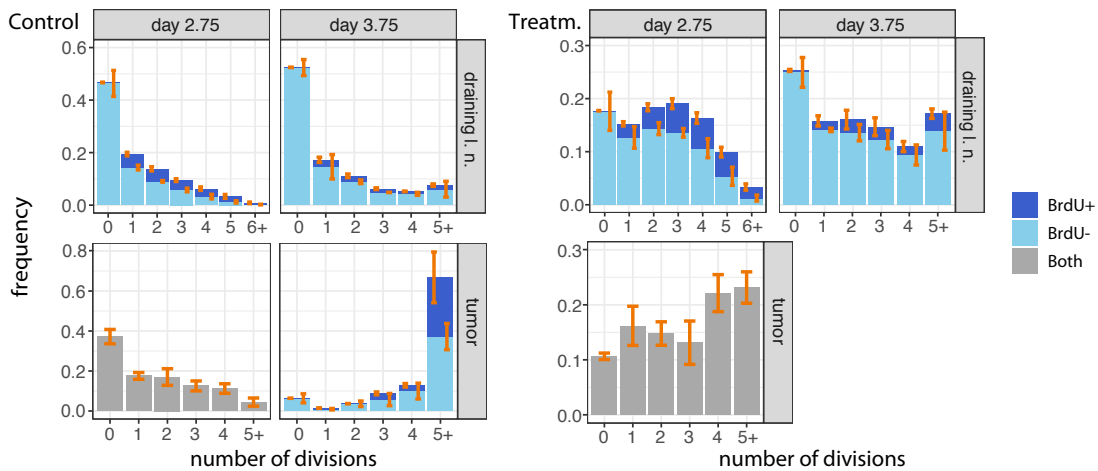


**Figure 3.6.:** Cell division profiles of OT-I T cells derived from the CFSE measurement data of Exp. 3 for control (left) and treatment (right) in the draining lymph node (upper panel) and tumor (lower panel). Fractions of all cells are grey and the fraction of BrdU+ and BrdU- cells, if known, are blue and light blue respectively. Experimental data: Lena Kranz and Mustafa Diken.

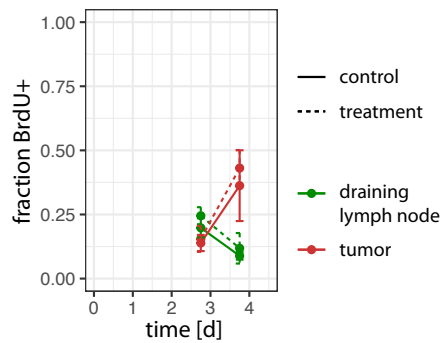


**Figure 3.7.:** Fraction of BrdU+ OT-I T cells from Exp. 3 in draining lymph node (green) and tumor (red) for the treatment (dashed) and control (solid) setting. Experimental data: Lena Kranz and Mustafa Diken.

we could see in all mice of this experiment. But as this dynamic was not reproducible in the follow-up experiments, it remains questionable, whether this is not an artefact. In the tumor, on the other hand, an infiltration by undivided cells or a distinct activation rate seems unlikely and it remains unclear by what the dynamics of the undivided cells (Fig. 3.4 - 3.6) are governed.

**Mean number of divisions** The mean number of divisions, see section 2.3.3, show a slightly enhanced proliferation for the anti-CD40 treatment setting in the draining lymph node in all experiments (see Fig. 3.8). In order to have a comparable measure for all days, the mean number of divisions  $MDiv_{5+}$  is shown, as the 4th generation is the maximum number of generations up to which we can trust the CFSE analysis on all days and in all experiments (see also Tab. 3.2). This is not always conveying a good idea of how much cells have divided, as it has no contribution from the highly proliferated generations (here, generation 5+). Especially on day 4 in the third experiment, this leads to a putatively low mean number of divisions in the draining lymph node in the treatment setting as a large part of the cells are already in generation 5+ and not contributing to the  $MDiv_{5+}$ .

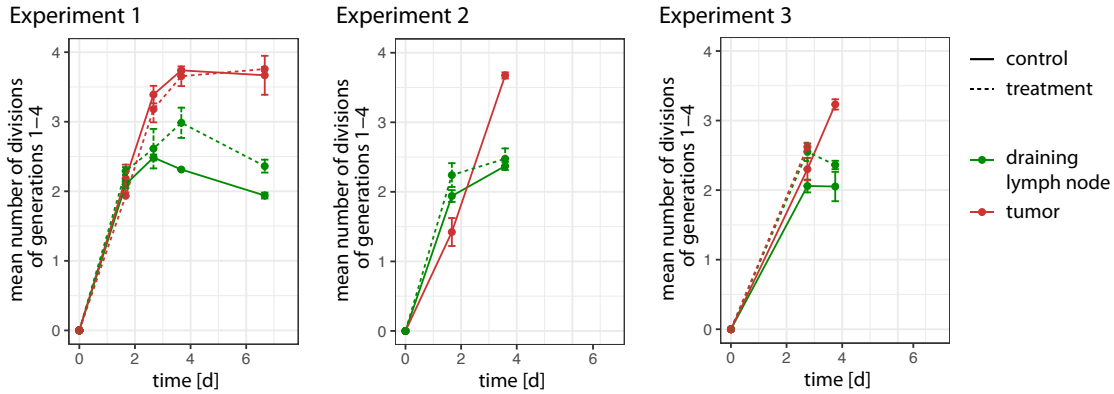


**Figure 3.8.:** Mean number of divisions of the OT-I T cells for treatment (dashed) and control (solid) in the draining lymph node (green) and tumor (red). Experimental data: Lena Kranz and Mustafa Diken.

### 3.2. Mathematical model describing the T cell dynamics in a melanoma mouse model

We aim at developing a comprehensive but simple model, which can describe the OT-I T cell dynamics and explain the differences between treatment and control data, which we observe in the first (time-resolved) and third (proliferation-resolved) experiment. The experiments contain complementary information: The first describes the T cell dynamic over an extended period of time, but lacks precise information on the proliferation dynamics. To augment this the proliferation-resolved experiment was conducted and focuses on the proliferative activity of the T cells in each generation at a given time point, but contains only two measurement time points.

The first section 3.2.1 motivates the construction of our “basic model structure”, which is kept as simple as possible. Subsequently, in section 3.2.2 we discuss other plausible model structures, which have been considered and we motivate our choice of the “basic model structure”. With “model structure” we refer to the set of differential equations and the used observation functions (see section 2.2), which can describe both the treatment and the control data separately. If we fit a certain model structure, i.e. our “basic model structure”, to the treatment and control data simultaneously, we can test many nested models. These nested models differ only with respect to the parameters which are different between the treatment and control. Choosing the best model among these means to find the parameters, which need to be different between the treatment and the control, i.e. are influenced by the treatment. Thus, in section 3.2.3 a model selection among the nested models is conducted and we define and present the best models of both experiments in sections 3.2.4 and 3.2.5. Finally, in section 3.3 the parameters of the best models of each experiment are compared.

### 3.2.1. Basic model structure construction

In this section the basic model structure (Fig. 3.9) used for our best model fits in sections 3.2.4 & 3.2.5 is presented. Some tested alternative model structure options are briefly outlined here, but the more arguable decisions are discussed separately in the next section 3.2.2.

#### A common model structure for both experiments

For the basic model structure (Fig. 3.9) the focus lies on the draining lymph nodes, where the naive OT-I T cells are primed and proliferate, as well as on the tumor, where the cells are expected to egress to and presumably take up their proliferative activity again [134]. Here, we expect to see the most pronounced effects of an immunomodulatory anti-CD40 treatment.

A source term describes the influx of naive cells into the draining lymph node. We also consider a time-dependent decrease of the source term. The time dependence improves the fit to the first experiment ( $\Delta \text{AIC} = 3.9$ ), but worsens the fit to the third experiment ( $\Delta \text{AIC} = 3.3$ ). In the first experiment the fit without a decreasing source term performs already well and in addition the number of undivided cells in the blood, which is a plausible source for the influx, stays constantly high (see suppl. Fig. B.2b). Thus, we decide to stay with a constant source term over time.

As discussed in section 2.3.2, we expect the time-to-first-division to be different and we introduce an activation rate for undivided cells in the draining lymph node, to govern their dynamics.

The undivided cells in the tumor cannot be explained by a simple migration of activated cells from the draining lymph node with our constructed model (tested for first experiment, not shown) and an infiltration of the tumor by naive undivided cells from the blood would be unexpected. Yet we see a non-negligible fraction of naive cells in this undivided cell population (percentage of CD44-CD62L+ cells:  $0.135 \pm 0.002$  in Exp. 3; no CD44 measurement in Exp. 1). In consequence, treating them as an artefact resulting from an unphysiologically high number of transferred OT-I T cells, which were circulating in the organism, is the simplest model assumption. In our basic model structure, we introduce a constant number of naive cells in the tumor, which does not change over time. Indeed, the number of undivided cells stays constant until day 4 in the first time-resolved experiment (suppl. Fig. B.2a).

Due to the observed decrease of the BrdU+ fraction in the draining lymph node (Fig. 3.7) and a seemingly attenuated proliferation seen in the cell division profiles (Fig. 3.4-3.6), we introduce an exponentially decreasing proliferation rate over time with

$$p_{dLN}(t) = p_{dLN,0} e^{-\alpha t}, \quad (3.1)$$

where  $p_{dLN,0}$  is the proliferation rate at  $t = 0$  and  $\alpha$  is the decay rate.  $\alpha$  is constraint to be positive, such that we only consider constant or decreasing proliferation rates over time in the draining lymph node. An increased proliferation rate would be unexpected, as the proliferative activity of T cells should be strongest after antigen encounter and priming

and then decline over time [135, 102, 136]. Other model options for the proliferation rate are discussed in section 3.2.2.

Due to the observed increasing BrdU+ fraction in the tumor (Fig. 3.7), we nevertheless test a time dependent increase of the proliferation in this compartment for the proliferation-resolved experiment. We find—as is discussed in section 3.2.2—that no significant improvement of the fit is observed and conclude that there is not a strong enough indication for an increasing proliferation in the tumor as well.

**Fitting errors** The errors of our data stem from a small number of mice (three to four) such that they are not reliable and we decide to estimate them instead, see also section 2.2 on error estimation. For example, the errors of the absolute cell numbers in the draining lymph node and tumor (Fig. 3.2) appear to be very variable without any evident explanation.

We choose relative errors for the absolute cell numbers and distinct absolute errors for the mean number of divisions and the frequency of cells in different generations. For the latter the errors of the draining lymph node and the tumor are allowed to be different. The reason behind this is that the CFSE intensity analysis of the tumor data is more challenging due to lower cell numbers on early days and due to the comparatively small number of undivided cells on later days, see section 2.1. In consequence, we trust these frequencies resulting from the CFSE data analysis less than the ones obtained from the analysis of the data from the draining lymph node. As the number of mice for each data point, i.e. each time point and treatment setting, is similar (three to four mice), we did not adapt the errors according to the number of mice contributing to it.

### Adaptations of the model structure for the different experiments

Four points need to be adapted for the basic model structure of the time-resolved experiment and the proliferation-resolved one. By and large, all adaptations can be regarded as simplifications/expansions of the same model structure—see also the discussion in section 3.3, where the results are compared:

First, we choose a time-dependent and growing egress rate  $e_{dLN}(t)$  for the time-resolved experiment. This dynamic egress rate is not needed for the proliferation-resolved experiment, where the model is only calibrated with data from two subsequent days. For a discussion of alternative options with respect to the egress rates, see section 3.2.2. As the egress needs an upper bound we use a logistic growth function:

$$e_{dLN}(t) = \frac{e_{dLN,max} \cdot e_{dLN,0} \cdot \exp(\beta t)}{(e_{dLN,max} + e_{dLN,0} \cdot (\exp(\beta t) - 1))}, \quad (3.2)$$

with  $e_{dLN,max}$  and  $e_{dLN,0}$  defining the upper and lower bound respectively and  $\beta$  shaping the inclination and the time scale of the increasing egress rate.

Second, in the model for the time-resolved experiment a division stop mechanism is introduced. Otherwise it is not possible to explain the abrupt decrease of frequencies after the fourth generation in the draining lymph node and a prominent accumulation of

cells in the fourth generation in the tumor. The model is implemented such that the cells can divide four times in the draining lymph node and twice after their egress into the tumor (abbreviated with “Gen 1 - 4” and “Gen +2”). For the model of the proliferation-resolved experiment no proliferation stop has been implemented. Again, other tested options can be found in section 3.2.2.

Third, in order to accurately reflect the incooperation of BrdU we subdivide the proliferation rate into rates determining the progression through the cell cycle phases. We follow the idea that the S, G<sub>2</sub> and M-Phase resemble a fixed program, which runs through once it is started and that the length of the G<sub>1</sub> phase can be subject to changes through which the cell cycle length is predominantly determined [127, 137, 112]. Thus, we combine the G<sub>2</sub> and M-phase with the S-phase and this is referred to as S/G<sub>2</sub>/M phase, with the corresponding rate  $p_S$ . The mean of the rate  $p_S$  is assumed to be constant over time and the same in the draining lymph node and the tumor, i.e.  $p_S = p_{S,dLN} = p_{S,T} = \text{constant}$ . The progression through the G<sub>1</sub>-phase is governed by the rate  $p_{G_1}$ . The rate  $p_{G_1}$  of the G<sub>1</sub> phase on the other hand can change. In our basic model structure it is time dependent in the draining lymph node ( $p_{G_1,dLN}(t) = p_{G_1,dLN,0} \exp(-at)$ ) and is determined by a different rate in the tumor  $p_{G_1,T}$ , which is constant over time. Alternative dependencies of  $p_{G_1,dLN}$  and  $p_{G_1,T}$  are tested in section 3.2.2.

With this implementation we implicitly assume that the length of the phases are independent, which is in good agreement with the modeling approaches in ref. [127, 137, 112], although this is a matter of debate [126]. With the phase distinction it is possible to distinguish the fraction of cells taking up BrdU at a given time point, which are the cells in S-Phase. Because the time spent in the G<sub>2</sub>/M-phase is reported to be small against the time spent in the S-phase [112], we assume that all cells in the S/G<sub>2</sub>/M-phase of our model are taking up BrdU. In addition the BrdU availability is reported to be short [133], such that we simplify this by assuming BrdU to be available only at the time point of its administration, i.e. 14h prior to the measurement, and that all cells in the S/G<sub>2</sub>/M-phase of our model instantaneously take up BrdU at this time point (Fig. 3.10).

Finally, for both experiments we fit different observables, i.e. quantities in the data to which the outcome of the model is compared to during the fitting procedure (see section 2.2). For the first experiment, besides the absolute cell numbers, we are fitting the mean number of divisions  $MDiv_{n+}$  (which is calculated from the relative frequencies of cells in generation 1 to  $n - 1$ ) and the relative frequencies of cells in the 0th and  $n+$  generation. For the proliferation-resolved experiment we want to make full use of the information on the fractions of BrdU+ cells in each generation and thus fit these directly. To test the robustness of these fits, we switch the observables, i.e. we fit each generation of the cell division profile in the time-resolved experiment and  $MDiv_{n+}$  in the proliferation-resolved experiment, and discuss this in the section introducing the best model (see section 3.2.4 and 3.2.5).

### Summary of the basic model structures

The schematic figure of the basic model structures for both experiments can be seen in Fig. 3.9.

### 3.2. Mathematical model describing the T cell dynamics in a melanoma mouse model

For the time-resolved experiment we have in total  $r=13$  parameters: source rate, activation rate, proliferation rate in the draining lymph node  $p_{dLN}$  defined by the parameters  $p_{dLN,0}$  and  $\alpha$ , proliferation rate in the tumor  $p_T$ , egress rate  $e_{dLN}$  defined by the parameters  $e_{dLN,0}$ ,  $e_{dLN,max}$  and  $\beta$ , the number of inactive cells in the tumor and four error parameters: a relative error for the absolute cell numbers  $sd_{abs}$ , an absolute error for the mean number of divisions  $sd_{MDiv}$  and absolute errors for the frequencies of cells in generation 0 and  $n+$  in the draining lymph node  $sd_{dLN}$  and tumor  $sd_T$ . We have 61 observables (see suppl. section B.2).

For the proliferation-resolved experiment we have in total  $r=11$  parameters: source rate, activation rate, proliferation rate in the draining lymph node  $p_{G1,dLN}$  &  $p_S$ , where  $p_{G1,dLN}$  is defined by the parameters  $p_{G1,dLN,0}$  &  $\alpha$ , proliferation rate in the tumor  $p_{G1,T}$  (&  $p_S$ ), egress rate  $e_{dLN}$ , the number of inactive cells in the tumor and three error parameters: a relative error  $sd_{abs}$  for the absolute cell numbers and absolute errors  $sd_{dLN}$  &  $sd_T$  for the frequencies of cells in all generations in the draining lymph node and tumor. We have 79 observables (see suppl. section B.2).

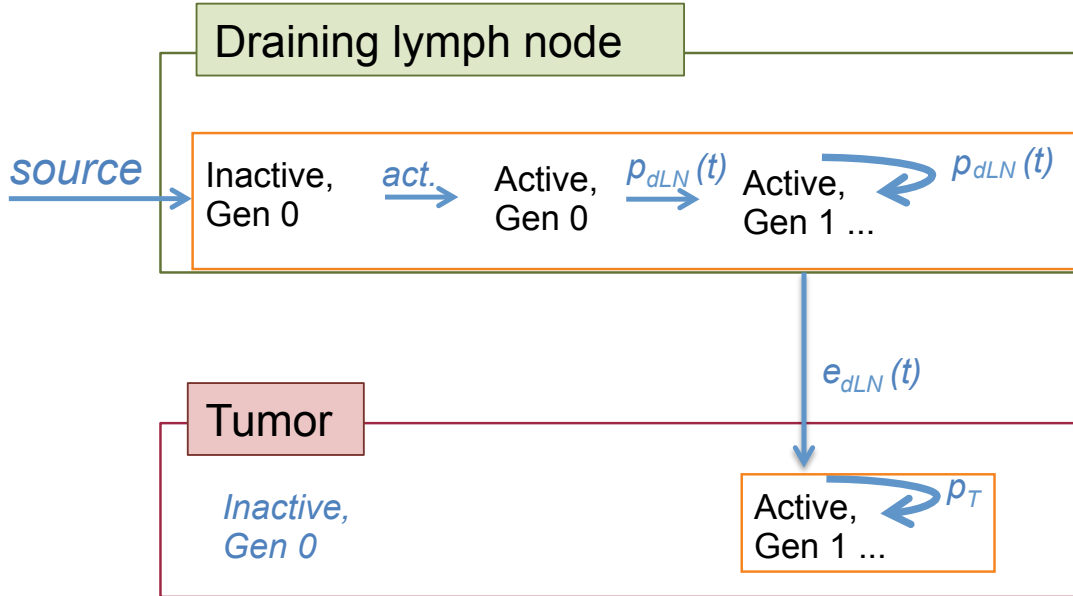


**Figure 3.9.:** Basic model structure applied for both experiments. States are in black and parameters are in blue. **States:** Active generations continue dividing in the model for the proliferation-resolved experiment. In the time-resolved experiment model division stop after 4 divisions in the draining lymph node and after 2 additional divisions in the tumor. **Parameters:** Logistic growth of the egress rate  $e_{dLN}(t)$  for the time-resolved experiment. For the proliferation-resolved experiment  $e_{dLN}$  is constant. Exponential decay of proliferation rate in the draining lymph node  $p_{dLN}(t)$  in both experiments, where  $p_{dLN}(t)$  is subdivided into  $p_{G1,dLN}(t)$  &  $p_S$  in the proliferation-resolved experiment. The detailed model for the BrdU uptake during the proliferation (orange boxes) for the proliferation-resolved experiment can be seen in Fig. 3.10.

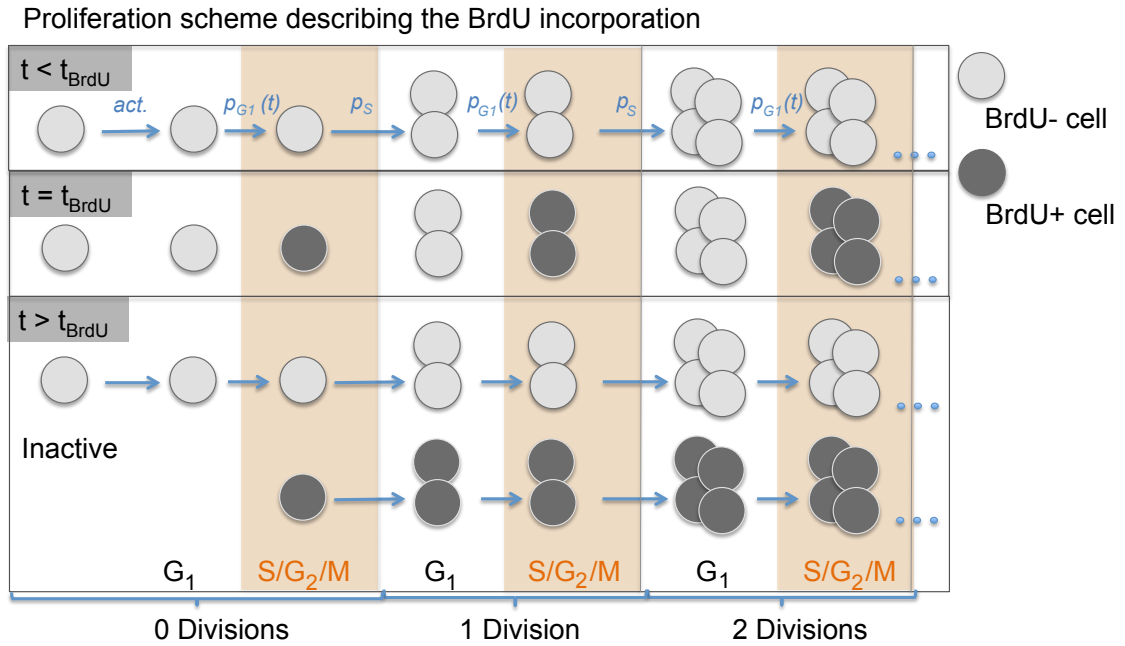


**Figure 3.10.:** Schematic figure for the model describing the BrdU uptake of dividing cells in the draining lymph nodes. Analogous mechanism is applied in the tumor albeit without undivided cells (cells with “0 divisions”). At the time point of BrdU administration ( $t = t_{\text{BrdU}}$ ) all cells in S phase instantaneously become BrdU+, but not anymore at later time points, which is reflecting the short BrdU availability. After this the proliferation continues independently for BrdU+ and BrdU- cells.

### 3.2.2. Alternative models

In the following, alternatives to the basic model structure for both experiments, which have been introduced in the preceding section (section 3.2.1 and Fig. 3.9), are modified and tested. For each model structure we compare the model fit, where the data of the treatment and control experiments are fitted simultaneously with all parameters being different, but for the errors and the source term. The latter parameters are equated, as there is no plausible reason, why they should be affected by the anti-CD40 treatment. Due to the fact that almost all parameters can be different, it is comparable to fitting the model structures to the treatment and the control data separately.

Of course we cannot look at all possible model modifications, such that we focused on replacing questionable assumptions, e.g. the division stop mechanism and time dependent rates, with plausible alternatives. We furthermore, pursue the question whether proliferation in the tumor is necessary.

## General considerations

**Two types of rate modifications: generation dependent and time dependent mechanisms** In our alternative model structures we use two types of rate modifications. One is to introduce a time dependency and the other is to use a generation dependency, in which the rates—in a simple case—depend on the number of divisions a cell underwent. If we want to test alternative time dependent mechanisms to the ones we have, there are a few obvious choices (i.e. constant, exponential, logistic), which are easily implemented and which we use in the following section. Our division stop mechanisms in the time-resolved experiment, however, is a special case of a generation dependency of the proliferation rate and if we want to test alternatives, it is important to see how our current mechanism compares with other generation dependent mechanisms. This is discussed in the following.

**Our division stop mechanism is a special case of a division destiny** Generally, with division destiny we refer to a mechanism, in which the number of divisions a cell can do is determined before its first division. Thus, our division stop mechanism in the draining lymph node is a way to implement a simple case of a division destiny, as all cells are determined to stop after four divisions. This is abbreviated with „Gen 1-4“. In the tumor two further divisions after entering this compartment are allowed. This is referred to as a local division stop mechanism. This can be viewed as a realization of a local and special case of a division destiny, which is determined upon entering the tumor and is denoted with “Gen +2”.

**Cases where our division stop can be generalized with a simple generation dependent proliferation** The obvious generalization of a simple division stop is a generation dependent proliferation, where every generation has its own proliferation rate. Thus, it comprises the possibility of the proliferation to cease after any number of divisions. In consequence, the division stop in the draining lymph node (“Gen 1-4”) is straightforward to generalize with a generation dependent proliferation. This is done in the alternative model structures in order to make the division stop more flexible.

However, the local division stop in the tumor cannot be generalized by replacing it with a simple generation dependent proliferation. This follows from the fact that here, the rate is not only dependent on the number of generations but also on the history of the cell, i.e. in which generation it entered the tumor. But combining the history with a generation dependent rate adds a lot to the complexity to the model. So, when we test alternatives, we try to replace this local division stop mechanism with a simple generation dependent proliferation, knowing that this is not a generalization, but a different mechanism.

It is interesting to note that a generation dependent decrease of the proliferation rate can be seen as a generalized division stop mechanism. It is not the number of divisions a cell can do, which is predetermined, but the number of divisions from which the cells starts to slow down its proliferation rate.

**Death rate** The information on cell death at hand is the fraction of dead OT-I T cells in the life/dead gate of the flow cytometry analysis. Generally, it is difficult to introduce this information into the model, because the dead cells in the life/dead gate have died and accumulated in an unknown time range before the measurement. Hence, the fraction of dead cells is not straightforward to interpret or compare: The number of dead cells depends on the number of cells which lived in that unknown time range and thus contributed to the measured dead cells, but these are compared to the number of cells living at the time point of measurement. Comparisons between different organs and time points are still possible, if we assume the time range in which the cells accumulate not to be large or the relative change of the absolute cell numbers at different time points and organs to be tolerably similar.

When introducing a death rate into the basic model structure, we have to keep in mind that, for example, a uniform death rate is difficult to identify: This rate is introducing an exponentially decreasing scaling factor with time in all compartments and thus, can be largely compensated by a source term (see section A.2). Nevertheless, for consecutive time points we should be able to discern a death rate.

We find dead cells in the draining lymph node and tumor with a generally higher fraction in the latter. This induced us to fit two simple model extensions to both experiments: to the basic model structure we either add a uniform death rate for all compartments or a death rate only in the tumor. We fit this model simultaneously to the treatment and control data with all parameters being different between the treatment and control, but for the source term and the errors. In the case of the time-resolved experiment the additional death rate does not improve the fit. In consequence, as these models are more complex than the basic model structure, they perform worse with respect to the AIC. In contrast, a fit including a death rate in the tumor—but not an overall death rate—improved the fit to the data of the proliferation-resolved experiment by  $\Delta\text{AIC} = 1.5$ .

Nevertheless, as the difference is not large and as we want to keep the basic model structures of both experiments comparable and simple, we decide to not include death rates. Still, it is noteworthy, that the model fit also provides evidence for a death rate in the tumor, albeit only in the case of the proliferation-resolved experiment. And, furthermore, these results do not mean that there is no or little cell death in the time-resolved experiment: It can be the case that we cannot identify this rate with the given model and data.

**Proliferation in the tumor** It has been reported that there is significant ongoing proliferation at the sight of inflammation [134, 138], but the question remains, whether this also holds for tumor sites, as the environments are known to be immunosuppressive [139, 140]. For this reason it is important to test, whether the proliferated cells in the tumor can be explained without a proliferation in the tumor. As we will see in both experiments we find that this is not the case.

### Alternative Models for the time-resolved experiment

All modifications are changes to the basic model structure of the time-resolved experiment (see Fig. 3.9). This model structure includes a division stop in both draining lymph node and tumor and a time dependent egress as well as a time dependent proliferation rate in the draining lymph node. The here presented modified model structures and the basic model structure are fitted to the data of the treatment and control experiments simultaneously with all parameters being different between the treatment and the control, but for the errors and the source term. The fit with the basic model structure returns a negative loglikelihood of 90.3 and an AIC of 358.4.

It is our aim to test, whether 1) the division stop can be omitted entirely, 2) whether time dependent proliferation rates can replace the division stop mechanisms, 3) whether only division stop mechanisms or a generation dependent proliferation can replace the time dependent proliferation, 4) whether the proliferation in the tumor can be replaced and 5) whether the time dependency of the egress rate can be replaced by a generation dependency. 1) - 3) are partly motivated by the fact that we combine a time dependent and a generation dependent mechanism to explain the attenuated proliferation dynamics in the draining lymph node, which renders the model complex. In consequence, we try to replace one or the other mechanism such that we only have either a time dependency or a generation dependency for our proliferation in both tumor and draining lymph node.

In the following, we find that a model with a generation dependent proliferation rate instead of a time dependent one in the draining lymph node and a model without proliferation in the tumor, but with a generation dependent egress rate, perform worse,  $\Delta AIC = 7.2$  &  $8.7$ , but cannot be rejected entirely. We also find evidence for a generation dependent egress rate instead of a time dependent one.

**1) Leaving out the division stop results in a significantly worse fit** Implementing a continued proliferation instead of a division stop mechanism and making no other changes to the model structure returns an AIC of 378.5 and a negative loglikelihood of 100.4, which is significantly worse than our basic model structure fit ( $\Delta AIC = 20.1$ ).

**2) A time dependent decrease of the proliferation cannot replace the division stop mechanism** Here we try to explain the attenuated proliferation with only a time dependent decrease of the proliferation.

To compensate for discarding the division stop mechanism, we try time dependent proliferation decrease mechanisms in both the tumor and the draining lymph node. More precisely, we try an exponential decrease of the proliferation rate in both compartments  $p_{dLN}(t) = p_{dLN,0} e^{-\alpha t}$  and  $p_T(t) = p_{T,0} e^{-\gamma t}$ , with individual decay rates  $\alpha$  and  $\gamma$ . We also try a logistic decrease of the proliferation rate,

$$p_{dLN}(t) = p_{dLN,max} - \frac{p_{dLN,max} \cdot p_{dLN,0} \cdot \exp(\alpha t)}{(p_{dLN,max} + p_{dLN,0} \cdot (\exp(\alpha t) - 1))}, \quad (3.3)$$

resulting in the dynamic shown on the right side of Fig. 3.11. The equation is simply a substraction of the logistic growth function from its upper bound  $p_{dLN,max}$ .  $\alpha$  shapes the

decay. We set  $p_{dLN,0} = 0.001/d$  to ensure that the proliferation rate is small after the decay and thus, skipped the necessity to estimate this parameter. The proliferation in the tumor is modeled analogously with its own decay parameter  $\gamma$  and an upper bound  $p_{T,max}$ .

An exponentially decreasing proliferation rate in both compartments performs better than a logistic decrease, but still significantly worse than our basic model ( $\Delta AIC= 17.9$ ) and returns  $AIC= 376.3$  and a negative loglikelihood of 94.2.

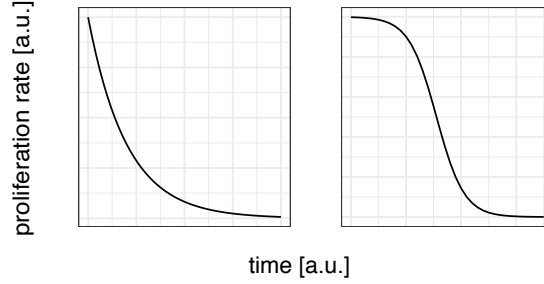


**Figure 3.11.:** Different time dependent proliferation decrease mechanisms, which are implemented instead of a generation dependent proliferation stop.

**3) A generation dependent proliferation performs worse than a time dependent proliferation and division stop, but cannot be rejected. The local division stop mechanism in the tumor is needed.** Here we try to explain the attenuated proliferation with only generation dependent mechanisms.

First, we introduce a generation dependent proliferation (linearly and exponentially decreasing), in the draining lymph node and tumor. In the draining lymph node this is replacing the time dependency. Both options perform worse with  $\Delta AIC \gg 10$ .

In a next step we keep the “Gen +2” local division stop mechanism in the tumor. If this mechanism is combined with a generation dependent exponential decrease of the proliferation rate in the draining lymph node we obtain an  $AIC = 365.6$  and a negative loglikelihood of 93.9. This is still worse by  $\Delta AIC= 7.2$  than our basic model fit, but cannot be rejected thus.

We conclude that, although less likely, the attenuated proliferation in the draining lymph node could be the result of a generalized division stop mechanism, as well. For this reason, the same modification is tested for the proliferation-resolved experiment and the results are discussed in detail in section 3.3.

**4) Replacing the proliferation in the tumor with a generation dependent egress performs worse but cannot be rejected** If the proliferation in the tumor is left out, we need to omit the division stop in the draining lymph node, as cells in higher generations in the tumor can now only stem from the draining lymph node. We try linearly and exponentially increasing generation dependent egress rates, as we need the cells in higher generations to egress faster in order to be able to explain the more highly proliferated

cells in the tumor. Furthermore, independent egress rates for each generation including a factor are tested, where the latter transforms the individual egress rates of the control to the ones of the treatment, as otherwise the model would have too many parameters. This model structure performs best. Indeed, the independent rates are estimated to increase with the number of generations and we obtain  $AIC=367.1$  and a negative loglikelihood of 97, which is worse by  $\Delta AIC=8.7$  than our basic model fit, but can just not be rejected.

**5) A generation dependent egress rate performs worse than a time dependent one but cannot be rejected** It is our aim to test an alternative for the time dependent egress rate. We replace it with generation dependent, linearly and exponentially increasing egress rates, as well as independent rates as described in 4). The exponentially increasing egress rate performs best and has the same AIC of 358.2 and a negative loglikelihood of 94.8.

The fit, i.e. the negative loglikelihood, performs worse, but the AIC is the same, since we use less parameters when modeling the exponential generation dependent increase compared to the time dependent logistic increase.

To make these two model structures better comparable we reduce the parameters, which are different between the treatment and the control, to the ones, which are necessary to explain the data. More precisely, we do a forward selection as is described in the next section 3.2.3 and compare the best minimal models. The best minimal model of the generation dependent egress model is worse by  $\Delta AIC=4.4$  and thus we decide for our basic model structure.

#### Alternative Models for the proliferation-resolved experiment

The basic model structure of the proliferation-resolved experiment has no division stop mechanism, but a proliferation which decreases with time in the draining lymph node and it has no other time dependent rates (Fig. 3.9). We modify this basic model structure and fit the alternative model structures to the treatment and control data simultaneously. For this comparison all parameters are different for the treatment and control, but for the errors and the source term. The fit with the basic model structure returns a negative loglikelihood of 34.8 and an AIC of 258.9.

We would like to answer the following questions here: 1) Can a generation dependent proliferation rate replace the time dependent proliferation rate in the draining lymph node, since this option could not be rejected for the time-resolved experiment? 2) Can the proliferation in the tumor be replaced? 3) Does a time dependent proliferation in the tumor improve the fit? This question is explored, as we see an increasing proportion of BrdU+ cells in the tumor, see Fig. 3.7. 4) Does a time dependent egress improve the fit? 5) Does a division stop mechanism improve the fit? 4) and 5) are motivated by the fact that these mechanisms are needed to describe the data of the time-resolved experiment such that we are interested whether these mechanisms would improve the fit to the data of the proliferation-resolved experiment, as well.

In the following, we confirm a proliferation in the tumor and a time dependent decrease of the proliferation rate in the draining lymph node. Furthermore, we conclude that the

time dependent egress and the division stop mechanisms included in the basic model structure of the time-resolved experiment cannot be rejected.

**1) A generation dependent proliferation cannot replace the time dependency** The time dependent proliferation rate in the draining lymph node is replaced with generation dependent proliferation rates (linearly, exponentially decreasing and independent rates) in the same way as it is done for the alternative models of the time-resolved experiment in 3). Here, the best AIC is achieved with exponentially decreasing proliferation rates, but it performs significantly worse than the time dependent proliferation and returns an AIC of 331.5 and a negative loglikelihood of 71.1. As opposed to the results from the time-resolved experiment, here we can reject the replacement of the time dependent proliferation by a generation dependent one. This is not surprising when we consider the decreasing proportion of BrdU+ cells in the draining lymph node from day 3 to day 4 (Fig. 3.7).

**2) The proliferation in the tumor cannot be replaced with a generation dependent egress rate** The proliferation in the tumor is left out and instead a generation dependent egress rate is introduced to explain the large fraction of cells in higher generations in the tumor. The tried generation dependent egress rate mechanisms are implemented in the same way as it is done for the alternative models of the time-resolved experiment in 4). All fitting results with these model structure modifications are within an  $\Delta\text{AIC} = 0.5$ , i.e. perform similar, but are far worse than the fit with our basic model structure. The slope of the linear and exponential increase is estimated to be small, indicating that the generation dependence is not needed.

We obtain an AIC of 282.7, a negative loglikelihood of 41.5 and a  $\Delta\text{AIC}$  of 23.8.

As opposed to the results from the time-resolved experiment, here we can clearly reject this possibility to replace the proliferation in the tumor and thus, have an indication of a continued proliferation in the tumor.

**3) A time dependent increase of the proliferation rate in the tumor cannot be rejected** The increasing number of BrdU+ cells in the tumor induced us to check whether a time dependent exponential increase of the proliferation rate can improve our fit. Some improvement is achieved, but as the model is more complex the AIC is slightly worse ( $\Delta\text{AIC} = 0.8$ ,  $\text{AIC} = 259.7$  and negative loglikelihood = 31.8). As the initial proliferation after antigen encounter and priming is thought to be fast [135, 102, 136], an increasing proliferation rate over time is unexpected and we decide for a constant proliferation.

**4) A time dependent egress rate as is used in the basic model structure of the time-resolved experiment and a generation dependent egress rate cannot be rejected** We try whether the introduction of a time dependent logistic increase of the egress rate, which is part of the basic model structure of the time-resolved experiment, improves the fit. We find that it improves the fit, but due to the increased complexity the AIC is worse

by  $\Delta\text{AIC} = 2.5$  ( $\text{AIC} = 261.4$ , negative loglikelihood = 29). An exponentially increasing generation dependent egress rate is tested as well, since it could not be rejected, while testing alternative models for the time-resolved experiment. We find, that it improves the fit less than the time dependent egress and—albeit being the less complex model—the AIC is worse. The difference to the fit with the basic model structure is  $\Delta\text{AIC} = 4.9$  ( $\text{AIC} = 264$ , negative loglikelihood = 34), such that out of these two egress rate options the time dependency is more likely, but still performs worse than the fit with the basic model structure.

Although we thus stay with the simpler model, i.e. a constant egress rate over time, it is interesting to note that there is evidence for the time dependent egress rate mechanism, which is employed in the time-resolved experiment. But due to the small time window in which the measurements are performed and the lack of further information about the dynamics, this can neither be confirmed nor rejected.

**5) A division stop mechanism improves the fit slightly** The division stop mechanism is confirmed in the alternative models for the time-resolved experiment and we therefore decide to test this for the proliferation-resolved experiment, too.

Looking at cell division profiles a division stop before the 6th generation does not make sense. So we test a division stop for both compartments after six divisions, a division stop only in the draining lymph node as well as a division stop after six generations in the draining lymph node and two further divisions in the tumor (“Gen 1 - 6” and “Gen +2”). The latter is motivated by the basic model structure used for the time-resolved experiment. The exclusive proliferation stop in the draining lymph node is motivated by the dynamics of the fraction of BrdU+ cells, see Fig. 3.7, which points at an attenuated proliferation in the draining lymph node and a continued proliferation in the tumor respectively. The division stop after six generations in both compartments worsens the AIC by  $\Delta\text{AIC} = 2.4$  and the division stop, which only takes place in the draining lymph node improves the AIC by  $\Delta\text{AIC} = 1$  ( $\text{AIC} = 258$  and negative loglikelihood = 34.3), which is an indication for this model, but by no means significant. To introduce a generation stop just after the generations, which we are able to observe, seems arbitrary and as the difference is small, we decided for the default option of a continued proliferation. Nevertheless we take from this, that a division stop mechanism is not unlikely in this experiment, too.

### 3.2.3. Model selection for the identification of treatment induced changes

In the previous sections 3.2.1 and 3.2.2 the basic model structure is constructed such that separate fits to the data from control and treatment work well, which result in independently optimized parameter sets. We now ask the question, in which way the anti-CD40 treatment is reshaping the OT-I T cell response. With regard to our model this means, that we would like to find the parameters  $\theta_{diff}$  (treatment-dependent parameters), which need to be different for the treatment and control, when fitting the basic model structure to both data sets simultaneously. As mentioned in the introduction to this section

(section 3.2) fitting both data sets simultaneously gives rise to a group of nested models: These differ with respect to the parameters, which are assumed to be different between the treatment and the control. If we have  $r$  parameters in our basic model structure, we obtain  $2^r$  nested models, as each parameter  $\theta = (\theta_1, \theta_2, \dots, \theta_r)$  can set to be either the same or different.

**Forward selection** As the fitting procedure of a single model is time intensive, a forward selection is applied [141, 142], which identifies locally optimal models among a set of nested models. In general, out of a set of nested models one starts with the simplest model and the complexity of the model is increased in each round. In every round all possible additional parameters are tried one by one and the best combination(s) are kept and taken into the next round, where again all kept combinations are tried with all possible additional parameters.

In our case, the simplest model is the model, where the same parameters are used to fit the data of the treatment and control setting. Additional parameters are introduced by allowing parameters to be different between the treatment and control. Whether one only takes the best model or considers more combinations in each round (e.g. all within an  $\Delta AIC \leq 10$  of the best model) is determining how global the search is. In this model selection all models within an  $\Delta AIC \leq 10$  of the best model in each round are considered. Computing the optimal negative loglikelihood of the model, where all parameters are allowed to be different between treatment and control (referred to as a full model), we learn the smallest possible negative loglikelihood, which can be expected for any model complexity. Thus, we have a lower bound for the AIC, which can be theoretically achieved in each round, i.e. for each model complexity, and we can stop, when no further improvement of the AIC can be expected by an increased complexity.

**Choice of the best minimal model** After the forward selection we consider all models within an  $\Delta AIC \leq 4$  of the best model in terms of AIC. Like this we can consider all models, which cannot be rejected [141]. Among these we choose the model with the least complexity, to which we refer as the best minimal model (BMM).

For both experiments this model had two interesting features: It is unique in the sense, that no other model of the same complexity is within  $\Delta AIC \leq 4$  of the best model. Furthermore, all parameters found to be different  $\theta_{diff, BMM}$  are a subset of the  $\theta_{diff}$  of the other best models within  $\Delta AIC \leq 4$ . This confirmed that  $\theta_{diff, BMM}$  indeed need to be different to describe the differences in the anti-CD40 treated setting.

In the following two sections (3.2.4 and 3.2.5) the BMMs of both experiments are discussed, in the course of which the profile likelihood of the estimated parameters and the prediction profile likelihood [143] of time-dependent parameters are calculated and shown as well. The parameters are often presented as rates in  $1/d$  or  $1/h$ . Sometimes their inverse is used, which is the expectation value of the corresponding exponentially distributed waiting time, and is referred to as the “(average) waiting time” or “(average) interdivision time”. The latter is used for the inverse of proliferation rates.

### 3.2.4. Best minimal model for the time-resolved experiment

The treatment dependent parameters in our best minimal model ( $\theta_{diff,BMM}$ ) for the time-resolved experiment are the parameter shaping the egress rate  $\beta$  and the undivided cell number in the tumor.

For the global best model, which is  $\Delta AIC = 1.8$  better than our BMM, the  $\theta_{diff}$  additionally includes the proliferation rate in the draining lymph node, i.e.  $p_{dLN,0}$  and  $\alpha$ . It predicts a higher initial proliferation rate, but a faster decay for the treatment. Calculating the integrated proliferation rate for this model, which determines the cell division profiles (see section 2.3.1), we see that the proliferation is stronger for the treatment until day 5.3.

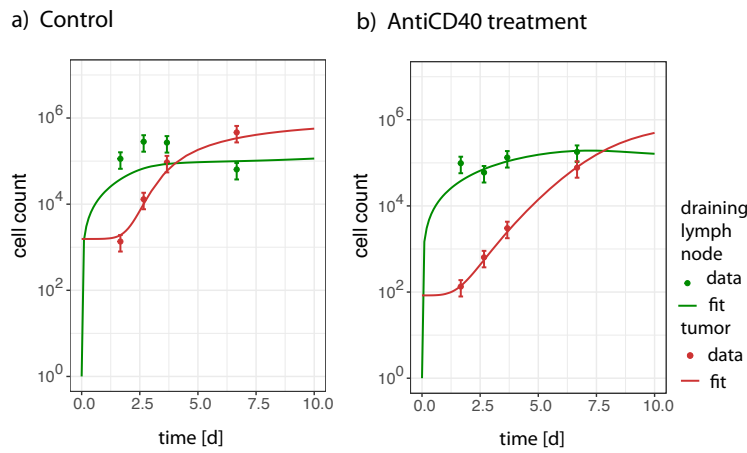
It is also important to mention that just above the threshold of  $\Delta AIC = 4$ , we find models of a similar complexity as our BMM, for which either  $e_{dLN,max}$ ,  $p_{dLN,0}$  or  $\alpha$  differ in addition to the undivided cells in the tumor. In these models  $p_{dLN,0}$  is larger and  $\alpha$  is smaller for the treatment, indicating a slightly enhanced proliferation in both models.

This suggests that the effect of the CD40 treatment lies in curbing the outflux from the draining lymph node and that it very likely affects the proliferation rate dynamics as well. Surprisingly, we do not find a different activation rate to be improving the fit, although we would have expected this, as CD40 has been thought to play a role in the priming of CD8 T cells [44, 45, 46, 47].

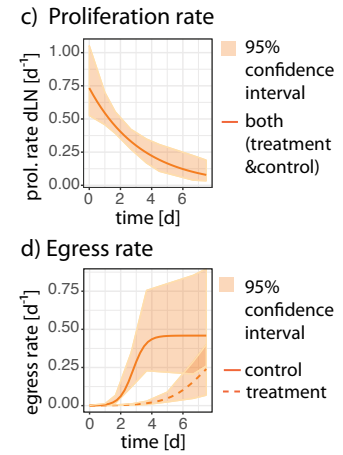
### Discussion of the fit and direct fit to the cell proliferation profiles

The difference in  $\beta$  between treatment and control leads to significant differences in the shape of the egress rate on days 2-5 (Fig. 3.12d). The fit to the overall cell numbers works well (Fig. 3.12a & b). The steep initial increase of the cell numbers from 0 in the draining lymph node is mainly determined by the source term of  $14000^{cells}/d$ , after which the proliferation and egress rate shape the dynamics. The increasing egress rate together with the decreasing proliferation rate in the draining lymph node (Fig. 3.12c), explains the attenuated increase of cells in the draining lymph node. However the decrease of cells in the draining lymph node after day 3 in the control is not captured. In the same way we see a decrease of the mean number of divisions and of highly proliferated cells on the seventh day in the draining lymph node in the control. Although, these effects are not strong, it could point towards a more complicated dynamics or mechanism, e.g. a more complicated time dependent egress dynamic, an additional generation dependent egress rate or a death rate of cells in higher generations. But with the activation and proliferation rate in the tumor already not being identifiable, introducing additional parameters leads very likely to an over-parametrization. A look at the shape of the absolute cell number increase for treatment and control in the tumor suggests that this dynamic dictates the initial dynamics of the egress rate. Other egress rate options, like a generation dependent egress, have been tested with less success, see also section 3.2.2. In any case, the smaller cell number in the tumor in the treated setting is very likely the reason for the smaller egress rate.

Fit to absolute cell numbers



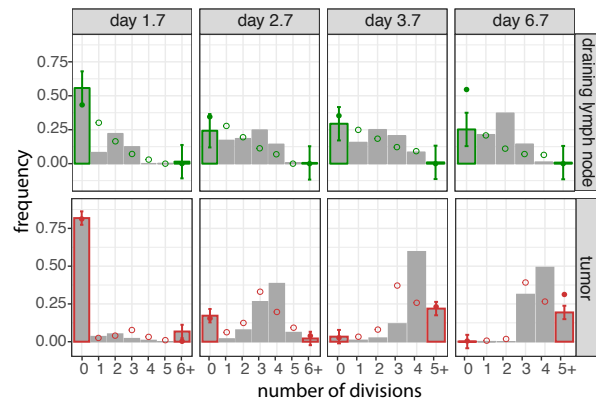
Estimated rates



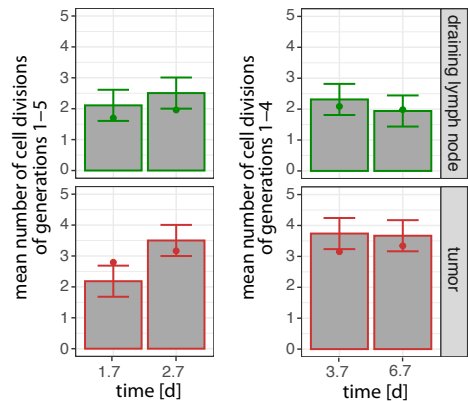
Fit to proliferation data



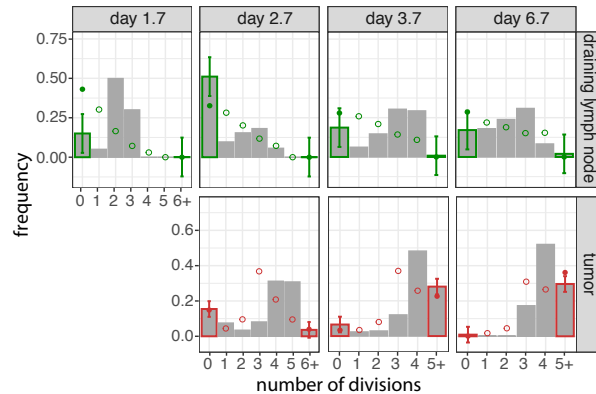
e) Cell division profile (control)



f) Mean number of cell divisions (control)



g) Cell division profile (treatment)



h) Mean number of cell divisions (treatment)

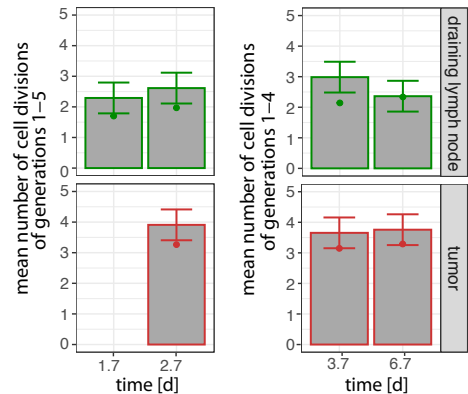


**Figure 3.12 (previous page):** Fit of the best minimal model to the data of the time-resolved experiment. a) & b) Fit to the absolute cell numbers in the draining lymph node (green) and tumor (red) for the a) control and b) anti-CD40 treatment. c) Estimated proliferation rate in the draining lymph node, which is the same for control and treatment. Filled area indicates the 95% confidence interval. d) Estimated egress rates for the control (solid) and treatment (dashed). Filled area indicates the 95% confidence interval. e) - h) Fit (dots) and prediction (circles) of the proliferation data. Only the color-bordered bars are used for fitting. e) Fitted and predicted cell division profiles and f) fitted mean number of divisions of the control. g) & h) Analogous plots for the treatment setting. Errors have been estimated and are indicated by error bars. Experimental data: Lena Kranz and Mustafa Diken.

The fit to the proliferation data, i.e. the frequency of cells in the 0th, 5+th and 6+th generation (Fig. 3.12e & g) and the mean number of divisions (Fig. 3.12f & h), overall works well and are mostly within the estimated error bounds. But, as expected, the predicted frequencies of the cell division profiles from generation 1 - 4 or 1 - 5 are off, as we only use the mean number of divisions to inform the fit. As discussed in section 2.3.2, it is not unexpected that the solution of an ordinary differential equation predicts a more variable distribution of the cell division profiles than what is measured, even when the mean number of divisions coincides. Nevertheless, fitting the BMM to the cell division profile directly, instead of fitting it to the mean number of divisions result in a similar fit (see suppl. Fig. B.4) and parameter estimates, which are well within the confidence intervals of the BMM (compare suppl. Tab. B.1 and Tab. 3.3). Only the initial proliferation rate in the draining lymph node with  $p_{dLN,0} = 1.2 \text{ 1/d}$  is just above the upper boundary of the proliferation rate estimate of the fit to the mean number of divisions. It is compensated by a faster decay rate of the proliferation  $\alpha = 0.35 \text{ cells/d}$ . Obtaining similar parameter values for different observables speaks for the robustness of the model fit to the data.

**Estimated parameter values** Apart from the activation rate and the proliferation rate in the tumor, most parameters are well confined by their confidence intervals, which have been obtained by calculating the profile likelihood (Tab. 3.3 and Fig. 3.13). The proliferation rate in the tumor is estimated to be fast with a mean interdivision time of 6h and no upper bound. 6h is possible, since an interdivision time of  $\approx 5.3\text{h}$  has been measured in strongly activated (i.e. vaccination + IL-2) T cells in the spleen of tumor bearing mice [144] and there are studies, which report even faster proliferation rates [135]. In consequence, when we fitted our model, we set the upper bound of the rate  $p_T$  to  $5 \text{ 1/d}$ , which corresponds to a lower bound for the interdivision time of 4.8h. Nevertheless, the interdivision time appears short in this setting, which is discussed in section 3.3.

The activation rate has no upper bound, i.e. can be arbitrarily fast. This means that the time to first division is predicted to be the same as the interdivision time of the subsequent divisions in the draining lymph node. This furthermore means that the estimated proliferation rate is likely an average of both rates with a slow initial rate estimate of  $p_{dLN,0} = 0.73 \text{ 1/d}$  (interdivision time 33h). The fact that the confidence

interval of the decay rate  $\alpha$  does not comprise 0 indicates that the proliferation is also attenuated over time. The upper limit of the egress rate  $e_{dLN,max} = 0.46$  1/d (waiting time 52h) is also rather slow, meaning that only a small part of the cells in the draining lymph node enter the tumor.

The source term of 14000cells/d appears to be large but plausible, given the high number of transferred cells ( $5 \cdot 10^6$  cells). And considering that on average we find 11000 undivided cells in the blood on all days for the control setting and 3100 cells with an increasing tendency in the anti-CD40 setting (average of all days:  $11000 \pm 1100$ cells/d and  $3100 \pm 900$ cells/d respectively, see also suppl. Fig B.2b), the estimated parameter fits into the picture. The significantly smaller undivided cell number in the tumor for the treatment setting (83 VS 1000 cells) reflects the data well until day 4, see suppl. Fig. B.2a. This data is indirectly used in the fit, as the frequency of undivided cells and the absolute cell number in the tumor are both used as observables.

**Table 3.3.:** Estimated rates for the BMM, time-resolved experiment

Parameter	Control	95%CI	anti-CD40	95%CI
source	14000 cells/d	[9100; 20000]	"	"
activation	31.0 1/d	[3.4; inf]	"	"
$p_{dLN,0}^*$	0.73 1/d	[0.53; 1.1]	"	"
$\alpha^*$	0.30 1/d	[0.13; 0.48]	"	"
$e_{dLN,0}^{**}$	0.001 1/d	[0.0002; 0.002]	"	"
$\beta^{**}$	2.4 1/d	[1.8; 3.3]	0.89 1/d	[0.53; 1.3]
$e_{dLN,max}^{**}$	0.46 1/d	[0.17; 1.0]	"	"
$p_T$	4.0 1/d	[1.6; inf]	"	"
Undivided cells, tumor	1600 cells	[860; 2400]	83 cells	[37; 150]
$sd_{abs}$	0.41	[0.30; 0.63]	"	"
$sd_{MDiv}$	0.50	[0.35; 0.76]	"	"
$sd_{Gen,dLN}$	0.12	[0.084; 0.19]	"	"
$sd_{Gen,T}$	0.044	[0.030; 0.087]	"	"

\* see eq.(3.1) \*\*see eq.(3.2)

### 3.2. Mathematical model describing the T cell dynamics in a melanoma mouse model

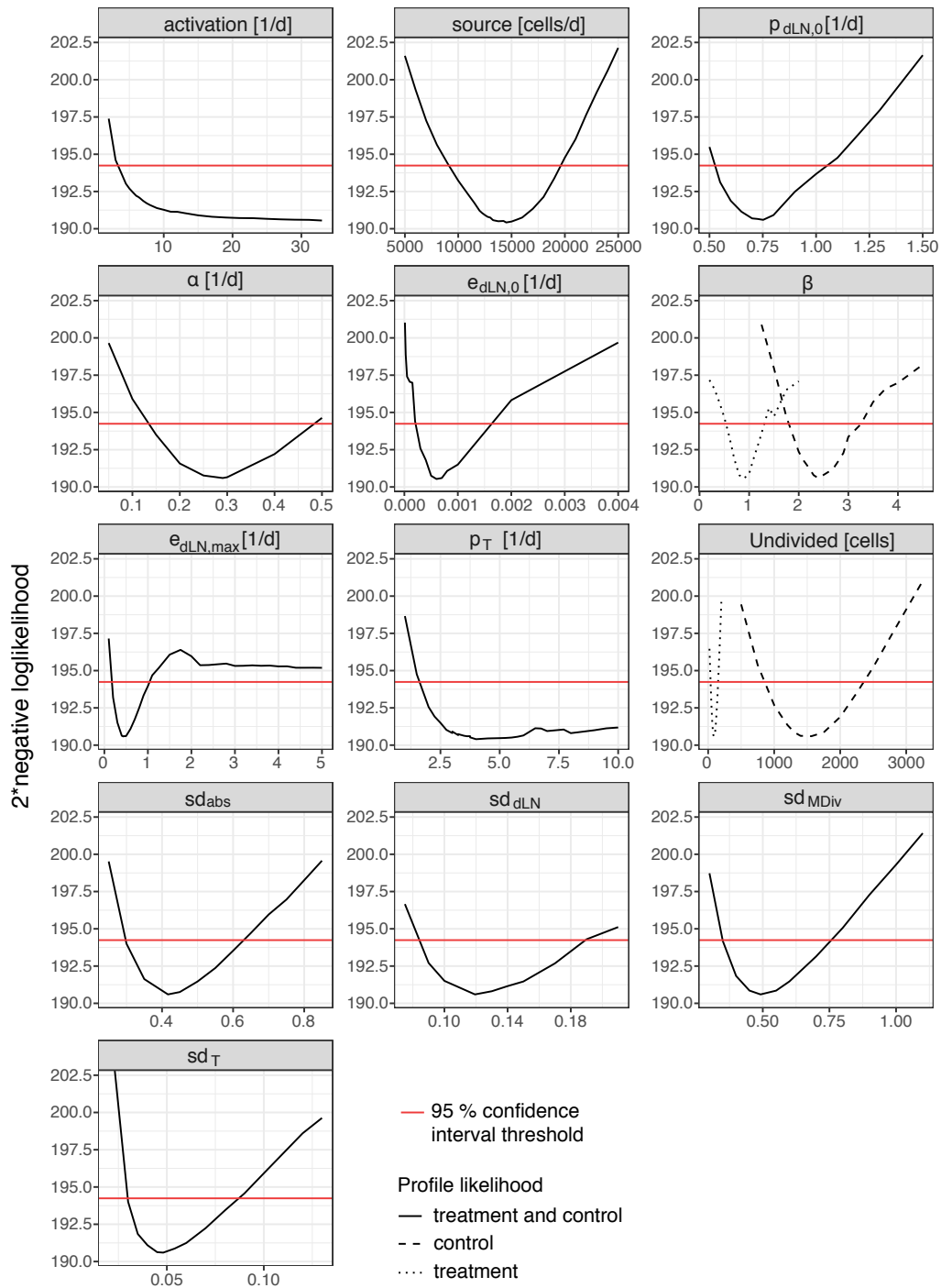


**Figure 3.13 :** Profile likelihoods of the best minimal model for the time-resolved experiment. All values besides the activation and the proliferation in the tumor are well constrained. The red line denotes the threshold for the 95% confidence interval.

### 3.2.5. Best minimal model for the proliferation-resolved experiment

The treatment dependent parameters in our best minimal model (BMM) for the proliferation-resolved experiment are again the egress rate and the undivided cell number in the tumor. Additionally the activation rate is different between the treatment and the control. As this differs from the result obtained for the previous experiment, we check how well the model can fit the data, if all parameters can differ between treatment and control except for the activation rate. This is done in addition to the forward selection. The AIC is, as expected, worse than the one of our BMM as this model has more parameters ( $\Delta\text{AIC} > 30$ ), but we also find that the negative loglikelihood is worse by  $\Delta\text{negLL} > 10$  than our BMM. This implies that any model with the same number of parameters as the BMM and with the same activation rate in both treatment and control can achieve at most a fit, which will still be worse by  $\Delta\text{negLL} > 10$ . In consequence, the same activation rate for the control and treatment setting can be excluded.

It is interesting to see that the BMM confirms our conclusion from the time-resolved experiment of an attenuated egress rate due to the anti-CD40 treatment and furthermore, adds the expected difference in activation/priming [44, 45, 46, 47].

#### Discussion of the fit and fit to the mean number of divisions

The model fit of the best minimal model to the data can be seen in Fig. 3.14. The agreement of the model fit with the absolute cell numbers looks good and the errors are estimated to be small (rel. error  $\text{sd}_{rel} = 0.26$ ). However, the decline in cell numbers in the draining lymph node after day 3 in the control is again not captured and could point towards an additional mechanism governing its dynamics. But the decrease is far less pronounced than in the time-resolved experiment data. The initial increase of absolute cell numbers in the draining lymph node is explained by the large source term with  $2.2 \cdot 10^4 \text{cells/d}$ . After this initial increase the dynamic is determined by the activation, proliferation and egress rate. The stronger activation and the smaller egress rate for the treatment setting lead to a higher predicted number of cells in the draining lymph node and a smaller predicted number of cells in the tumor. Indeed, the smaller egress rate is very likely the consequence lower cell numbers in the tumor in the treatment setting and the enhanced activation rate for the treatment is determined by the differences in the cell divisions profiles, which contain more strongly proliferated cells in the treatment data.

The fit to the BrdU+/- fraction of each generation in the cell division profile is acceptable (Fig. 3.14 d) & f). We furthermore see that the lack of BrdU+ cells in the undivided generation and the relatively high fraction of BrdU+ cells (compared to the BrdU- cell fraction) in higher generations can be explained in large parts with our model assuming a short BrdU availability and a simple proliferation, see also discussion in section 3.1.2.

In some cases the CFSE data cannot be analyzed, see section 3.1.2. This is the case for the tumor on day 3.75 in the treatment. For the tumor on day 2.75 in both treatment and control the CFSE data for BrdU+ and BrdU- cannot be analyzed individually, but the combined data can be such that this is used for the fit. In these three cases we

### 3.2. Mathematical model describing the T cell dynamics in a melanoma mouse model

fit the overall fraction of BrdU+ cells (Fig. 3.14 e & g, solid line). The agreement of the fit with the data is mediocre, as opposed to the predicted frequencies (Fig. 3.14 e & g, dashed line). The latter is not surprising as already the BrdU+/- frequencies in individual generations are fitting well (Fig. 3.14 d & f).

**Fit to the mean number of divisions** It could be assumed that the fit to the overall BrdU+ fraction in the tumor is neglected at the cost of fitting each generation individually. To test this we fit only the mean division number and the overall BrdU+ fraction, but the result looks similar (see suppl. Fig. B.5). In addition, for this fit all but one parameter are well within the confidence interval of our BMM estimates (compare suppl. Tab. B.2 to Tab. 3.4). Only the progression rate through the S phase in the fit to the mean number of divisions is slightly slower (2.7 1/d) than the lower bound of the confidence interval (2.8 1/d). Thus, the poor fit to the BrdU+ fraction in the tumor is not a consequence of our choice of observables and we see that the fit is robust under the change of observables.

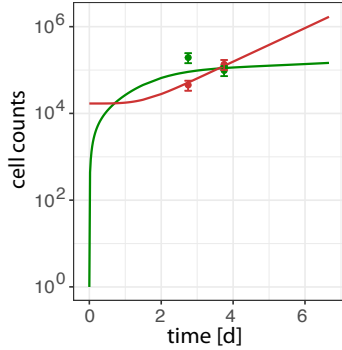
**Table 3.4.:** Estimated rates for the BMM, proliferation-resolved experiment

Parameter	Control	95%CI	CD40	95%CI
source	22000 cells/d	[14000; 26000]	"	"
activation	1.1 1/d	[0.94; 1.3]	3.9 1/d	[2.9; 6.2]
$p_{G1,dLN,0}^*$	10 1/d	[7.5; 15]	"	"
$\alpha^*$	1.3 1/d	[1.1; 1.5]	"	"
$p_S$	3.1 1/d	[2.8; 3.5]	"	"
$e_{dLN}$	0.31 1/d	[0.23; 0.43]	0.035 1/d	[0.023; 0.065]
$p_{G1,T}$	1.7 1/d	[1.1; 2.2]	"	"
Undivided cells, tumor	17000 cells	[11000; 26000]	1600 cells	[280; 3500]
$sd_{abs}$	0.26	[0.17; 0.47]	"	"
$sd_{Gen,dLN}$	0.011	[0.0091; 0.014]	"	"
$sd_{Gen,T}$	0.064	[0.049; 0.087]	"	"

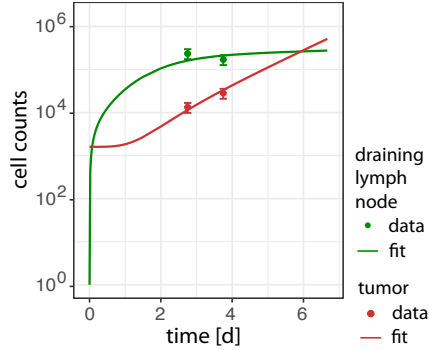
\* see eq.(3.1)

Fit to absolute cell numbers

a) Control

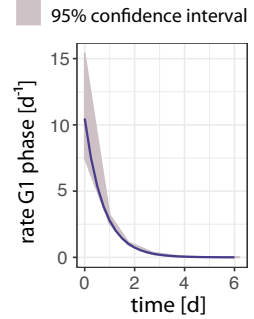


b) AntiCD40 treatment



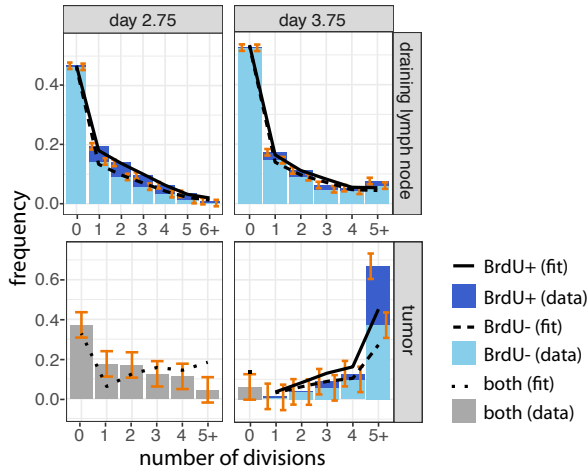
Proliferation rates

c) Rate G2M Phase:  $3.1d^{-1}$   
Rate G1 Phase:

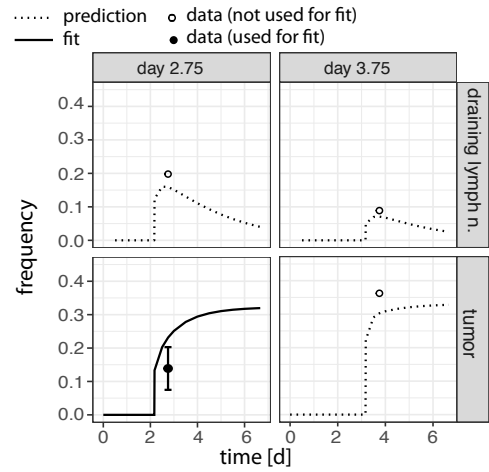


Fit to proliferation data

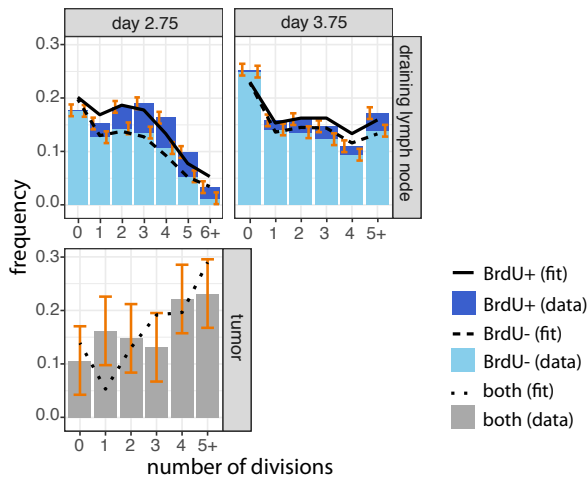
d) Cell division profile (control)



e) Proportion of BrdU+ cells (control)



f) Cell division profile (treatment)



g) Proportion of BrdU+ cells (treatment)

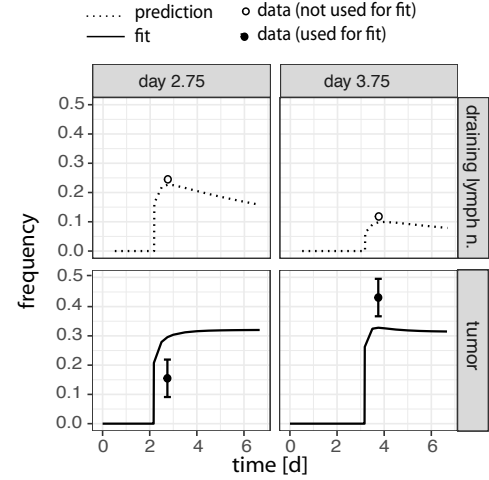


**Figure 3.14 (previous page):** Fit of the best minimal model to the data of the proliferation-resolved experiment. a) & b) Fit to the absolute cell numbers in the draining lymph node (green) and tumor (red) for the a) control and b) anti-CD40 treatment. c) Estimated proliferation rate in the draining lymph node, which is the same for control and treatment. Filled area indicates the 95% confidence interval. d) Fitted (line) cell division profiles (bars) for the control setting. If available, the fraction of BrdU+/- cells is fitted (solid line/dashed line) for each generation otherwise the combined fraction is fitted (dotted line).<sup>1</sup> e) Fitted (solid line) and predicted (dashed line) total fraction of BrdU+ cells for the control setting. This is only fitted if the BrdU+/- fractions are not available for single generations. f) & g) Analogous plots for the treatment setting. Errors have been estimated and are indicated by error bars. Experimental data: Lena Kranz and Mustafa Diken.

**Estimated parameter values** All parameters are well constrained by confidence intervals which have been obtained by calculating the profile likelihood (Tab. 3.4, and Fig. 3.15). The initial proliferation rate in the draining lymph node is reasonably fast: Adding the initial waiting time of the G1 phase (2.3h) and  $S/G_2/M$  phase (7.8h), we obtain a waiting time of 10.1h. This is very similar to the cell cycle phase times for activated OT-I T cells in ref. [126], where they found an interdivision time of 10.1h and the length of the  $S/G_2M$  phase to be  $\approx 7.2h$ . At the first measurement time point (2.75d), however, we already have very slowly cycling cells with a waiting time of 96h, which implies that the proliferation came almost to a halt at that point. The interdivision time in the tumor of 22.3h is rather slow for activated T cells, but within a reasonable range if we consider the immunosuppressive environment of tumors. Both proliferation rates are discussed in more detail in section 3.3.

The egress rates of  $0.35/d$  and  $0.035/d$  are slow, but comparable to the rates estimated with the best model fit to the first melanoma experiment.

The significantly smaller undivided cell number in the tumor for the treatment setting reflects the data well, see suppl. Fig. B.2a. This quantity is indirectly fitted, as the frequency of undivided cells and the absolute cell number in the tumor are both used as observables.

The estimated influx of undivided cells into the draining lymph node with  $2.2 \cdot 10^4 \text{cells}/d$  seems high. But regarding the high number of transferred cells ( $5 \cdot 10^6$  cells), this is less surprising. Furthermore, this influx rate is far smaller than the undivided cell number found in the blood on both days with an average number of  $1.2 \cdot 10^5 \pm 3 \cdot 10^4 \text{cells}/\text{day}$  in the control setting and  $10^5 \pm 2.9 \cdot 10^4 \text{cells}/\text{day}$  in the treatment setting, see also suppl. Fig. B.2b. This makes the influx rate plausible.

We can further calculate the time to first division by adding the waiting times for the activation and for division in the draining lymph node. We find that the time to first division in the control of 32h agrees very well with the literature, where it is reported to be between 24h and 48h [123, 145, 146]. However the time to first division predicted in the treatment setting with 16h (CI: [14, 18]h) is quite fast.

---

<sup>1</sup>For each cell division profile we fit all fractions but one.

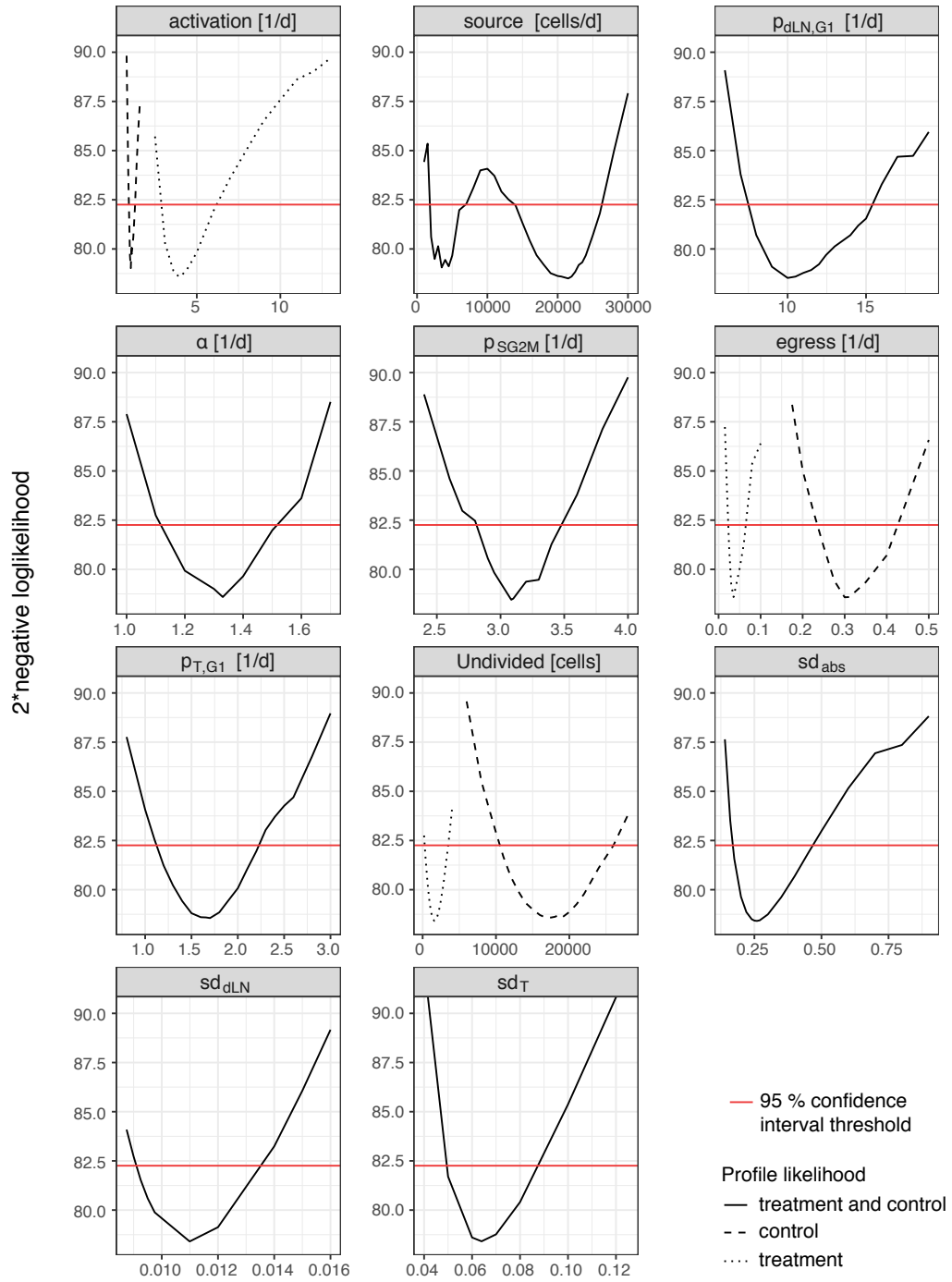


**Figure 3.15 :** Profile likelihoods of the best minimal model for the proliferation-resolved experiment. The red line denotes the threshold for the 95% confidence interval.

### 3.3. Comparison of the results obtained from the melanoma mouse model experiments

In this chapter we considered two distinct experimental data sets to inform our mathematical model: We have data from the time-resolved experiment (Exp. 1), where the measurement time points span 5 days, and data from the proliferation-resolved experiment (Exp. 3), where the measurement time points only span one day, but where we have additional information on the proliferation. As expected the data of these experiments exhibit some differences, e.g. in the absolute cell numbers of the recovered OT-I T cells, the tumor sizes and the cell division profiles. Especially the absence of cells in higher generations in Exp. 1 is remarkable. This leads to different basic model structures and raises the question to what extent the mechanisms that determine the dynamics of the OT-I T cells in the two experiments differ. This is discussed in the first part 3.3.1.

These differences between the experiments complicate the finding of commonalities of the OT-I T cell dynamics and common effects of the anti-CD40 treatment. Still, already by taking a closer look at the data we found similar tendencies in both experiments: 1) an attenuated proliferation in the draining lymph node, which is contrasted to an ongoing proliferation in the tumor 2) higher numbers of OT-I T cells in the tumor for the control data 3) a higher number of divisions in the treatment data and 4) lower fraction of undivided cells in the draining lymph node in the treatment data. To some extent these dynamics and treatment induced differences are reflected in the best model fits: In both experiments the proliferation dynamic in the draining lymph node is decreasing, while we have a continued proliferation in the tumor. A curbed egress rate due to the treatment is predicted in both experiments and an enhanced activation rate for the treatment setting is predicted by the third experiment. How these largely concurring parameter estimates, conclusions and selection of models for both experiments compare in detail and how this is determined by the available data, is discussed in the second part, section 3.3.2.

#### 3.3.1. Adaptations of the model and differences between the experiments

Differences in the experimental data lead to adapted models. Here we can distinguish between simplifications and changes to the model structure, which do not necessary point at different mechanisms, but need to be discussed here.

Simplifications are made where a less complex model fits the data similarly well. Although there is evidence for a time dependent egress rate in the third experiment, it is not necessary to describe the data, as only two consecutive time points have been measured. Similarly it is unnecessary to distinguish between cell cycle phases in an experiment where no BrdU has been measured, which could inform the length of the different phases.

A change to the model structure is done for the basic model of the time-resolved experiment. In the respective data, we can see a sudden decrease of cells in higher generations, which entails the necessity of a division stop mechanism in both organs in addition to a time dependent decrease of the proliferation rate in the draining lymph node. In principle, the idea that either only generation or time dependent mechanisms

can explain the dynamics is neat, as we do not have to combine two different mechanisms. But for this experiment using only a time dependent proliferation without a division stop does not work. And the attempt to replace the time dependent proliferation with generation dependent mechanisms cannot be rejected but worsens the fit (see section 3.2.2). In the third experiment, the BrdU measurements provide clear evidence of a time dependent proliferation rate. Here, the time dependence cannot be replaced with only a generation dependent proliferation, see section 3.2.2. Interestingly, although no division stop mechanism is needed for the third experiment, we also see evidence of an additional proliferation stop at a later generation than in the first experiment (after six divisions), especially in the draining lymph node.

Overall, this leads to the conclusion that a time dependent decrease and very likely a generation dependent stop is governing the proliferation rate in the draining lymph node in both experiments but to different degrees. Similarly, a generation stop in the tumor is likely in both experiments, but again to different degrees. In consequence, we use both mechanisms for the time-resolved experiment and for the proliferation-resolved experiment it suffices to only implement the time dependency, but this choice does not imply a fundamental difference of mechanisms between the experiments. It is for example conceivable that the higher tumor burden postpones the proliferation stop to a later generation in the proliferation-resolved experiment.

### 3.3.2. Comparison of the parameter estimates

In spite of the differences between the experiments, fairly similar conclusions can be drawn from the model fits to both experiments. In the following parameter estimates are compared.

**Egress rate** Both experiments agree in so far as they confirm a curbed flux from the draining lymph node to the tumor due to the treatment with anti-CD40. In addition, the ratio between the egress rates of treatment and control are in the same range, see Fig. 3.16b, with an average of 13.6 for the Exp. 1 and 8.8 for the Exp. 3.

But the initial dynamic of the egress rate varies, as we assume a constant rate in the third experiment and a time dependent one in the first experiment, see Fig. 3.16a. Substantiating a time dependent rate for the third experiment is difficult, as we only have measurements from two consecutive days (time points indicated by red triangles in Fig. 3.16a). Indeed, the introduction of this mechanism leads to a worse AIC. But this difference ( $\Delta\text{AIC} = 2.5$ , see section 3.2.2) is small and the negative loglikelihood is improved, i.e. the fit improves, which provides evidence for a time dependent egress rate after all.

At the time points, where the third experiment was measured, days 2.75 and 3.75, the egress rates are similar between the experiments (Fig. 3.16a), which leads to the assumption that the egress rates in both experiments are conform, if they can be assessed.

For both experiments, we have more evidence for a time than a generation dependent egress rate, but the difference is small. This is not surprising as the time and generation

### 3.3. Comparison of the results obtained from the melanoma mouse model experiments

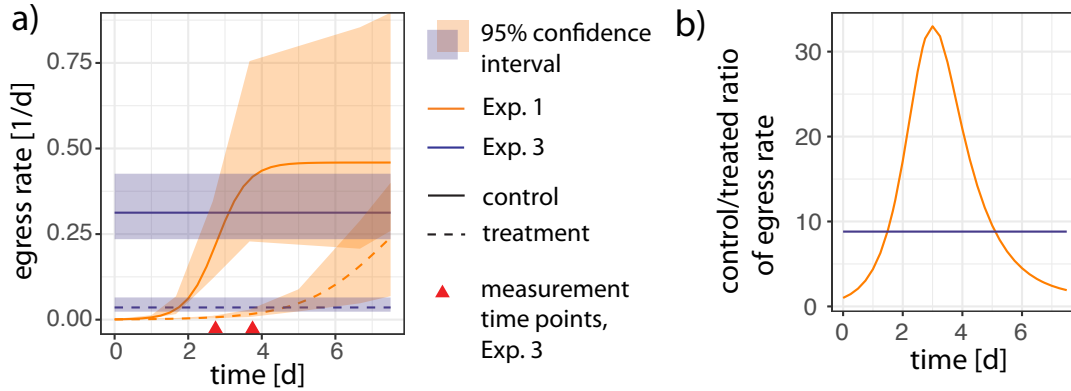


**Figure 3.16 :** Comparison of estimated egress rates between both experiments. a) Predicted egress rate for treatment and control. b) Ratio of the estimated egress rates between control and treatment.

dependent egress rate have a similar effect: An egress in higher generations implies an egress at later time points and hence, both model predictions point at a similar mechanism. With the evidence provided from testing both alternatives for both experiments, it makes sense to focus on the time dependent mechanism, while keeping in mind that the generation dependency is a possible explanation as well.

**Proliferation rate** For both experiments the average waiting time until proliferation is shorter in the tumor with 6h (Exp. 1) and 22.3h (Exp. 3) than in the draining lymph node, if the initial proliferation rate, which quickly decays in the draining lymph node, is disregarded: In the first experiment the initial time to division is 33h and reaches 74h on day 2.75. In the third experiment the initial time to division is 10.1h and increases rapidly to 96h on day 2.75, see Fig 3.17. Thus, the estimates from both experiments agree that the proliferation in the draining lymph node is slow after an initial rapid proliferation phase. Indeed, an attenuated proliferation rate over time in the draining lymph node in response to an immunogenic graft is reported in ref. [134]. It is also possible that due to the large number of cells flooding the draining lymph node, a repeated encounter with their antigen becomes unlikely at later time points and hence, many become inactive. Compared to the large number of OT-I T cells in the draining lymph node, only few and very likely active OT-I T cells enter the tumor, where they proliferate more strongly.

In any case, it is interesting to note, that the proliferation in the tumor is not only needed to explain the data (see section 3.2.2) for both experiments, but that it is relatively fast. This confirms the response of T cells reported in ref. [134] very nicely: In this study Sutherland et al. claim that T cells are stimulated to have a “mezzanine” response in an inflamed tissue due to the antigen presentation by parenchymal cells, which is distinct from the primary and the secondary response of the immune system to an acute infection.

It is hard to judge how plausible the proliferation estimates are as it has not been studied for this particular system, but one can put it into relation with studies of activated

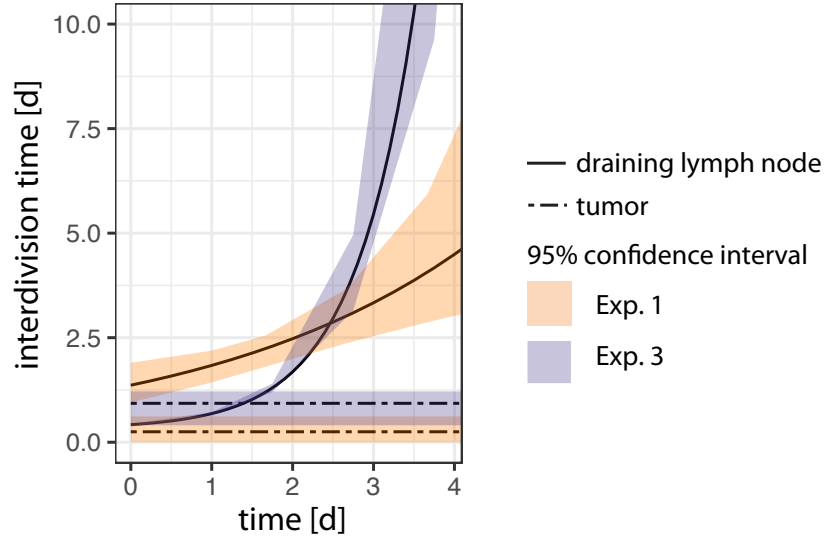


**Figure 3.17 :** Comparison of estimated interdivision times for both experiments

T cells. T cells are among the fastest dividing cells in the human body. In a B16 tumor study, where T cells were treated with IL-2 and immunized with the tumor antigen, they are reported to have an average interdivision time of only 5.3h [144] in the spleen. But, in general activated and stimulated T cells *in vitro* and *in vivo* are reported to have larger interdivision times of  $\approx 8\text{h} - 13\text{h}$ , [125, 126, 102]. As no other immunostimulatory agent apart from anti-CD40 has been applied in our system, we would expect the proliferation to be in this range or slower, especially as tumor environments are known to be immunosuppressive [139, 140]. Due to this considerations the 6h interdivision time in the tumor for our time-resolved experiment seems slightly too fast and at odds with the proliferation stop after a few divisions. On the other hand, the initial proliferation rate in the draining lymph node of the proliferation-resolved experiment (10.1h) is well within the expected range. In general, there is more reason to believe that the estimates from the proliferation-resolved experiment are more accurate: First, the proliferation parameters are better confined by the data, i.e. better identifiable (see Tab. 3.4), which is probably due to the proliferative information obtained from both the BrdU and CFSE staining. Secondly, our estimated length of the  $S/G_2/M$  and  $G_1$  phase of 7.8h and 2.3h agrees well with the directly measured interdivision time of stimulated OT-I T cells *in vitro* [126], where the  $S/G_2/M$  phase is claimed to occupy 72% of the average cell cycle time of 10.1h. Although we do not follow the idea of a linear relationship between the cell cycle length and the  $S/G_2/M$  phase, see also refs. [127, 137, 112], this renders us confident with the estimations obtained from the proliferation-resolved experiment.

**Activation rate** We would expect an enhanced activation in the anti-CD40 treated group due to the reported importance of CD40 for T cell priming. In the time-resolved

### 3.3. Comparison of the results obtained from the melanoma mouse model experiments

---

experiment we can unfortunately not identify this parameter. It can be arbitrarily fast meaning that the rate of the first division in the draining lymph node is the same as the general proliferation rate. As the time to first division is known to be larger than the interdivision times of the following divisions [123, 145, 146], this again confirms that the estimates of proliferation related rates might not be very accurate for the time-resolved experiment. In contrast, the best fit to the proliferation-resolved experiment predicts distinct and identifiable activation rates for treatment and control, where the activation rate is four times larger for the anti-CD40 treated group. The improved identifiability of the activation rate (and also of the proliferation rate in the tumor) in the proliferation-resolved experiment is very likely due to the information contained in the combined measurements of CFSE and BrdU. This turns out to be a useful combination to understand proliferative dynamics.

**Source term and undivided cell numbers** We predict a high and continued influx of cells into the draining lymph node in both experiments (Exp.1: 14000  $1/d$  and Exp.3: 22000  $1/d$ , see Tab. 3.5). This is likely the consequence of a high number of transferred cells (5 million OT-I T cells). The rate, furthermore, does not exceed the number of undivided cells in the blood, apart from the treatment setting in the first experiment (see suppl. Fig. B.2b), which makes the influx rate plausible. The absolute numbers of undivided cells in the tumor, of which we do not know whether they are an artefact, are fitted well (Exp. 1, control: 1600 cells, Exp. 1, treatment: 83 cells, Exp. 3, control: 17000 and Exp. 3, treatment: 1600 cells, see Tab. 3.5 and suppl. Fig. B.2a). Interestingly, in both experiments the number of undivided cells in the tumor is larger by an order of magnitude for the control, which coincides with the generally higher cell numbers in the tumor in the control setting. As the latter is explained by a larger egress rate, the same explanation might be determining the numbers of the undivided cells, too. But a mere egress of the activated undivided cells from the draining lymph node to the tumor in our model could not explain the data (tried for the first experiment, not shown).

Both, the undivided cell number in the tumor as well as the source term, are larger for the proliferation-resolved experiment, which reflects the higher cell numbers in the tumor (see Fig. 3.2b).

**Table 3.5.:** Table comparing selected parameters estimate from Exp. 1 and Exp. 3

Data	source [cells/day]	activation [h]	Interdiv. time* in dLN [d]	Time to egress* [d]	Interdiv. time in tumor [h]	Undiv. cells tumor [cells]
Contr Exp1	14000	0	3.6	2.9	6	1600
CD40 Exp1	"	"	"	92	"	83
Contr Exp3	22000	22	7.5	3.2	22	17000
CD40 Exp3	"	6.1	"	28	"	1600

\*on day 3.25

### 3.3.3. Concluding remarks on the results of the melanoma mouse model

Although the decreased number of OT-I T cells in the tumor for the treatment setting is unintuitive, this feature has been confirmed in all three experiments. The resulting curbed influx into the tumor, which is predicted by both best minimal models, is at first surprising, as this does not seem to reflect an enhanced tumor response. On the other hand we observe more proliferated cells in the treatment setting, especially in the proliferation-resolved experiment. This is confirmed by the best fitting models which reveal an elevated activation rate (proliferation-resolved experiment) and evidence of an increased proliferation (time-resolved experiment). These are plausible effects of an anti-CD40 treatment on T cells which can be found in the literature [63, 62, 47, 44]. Putting this together we draw the conclusion that the anti-CD40 treatment activates T cells more strongly and induces a prolonged residence in the draining lymph node. Unfortunately, when we checked for the surface markers CD27 and CD62L, we could not see a clearly distinct dynamics between treatment and control (see suppl. Fig. B.3). But we see a tendency towards a smaller fraction of CD27hi cells in the treatment setting either in the tumor (Exp. 1) or in the draining lymph node (Exp. 3). The loss of CD27 is correlated with the acquisition of a terminal effector phenotype [148, 149]. Taken together, one can speculate that the prolonged residence can contribute to a more strongly activated and arguably more terminal effector like phenotype. Whether these cells contribute better to a T cell mediated antitumor response, of course, would need further investigation and cannot be concluded from our conclusions so far or the diminished tumor growth alone. The early growth inhibition of the tumor might alternatively also be a result of the anti-CD40 acting on other immune cells in the tumor environment.

Independently of the anti-CD40 effect, we found that T cells divide fast in the tumor for a minimum of two divisions and very likely even more. It is expected that T cells continue to divide at the site of inflammation [134], yet a faster proliferation than in the draining lymph node given the suppressive environment for T cell proliferation is unexpected [150, 151].

---

## T cell dynamics in a pancreatic ductal adenocarcinoma mouse model

---

In this chapter we discuss and mathematically model the early dynamics of a T cell tumor response and the effects of an agonistic anti-CD40 treatment on this dynamics in a pancreatic ductal adenocarcinoma (PDAC) setting. Both the experiments and the model are motivated by our investigation of the T cell response in a melanoma setting in chapter 3. In this way we can compare the model predictions calibrated with data from the non-orthotopic melanoma experiments with the results from an orthotopic pancreatic cancer model.

Three PDAC experiments were conducted by our collaboration partners, where the first experiment only comprises untreated mice and is analyzed at three measurement time points. The second and third have a treatment and control group. The measurement time points were motivated by our experiences with the melanoma experiments and the first PDAC experiment. In general the experiments were of an explorative nature, with a tumor cell line, which has been developed by our collaboration partners and few mice per time point and treatment group. Hence, it is not our aim to develop an entirely new model, but to test whether a similar model to the one established in chapter 3 can also describe this data. This way, we intend to understand differences caused by the variation of the tumor site and the tumor itself. In addition, with a model selection we retrieve again the parameters which are significantly influenced by the treatment and compare this to what we found for the melanoma setting. For this reason only data from the second and third experiment are modeled, where we have data from both treatment and control.

The first section 4.1 presents and discusses the data. The second section 4.2 discusses the chosen model structure, other model alternatives, which have been considered, and presents the best model fits for both experiments. The final section 4.3 reviews the suitability of the data for this analysis, summarizes the insights obtained from modeling and compares it to the results from the analysis of the melanoma experiment.

All experiments in this chapter have been conducted by Susann Wendler, Aaron Rodriguez Ehrenfried and Isabel Poschke at dkfz (German Cancer Research Center) in Heidelberg, Germany. The tumor cell line has been provided by Daniel Baumann and additional experimental support was given by Daria Jaeger. The experiments and the analysis of the flow cytometry data were jointly consulted with Isabel Poschke in order to obtain adequate data for modeling.

## 4.1. Results of the pancreatic ductal adenocarcinoma mouse experiments

### 4.1.1. Experimental setup

Our collaboration partners developed the pancreatic tumor cell line, which is taken from genetically engineered mice expressing a mutated tumor suppressor gene p53 and a proto-oncogene Kras in the pancreas. By repeated injections of the cholecystokinin analogue ceerulein, which stimulates pancreatic secretion, a chronic pancreatitis was induced leading eventually to the development of a tumor. The particular tumor cell line, 30364-OVA, was chosen due to its similarity to the human PDAC with respect to the histopathology. It was subsequently engineered to express Ovalbumin via retroviral transfer such that it has a mediocre immunogenicity.

In three experiments one million cells of 30364-OVA were injected orthotopically into mice and the size was monitored via PET scan. The scan turned out to be hard to interpret as signals were often diffuse. In consequence reliable tumor size data could not be obtained. Nevertheless, the PET scan information was used to get a rough estimate of the tumor sizes and after 31 to 38 days  $5 \cdot 10^6$  CFSE-dyed OT-I T cells, which recognize an Ovalbumin derived peptide, were injected intravenously, see Fig. 4.1. The number of transferred cells was chosen to be high such that enough cells can be recovered for a sound statistical analysis. On the same day, which is referred to as day 0, mice in the second and third experiment were divided into two groups and received either an agonistic anti-CD40 antibody (3/23 mIgG1) or a control (PBS) intraperitoneally. Since the antibody, the sequence of which was obtained from Prof. Martin Glennie (University of Southampton), has a mouse and not a rat derived Fc part as opposed to the commercially available clone 3/23, it is less immunogenic and can be given several times. Here, the injection of  $400\mu\text{l}$  anti-CD40 was shared over two days (day 0 and day 1).

Samples from the blood, the tumor and two draining lymph nodes were read out on day 2, 3 and 4 for the first experiment, 2 and 3 for the second experiment and 3 and 4 for the third experiment, which left us with 1-4 mice per time point and treatment group (Fig. 4.1). Subsequently, the OT-I T cells and endogenous T cells in the samples were identified and analyzed with flow cytometry. The cell numbers were extrapolated with true count to the whole sample and eventually to the whole organ. In this context the blood volume of a mouse was estimated to  $1500\mu\text{l}$ . The proliferative information was gained by recording the CFSE intensity with flow cytometry and analyzing this data with the methods introduced in section 2.1.

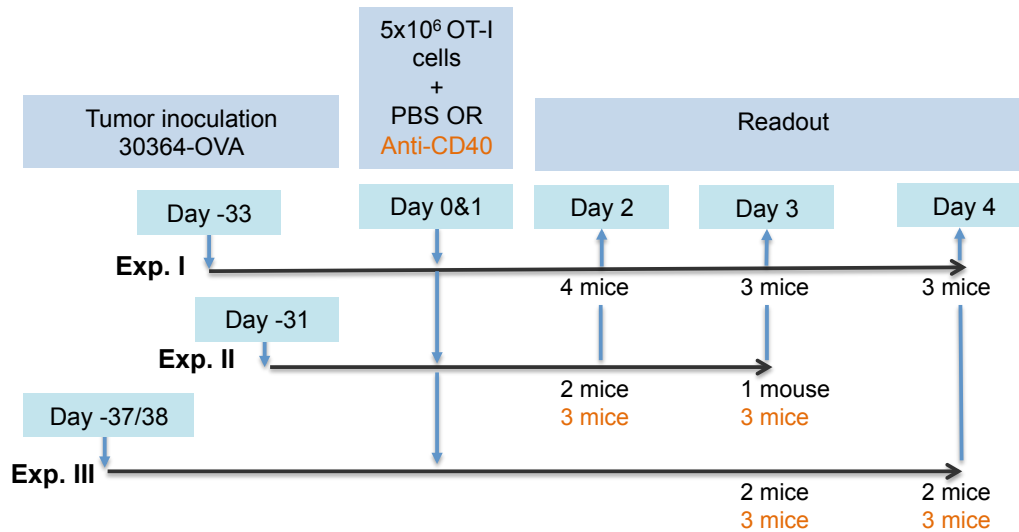


**Figure 4.1 :** Overview over the PDAC experiments. The number of available mice at different time points in the control (black) and treatment (orange) groups are indicated. Experiments conducted by Susann Wendler, Aaron Rodriguez Ehrenfried and Isabel Poschke.

The exact times when the samples were taken are 7h less than specified in Fig. 4.1. In all figures and calculations this is taken into account. The PDAC experiments are numbered with roman numerals.

#### 4.1.2. Changes induced by the anti-CD40 treatment and common features of the experiments

Generally the data is sparse, as we do not have many analyzable mice per sample group, i.e. samples from the same organ, with the same treatment and taken at the same time point, see Fig. 4.1. For this reason data obtained from only one sample, i.e. one mouse, is shown as well—without standard deviations—such that one can discern tendencies. Furthermore, many samples do not have enough cells for our CFSE data analysis (> 15 cells). If we only have one mouse in a sample group we furthermore require the number of measured cells to be greater than 50 for the CFSE analysis to be reliable. An overview of the number of analyzable samples per sample group is given in Tab. 4.1. The number of generations that can be distinguished for different organs, days and experiments are found in the Tab. 4.2.

**Absolute cell numbers** In general, as opposed to experiment I, experiment II and III have similar total cell numbers (see Fig. 4.2a and 4.2b). But the distinct dynamics of the cell numbers in the treatment compared to the control in the tumor in experiment III is curious, as this is not reflected in experiment II. The same holds for the opposing dynam-

**Table 4.1.:** Number of samples available for CFSE intensity analysis in every sample group

Experiment		Day 2		Day 3		Day 4	
		dLN	tumor	dLN	tumor	dLN	tumor
Exp 1	control	4	1	3	3	3	3
	treated	-	-	-	-	-	-
Exp 2	control	2	1	1	1	-	-
	treated	3	0	2	3	-	-
Exp 3	control	-	-	2	-	2	2
	treated	-	-	3	1	3	-

**Table 4.2.:** Number of distinguishable generations in the CFSE intensity analysis

Experiment	Day 2		Day 3		Day 4	
	dLN	tumor	dLN	tumor	dLN	tumor
Exp 1*	0-4	0-4	0-4	0-4	0-4	0-3
Exp 2*	0-4	0-3	0-3	0-3	-	-
Exp 3*	-	-	0-5	0-5	0-5	0-5

\*A distinction between treatment and control is not necessary for the number of distinguishable generations, as the CFSE brightness should be the same.

ics in the draining lymph node for experiment II, which is not reflected in experiment III. This hints at a high variability of the absolute cell number measurements.

The decreased OT-I T cell numbers in the tumor for the treatment setting, which is observed in the melanoma experiments, can only be suspected in the second experiment (Fig. 4.2b). Equally, a treatment induced decrease of the tumor weight is only seen in the second experiment, but not in the third (Fig. 4.3a). However, a treatment induced effect is also far less clear if we only consider the tumor weights instead of the size in the melanoma experiments (not shown). But unfortunately size measurements are not available for the PDAC experiments, since the PET scan cannot be trusted.

A shared property with the results from the melanoma experiment is that the absolute number of OT-I T cells in the tumor reflects their density in the tumor (Fig. 4.3b).

**Cell division profiles** In the draining lymph node we see an ongoing proliferation from day 1.7 to day 2.7 in experiments I and II (Fig. 4.4 and Fig. 4.5). The change is less pronounced from day 2.7 to day 3.7 in experiments I and III (Fig. 4.4 and Fig. 4.6). In the tumor we also see a change from day 1.7 to 2.7 (Fig. 4.4 and Fig. 4.5, lower panel) and from day 2.7 to 3.7 the proliferation seems to be attenuated as well. However, the seemingly smaller difference between the cell division profiles of day 2.7 and day 3.7 is

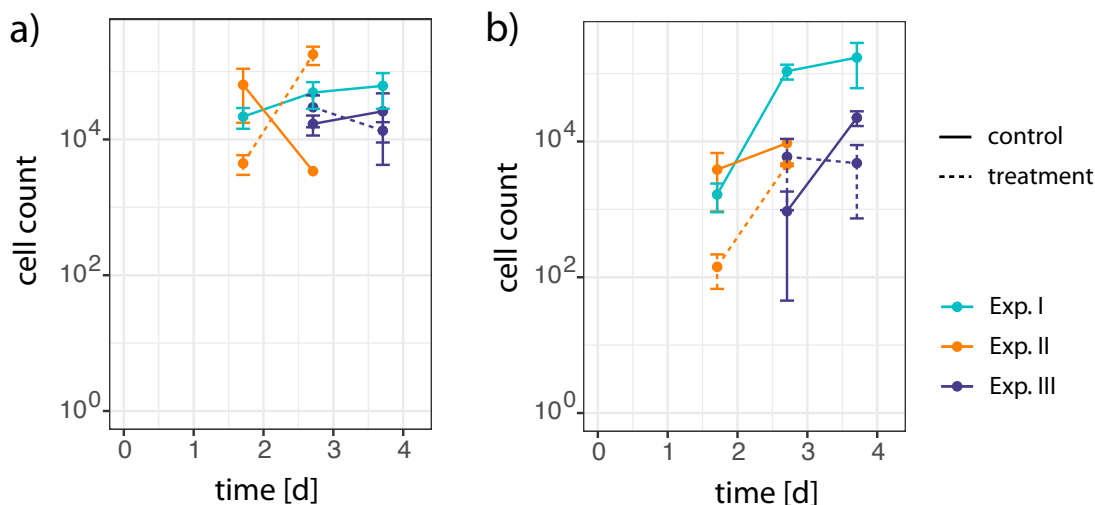


**Figure 4.2 :** Absolute numbers of OT-I T cells in a) draining lymph node and b) tumor for control (solid) and treatment (dashed) in Exp. I (light blue), Exp. II (orange) and Exp. III (purple). Experimental data: Susann Wendler, Aaron Rodriguez Ehrenfried and Isabel Poschke.

less certain, since the cells are already highly proliferated such that changes are not well distinguishable.

In experiments II and III we can perceive that cells in the treatment setting have proliferated stronger, especially in the draining lymph node. In order to be able to compare these profiles between experiments, we consider the fraction of cells in the generation 4+ directly (see Fig. 4.7), since three is the highest number of divisions that can still be resolved by the CFSE analysis in all experiments. We see that the fraction of highly proliferated cells are larger in experiment III in the draining lymph node, especially in comparison to experiment II. Curiously we see the opposite tendency, when looking at the proliferated cells in tumor. However, for the tumor reliable conclusions cannot be drawn, as we have only one mouse for experiment II and III in the control setting and all cells are in the generation 4+ in the treatment. From the observation of the proliferation in the draining lymph node we conclude that the data—although exhibiting similar characteristics—are not very well comparable and cannot be pooled.

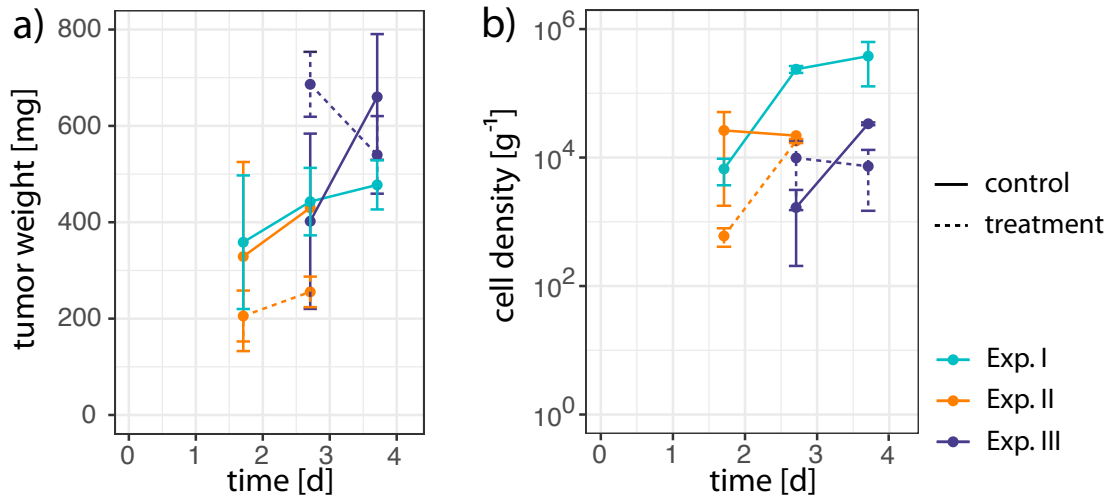


**Figure 4.3 :** a) Tumor weight and b) OT-I T cell density in the tumor for control (solid) and treatment (dashed) in Exp. I (light blue), Exp. II (orange) and Exp. III (purple). Experimental data: Susann Wendler and Aaron Rodriguez Ehrenfried and Isabel Poschke.

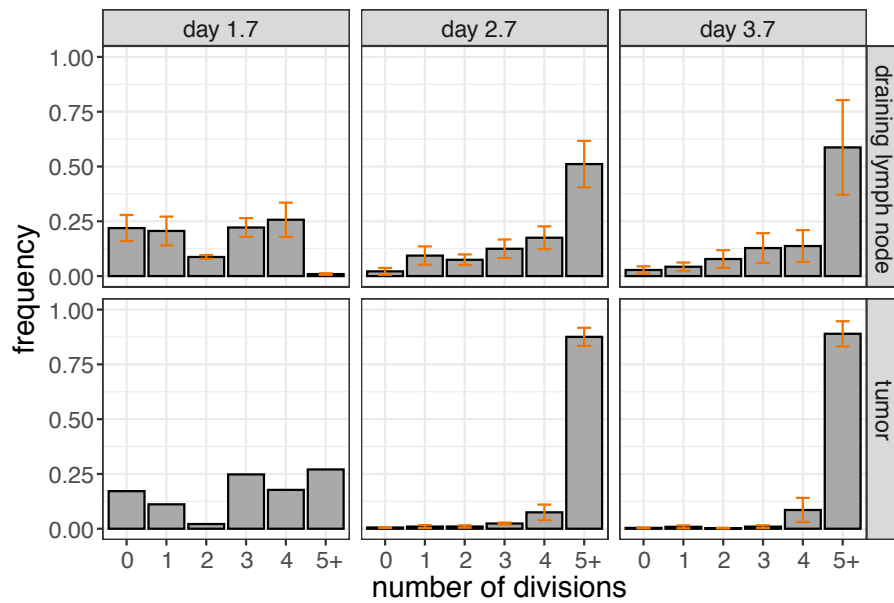


**Figure 4.4 :** Cell division profile of the first experiment (only control). For reasons of better comparability the profile on day 3.7 in the tumor is shown until Gen. 5+. Experimental data: Susann Wendler and Isabel Poschke.

4.1. Results of the pancreatic ductal adenocarcinoma mouse experiments

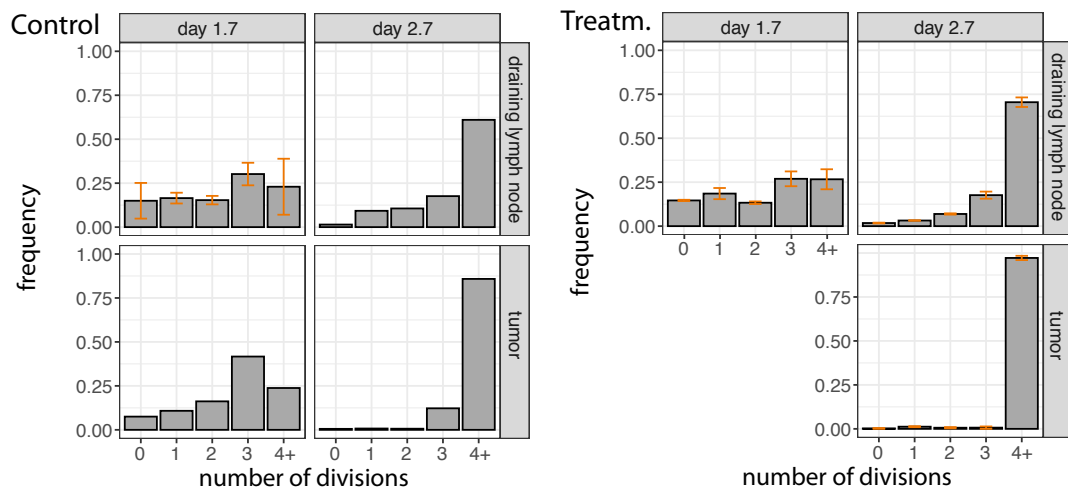


**Figure 4.5 :** Cell division profile of the second experiment for control (left) and treatment (right). For reasons of better comparability the profile on day 1.7 in the draining lymph node is only shown until gen. 4+. For the fit gen. 4 is distinguished from gen. 5+. Experimental data: Susann Wendler and Isabel Poschke.

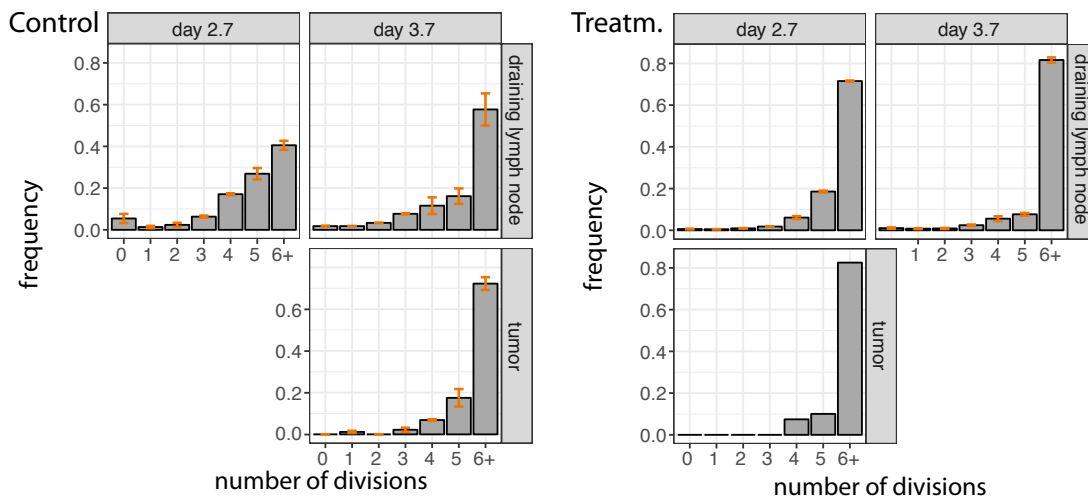


**Figure 4.6 :** Cell division profile of the third experiment for control (left) and treatment (right). Experimental data: Susann Wendler, Aaron Rodriguez Ehrenfried and Isabel Poschke.

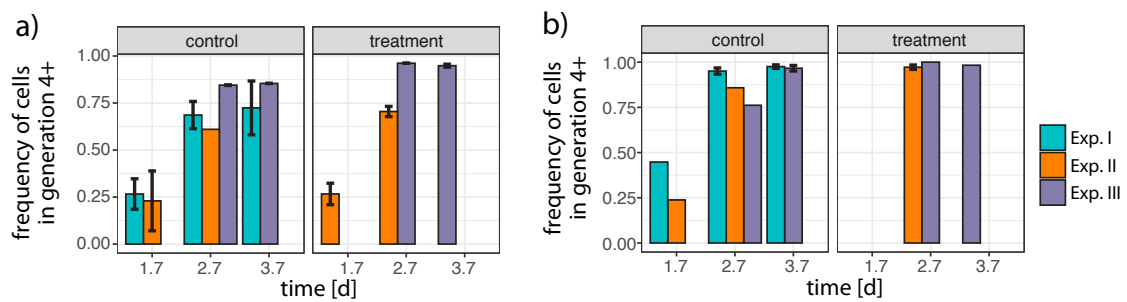


**Figure 4.7 :** Frequency of cells in generation 4+ in the a) draining lymph node and b) tumor in Exp. I (light blue), Exp. II (orange) and Exp. III (purple). Experimental data: Susann Wendler, Aaron Rodriguez Ehrenfried and Isabel Poschke.

## 4.2. Mathematical model describing the T cell dynamics in a pancreatic cancer mouse model

In chapter 3 we developed a mathematical model describing the T cell response to the subcutaneously injected melanoma cell line B16/OVA. By fitting a similar model to the data from an orthotopic pancreatic ductal adenocarcinoma (PDAC) mouse model we aim at understanding differences caused by the changed tumor site and tumor. Furthermore, we pursue the question in how far the model fit can reveal treatment induced changes and how these compare to the ones found in the melanoma mouse model fit. As only experiment two and three had both treatment and control, we analyze these.

First, in section 4.2.1 we present the “basic model structures” for fitting the OT-I T cell dynamics in both PDAC experiments. With the term “model structure” we refer to a set of differential equations and observables. The “basic model structure” is the model structure, which returns a good fit to both the treatment and control data and is used for further analysis. Subsequently, in section 4.2.2, we discuss alternative model structures, which we considered. Fitting the “basic model structure” to the treatment and control data simultaneously gives rise to many nested models. These differ with respect to the parameters, which are allowed to be different between the treatment and the control setting. The best model among these is decided on with a model selection and we can conclude whether different parameter estimates are required for explaining the treatment and control data. The model selection and the results of the best model fits are discussed in the section 4.2.3 for the second experiment and in section 4.2.4 for the third experiment.

### 4.2.1. Basic model structure construction

Starting from the existing model structures found in the melanoma mouse experiment (see section 3.2.1) we introduce extensions and simplifications with which we arrive at a basic model structure, which can fit the treatment and control data independently, see Fig. 4.8. These adaptations are discussed in the following. A more thorough discussion of alternative model structures is found in the next section 4.2.2.

**Undivided cells in the tumor and observables** We first test whether undivided cells in the tumor are needed to describe the data with our model. Since there are no undivided cells in the tumor in the third experiment, we omitted the respective parameter as well as the observable, i.e the fraction of undivided cells in the tumor. By not having this parameter we implicitly assumed it to be zero and thus not contributing to the absolute cell number in the tumor. In the second experiment we have a small fraction of undivided cells in the tumor, especially on day 1.7 (see Fig. 4.5) and we aim to find out whether the parameter for the undivided cells in the tumor is needed. To this end, we test two alternative model structures by fitting them to the treatment and control data simultaneously: one with the undivided cells as a parameter and the other, where this parameter is fixed to zero. For both fits the observable for the undivided fraction of cells

in the tumor is used and all parameters are allowed to be different between treatment and control except for the errors and the source term. This is the most general choice of parameters, as we do not expect these parameters to be changed by the treatment. The option with the undivided cells only improves the fit slightly, but has a decidedly worse AIC ( $\Delta\text{AIC}=16.8$ ), due to the added complexity. Thus, in the basic model structures for both experiments, we do not introduce a parameter for the undivided cells in the tumor. Without this parameter the model predicts no undivided cells in the tumor at all, since we excluded the possibility of undivided cells egressing from the draining lymph node to the tumor, see in section 3.2.1. Thus, we omit the frequency of the 0th generation in the tumor as an observable, as well. The fitted observables for both experiments are now the absolute cell numbers, the mean number of divisions (see section 2.3.3) and the fraction of cells in the  $n$ +th generation in both compartments and the 0th generation in the draining lymph node.

**Error estimation** We again estimate the errors and have three error parameters: a relative error for the absolute cell numbers  $sd_{abs}$ , an absolute error for the mean number of divisions  $sd_{MDiv}$  and—in contrast to the melanoma models—the same absolute error for the draining lymph node and the tumor,  $sd_{Gen}$ , for the fraction of cells in generation 0 and  $n$ +. Due to the little data available we do not distinguish anymore between the two compartments for the estimation of  $sd_{Gen}$ . Since the relative error for the absolute cell numbers,  $sd_{abs}$ , gets large when estimated, we introduce an upper bound of 0.7. This is motivated by the upper bounds of the 95% confidence intervals of the error parameter,  $sd_{abs}$ , of the melanoma fit, see Tab. 3.3 and 3.4.

**Proliferation stop** We try different generation stop mechanisms in the draining lymph node and the tumor, which are discussed in detail in section 4.2.2.

After testing these options, for the second experiment we decide for a simple continued proliferation. For the third experiment a division stop at generation six in both compartments improves the model significantly and is thus chosen for its basic model structure.

**Time dependent rates** Like in the melanoma experiments the proliferation is time dependent in the draining lymph node with

$$p_{dLN}(t) = p_{dLN,0} e^{-\alpha t}, \quad (4.1)$$

where  $p_{dLN,0}$  is the proliferation rate at  $t = 0$  and  $\alpha$  is the decay rate. The parameter  $\alpha$  is constrained to be positive, such that we only consider decreasing proliferation rates, as the initial proliferation of T cells is expected to be fast and then decaying [135, 102, 136]. Since no BrdU is measured, we do not distinguish between cell cycle phases. A time dependent egress rate as in the time-resolved melanoma experiment (see eq. (3.2)) is not included, but discussed in the section on alternative models (4.2.2).

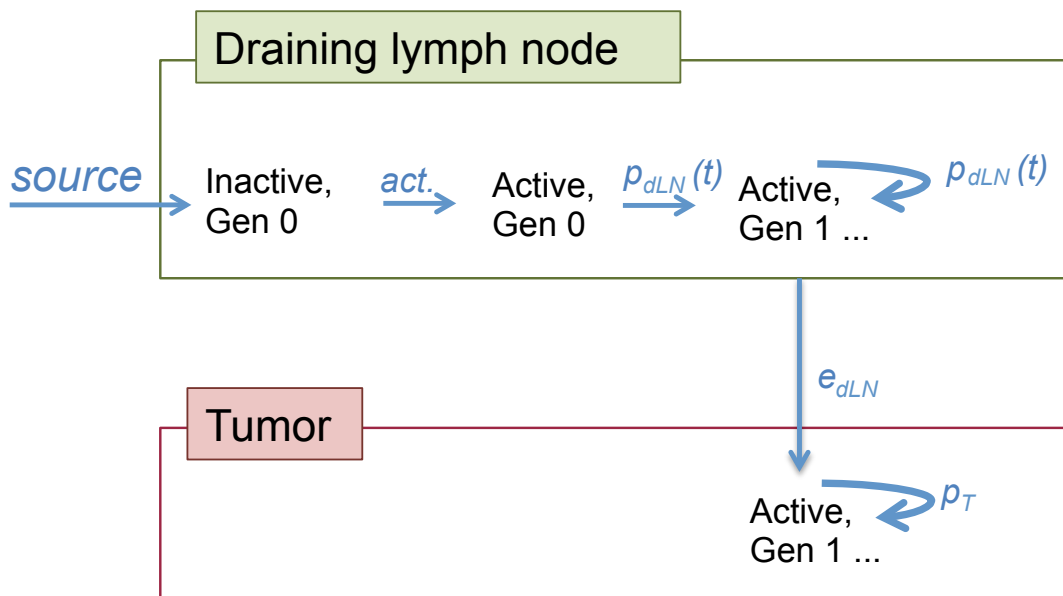


**Figure 4.8 :** Basic model structure applied for both experimental data sets. States are in black and parameters are in blue. **States:** Active cells continue dividing in the second experiment in both compartments. For the third experiment a division stop after 6 generations is introduced in both compartments. **Parameters:** Exponential decay of the proliferation rate in the draining lymph node  $p_{dLN}(t)$  in both experiments.

### Summary of the basic model structure

We have in total  $r=9$  parameters for the basic model structures of both experiments (Fig. 4.8). These are a source rate, an activation rate, a proliferation rate in the draining lymph node  $p_{dLN}$  defined by  $p_{dLN,0}$  and  $\alpha$ , a proliferation rate in the tumor  $p_T$ , an egress rate  $e_{dLN}$  and three error parameters: a relative error for the absolute cell numbers  $sd_{abs}$ , an absolute error for the mean number of divisions  $sd_{MDiv}$  and an absolute error for the frequencies of cells in generation 0 and  $n+$  in the draining lymph node and tumor,  $sd_{Gen}$ . We have 26 and 24 observables for the second and third experiment respectively (see suppl. section C.2).

### 4.2.2. Alternative models

In this section a more thorough discussion of the considered alternatives during the construction of the basic model structure is presented. For each alternative model structure we compare the model, where all parameters are chosen to be different between the treatment and control, but for the errors and the source term. The latter was set to be the same as there is no good reason to assume that the errors or the number of inactive cells entering the draining lymph node are influenced by the treatment.

Similar model structure changes are summarized and discussed in groups. The AIC and the negative loglikelihood of the best performing model structure of each group is noted. The latter is calculated following eq. (2.7) without the constant term.

Obviously, we cannot check all possible model alternatives and we focus on varying the division stop mechanisms and time dependent rates, with plausible alternatives. We furthermore pursue the question whether proliferation in the tumor is necessary.

General considerations about time dependent and generation dependent rates, the necessity of a proliferation in the tumor, the introduction of a death rate and the comparability of the different division stop mechanisms are discussed in section 3.2.2 in detail and are not repeated here. Here, we add a remark on the death rates and on the effect of introducing a division stop into the model.

**Death rate** Similar to the melanoma experiments, we extend the basic model structure by introducing either the same constant death rate in all compartments or only in the tumor. This should be identifiable, although we expect the death rate to be compensated by the source term to some degree, see section 3.2.2 and suppl. section A.2. We fit the extended model simultaneously to the treatment and control data with all parameters different between the treatment and control, but for the source and error terms. We only test this for the third experiment, since the data of the second experiment is too sparse to select models, which will be discussed later in this section. We find, that only the model with the death rate in all compartments improves the fit ( $\Delta\text{negLL} = 4$ ), but the AIC is still worse due to the increase in model complexity ( $\Delta\text{AIC} > 10$ ). Hence, the improvement is not large enough to justify the introduction of this additional parameter.

The evidence for an overall death rate is still noteworthy. Indeed, we see similar fractions of dead OT-I T cells in the draining lymph node and the tumor, when comparing the life/dead gates of the flow cytometry analysis. This is not the case for the melanoma experiments, where we tend to find more dead cells in the tumor than in the draining lymph node. Still, we have an overall higher fraction of dead cells in the pancreatic experiment in comparison to the melanoma experiment. The observations in the data are also reflected in the fits to the melanoma data, see section 3.2.2: The introduction of death rates did not improve the fit to the data of the time-resolved experiment and in the case of the proliferation-resolved experiment we only find evidence for a death rate in the tumor. But as discussed in section 3.2.2, when interpreting these tendencies care must be taken: For one thing, the identifiability of the death rate is impeded by the estimation of the source term and furthermore, comparisons between the life/dead gate fractions can only be made to a certain extent between different organs, time points and even less between different experiments. The latter is due to the fact that different amine reactive dyes are used in the PDAC and melanoma experiment. Hence, some part of the difference between the experiments might be the consequence of different staining protocols.

Although we do not introduce a death rate, from these observations we can still conclude that an overall death rate is more likely than in the melanoma experiment.

**Effect of division stop mechanisms** Division stop mechanisms can reconcile large absolute cell numbers with a cell division profile, which does not have a large fraction of highly divided cells. It allows the cells to divide and increase without overpopulating higher generations. This is the reason why the fit to the data of the third experiment performs much better with a divisions stop mechanism than with a continued proliferation. In the case of the third experiment, this is remarkable since a division stop does not suggest itself, when looking at the cell division profiles (Fig. 4.6), as opposed to the cell division profiles in the first melanoma experiment, see section 3.1.

### **Alternative models for the second experiment**

The performance of the basic model structure (Fig. 4.8) for the second experiment is compared to alternative model structures in the following. If fitted to both the treatment and control data simultaneously with all parameters different except for the source term and the errors, the basic model structure returns a fit with an AIC of 210.8 and a negative loglikelihood of 48.4.

**General remarks** None of the alternative model structures discussed in the following improve or worsen the fit by much. The same holds if the number of parameters which can be different between treatment and control is changed within the same model structure. In both cases the fit is not improved or worsened beyond  $\Delta_{negLL} = 5$ .

In consequence, none of the following model structures, with the same model complexity, i.e. the same number of parameters, can be rejected. And more complex model structures are discarded in terms of the AIC, since the improvement of the fit is always outcompeted by the increasing number of parameters: for example, the introduction of a dynamic egress rate or a generation dependent proliferation, which in principle improve the fit slightly ( $\Delta_{negLL} = 3.5$  and  $0.9$  respectively) are worse by  $\Delta_{AIC} > 20$ .

We observe a similar situation, when a model selection as is described in section 3.2.3 for one of the alternative model structures is conducted. During this selection we change the number of parameters which can be different between the treatment and control for the given model structure. Since additional parameters do not improve the fit by much, the model, where all parameters are the same between the treatment and the control, i.e. the one which has minimum complexity, performs best.

Altogether, the data seems too sparse to distinguish between models. Reasons for this are discussed in detail in the last section of this chapter, see section 4.3.1. Still, in the following we point out tendencies, when we test alternative model structures with 1) different generation stop mechanisms and 2) a generation dependent egress replacing the proliferation in the tumor.

**1) A division stop can also explain the data** We try proliferation stops in the draining lymph node after four, five and six generations with either a division stop in the same generation in the tumor or two more possible divisions after entering the tumor. The latter mechanism is motivated by the basic model structure of the first melanoma

experiment. All models, including our basic model structure with a continued proliferation, are within an  $\Delta\text{AIC}=5$ , as they have the same complexity. If a proliferation stop is considered, interestingly the models perform better the earlier the proliferation stop is. The division stop after four generations in both compartments performs best among the tried model structures and performs equal to our basic model structure. Thus, we also try this with only a division stop in the draining lymph node, which improves the fit by a  $\Delta\text{AIC}=4.5$ . We test this model structure further and a model selection returns a best minimal model, where—as expected—all parameters are the same for the treatment and the control. It is  $\Delta\text{AIC}=2.6$  better than the best minimal model of our basic model structure. As the improvement is not large we stay with the default option of a continued proliferation, as is done in the case of the basic model structure for the proliferation-resolved melanoma experiment. We conclude that we have evidence for a proliferation stop in the draining lymph node, that we have slightly less evidence for a continued proliferation or any of the other division stop mechanisms, but cannot reject any of these options.

**2) Replacing the proliferation in the tumor with a generation dependent egress rate leads to a worse fit** We replace the proliferation in the tumor with exponentially and linearly increasing generation dependent egress rates, as well as independent egress rates for each generation. The latter includes a factor, which is estimated and transforms the individual egress rates of the control to the ones of the treatment, as otherwise the model structure would have too many parameters. All perform slightly worse in terms of the negative loglikelihood and the latter has too many parameters and is rejected thus. The model structures with an exponentially and linearly increasing generation dependent egress rate have the same complexity, but perform slightly worse and lead to a  $\Delta\text{AIC}=5.3$  worse fit. These model structures cannot be rejected, but are less likely.

### Alternative models for the third experiment

The basic model structure of the third experiment, see Fig. 4.8, includes a division stop after six generations, both in tumor and the draining lymph node. Fitting it with all parameters being different but for the errors and the source term, we obtain AIC of 152.1 and a negative loglikelihood of 16.7. In the following we explore 1) whether division stop mechanisms are needed and which perform best, 2) whether we can replace the proliferation in the tumor with a generation dependent egress rate or a time dependent egress rate and 3) whether a time dependent egress rate improves the fit.

We do not test a generation dependent proliferation rate instead of the time dependent one, since already a constant proliferation rate fits the data well in the best minimal model of our basic model structure, see section 4.2.4.

**1) A division stop after six generations in both compartments performs best** The basic model structure includes a division stop at generation six. Considering the cell division profiles a division stop before generation six is not possible, see Fig. 4.6.

We furthermore test division stops at generation seven in both compartments, as well as a division stop after generation six in the draining lymph node with either a continued proliferation in the tumor or two more possible divisions in the tumor. The latter mechanism is motivated by the basic model structure for the first melanoma experiment. And we explore whether a generation dependent exponentially decreasing proliferation rate in both compartments performs better. All these model structures are different ways of introducing a special case of a division destiny, see section 3.2.2. Finally we also test, how a continued proliferation in both compartments performs.

All models with a division stop perform similar ( $\Delta\text{AIC} = 2$ ) and better than models with an exponentially decreasing generation dependent proliferation or a continued proliferation ( $\Delta\text{AIC} > 10$ ). The latter performs worse because a division stop mechanism can reconcile high absolute cell numbers with a relatively small fraction of highly divided cells. The division stop mechanism prevents an overpopulation of these higher generations. In consequence the fit with the continued proliferation underestimates the absolute numbers at the cost of fitting the last generation accurately.

Among the tested model alternatives with a division stop, a stop at generation six in the draining lymph node and a continued proliferation in the tumor performs best with  $\text{AIC} = 155.7$  and a negative loglikelihood of 18.5. But this is still  $\Delta\text{AIC} = 3.6$  worse than the fit with our basic model structure, where the divisions stops after six generations in both compartments.

From this analysis, we can conclude that some kind of division stop mechanism is needed to explain the data and that among these our basic model structure with a division stop after generation six in both compartments performs best.

**2) The proliferation in the tumor cannot be replaced with a generation dependent egress rate** Here, we try several model structures, where the proliferation in the tumor is replaced by different egress mechanisms, which are described earlier in this section 4.2.2, when the alternative models for the second experiment are discussed. Furthermore, a time dependent logistic egress rate is tested, which is motivated from the basic model structure of the time-resolved melanoma experiment. All models are  $\Delta\text{AIC} = 39$  worse than our discussed model structure and the best (linear generation dependent egress rate) leads to an  $\text{AIC}$  of 197.1 and a negative loglikelihood of 39.2.

We conclude that a proliferation in the tumor is needed in our model to explain the data.

**3) A time dependent egress rate does not improve the fit** We try a time dependent logistic egress rate, which is motivated by the basic model structure of the first melanoma experiment, to see whether this improves the fit and performs better in terms of the  $\text{AIC}$ . However the fit returning a negative loglikelihood of 16.7 is not improved, leads to an  $\text{AIC}$  of 250.2 ( $\Delta\text{AIC} = 98.1$  worse) and is accordingly rejected.

### 4.2.3. Model selection for the identification of the treatment induced changes in the second experiment

We aim at finding parameters which need to be different between the treatment and the control, when fitting both data sets simultaneously. This is achieved by performing a model selection, see section 3.2.3, with the basic model structure for the second experiment (Fig. 4.8). The selection is conducted by increasing the number of parameters which can be different between treatment and control,  $\Theta_{diff}$ , in a step wise fashion and keeping the models which improve the fit in every round. We again consider the models within  $\Delta AIC < 4$  of the global best model and determine the best minimal model (BMM), which is the model with the fewest parameters among these.

The fit does not improve much by increasing  $\Theta_{diff}$  (max.  $\Delta negLL = 6.5$ ), such that all complexer models perform worse with respect to AIC. As a consequence the BMM is the model, where all parameters are the same. It is also the global best model and closely followed with an AIC difference between 1.2 and 5 by all combinations where single parameters are different between the treatment and control. Among these the models with a different proliferation in the tumor and a different egress rate perform slightly better ( $\Delta AIC = 1.2$  und  $\Delta AIC = 2.7$ ). Indeed, compared to the BMM the most striking improvement of the model fit where  $\Theta_{diff}$  comprises all parameters (i.e. full model) is the fit to the absolute cell numbers in the tumor. This is owing to a different proliferation rate in the tumor and a different egress rate (suppl. Fig. C.3). However, the improvement of the negative loglikelihood is small and shows that the differences between the treatment and control data do not suffice to justify the introduction of more parameters to explain these differences. Additional measurements at later time points could resolve this to some extent, see discussion in section 4.3.

**Challenging tendencies in the data** Even between the prediction of the full model and the data there are still some discrepancies, which are also problematic in our best minimal model fit (Fig. 4.9):

First, the mean number of divisions seems to contradict the high number of proliferated cells in the tumor in the treatment setting (Figs. 4.9 f and g) and can neither be reconciled with the slower proliferation in our BMM nor with the faster one in the full model (interdivision times of 18.5h and 7.5h, respectively). The problem very likely arises from the fact that there are only few cells in the generations 1-3, from which the mean number of divisions is calculated. Thus, their fractions are not reliable and the observable calculated from them poorly reflects the mean number of divisions.

Secondly, the dynamic of the absolute cell numbers in the draining lymph node for the control is difficult to reconcile with the respective cell division profiles, see Fig. 4.9 a and d. The number of cells in the draining lymph node increases fast, but is then followed by a steep decline from day 1.7 to day 2.7, which contradicts the increasing number of cell divisions in the same time period. A sudden death leading to a loss of cells in the range of an order of a magnitude seems unlikely, too. In any case, it is necessary to consider that the first time point in the draining lymph node stems from mice with strongly varying total cell numbers ( $1.7 \cdot 10^3$  VS  $1.1 \cdot 10^4$ ) and the second time point stems from only one

mouse, so this decline should not be overrated.

Thirdly, the exact opposite tendency is seen for the absolute cell numbers in the draining lymph node in the treatment setting. It points at a strong increase of cell numbers from day 1.7 to 2.7 (Fig. 4.9b). This implies a fast exponential growth and—extrapolating this to early time points with a straight line—a small contribution from the source term. But the cell division profile on day 1.7 contradicts a fast proliferation. A slow activation and a consecutive fast proliferation is equally unlikely due to the small cell number in the undivided generation. The profile likelihood (see Fig. 4.10) suggests that a time dependent increase of the proliferation in the draining lymph node, i.e. a negative decay rate  $\alpha$ , can reconcile the small number of divisions on day 1.7 with the more highly proliferated cells on day 2.7 and the rapid increase of the absolute cell numbers. As this is an unlikely mechanism (see the discussion of time dependent parameters in section 3.2.1), we exclude this possibility by setting the lower bound of the decay parameter  $\alpha$  to zero.

In general, the fit to the cell division profiles on day 1.7 is posing a problem (Fig. 4.9 d and f). By modeling cell divisions with an ODE we assume an exponentially distributed waiting time until division, whereas cells are known to have a finite interdivision time. This leads to a distribution of the waiting time with a smaller coefficient of variation, especially at early time points, see section 2.3. In consequence, cell division profiles obtained from the measurement and from the model solution have different variances, which impedes a good fit.

When we fitted our best minimal model to the cell division profiles directly instead of the mean number of divisions, the model performed similar and we had the same issues which are mentioned above (not shown).

**Estimated parameters** It is important to mention that the mediocre fit to the data makes a sound interpretation difficult. Still, as the fit is in parts describing the data well, it is worth while having a look at its predictions.

The estimated parameters and their confidence intervals can be found in Tab. 4.3. Compared to the melanoma experiments the influx (source term) is smaller by far, which is remarkable as the same number of OT-I T cells have been transferred. Indeed, in this experiment we also see far less undivided cells in the blood, which are even too small to explain the source term alone, see suppl. Fig. C.1. Another source replenishing the cells in the blood is likely.

The activation rate cannot be constrained with this model. As it can be arbitrarily fast it implies that the time to first division is not distinguishable from the following interdivision times. The interdivision times in the draining lymph node and the tumor are similar (19h and 18.5h respectively). Both are somewhat slower than can be expected from recently and optimally activated T cells (10.1h *in vitro* [126]). As contrasted to the melanoma experiments there is only little evidence of a decreasing proliferation rate and the best fit predicts a constant proliferation rate over time, see Fig 4.9 c. The waiting time for egress of 5d is slow, but comparable to the rates, which have been observed in the melanoma experiments, see section 4.3.

**Conclusion** In conclusion, we see hints towards a changed proliferation and egress rate induced by the anti-CD40 treatment, but they are not significant. These could perhaps be substantiated with more data.

The fact that it is difficult to make a distinction between different model options, i.e. the  $\Delta AIC$  does not differ significantly for the different model options, has likely two reasons. On the one hand the data is not informative and sparse and on the other hand, there are opposing tendencies in the data, which lead to different models returning similarly mediocre fits.

Since we cannot distinguish very well between different model options and since the chosen best minimal model does not fit the data well, it is hard to draw reliable conclusions. Both, the hints towards an enhanced egress and proliferation rate, as well as the fact, that the best model does not predict any effect induced by the anti-CD40 treatment, have to be interpreted cautiously.

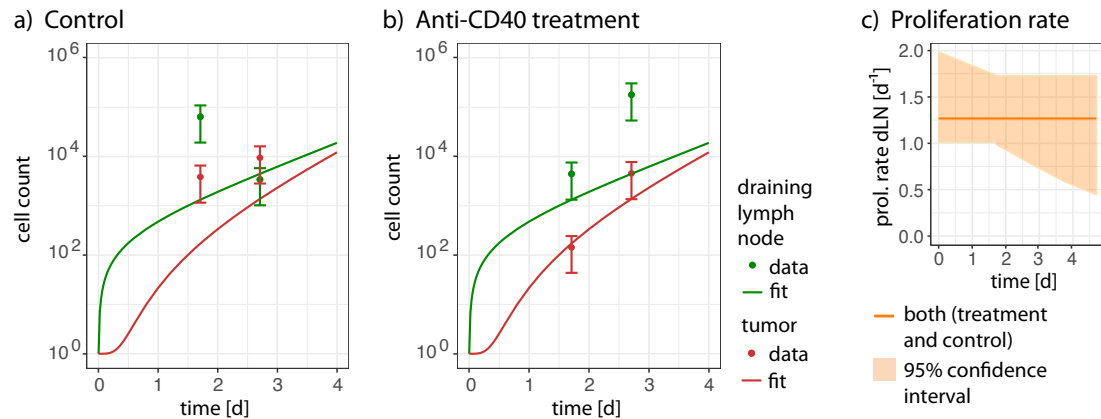
**Table 4.3.:** Estimated rates for the BMM, second PDAC experiment

Parameter	Control	95%CI	CD40	95%CI
source	290 cells/d	[66; 590]	"	"
activation	7.0 1/d	[1.4; <i>Inf</i> ]	"	"
$\alpha^*$	0 1/d	[0; 0.30]	"	"
$p_{dLN}^*$	1.3 1/d	[1.0; 2.0]	"	"
$e_{dLN}$	0.20 1/d	[0; 2.0]	"	"
$p_T$	1.3 1/d	[0.70; 1.9]	"	"
$sd_{abs}$	0.70	[0.50; 0.70]	"	"
$sd_{Gen}$	0.11	[0.082; 0.19]	"	"
$sd_{MDiv}$	0.44	[0.28; 0.83]	"	"

\* see eq.(3.1)

4.2. Mathematical model describing the T cell dynamics in a pancreatic cancer mouse model

Fit to absolute cell numbers



Fit to proliferation data

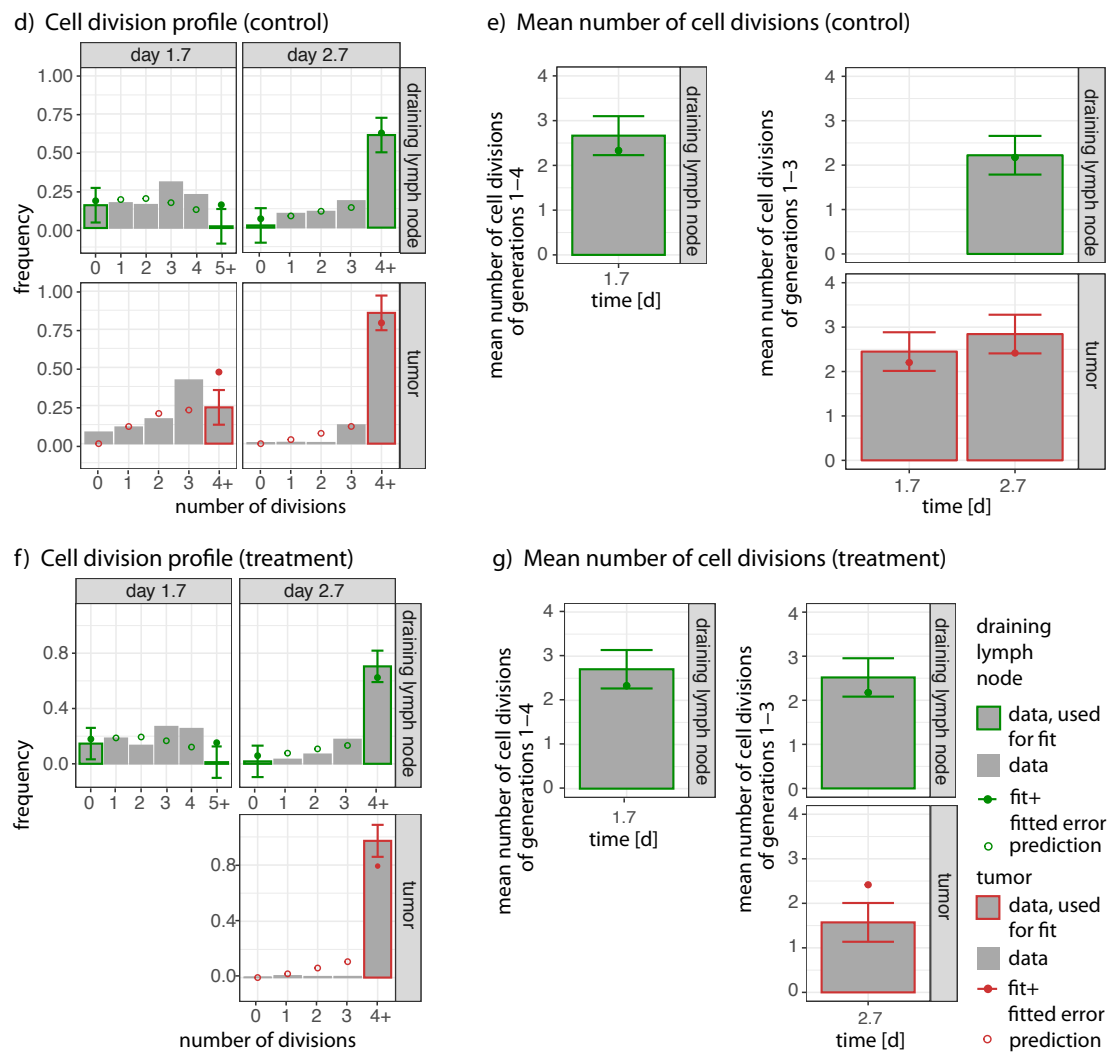


**Figure 4.9 (previous page):** Fit of best minimal model to the data of the second experiment. a) & b) Fit to the absolute cell numbers in the draining lymph node (green) and tumor (red) for the a) control and b) anti-CD40 treatment. c) Estimated proliferation rate in the draining lymph node, which is the same for control and treatment. Filled area indicates the 95% confidence interval. d) - g) Fit (dots) and prediction (circles) of the proliferation data: Only the color-bordered bars are used for fitting. d) Fitted and predicted cell division profiles and e) fitted mean number of divisions of the control. f) & g) Analogous plots for the treatment setting. Errors have been estimated and are indicated by error bars. Experimental data: Susann Wendler and Isabel Poschke.

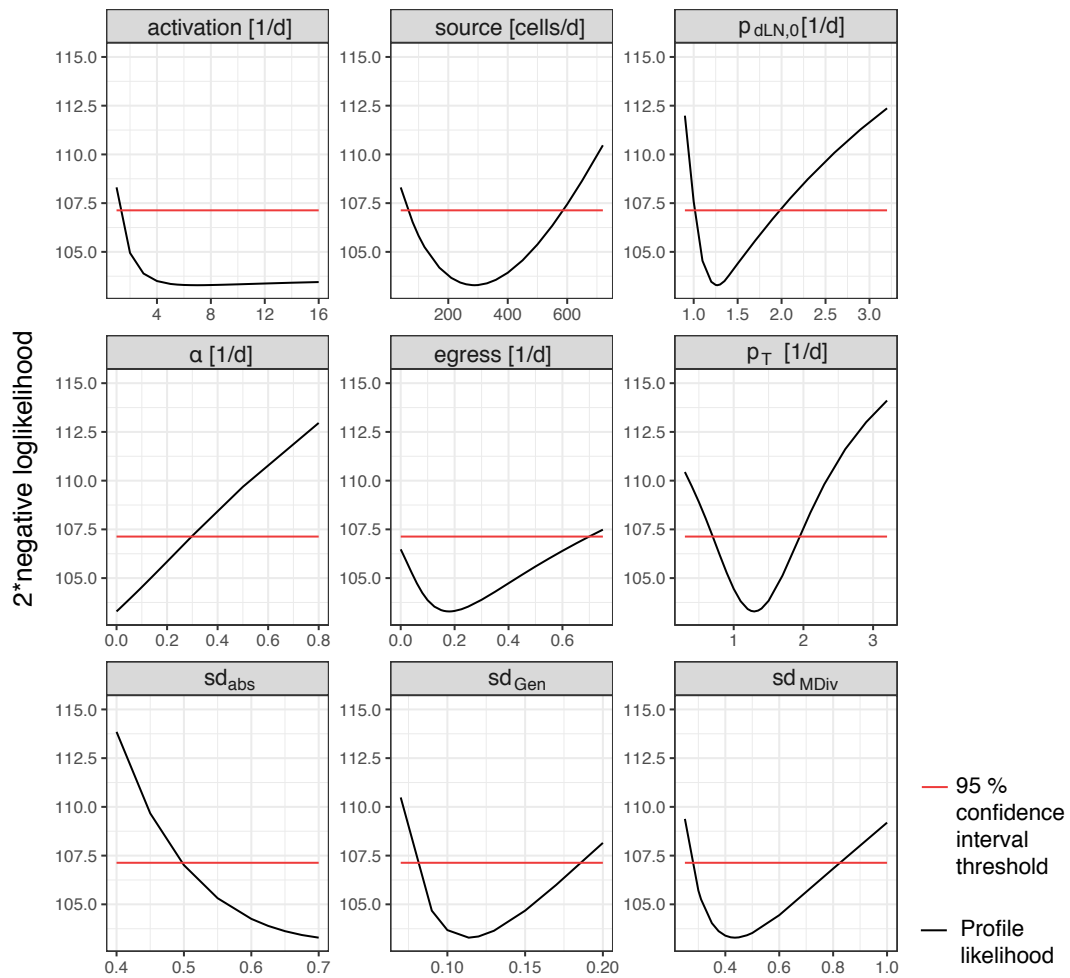


**Figure 4.10 :** Profile likelihoods of the best minimal model for the second PDAC experiment. Lower thresholds are set to 0. Upper threshold is introduced for the relative error for the absolute cell numbers,  $sd_{abs}$ , at 0.7. The red line denotes the threshold for the 95% confidence interval.

#### 4.2.4. Model selection for the identification of the treatment induced changes in the third experiment

It is our aim to find parameters which need to be different between treatment and control, when fitting both data sets of experiment III simultaneously. To this end, we perform a model selection as described in section 3.2.3 with the basic model structure of the third experiment (Fig. 4.8). This model includes a proliferation stop after six divisions. During the process of a model selection the number of parameters which can differ between treatment and control,  $\Theta_{diff}$ , are increased in a step wise fashion, the best models in each step is kept for the next round and thus a global best model among these models is found. We consider the models within  $\Delta AIC < 4$  of the global best model and choose the model with the smallest number of parameters among these, to which we refer as the best minimal model (BMM).

Here, the BMM predicts higher proliferation rates in the draining lymph node  $p_{dLN}$  and the tumor  $p_T$  in the treatment setting. The second best model ( $\Delta AIC = 2.2$ ) additionally predicts an enhanced activation rate for the treatment setting. With  $\Delta AIC = 8$  models follow which predict further parameters to be different besides the proliferation rates, but these do not improve the fit with respect to the negative loglikelihood.

The fit to the proliferation data, i.e. the mean number of divisions and the cell division profiles, performs well (see Fig. 4.11 c - f). Indeed, the frequencies of the cell division profiles are predicted perfectly and the corresponding errors  $sd_{Gen}$  are estimated to be very small, such that this can be seen as a sign of an over-parameterization. On the other hand, the prediction of the absolute cell numbers is mostly at the borders of the estimated error boundaries, but still satisfactory. The only data point which the model fails to explain is the absolute cell number in the tumor on day 3.7 in the control. As the corresponding mean number of divisions, as well as the cell division profile, are explained well by the fit, there appears to be a discrepancy between the absolute cell numbers and proliferation data. Since the accuracy of the absolute cell number measurement could very well vary between different read out days and organs, it is conceivable that our error model is not adequate and some measurements are subject to a higher variability than is estimated here.

**Fit to the cell division profiles** To test whether our results are robust with respect to the choice of the observables for the proliferation data, we perform a direct fit to the cell division profile instead of the mean number of divisions. Indeed, the direct fit to the cell division profile and the prediction of the fractions in the cell division profile, when fitting the mean number of divisions, are similar, compare suppl. Fig. C.3 and Fig. 4.11. Furthermore, the fit to the absolute cell numbers is similar and most estimated parameters of the direct fit to the cell division profiles are within the confidence bounds of our best minimal model fit to the mean number of divisions. Only the proliferation rates are predicted to be slightly smaller, which is counteracted by a very fast activation rate: The interdivision time for the control is  $13h$  (contrasted to  $11.7h$ ) for both compartments and for the treatment setting  $7.3h$  in the tumor and  $8.3h$  in the draining lymph node (contrasted to  $6.4h$  and  $6.7h$ ). The activation has no upper bound, implying that the

time to first division is the same as the interdivision times of the subsequent divisions. This suggests that the fit, except for the identifiability of the activation rate, is fairly robust with respect to the choice of the observables.

**Table 4.4.:** Estimated rates for the BMM, third PDAC experiment

Parameter	Control	95%CI	CD40	95%CI
source	230 cells/d	[92; 390]	"	"
activation	2.1 1/d	[1.7; 3.2]	"	"
$\alpha^*$	0.05 1/d	[0; 0.085]	"	"
$p_{dLN}^*$	2.1 1/d	[1.9; 2.2]	3.7 1/d	[3.5; 4.0]
$e_{dLN}$	0.12 1/d	[0.028; 0.31]	"	"
$p_T$	2.05 1/d	[1.97; 2.14]	3.6 1/d	[3.4; 3.8]
$sd_{abs}$	0.58	[0.38; 1.2]	"	"
$sd_{Gen}$	0.004	[0.0029; 0.0070]	"	"
$sd_{MDiv}$	0.33	[0.20; 0.67]	"	"

\* see eq.(3.1)

**Estimated parameters** The estimated parameters and their confidence intervals can be found in Tab. 4.4. All parameters are well constrained—however, in the case of the relative error estimate  $sd_{abs}$  and the decay rate  $\alpha$  with an upper (0.7) or lower bound (0 *nicefrac*1d) respectively, which were set to ensure plausible parameter ranges. Like in the model fit to the second experiment, compared to the melanoma experiments the source term is smaller by far, which is remarkable given that the same number of OT-I T cells have been transferred. Indeed, in this experiment we even see less undivided cells in the blood than in the second experiment, such that these are too few to explain even the small influx rate, see suppl. Fig. C.1. It is therefore plausible to assume that the undivided cells in blood are replenished by other reservoirs of T cells like the spleen.

The time to division is similar for the draining lymph node and the tumor and distinct for the treatment and control setting. The estimated interdivision time for the treatment with 6.4h (tumor) and 6.7h (draining lymph node) is fast compared to the interdivision time measured for optimally activated cells *in vitro* of 8h – 13h [125, 126, 102]. On the other hand, these studies confirm the interdivision time of 11.7h estimated in the control setting for both the tumor and the draining lymph node.

The egress rate of 0.12 1/d, i.e. a waiting time to egress of 8 days, is slow. But it coincides well with the dynamic range of the rates estimated in the first melanoma experiment and the constant rates estimated in the third melanoma experiment. The latter are included in the 95% confidence interval.

The activation rate of 2.1 1/d lies between the estimated activation rates of the third melanoma experiment with 1.1 1/d for the control and 3.9 1/d for the treatment.

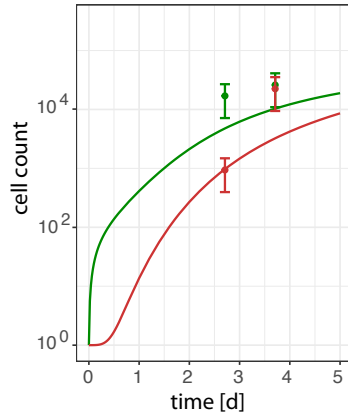
By summing the interdivision time in the draining lymph node to the waiting time until activation we obtain the time to first division with 23h and 18h for the control

and treatment respectively. Especially the latter (CI: [14;21]h) is at the fast end of the measured times to first division, which are reported to be between 24h and 48h [123, 145, 146].

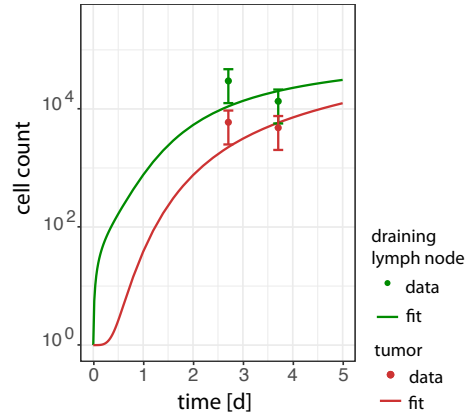
**Conclusion** The fit to the data of the third PDAC experiment performed well and is a contrast to the mediocre fit to the second experiment. This might be due to the later measurement time points, at which we have more cells, leading to less variable measurements and hence, resulting in less contradicting tendencies in the data. In addition, we have more proliferative information, i.e. we can distinguish more generations in the cell division profiles. These characteristics of the data contribute also to the fact that we can differentiate better between model alternatives. Although we still suspect an over-parametrization, the parameters are well constrained and realistic and we can determine which of them are influenced by the treatment. These are the proliferation rates in the draining lymph node and tumor, which is not surprising given that these differences can already be seen in the data. Furthermore, we have evidence for an enhanced activation rate, which was expected, since CD40 is reported to play an important role during priming [44, 45, 46, 47].

Fit to absolute cell numbers

a) Control

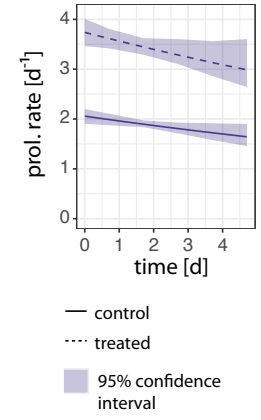


b) Anti-CD40 treatment



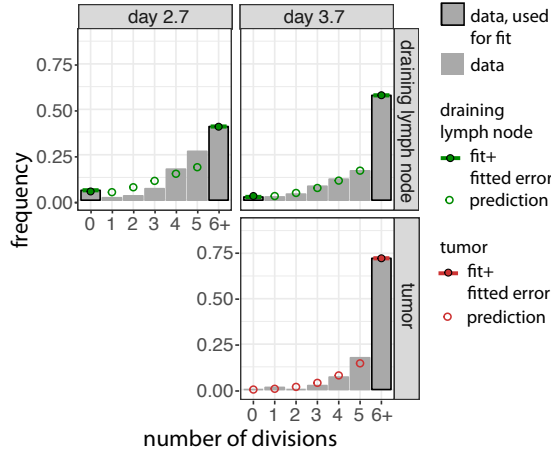
Estimated rates

c) Proliferation rates

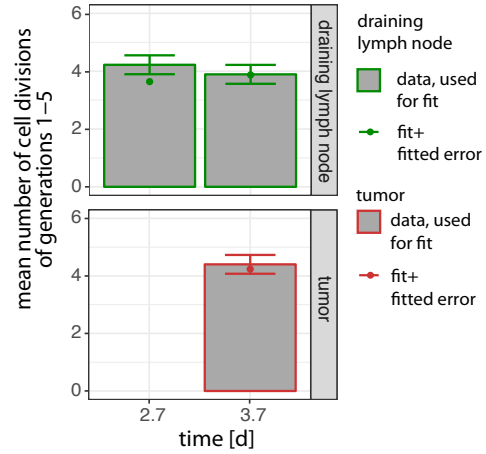


Fit to proliferation data

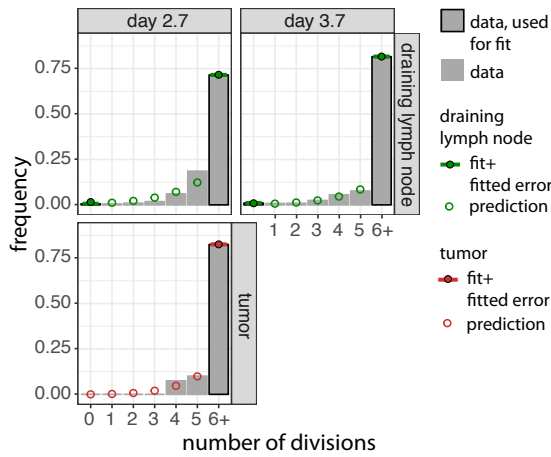
d) Cell division profile (control)



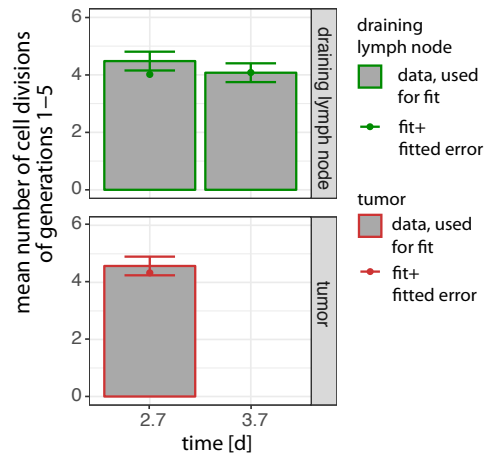
e) Mean number of cell divisions (control)



f) Cell division profile (treatment)



g) Mean number of cell divisions (treatm.)



4.2. Mathematical model describing the T cell dynamics in a pancreatic cancer mouse model

**Figure 4.11 (previous page):** Fit of the best minimal model to the data of the third experiment. a) & b) Fit to the absolute cell numbers in the draining lymph node (green) and tumor (red) for the a) control and b) anti-CD40 treatment. c) Estimated proliferation rate in the draining lymph node for control (solid line) and treatment (dashed line). Filled area indicates the 95% confidence interval. d) - g) Fit (dots) and prediction (circles) of the proliferation data. Only the bordered bars are used for fitting. d) Fitted and predicted cell division profiles and e) fitted mean number of divisions of the control. f) & g) Analogous plots for the treatment. Errors have been estimated and are indicated by error bars. Errors of the cell division profiles are very small such that only the horizontal line is visible. Experimental data: Susann Wendler, Aaron Rodriguez Ehrenfried and Isabel Poschke.

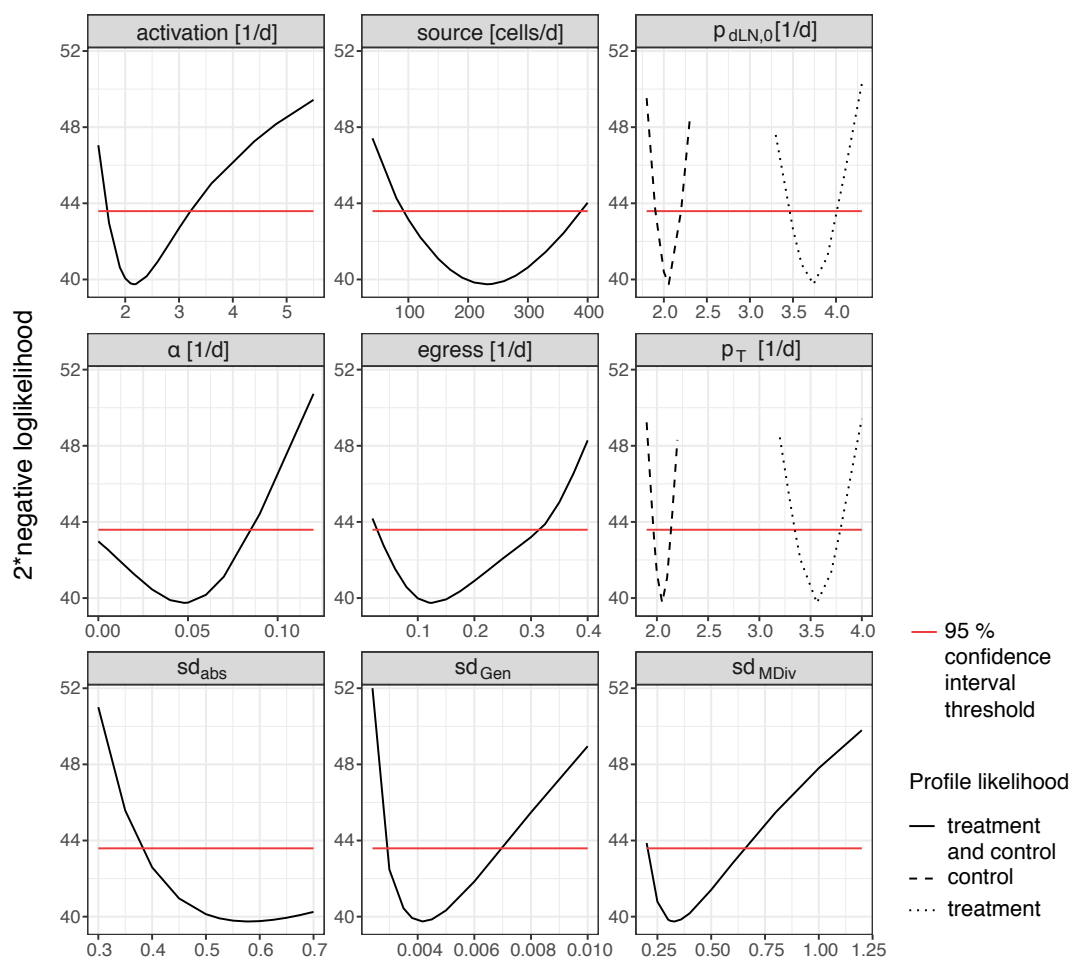


**Figure 4.12 :** Profile likelihoods of the best minimal model for the third PDAC experiment. Lower thresholds are set to 0. Upper threshold is introduced for the relative error for absolute cell numbers,  $sd_{abs}$ , at 0.7. The red line denotes the threshold for the 95% confidence interval.

### 4.3. Review of the results of the pancreatic ductal adenocarcinoma experiments

In the following, we discuss the results of the fit to the data of the pancreatic ductal adenocarcinoma (PDAC) mouse model experiments. In section 4.3.1 we focus on the performance of the fits and explain, why we do not consider the second experiment any further. In section 4.3.2 we summarize the fitting results from the PDAC experiment, compare it to the results from the melanoma experiments and point out how this reflects the characteristics found in the data analysis of the PDAC experiments.

#### 4.3.1. Challenges when fitting the sparse data of the PDAC experiments

Fitting a model, which is motivated from the melanoma experiment, can explain the data of the PDAC experiments to different degrees. Unfortunately both modeled experiments have less data than the melanoma experiments: there are two measurement time points and no additional proliferative information, e.g. BrdU.

This, however, is not problematic for the third experiment, where the data can be well explained by the model. Here, a likely over-parametrization can be inferred from the very small estimate of the error for the fraction of cells in different generations ( $sd_{Gen} = 0.004$ ,  $[0.0029; 0.0070]$ ). Nevertheless, the data suffices to distinguish different model options.

In the second experiment, however, the sparsity of the data is worse, as we can only distinguish the fractions of cells in different generations until the third or fourth division. This leaves this experimental data with almost no information on the proliferative activity. In addition, the early time point (day 1.7), where the few distinguishable generations could be informative, cannot be well described with our fit (Fig. 4.9 d and f). This is the likely consequence of the exponentially distributed waiting time until division assumed in our model, but cells are known to have a finite interdivision time. The model thus predicts a higher variance with respect the distribution of cells in different generations compared to the distribution resulting from the measurements (discussed in section 2.3). Furthermore, in the second experiment we do not only have the problem of a lack of data to inform a model, but also tendencies in the data, which are difficult to reconcile. A detailed description of these is found in section 4.2.3.

All of this contributes to the phenomenon that a range of different model structures returns equally mediocre fits. Hence, models with the same complexity have a similar AIC. Models with a more complex proliferation mechanism, which in principle improve the fit, are rejected, since the small improvement does not suffice to justify the increased complexity. For example, all models with and without different division stop mechanisms and consequently different proliferation rate estimates still perform similar and span a small range of AICs, since they have the same complexity. In contrast, during the model selection, we reject models, which improve the fit by introducing a treatment and control specific proliferation and egress—the improvement is not enough to compensate the increased model complexity.

We can conclude that less variable data and more measurements, perhaps also at later

time points, would improve the ability to distinguish different model options. But as it is, there is uncertainty about the correctness of the basic model structure that we choose for the second experiment and consequently about the resulting parameter estimates. Hence, the parameters of the second experiment are not discussed, when we compare the results from the PDAC experiments to the results from the melanoma experiments in the next section.

### 4.3.2. Comparison of the results of the PDAC and melanoma experiments

For reasons discussed in the previous section 4.3.1, we focus on the best minimal model fitting results of the third PDAC experiment and compare it to the results of both melanoma experiments. The studied murine tumor models are clearly different between the PDAC and the melanoma experiment with respect to the tumor microenvironment, the tumor location and the method applied for its inoculation. Given these differences it is surprising to see that a similar model can fit all three data sets. The model fitted to the third PDAC experiment is a mixture of the model structure of both melanoma experiments: It includes a division stop like the model for the first melanoma experiment and has a constant egress rate over time as in the model for the third melanoma experiment. In the following we discuss in how far the parameters, model alternatives and the predicted treatment induced changes of the best minimal model of the PDAC experiment compare to the results from the melanoma experiments and how this is determined by the available data.

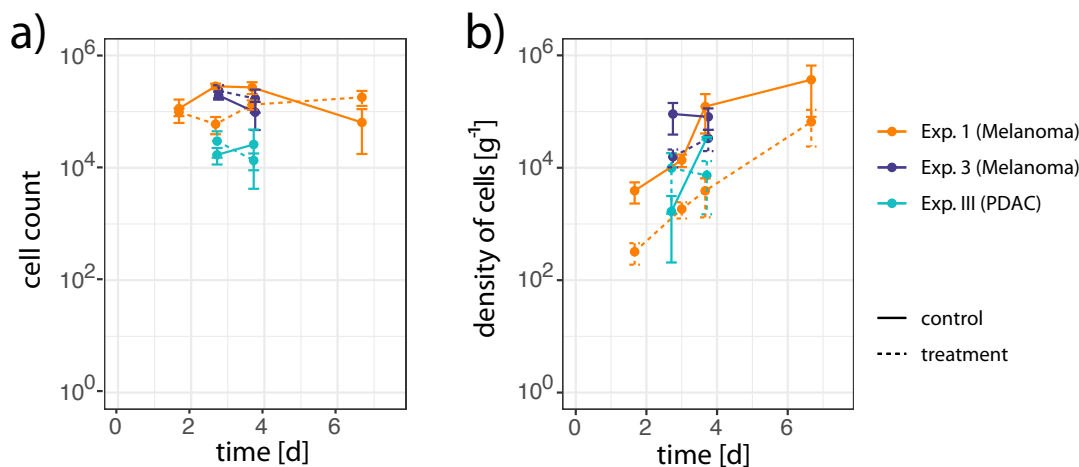


**Figure 4.13 :** a) Absolute cell number of OT-I T cells in the in the draining lymph node and b) density of OT-I T cells in the tumor. Plots for melanoma experiment 1 and 3 and in PDAC experiment III.

**Comparison of the proliferation dynamics** When discussing the results of the melanoma experiments in section 3.3.1, we conclude that a decreasing proliferation over

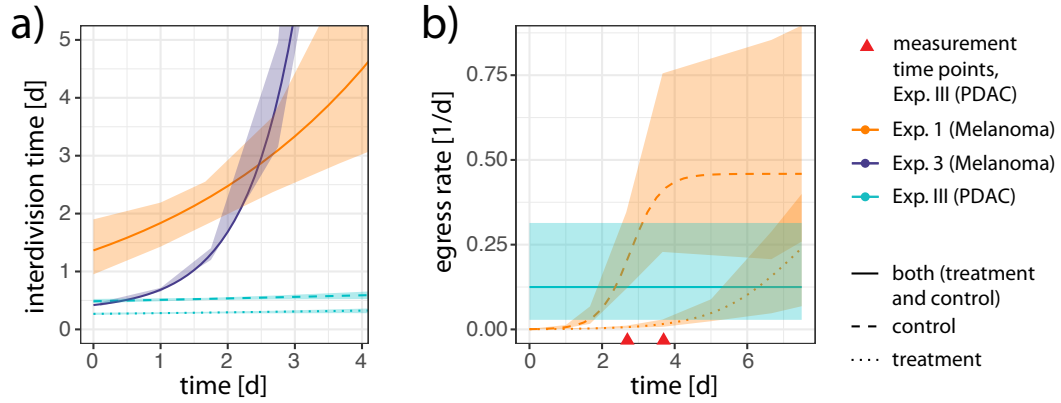


**Figure 4.14 :** Comparison of estimated rates: a) interdivision time in the draining lymph node b) egress rate.

time is governing the dynamics of the OT-I T cells in the draining lymph node. We furthermore argue, that a division stop mechanism is needed for the first experiment and that there is evidence for it in the third experiment. By testing alternative model structures, we confirm a division stop mechanism for the model fitting the PDAC data, too. The decreasing proliferation, however, is not necessary to explain the data. Indeed, when regarding the profile likelihood of the best minimal model of the PDAC experiment, we can see that a constant proliferation, i.e. the decay of the proliferation rate equaling zero, is well within a confidence interval of 95%. This is also reflected in the maximum likelihood estimate of the best minimal model leading to a faster and an almost constant proliferation in the draining lymph node for both the treatment and the control, see Fig. 4.14 a). The proliferation in the tumor is fast as well, but comparable to what is estimated in the melanoma experiments, see Tab. 4.5. Considering the differences in the cell divisions profiles of the melanoma and PDAC experiments, the faster proliferation estimates for the PDAC model are not surprising.

**Comparison of the proliferation rates** Regarding the results of the PDAC experiment, we find that the initial interdivision time in the draining lymph node, which does not increase by much over time, and the interdivision time in the tumor are the same (control: 11.7h and 11.7h, treatment: 6.4h and 6.7h). The interdivision time for the control is what can be reasonably expected of activated T cells as discussed in section 3.3.2. It is furthermore similar to the fastest proliferation rate, which we estimate for the third melanoma experiment. In the same section we discuss that rates estimated from this melanoma experiment are credible, due to the additional BrdU measurements and a better identifiability. In consequence we tend to believe the interdivision time estimate in the tumor of the third melanoma experiment (22h) and doubt the unexpectedly fast interdivision time in the tumor of the first melanoma experiment (6h). Interestingly the latter rate is now confirmed by the proliferation rate estimates of the PDAC model. We have a proliferation stop after a few divisions in both experiments with these fast

proliferation rate estimates. Hence, there is also the possibility, that instead of a slow proliferation cells can continue to rapidly divide after entering the tumor, but are stopped after a few divisions.

**Absolute numbers** Another noteworthy difference in the data is that far less cells can be found in the draining lymph node in the pancreatic experiment, although the same number of OT-I T cells have been transferred in all experiments. To a lesser extent this is also the case in the tumor. Indeed, the number of OT-I T cells in the draining lymph node is an order of magnitude larger in the melanoma experiments, see Fig. 4.13a. This is also reflected in the best minimal model estimates of the source term, which is two orders of magnitude smaller for the PDAC experiment, see tab. 4.5. Intriguingly, the density of OT-I T cells in the tumor is comparable for all experiments, see Fig. 4.13b. These observations coincide well with the hint towards dying cells in all organs in the PDAC experiment, which stands in contrast to the evidence of cell death being confined to the tumor compartment in the melanoma experiments, as is discussed in section 4.2.2.

**Activation rate** Both in the PDAC experiment and the third melanoma experiment we clearly see more highly proliferated cells in the anti-CD40 treatment setting, especially in the draining lymph node. In the model fit to the PDAC experiment, this is mainly attributed to a changed proliferation rate, but there is also strong evidence for an additionally enhanced activation rate. A correct estimate of the activation rate very likely depends on the availability of undivided cells in the draining lymph node, which do not exist for the measurements of the PDAC experiment, since the cells have divided too often. Thus, if the the information on the undivided cells was given, it would be interesting to see whether the results with respect to the anti-CD40 effect would coincide better with the results obtained from the third melanoma experiment: The latter attributes the difference of the cell proliferation profiles solely to a changed activation rate.

Interestingly the activation rate estimates of these two experiments are comparable, as the PDAC model estimate is in between the activation rate estimates of the treatment and control of the third melanoma experiment, see tab. 4.5.

How realistic the activation rates of these two experiments are, can be indirectly assessed, by comparing the time to first division. It is calculated by summing the waiting time until activation and the waiting time until proliferation in the draining lymph node. These are similar for the treatment setting of the third melanoma experiment with 16h (CI: [14; 18]h) and the treatment setting of the PDAC experiment with 18h (CI: [14; 21]h). Since this is on the fast side of the values found in the literature, which are reported to be between 24h and 48h, see refs. [123, 145, 146], this points at a slight overestimation of the proliferation or activation rate. On the other hand, the waiting time estimated for the control setting of the third melanoma experiment with 32h and the PDAC experiment with 23h are realistic.

Unfortunately the fit to the first melanoma experiment returns an unidentifiable activation rate, which can be arbitrarily fast, such that the interdivision time of the subsequent divisions (33h, initially) is the same as the time to first division. The lacking distinction

between the first and the subsequent divisions is certainly to be doubted and the estimated interdivision time could be an average of the two. Hence, the estimated rate for the time to first division, i.e. 33h initially, is likely a lower estimate for the real time to first division and with this likely in the expected range.

**Table 4.5.:** Comparison of selected parameter estimates from the third PDAC and both melanoma best model fits

		source rate [cells/day]	waiting time activation [h]	egress rate [1/d]	interdivision time tumor [h]
Exp. 1 melanoma	contr.	14000 [9100; 20000]	0.8 [0; 7.2]	see Fig. 4.14	6 [0; 15]
	treat.	" "	" "	see Fig. 4.14	" "
Exp. 3 melanoma	contr.	22000 [14000; 26000]	22 [18; 26]	0.31 [0.23; 0.43]	22.3 [18.5; 29.2]
	treat.	" "	6.1 [3.9; 8.3]	0.035 [0.023; 0.065]	" "
Exp. III PDAC	contr.	230 [92; 390]	11 [7.5; 14]	0.12 [0.028; 0.31]	11.7 [11.2; 12.2]
	treat.	" "	" "	" "	6.7 [6.3; 7.2]

**Time dependency and treatment induced effects on the egress rate** As opposed to the first melanoma experiment, a time dependent increase of the egress rate for the PDAC experiment is not needed. Since the change in the egress rate within 24h is not expected to be large, inferring a dynamic rate from two measurement time points on consecutive days turns out to be difficult (measurement time points are indicated with red triangles in Fig. 3.16a)—a problem, which has been already discussed for the third melanoma experiment in section 3.3.2. But in contrast to the latter case a model with a time dependent egress rate for the PDAC experiment does not perform better even when the increase in model complexity is disregarded. Furthermore, in contrast to the results from the melanoma experiments the egress rate of the PDAC model fit seems not to be influenced by the anti-CD40 treatment either. This is very likely a consequence of the similar absolute OT-I T cell numbers in the tumor for both treatment and control, which are different in the melanoma experiments.

We could conclude that the egress rate in the PDAC experiment is neither time nor treatment dependent. However, this rate is not well constrained. This becomes obvious, when comparing the rate and its error bounds to the rates in the first melanoma experiment in Fig. 4.14b. In addition, the egress rates of both treatment and control of the third melanoma experiment are within the error bounds of the PDAC egress rate, see Tab. 4.5. Since the confidence interval encompasses almost the whole dynamic and treat-

ment dependent range of the melanoma egress rates, it is conceivable that constraining the egress rate better could reveal a time and/or a treatment dependency, after all.

In any case it is interesting to note, that the egress rate is similar in all three experiments, suggesting that the small rate is independent of the cell numbers and the proliferative activity in the draining lymph node and of the tumor setting.

#### **Concluding remarks**

All in all, it is satisfactory that the model structure, which has been developed for the melanoma experiments, can explain the data obtained from the PDAC experiments, albeit to different degrees. The PDAC experiments have an explorative character and we see that especially for the second experiment we would need more measurement time points, better CFSE measurements and perhaps additional information on the proliferation, e.g. with BrdU. Nevertheless, the third experiment yields interesting insights into the dynamics of the naive T cell response to the PDAC tumor with generally comparable rates to the ones found for the melanoma setting. In addition, for all experiments we find that the anti-CD40 treatment has an effect on the number of divisions transferred OT-I T cells do. But, as we will continue to discuss in the next chapter, our analysis of the PDAC experiment suggests a slightly different mechanism leading to this effect. From the model selection we infer that this is the consequence of an enhanced proliferation and to a lesser degree of a stronger activation/priming of naive T cells. In contrast, the literature and the melanoma experiments rather suggest the latter to be affected by an anti-CD40 treatment [44, 45, 46, 47].



In this thesis we introduced a suitable data-preprocessing method and combined it with data-driven modeling to understand the influence of an immunomodulatory intervention on the T cell dynamics in a tumor context. The close alignment of the model with the data yielded a detailed insight into the naive T cell tumor response and enabled us to exclude plausible model alternatives. In the end, this gave us the possibility to discern tumor and tumor site effects on the T cell dynamics and to understand treatment effects of the immunostimulatory agonistic antibody against CD40. To our knowledge a mechanistic understanding of this treatment option's effect on the T cell compartment has not been investigated yet, despite its use in various clinical trials against different tumors. Consequently, through this work we contribute to a quantitative understanding of T cell migration, activation and proliferation in two tumor settings under an anti-CD40 treatment.

### **Analyzing dye dilution measurements**

In the second chapter we introduce a flexible mixture model for the analysis of dye dilution measurements to obtain information on the proliferative activity of cells *in vivo*. Cell proliferation dyes like Carboxyfluorescein succinimidyl ester (CFSE), where the fluorescence intensity is halved with each division of the cell, are widely used and in consequence many methods for its analysis have been developed. But mostly these methods have been optimized for data from *in vitro* measurements [152, 114, 113, 119], where the noise related broadening and overlap of the fluorescence peaks in different generations, i.e. the number of divisions a cell has accomplished, is not strongly impeding the analysis. In this work, we account for the additional variability in *in vivo* data, by consequently using data inherent information, i.e. the shape of the undivided and autofluorescence peaks. The mixture model is built by halving the dye intensities of an undivided model peak

taken from the data and by convoluting the constructed model peaks with the autofluorescence intensities in a discrete manner by sampling. Subsequently the kernel density estimates are calculated and the mixture model is smoothed. This is then binned in the same way as the data and the model is fitted to the data. In this way one obtains the relative weights for each model peak. As opposed to other approaches [114, 113] it is not linked to a division cascade model, but simply gives back the fraction of cells in different generations. This provides the possibility to use this information without having to incorporate the analysis of the CFSE profiles into a proliferation model. Furthermore, with this scheme different CFSE profiles can be flexibly combined for simultaneous optimization, but it also leaves the possibility to stay with a separate analysis of the data, if this is needed due to differences in the CFSE brightness.

We tested our method for six experimental data sets provided by two different collaboration partners and got satisfactory results. The variability in the different data sets motivated the introduction of flexible parameters with which one can change the binning of the data, the range and distance of initial CFSE intensities to be tested and the number of model peaks to be used. We also added the possibility to use a lognormal distribution for the description of an undivided/single model peak, if the data of an undivided peak is not at hand.

In summary this method provides the possibility to pass the CFSE intensities of the samples to be analyzed to the algorithm together with an undivided model peak, if available, and an autofluorescence peak. It returns the distribution of cells in different generations and if needed also for jointly optimized results of different samples. With this we present an opportunity to flexibly and accurately analyze dye dilution measurements.

To provide complementary proliferative information, it proved to be helpful to add BrdU, which is incorporated by dividing cells, shortly before the measurement time points. The knowledge about the short BrdU availability [133] and the assumption that the average S/G<sub>2</sub>/M phase length does not change a lot [126, 112], enabled us to incorporate the BrdU dynamics into the model in a simple way. This resulted in well identifiable and realistic estimates of the activation rate and dwelling times in S/G<sub>2</sub>/M and G<sub>1</sub> phase.

### **T cell proliferation in response to different tumors**

While the CD8+ T cell response has been studied in close accordance with experimental data in contexts like the acute [115] and chronic immune response [105], so far we do not know of similar approaches that describe the T cell response to tumor. Focusing only on the T cells in the tumor-immune cell interaction enabled us to integrate relevant external influences into the parameters of interest and simplify the model in a way, which leaves these parameters identifiable with the given data. The basis of the model is built in line with the well established dynamics of T cells in an acute infection setting: naive T cells are attracted to and activated in the draining lymph node and subsequently proliferate and egress to the tumor (site of infection). Starting from this basic model we tested plausible variations by changing the time and division dependency of variables, while keeping the complexity of the model within limits.

---

Two tumor models were considered in this thesis: melanoma and pancreatic ductal adenocarcinoma. Being an immunogenic tumor most advances in the field of immunotherapy have been achieved by studying responses to treatment strategies in melanoma [74]. The hope to find transferable results in this model, as well as the need for new treatment strategies for melanoma itself motivated its choice. Here, we analyzed data from two experiments with the well established subcutaneous murine B16/OVA model, which is not physiological with respect to the inoculation site, but should reflect the principle dynamics of a T cell response to tumor and the effect of an anti-CD40 treatment on it. Equipped with our experiences and the mathematical model established and adjusted with the first melanoma experiment, we moved on to a pancreatic cancer model and applied a similar experimental setup and model. This tumor is more physiological due to its orthotopic inoculation site and was developed to be close to the clinical setting in so far as it resembles the histopathology of human PDAC—a tumor for which therapeutic options are urgently needed.

Although the data of both melanoma experiments vary with respect to the absolute recovered T cell numbers and the proliferative data, the models predict a similar dynamic. We confirm a time dependent decrease of the proliferation in the draining lymph node and an on average faster proliferation in the tumor, albeit only for two divisions in the time-resolved experiment. This proliferation at the tumor site is likely needed, since model alternatives, where highly proliferated cells can preferentially egress into the tumor and thereby replace the proliferation, could not explain the data. The nature of the PDAC experiments, discussed in chapter 4, was more explorative with few measurement time points, but we succeeded in fitting a similar model to the more informative experiment among them. Here, the proliferation in the tumor could be confirmed in the same way. Overall, we obtained interdivision time estimates for the tumor ranging from 6h to 22h, where the shorter interdivision time—although not unrealistic [144]—is fast, even for optimally activated T cells (8 to 13h, see refs. [125, 126, 102]).

Further similarities in spite of the differences between the tumor settings are the initial interdivision times in the draining lymph node. They range from 7 to 12h, but for the initial interdivision time estimate in the best model fit of the first melanoma experiment with 33h—a fit where the identifiability of proliferation associated rates was generally more challenging. This might point at a weakness of the approach which only uses CFSE to inform these parameters. Indeed, without the combination of both BrdU and CFSE measurements, we observed also in other cases (not the best model fits) that we could not identify the activation rate, which was then estimated to be arbitrarily fast. This in turn implies that the time to first division has the same length as the consecutive interdivision times, which we know to be unrealistic [123, 145, 146]. On the other hand, the combination of both proliferative dyes turned out to be a useful tool to determine proliferation rates and provided good fits. For example, the estimated initial interdivision times in the melanoma experiment using BrdU are surprisingly close to the reported interdivision times of activated OT-I T cells in ref. [126]: the authors measure an average cell cycle time of 10.1h and find that 72% of the time is spent in  $S/G_2/M$ . Although the implied linear relationship between the length of the  $S/G_2/M$  phase and

the total cell cycle time in this study is debatable [127, 137, 112] and not used in our model assumption, we find astoundingly similar results with a dwelling time of 2.3h in the  $G_1$  phase and 7.8h in the  $S/G_2/M$  phase.

A noteworthy difference between the model fits of the two tumor settings is the prediction of a fast continued proliferation in the draining lymph node in PDAC as opposed to an attenuated proliferation over time in melanoma. These differences could already be guessed by observing the more highly proliferated cells in the PDAC data. Modeling, in addition, suggested a moderately higher proliferative activity in the tumor, since the fast proliferation is kept up for six generations.

This phenomenon can be attributed to the different tumor cell lines and their microenvironment and immunogenicity, but also other reasons can be considered. We already suggested that an overpopulation of the draining lymph node might dampen the proliferative response, as we have an order of magnitude more cells in the melanoma experiments. But also different tumor inoculation sites can lead to differences in its local architecture, which influences the immune response. For example it is reported, that the tumor site changes the lymph node like vasculature in B16 melanoma [153], as well as the development of tertiary lymphoid structures (TLS) [154, 155]. In addition, the differences in infection sites are known to have various influences on the dendritic cell priming and T cell homing [156, 157, 158]. With respect to the TLS, however, we know that most likely both tumors did not develop these, since it is unlikely in primary subcutaneous murine melanoma [155] and our collaboration partners have not observed TLS in their 30364-OVA cell line, so far. Bearing in mind the studies concerning the lymph node like vasculature in tumors, the mathematical model could be expanded to include a separate naive T cell recruitment and activation rate for the tumor. Indeed, naive T cell recruitment and activation is reported in ref. [153, 159]. But this is not easily induced in an effective manner [160]—not least due to the metabolic activity of melanoma producing lactate [161], which creates a hostile environment, especially for naive T cells [162]. Furthermore, these model parameters would be hard to identify due to the increased complexity. In consequence, neither the literature nor the feasibility strongly suggested the introduction of this mechanism. All in all, the studies on the site-dependency of the TLS and the lymph node like vasculature still permit the assumption of an influence of the tumor location on the proliferation dynamics.

However, the difference of the proliferative activity between the PDAC and melanoma setting is put into perspective by the fact that in all three experiments we found evidence for cells to stop after a certain number of divisions. This in particular means that the fast proliferation in the draining lymph node in the PDAC setting will eventually also come to a halt. It is noteworthy that an attenuated proliferation over time and a division stop mechanism were not interchangeable, i.e. could be distinguished by fitting the respective model. The division stop mechanism was introduced when a large absolute cell number needed to be reconciled to a CFSE profile with relatively few cells which have divided often, such that cells could divide and accumulate without overpopulating the higher generations. Although we cannot tell from our study how the abrupt division stop is regulated, it could be the result of a division destiny—a concept, in which the number of

---

divisions a cell undergoes, i.e. their division destiny, is determined before its first division and influenced by early costimulatory signals [108]. Interestingly the generation in which the proliferation in the tumor stops is different between the two melanoma experiments. This might be a consequence of a general variability between the experiments, but a likely explanation is the tumor size, which correlates with the number of divisions a cell did. It remains to be investigated, whether the observed difference is indeed a consequence of a larger tumor, entailing, for example, a higher concentration of antigens, cytokines and more costimulation by other immune cells. These stimuli could then lead to an increased mean division destiny [108]. For future investigations a way to test this hypothesis would be to measure antigen concentrations as a proxy for the stimulation of T cells in the draining lymph node.

Altogether, we observed different ceasing mechanisms for the proliferation in the draining lymph node (division stop and the attenuated proliferative activity). In the tumor the likely division destiny provides an interesting contrast to the fast proliferation, which could not be explained by other mechanisms. Yet a fast proliferation at the site of inflammation is in principle not unexpected. In refs. [134, 138] it has been shown that the highly proliferated cells at these sites are not the consequence of a preferential egress of highly divided cells from the draining lymph node, but the result of local proliferation, which we also suggest with our analysis. Furthermore, this is in line with various measurements of Ki-67 in CD8+ T cells at the tumor site [163, 164, 165] or measurements of T cell proliferation in the tumor [159]. Nevertheless, a continued proliferation at the tumor site would have been unexpected: The tumor environment consists of a variety of immunosuppressive myeloid and lymphoid cells, suppressive metabolites and cytokines, which casts doubt on the ability of T cells to proliferate there [151, 166, 167]. For this reason, our study, which predicts a moderately fast proliferation and a likely cessation after a few divisions suggests a realistic mechanism.

**Distinct death rates due to different tumors?** The enhanced proliferation in the pancreatic model compared to the melanoma model is contrasted by lower OT-I T cell numbers in all organs. A possible explanation is the higher fraction of dead cells among the transferred T cells seen in the life/dead gate of the flow cytometry analysis. This difference between the experiments was more pronounced in the draining lymph node, although in general a limited comparability of these gates has to be taken into account. Interestingly, the tendency of an overall death rate in the pancreatic cancer experiment was confirmed by fitting corresponding models, in spite of the limited identifiability of the death rate. Indeed, the introduction of an overall death rate—as opposed to one only in the tumor—improved the fit, which was not the case for the melanoma experiment. Yet, an introduction of this rate into the model of the pancreatic cancer experiment could not be justified by the improvement, due to the increase in model complexity. In the melanoma experiment, we had either no evidence for a death rate or evidence for a death rate which is confined to the tumor.

It would not be surprising for PDAC to be giving rise to an immunosuppressive tumor environment with cells controlling an effective immune response [73] and it is interesting

to note, that the melanoma might be creating a similarly hostile tumor microenvironment. But with this observation, we can assume that the pancreatic tumor unlike melanoma induced a systemic immunosuppressive response which goes beyond the immediate tumor environment. Death in the periphery can affect several T cell subsets [162, 168] and is reported to be triggered by different mechanisms than in the tumor environment, for example by not properly activated dendritic cells or a cessation of cytokines and growth factors [169]. Whether a mechanism like an activation induced death is really contributing to this phenomenon, would need further investigation.

It is noteworthy that these differences between the two tumor settings, i.e. T cell death and proliferation, are more pronounced in the draining lymph node and not in the tumor environment. Since studies report the importance of the systemic immune response as opposed to the local response in the tumor during tumor rejection [170], it would be interesting to better understand in further studies how and with what consequences the pancreatic tumor shapes the T cell response to the same antigen outside of the tumor.

### **The effect of anti-CD40**

The treatment of immunologically cold tumors still poses a challenge for immune therapy, which established itself as a fourth pillar in cancer therapy. A recent review by Vonderheide, ref. [4], suggests anti-CD40 treatment as an option to aid the conversion of a cold tumor into a hot one and in order to fully exploit the potential of other immunotherapeutic interventions and chemotherapies [65, 63, 57]. Indeed, on its own its treatment effects so far are limited [57, 63, 60], which we could confirm with the analyzed experiments. In the melanoma experiments we could perceive a slightly decreased tumor growth, but no effect was observed in the PDAC experiments. Nevertheless, with our modeling approach we could point out mechanisms and dynamics of T cells which are influenced by the anti-CD40 treatment. This was achieved by determining parameters which need to be different, if both the treatment and the control data are fitted simultaneously.

**The egress rate is attenuated by the anti-CD40 treatment** The perhaps most surprising finding was the attenuated egress of T cells under treatment in both melanoma experiments. With our modeling of the time-resolved melanoma experiment which encompassed a time range of 5 days we could, furthermore, identify an increasing egress rate in a time dependent manner. In contrast, when fitting the proliferation-resolved melanoma experiment, the time dependence could not be well resolved. A reason could be that the measurements span only one day. Still, there was evidence for this mechanism, as its introduction improved the fit—albeit not sufficiently to justify the added model complexity. For the PDAC experiment in turn, there was no indication of a time or treatment dependent egress, but the rate is also poorly constrained. Indeed, its confidence boundary largely overlaps with the confidence boundaries of the other egress rates, irrespective of their time and treatment dependency. The similar range of these rates is surprising, given that many factors like the local vasculature and tumor microenvironment influence the egress rate (and probably more than they influence the proliferation rate).

---

In both melanoma experiments we could on average confirm a tenfold decrease of the egress rate due to the treatment. The rates are comparable from day 3 onwards, which happens to be the earliest measurement time point for the proliferation-resolved melanoma experiment and implies that further measurement time points might have revealed a similar time dependency. In the experiment where we could resolve the time dependency, the egress starts to increase from day 2 onwards in the control and from day 4 onwards in the treatment setting. A similar range for the initiation of egress is reported in an acute infection setting and a setting where T cells are activated by antigen loaded dendritic cells, see refs. [171, 172]. Interestingly the authors claim that T cells with a higher affinity to the presented antigen remain longer in the lymph nodes and spleen ( $> 4days$ ) than low affinity T cells, which interact less stably with dendritic cells. Indeed, it has been shown that an anti-CD40 treatment enhances the interaction between dendritic cells and T cells [173]. In consequence, one could speculate that this mechanism is enhancing the dwelling time in the draining lymph node. On the other hand, in ref. [171] it is reported that the prolonged dwelling time is correlated with the slower development of an effector phenotype, which we cannot confirm with our data—if at all, we see a slightly increased proportion of CD27<sup>low</sup> cells due to the treatment, which is indicative of a more terminal effector phenotype. To analyze and compare this further, future work could incorporate measurements of granzyme B (GzmB), which is expressed by effector cells, or measurements of the transcriptional factors regulating the effector functions, like the basic leucine zipper transcription factor, ATF-like (BATF) and interferon-regulated factor 4 (IRF4), which are mentioned in ref. [171]. Furthermore in order to have a more direct measurement of the propensity to egress one could investigate the expression of sphingosine 1-phosphate receptor type 1 (S1PR1) on T cells, which controls their exit from the lymph node [174] and should be internalized upon T cell activation [38]. This mechanism would be of particular interest since it provides a direct link between the egress rate, which according to our analysis is attenuated by the anti-CD40 treatment and the activation rate, which we found to be increased by the treatment.

**Does anti-CD40 influence the activation and/or the proliferation?** The results of the proliferation-resolved melanoma experiment, the PDAC experiment and to some degree the time-resolved melanoma experiment agree in so far as we can discern more highly divided cells in the anti-CD40 treatment setting. The explanation obtained from the model fit however vary slightly. The model fit to the data of the melanoma experiment with additional proliferative information (BrdU) unambiguously points at an enhanced activation rate of T cells, which could be expected from the literature [38]. There is also evidence for an altered activation in the pancreatic model, however to a lesser degree than an enhanced proliferation. Finally we have evidence towards an increased proliferation at early time points in the time-resolved melanoma experiment, albeit in combination with an unidentifiable activation rate, such that it is hard to draw a conclusion concerning this rate from the model fit. Thus, having either an unidentifiable activation rate or no undivided cells to inform this rate properly in the PDAC experiment, there is no real counterargument to the evidence of an enhanced activation obtained from the fit to the

data combining BrdU and CFSE. The increased proliferation cannot be rejected, but is more arguable.

This conclusion contributes to the answer of the question raised in a recent review paper [4], whether an anti-CD40 treatment is recruiting new naive T cells to respond to tumor and/or is just enhancing the proliferation of already activated T cells. Here, we provide evidence that previously naive T cells are more strongly activated, i.e. recruited, as a consequence of the anti-CD40 treatment. The second part of the question is harder to answer: although there is evidence of an enhanced proliferation, it is weaker and we do not know whether this is just a consequence of the enhanced activation or a separate mechanism acting on already activated cells. To pursue this question further, a future study could test the effect of anti-CD40 on already activated T cells with a similar approach as is presented here.

In principle, the fact that slightly different anti-CD40 antibodies were used could contribute to the observed differences between the PDAC and the melanoma setting. But personal communication with my collaboration partners suggest, that the anti-CD40 effect should be similar and furthermore, the constant part is known to bind to the same  $Fc\gamma$  receptor [18, 21]. In consequence, it is unlikely that a significant difference can stem from the distinct antibodies. Our observation that for the PDAC experiment the anti-CD40 effect is leaning more towards an enhanced proliferation than activation could also be affected by the fact that the administration was shared between two days. This means that half of the dosis was applied one day later than in the melanoma experiment. Another point of concern could be, that we have a PBS control (as opposed to an isotype control) in the PDAC setting such that we do not know whether the observed effects of anti-CD40 in this experiment might also be caused by unspecific activation. But as the observed anti-CD40 effects in the PDAC setting are similar to the ones in the melanoma, this does not seem very likely either. Nevertheless, in order to rule out these possibilities one would need to perform the experiments with the same anti-CD40 antibody, the same administration time points and the same isotype control.

An interesting question which is beyond the scope of this work, is whether the anti-CD40 treated T cells can also provide a better tumor killing capacity either phenotypically or as a whole due to increased numbers. In any case, this effect, if existent, is expected to be small [57, 63, 60]. Although at early time points we seem to have fewer T cells in the tumor of the anti-CD40 treated mice, it is conceivable that they increase more at later time points due to a delayed egress and an increased proliferation and activation. A follow-up over an extended period of time would be needed to resolve these longterm dynamics. As for the phenotype of a single T cell, it would be expedient to conduct killing essays and to check with different markers, whether the cells have acquired better effector functions: So far in our study neither our measurements of CD62L and CD27, with the help of which effector and memory T cells can be distinguished [38, 148, 149], nor the activation and exhaustion marker PD-1 (not shown) were differently expressed in different organs or showed conspicuous tendencies over time. Furthermore, the attenuated growth of the tumor cannot necessarily be attributed to the anti-CD40 treatment effect on naive T cells, which need to be activated first, because the decelerated growth

---

starts shortly after the beginning of the treatment. Hence, a direct effect of anti-CD40 on immune cells in the tumor environment seems more likely.

In summary, in this work, we show how a data-driven modeling approach can reveal new aspects of an already well studied immunotherapeutic treatment option. To this end, we introduced a generally applicable method for the analysis of cell proliferation dye measurements. By exploiting the proliferative measurements analyzed with this method and combining them with the information from absolute cell number counts, we could establish a data-driven model. This sheds light on the way an anti-CD40 treatment shapes the dynamics of the T cell tumor response. We can conclude that it is affecting this response in at least two ways—through an enhanced activation of naive T cells and through their retention in the draining lymph node—and provide, herewith, a good starting point for follow-up studies. Future studies investigating the predicted anti-CD40 effect on the naive T cell response could be performed, for example, by measuring the delay in the upregulation of egress surface markers (e.g., S1PR1) or effector molecules (e.g., granzyme B). In addition, the treatment’s influence on the proliferative capacity of already activated T cells could be tested. Furthermore, research on other immunotherapeutic treatments using a similar approach, as is outlined in this thesis, could be conducted. Results from these studies should contribute to inform optimized treatment schedules to mount a successful and lasting immune response against cancer.



---

## Bibliography

---

- [1] S. A. Rosenberg, B. S. Packard, P. M. Aebbersold, D. Solomon, S. L. Topalian, S. T. Toy, P. Simon, M. T. Lotze, J. C. Yang, C. A. Seipp, C. Simpson, C. Carter, S. Bock, D. Schwartzentruber, J. P. Wei, and D. E. White, "Use of Tumor-Infiltrating Lymphocytes and Interleukin-2 in the Immunotherapy of Patients with Metastatic Melanoma," *New England Journal of Medicine*, vol. 319, pp. 1676–1680, Dec. 1988.
- [2] L. Galluzzi, E. Vacchelli, J.-M. B.-S. Pedro, A. Buqué, L. Senovilla, E. E. Baracco, N. Bloy, F. Castoldi, J.-P. Abastado, P. Agostinis, R. N. Apte, F. Aranda, M. Ayyoub, P. Beckhove, J.-Y. Blay, L. Bracci, A. Caignard, C. Castelli, F. Cavallo, E. Celis, V. Cerundolo, A. Clayton, M. P. Colombo, L. Coussens, M. V. Dhodapkar, A. M. Eggermont, D. T. Fearon, W. H. Fridman, J. Fučíková, D. I. Gabrilovich, J. Galon, A. Garg, F. Ghiringhelli, G. Giaccone, E. Gilboa, S. Gnjatic, A. Hoos, A. Hosmalin, D. Jäger, P. Kalinski, K. Kärre, O. Kepp, R. Kiessling, J. M. Kirkwood, E. Klein, A. Knuth, C. E. Lewis, R. Liblau, M. T. Lotze, E. Lugli, J.-P. Mach, F. Mattei, D. Mavilio, I. Melero, C. J. Melief, E. A. Mittendorf, L. Moretta, A. Odunsi, H. Okada, A. K. Palucka, M. E. Peter, K. J. Pienta, A. Porgador, G. C. Prendergast, G. A. Rabinovich, N. P. Restifo, N. Rizvi, C. Sautès-Fridman, H. Schreiber, B. Seliger, H. Shiku, B. Silva-Santos, M. J. Smyth, D. E. Speiser, R. Spisek, P. K. Srivastava, J. E. Talmadge, E. Tartour, S. H. Van Der Burg, B. J. V. D. Eynde, R. Vile, H. Wagner, J. S. Weber, T. L. Whiteside, J. D. Wolchok, L. Zitvogel, W. Zou, and G. Kroemer, "Classification of current anticancer immunotherapies," *Oncotarget*, vol. 5, Dec. 2014.
- [3] I. Melero, D. Hirschhorn-Cymerman, A. Morales-Kastresana, M. F. Sanmamed, and J. D. Wolchok, "Agonist Antibodies to TNFR Molecules That Costimulate T and NK Cells," *Clinical Cancer Research*, vol. 19, pp. 1044–1053, Mar. 2013.
- [4] R. H. Vonderheide, "The Immune Revolution: A Case for Priming, Not Checkpoint," *Cancer Cell*, vol. 33, pp. 563–569, Apr. 2018.

- [5] A. L. Rakhmilevich, K. L. Alderson, and P. M. Sondel, “T-cell-independent Antitumor Effects of CD40 Ligation,” *International Reviews of Immunology*, vol. 31, pp. 267–278, July 2012.
- [6] S. Kurtulus, A. Madi, G. Escobar, M. Klapholz, J. Nyman, E. Christian, M. Pawlak, D. Dionne, J. Xia, O. Rozenblatt-Rosen, V. K. Kuchroo, A. Regev, and A. C. Anderson, “Checkpoint Blockade Immunotherapy Induces Dynamic Changes in PD-1-CD8<sup>+</sup> Tumor-Infiltrating T Cells,” *Immunity*, vol. 50, pp. 181–194.e6, Jan. 2019.
- [7] B. C. Miller, D. R. Sen, R. Al Abosy, K. Bi, Y. V. Virkud, M. W. LaFleur, K. B. Yates, A. Lako, K. Felt, G. S. Naik, M. Manos, E. Gjini, J. R. Kuchroo, J. J. Ishizuka, J. L. Collier, G. K. Griffin, S. Maleri, D. E. Comstock, S. A. Weiss, F. D. Brown, A. Panda, M. D. Zimmer, R. T. Manguso, F. S. Hodi, S. J. Rodig, A. H. Sharpe, and W. N. Haining, “Subsets of exhausted CD8<sup>+</sup> T cells differentially mediate tumor control and respond to checkpoint blockade,” *Nature Immunology*, vol. 20, pp. 326–336, Mar. 2019.
- [8] A. Casrouge, E. Beaudoin, S. Dalle, C. Pannetier, J. Kanellopoulos, and P. Kourilsky, “Size Estimate of the  $\alpha\beta$  TCR Repertoire of Naive Mouse Splenocytes,” *The Journal of Immunology*, vol. 164, pp. 5782–5787, June 2000.
- [9] A. Durgeau, Y. Virk, S. Corgnac, and F. Mami-Chouaib, “Recent Advances in Targeting CD8 T-Cell Immunity for More Effective Cancer Immunotherapy,” *Frontiers in Immunology*, vol. 9, p. 14, Jan. 2018.
- [10] A. C. Huang, M. A. Postow, R. J. Orlowski, R. Mick, B. Bengsch, S. Manne, W. Xu, S. Harmon, J. R. Giles, B. Wenz, M. Adamow, D. Kuk, K. S. Panageas, C. Carrera, P. Wong, F. Quagliarello, B. Wubbenhorst, K. D’Andrea, K. E. Pauken, R. S. Herati, R. P. Staupe, J. M. Schenkel, S. McGettigan, S. Kothari, S. M. George, R. H. Vonderheide, R. K. Amaravadi, G. C. Karakousis, L. M. Schuchter, X. Xu, K. L. Nathanson, J. D. Wolchok, T. C. Gangadhar, and E. J. Wherry, “T-cell invigoration to tumour burden ratio associated with anti-PD-1 response,” *Nature*, vol. 545, pp. 60–65, May 2017.
- [11] W. H. Fridman, F. Pagès, C. Sautès-Fridman, and J. Galon, “The immune contexture in human tumours: impact on clinical outcome,” *Nature Reviews Cancer*, vol. 12, pp. 298–306, Apr. 2012.
- [12] H. Angell and J. Galon, “From the immune contexture to the Immunoscore: the role of prognostic and predictive immune markers in cancer,” *Current Opinion in Immunology*, vol. 25, pp. 261–267, Apr. 2013.
- [13] P. C. Tumeh, C. L. Harview, J. H. Yearley, I. P. Shintaku, E. J. M. Taylor, L. Robert, B. Chmielowski, M. Spasic, G. Henry, V. Ciobanu, A. N. West, M. Carmona, C. Kivork, E. Seja, G. Cherry, A. J. Gutierrez, T. R. Grogan, C. Mateus,

- G. Tomasic, J. A. Glaspy, R. O. Emerson, H. Robins, R. H. Pierce, D. A. Elashoff, C. Robert, and A. Ribas, "PD-1 blockade induces responses by inhibiting adaptive immune resistance," *Nature*, vol. 515, pp. 568–571, Nov. 2014.
- [14] X. Chen, X. Song, K. Li, and T. Zhang, "Fc $\gamma$ R-Binding Is an Important Functional Attribute for Immune Checkpoint Antibodies in Cancer Immunotherapy," *Frontiers in Immunology*, vol. 10, p. 292, Feb. 2019.
- [15] S. A. Beers, M. J. Glennie, and A. L. White, "Influence of immunoglobulin isotype on therapeutic antibody function," *Blood*, vol. 127, pp. 1097–1101, Mar. 2016.
- [16] D. Zhang, M. V. Goldberg, and M. L. Chiu, "Fc Engineering Approaches to Enhance the Agonism and Effector Functions of an Anti-OX40 Antibody," *Journal of Biological Chemistry*, vol. 291, pp. 27134–27146, Dec. 2016.
- [17] R. Dahan, B. C. Barnhart, F. Li, A. P. Yamniuk, A. J. Korman, and J. V. Ravetch, "Therapeutic Activity of Agonistic, Human Anti-CD40 Monoclonal Antibodies Requires Selective Fc $\gamma$ R Engagement," *Cancer Cell*, vol. 29, pp. 820–831, June 2016.
- [18] A. L. White, H. T. C. Chan, A. Roghanian, R. R. French, C. I. Mockridge, A. L. Tutt, S. V. Dixon, D. Ajona, J. S. Verbeek, A. Al-Shamkhani, M. S. Cragg, S. A. Beers, and M. J. Glennie, "Interaction with Fc $\gamma$ RIIB Is Critical for the Agonistic Activity of Anti-CD40 Monoclonal Antibody," *The Journal of Immunology*, vol. 187, pp. 1754–1763, Aug. 2011.
- [19] A. L. White, H. C. Chan, R. R. French, J. Willoughby, C. I. Mockridge, A. Roghanian, C. A. Penfold, S. G. Booth, A. Dodhy, M. E. Polak, E. A. Potter, M. R. Ardern-Jones, J. S. Verbeek, P. W. Johnson, A. Al-Shamkhani, M. S. Cragg, S. A. Beers, and M. J. Glennie, "Conformation of the Human Immunoglobulin G2 Hinge Imparts Superagonistic Properties to Immunostimulatory Anticancer Antibodies," *Cancer Cell*, vol. 27, pp. 138–148, Jan. 2015.
- [20] L. P. Richman and R. H. Vonderheide, "Role of Crosslinking for Agonistic CD40 Monoclonal Antibodies as Immune Therapy of Cancer," *Cancer Immunology Research*, vol. 2, pp. 19–26, Jan. 2014.
- [21] N. S. Wilson, B. Yang, A. Yang, S. Loeser, S. Marsters, D. Lawrence, Y. Li, R. Pitti, K. Totpal, S. Yee, S. Ross, J.-M. Vernes, Y. Lu, C. Adams, R. Offringa, B. Kelley, S. Hymowitz, D. Daniel, G. Meng, and A. Ashkenazi, "An Fc $\gamma$  Receptor-Dependent Mechanism Drives Antibody-Mediated Target-Receptor Signaling in Cancer Cells," *Cancer Cell*, vol. 19, pp. 101–113, Jan. 2011.
- [22] E. F. McKinney, J. C. Lee, D. R. W. Jayne, P. A. Lyons, and K. G. C. Smith, "T-cell exhaustion, co-stimulation and clinical outcome in autoimmunity and infection," *Nature*, vol. 523, pp. 612–616, July 2015.
- [23] D. M. Pardoll, "The blockade of immune checkpoints in cancer immunotherapy," *Nature Reviews Cancer*, vol. 12, no. 4, pp. 252–264, 2012.

- [24] J. A. Seidel, A. Otsuka, and K. Kabashima, “Anti-PD-1 and Anti-CTLA-4 Therapies in Cancer: Mechanisms of Action, Efficacy, and Limitations,” *Frontiers in Oncology*, vol. 8, Mar. 2018.
- [25] S. Spranger, R. M. Spaapen, Y. Zha, J. Williams, Y. Meng, T. T. Ha, and T. F. Gajewski, “Up-regulation of PD-L1, IDO, and T(regs) in the melanoma tumor microenvironment is driven by CD8(+) T cells.,” *Science translational medicine*, vol. 5, p. 200ra116, Aug. 2013.
- [26] D. Schadendorf, F. S. Hodi, C. Robert, J. S. Weber, K. Margolin, O. Hamid, D. Patt, T.-T. Chen, D. M. Berman, and J. D. Wolchok, “Pooled Analysis of Long-Term Survival Data From Phase II and Phase III Trials of Ipilimumab in Unresectable or Metastatic Melanoma.,” *Journal of clinical oncology : official journal of the American Society of Clinical Oncology*, vol. 33, pp. 1889–1894, June 2015.
- [27] P. A. Prieto, J. C. Yang, R. M. Sherry, M. S. Hughes, U. S. Kammula, D. E. White, C. L. Levy, S. A. Rosenberg, and G. Q. Phan, “CTLA-4 blockade with ipilimumab: long-term follow-up of 177 patients with metastatic melanoma.,” *Clinical cancer research : an official journal of the American Association for Cancer Research*, vol. 18, pp. 2039–2047, Apr. 2012.
- [28] F. S. Hodi, S. J. O’Day, D. F. McDermott, R. W. Weber, J. A. Sosman, J. B. Haanen, R. Gonzalez, C. Robert, D. Schadendorf, J. C. Hassel, W. Akerley, A. J. M. van den Eertwegh, J. Lutzky, P. Lorigan, J. M. Vaubel, G. P. Linette, D. Hogg, C. H. Ottensmeier, C. Lebbé, C. Peschel, I. Quirt, J. I. Clark, J. D. Wolchok, J. S. Weber, J. Tian, M. J. Yellin, G. M. Nichol, A. Hoos, and W. J. Urba, “Improved survival with ipilimumab in patients with metastatic melanoma.,” *The New England journal of medicine*, vol. 363, pp. 711–723, Aug. 2010.
- [29] O. Hamid, C. Robert, A. Daud, F. S. Hodi, W. J. Hwu, R. Kefford, J. D. Wolchok, P. Hersey, R. Joseph, J. S. Weber, R. Dronca, T. C. Mitchell, A. Patnaik, H. M. Zarour, A. M. Joshua, Q. Zhao, E. Jensen, S. Ahsan, N. Ibrahim, and A. Ribas, “Five-year survival outcomes for patients with advanced melanoma treated with pembrolizumab in KEYNOTE-001.,” *Annals of oncology : official journal of the European Society for Medical Oncology*, vol. 30, pp. 582–588, Apr. 2019.
- [30] E. I. Buchbinder and A. Desai, “CTLA-4 and PD-1 Pathways: Similarities, Differences, and Implications of Their Inhibition.,” *American journal of clinical oncology*, vol. 39, pp. 98–106, Feb. 2016.
- [31] R. R. Munhoz and M. A. Postow, “Clinical Development of PD-1 in Advanced Melanoma.,” *Cancer journal (Sudbury, Mass.)*, vol. 24, pp. 7–14, Jan. 2018.
- [32] T. N. Schumacher and R. D. Schreiber, “Neoantigens in cancer immunotherapy,” *Science*, vol. 348, pp. 69–74, Apr. 2015.

- [33] T. Rivera Vargas and L. Apetoh, “Can Immunogenic Chemotherapies Relieve Cancer Cell Resistance to Immune Checkpoint Inhibitors?,” *Frontiers in immunology*, vol. 10, p. 1181, 2019.
- [34] F. H. Igney and P. H. Krammer, “Immune escape of tumors: apoptosis resistance and tumor counterattack,” *Journal of Leukocyte Biology*, vol. 71, pp. 907–920, June 2002.
- [35] K. C. Valkenburg, A. E. de Groot, and K. J. Pienta, “Targeting the tumour stroma to improve cancer therapy,” *Nature Reviews Clinical Oncology*, vol. 15, pp. 366–381, June 2018.
- [36] P. Sharma and J. P. Allison, “The future of immune checkpoint therapy,” *Science*, vol. 348, pp. 56–61, Apr. 2015.
- [37] J. L. Karnell, S. A. Rieder, R. Ettinger, and R. Kolbeck, “Targeting the CD40-CD40l pathway in autoimmune diseases: Humoral immunity and beyond,” *Advanced Drug Delivery Reviews*, vol. 141, pp. 92–103, Feb. 2019.
- [38] K. Murphy and C. Weaver, *Janeway’s immunobiology*. New York, NY: Garland Science/Taylor & Francis Group, LLC, 9th edition ed., 2016.
- [39] R. Snanoudj, C. Frangié, B. Deroure, H. François, C. Créput, S. Beaudreuil, A. Dürbach, and B. Charpentier, “The blockade of T-cell co-stimulation as a therapeutic stratagem for immunosuppression: Focus on belatacept,” *Biologics: Targets & Therapy*, vol. 1, pp. 203–213, Sept. 2007.
- [40] I. S. Grewal and R. A. Flavell, “A central role of CD40 ligand in the regulation of CD4+ T-cell responses,” *Immunology Today*, vol. 17, pp. 410–414, Sept. 1996.
- [41] B. L. Kelsall, E. Stüber, M. Neurath, and W. Strober, “Interleukin-12 Production by Dendritic Cells: The Role of CD40/CD40l Interactions in Th1 T-Cell Responses,” *Annals of the New York Academy of Sciences*, vol. 795, pp. 116–126, Oct. 1996.
- [42] E. Stuber, “Blocking the CD40l-CD40 interaction in vivo specifically prevents the priming of T helper 1 cells through the inhibition of interleukin 12 secretion,” *Journal of Experimental Medicine*, vol. 183, pp. 693–698, Feb. 1996.
- [43] D. Y. Ma and E. A. Clark, “The role of CD40 and CD154/CD40l in dendritic cells,” *Seminars in Immunology*, vol. 21, pp. 265–272, Oct. 2009.
- [44] S. P. Schoenberger, R. E. Toes, E. I. van der Voort, R. Offringa, and C. J. Melief, “T-cell help for cytotoxic T lymphocytes is mediated by CD40-CD40l interactions,” *Nature*, vol. 393, pp. 480–483, June 1998.
- [45] S. R. M. Bennett, F. R. Carbone, F. Karamalis, R. A. Flavell, J. F. A. P. Miller, and W. R. Heath, “Help for cytotoxic-T-cell responses is mediated by CD40 signalling,” *Nature*, vol. 393, pp. 478–480, June 1998.

- [46] J. P. Ridge, F. Di Rosa, and P. Matzinger, "A conditioned dendritic cell can be a temporal bridge between a CD4<sup>+</sup> T-helper and a T-killer cell," *Nature*, vol. 393, pp. 474–478, June 1998.
- [47] P. Terheyden, P. t. Straten, E.-B. Bröcker, E. Kämpgen, and J. C. Becker, "CD40-Ligated Dendritic Cells Effectively Expand Melanoma-Specific CD8<sup>+</sup> CTLs and CD4<sup>+</sup> IFN- $\gamma$ -Producing T Cells from Tumor-Infiltrating Lymphocytes," *The Journal of Immunology*, vol. 164, pp. 6633–6639, June 2000.
- [48] K. M. Huster, V. Busch, M. Schiemann, K. Linkemann, K. M. Kerksiek, H. Wagner, and D. H. Busch, "Selective expression of IL-7 receptor on memory T cells identifies early CD40l-dependent generation of distinct CD8<sup>+</sup> memory T cell subsets," *Proceedings of the National Academy of Sciences*, vol. 101, pp. 5610–5615, Apr. 2004.
- [49] P. Borrow, "CD40l-deficient mice show deficits in antiviral immunity and have an impaired memory CD8<sup>+</sup> CTL response," *Journal of Experimental Medicine*, vol. 183, pp. 2129–2142, May 1996.
- [50] E. Trella, N. Raafat, C. Mengus, E. Traunecker, V. Governa, S. Heidtmann, M. Heberer, D. Oertli, G. C. Spagnoli, and P. Zajac, "CD40 ligand-expressing recombinant vaccinia virus promotes the generation of CD8<sup>+</sup> central memory T cells: Immunomodulation," *European Journal of Immunology*, vol. 46, pp. 420–431, Feb. 2016.
- [51] R. Elgueta, M. J. Benson, V. C. de Vries, A. Wasiuk, Y. Guo, and R. J. Noelle, "Molecular mechanism and function of CD40/CD40l engagement in the immune system," *Immunological Reviews*, vol. 229, pp. 152–172, May 2009.
- [52] R. H. Vonderheide, K. T. Flaherty, M. Khalil, M. S. Stumacher, D. L. Bajor, N. A. Hutnick, P. Sullivan, J. J. Mahany, M. Gallagher, A. Kramer, S. J. Green, P. J. O'Dwyer, K. L. Running, R. D. Huhn, and S. J. Antonia, "Clinical Activity and Immune Modulation in Cancer Patients Treated With CP-870,893, a Novel CD40 Agonist Monoclonal Antibody," *Journal of Clinical Oncology*, vol. 25, pp. 876–883, Mar. 2007.
- [53] G. L. Beatty, Y. Li, and K. B. Long, "Cancer immunotherapy: activating innate and adaptive immunity through CD40 agonists," *Expert Review of Anticancer Therapy*, vol. 17, pp. 175–186, Feb. 2017.
- [54] J. E. Grilley-Olson, B. D. Curti, D. C. Smith, S. Goel, T. Gajewski, S. Markovic, O. Rixe, D. L. Bajor, M. Gutierrez, T. Kuzel, A. N. Mehta, B. Amore, A. Guerrero, Z. Wang, and A. L. Coveler, "Sea-cd40, a non-fucosylated cd40 agonist: Interim results from a phase 1 study in advanced solid tumors.," *Journal of Clinical Oncology*, vol. 36, no. 15\_suppl, pp. 3093–3093, 2018.

- [55] D. L. Bajor, X. Xu, D. A. Torigian, R. Mick, L. R. Garcia, L. P. Richman, C. Desmarais, K. L. Nathanson, L. M. Schuchter, M. Kalos, and R. H. Vonderheide, "Immune Activation and a 9-Year Ongoing Complete Remission Following CD40 Antibody Therapy and Metastasectomy in a Patient with Metastatic Melanoma," *Cancer Immunology Research*, vol. 2, pp. 1051–1058, Nov. 2014.
- [56] G. L. Beatty, E. G. Chiorean, M. P. Fishman, B. Saboury, U. R. Teitelbaum, W. Sun, R. D. Huhn, W. Song, D. Li, L. L. Sharp, D. A. Torigian, P. J. O'Dwyer, and R. H. Vonderheide, "CD40 agonists alter tumor stroma and show efficacy against pancreatic carcinoma in mice and humans," *Science (New York, N.Y.)*, vol. 331, pp. 1612–1616, Mar. 2011.
- [57] A. J. Rech, H. Dada, J. J. Kotzin, J. Henao-Mejia, A. J. Minn, C. Twyman-Saint Victor, and R. H. Vonderheide, "Radiotherapy and CD40 Activation Separately Augment Immunity to Checkpoint Blockade in Cancer," *Cancer Research*, vol. 78, pp. 4282–4291, Aug. 2018.
- [58] R. R. French, H. C. Chan, A. L. Tutt, and M. J. Glennie, "CD40 antibody evokes a cytotoxic T-cell response that eradicates lymphoma and bypasses T-cell help," *Nature Medicine*, vol. 5, pp. 548–553, May 1999.
- [59] L. C. Sandin, A. Orlova, E. Gustafsson, P. Ellmark, V. Tolmachev, T. H. Totterman, and S. M. Mangsbo, "Locally Delivered CD40 Agonist Antibody Accumulates in Secondary Lymphoid Organs and Eradicates Experimental Disseminated Bladder Cancer," *Cancer Immunology Research*, vol. 2, pp. 80–90, Jan. 2014.
- [60] A. K. Nowak, B. W. S. Robinson, and R. A. Lake, "Synergy between chemotherapy and immunotherapy in the treatment of established murine solid tumors," *Cancer Research*, vol. 63, pp. 4490–4496, Aug. 2003.
- [61] L. Diehl, A. T. den Boer, S. P. Schoenberger, E. I. van der Voort, T. N. Schumacher, C. J. Melief, R. Offringa, and R. E. M. Toes, "CD40 activation in vivo overcomes peptide-induced peripheral cytotoxic T-lymphocyte tolerance and augments anti-tumor vaccine efficacy," *Nature Medicine*, vol. 5, pp. 774–779, July 1999.
- [62] K. Staveley-O'Carroll, T. D. Schell, M. Jimenez, L. M. Mylin, M. J. Tevethia, S. P. Schoenberger, and S. S. Tevethia, "In Vivo Ligation of CD40 Enhances Priming Against the Endogenous Tumor Antigen and Promotes CD8<sup>+</sup> T Cell Effector Function in SV40 T Antigen Transgenic Mice," *The Journal of Immunology*, vol. 171, pp. 697–707, July 2003.
- [63] K. T. Byrne and R. H. Vonderheide, "CD40 Stimulation Obviates Innate Sensors and Drives T Cell Immunity in Cancer," *Cell Reports*, vol. 15, pp. 2719–2732, June 2016.

- [64] G. L. Beatty, R. Winograd, R. A. Evans, K. B. Long, S. L. Luque, J. W. Lee, C. Clendenin, W. L. Gladney, D. M. Knoblock, P. D. Guirnalda, and R. H. Vonderheide, "Exclusion of T Cells From Pancreatic Carcinomas in Mice Is Regulated by Ly6clow F4/80+ Extratumoral Macrophages," *Gastroenterology*, vol. 149, pp. 201–210, July 2015.
- [65] S. F. Ngiow, A. Young, S. J. Blake, G. R. Hill, H. Yagita, M. W. L. Teng, A. J. Korman, and M. J. Smyth, "Agonistic CD40 mAb-Driven IL12 Reverses Resistance to Anti-PD1 in a T-cell-Rich Tumor," *Cancer Research*, vol. 76, pp. 6266–6277, Nov. 2016.
- [66] Department of Surgical Oncology, Fox Chase Cancer Center, Philadelphia, PA, USA, W. H. Ward, J. M. Farma, and Department of Surgical Oncology, Fox Chase Cancer Center, Philadelphia, PA, USA, eds., *Cutaneous Melanoma: Etiology and Therapy*. Codon Publications, Dec. 2017.
- [67] D. S. Rigel and J. A. Carucci, "Malignant melanoma: prevention, early detection, and treatment in the 21st century," *CA: A Cancer Journal for Clinicians*, vol. 50, pp. 215–236, July 2000.
- [68] M. Maio, J.-J. Grob, S. Aamdal, I. Bondarenko, C. Robert, L. Thomas, C. Garbe, V. Chiarion-Sileni, A. Testori, T.-T. Chen, M. Tschaika, and J. D. Wolchok, "Five-Year Survival Rates for Treatment-Naive Patients With Advanced Melanoma Who Received Ipilimumab Plus Dacarbazine in a Phase III Trial," *Journal of Clinical Oncology*, vol. 33, pp. 1191–1196, Apr. 2015.
- [69] J. D. Wolchok, V. Chiarion-Sileni, R. Gonzalez, P. Rutkowski, J.-J. Grob, C. L. Cowey, C. D. Lao, J. Wagstaff, D. Schadendorf, P. F. Ferrucci, M. Smylie, R. Dummer, A. Hill, D. Hogg, J. Haanen, M. S. Carlino, O. Bechter, M. Maio, I. Marquez-Rodas, M. Guidoboni, G. McArthur, C. Lebbé, P. A. Ascierto, G. V. Long, J. Cebron, J. Sosman, M. A. Postow, M. K. Callahan, D. Walker, L. Rollin, R. Bhole, F. S. Hodi, and J. Larkin, "Overall Survival with Combined Nivolumab and Ipilimumab in Advanced Melanoma," *New England Journal of Medicine*, vol. 377, pp. 1345–1356, Oct. 2017.
- [70] M. Antohe, R. Nedelcu, L. Nichita, C. Popp, M. Cioplea, A. Brinzea, A. Hodoroagea, A. Calinescu, M. Balaban, D. Ion, C. Diaconu, C. Bleotu, D. Pirici, S. Zurac, and G. Turcu, "Tumor infiltrating lymphocytes: The regulator of melanoma evolution (Review)," *Oncology Letters*, Jan. 2019.
- [71] Australian Pancreatic Cancer Genome Initiative, ICGC Breast Cancer Consortium, ICGC MMML-Seq Consortium, ICGC PedBrain, L. B. Alexandrov, S. Nik-Zainal, D. C. Wedge, S. A. J. R. Aparicio, S. Behjati, A. V. Biankin, G. R. Bignell, N. Bolli, A. Borg, A.-L. Børresen-Dale, S. Boyault, B. Burkhardt, A. P. Butler, C. Caldas, H. R. Davies, C. Desmedt, R. Eils, J. E. Eyfjörd, J. A. Foekens, M. Greaves, F. Hosoda, B. Hutter, T. Ilicic, S. Imbeaud, M. Imielinski, N. Jäger, D. T. W.

- Jones, D. Jones, S. Knappskog, M. Kool, S. R. Lakhani, C. López-Otín, S. Martin, N. C. Munshi, H. Nakamura, P. A. Northcott, M. Pajic, E. Papaemmanuil, A. Paradiso, J. V. Pearson, X. S. Puente, K. Raine, M. Ramakrishna, A. L. Richardson, J. Richter, P. Rosenstiel, M. Schlesner, T. N. Schumacher, P. N. Span, J. W. Teague, Y. Totoki, A. N. J. Tutt, R. Valdés-Mas, M. M. van Buuren, L. van 't Veer, A. Vincent-Salomon, N. Waddell, L. R. Yates, J. Zucman-Rossi, P. Andrew Futreal, U. McDermott, P. Lichter, M. Meyerson, S. M. Grimmond, R. Siebert, E. Campo, T. Shibata, S. M. Pfister, P. J. Campbell, and M. R. Stratton, "Signatures of mutational processes in human cancer," *Nature*, vol. 500, pp. 415–421, Aug. 2013.
- [72] S. A. Hogan, M. P. Levesque, and P. F. Cheng, "Melanoma Immunotherapy: Next-Generation Biomarkers," *Frontiers in Oncology*, vol. 8, p. 178, May 2018.
- [73] J. Blando, A. Sharma, M. G. Higa, H. Zhao, L. Vence, S. S. Yadav, J. Kim, A. M. Sepulveda, M. Sharp, A. Maitra, J. Wargo, M. Tetzlaff, R. Broaddus, M. H. G. Katz, G. R. Varadhachary, M. Overman, H. Wang, C. Yee, C. Bernatchez, C. Iacobuzio-Donahue, S. Basu, J. P. Allison, and P. Sharma, "Comparison of immune infiltrates in melanoma and pancreatic cancer highlights VISTA as a potential target in pancreatic cancer," *Proceedings of the National Academy of Sciences*, vol. 116, pp. 1692–1697, Jan. 2019.
- [74] D. T. Alexandrescu, T. E. Ichim, N. H. Riordan, F. M. Marincola, A. Di Nardo, F. D. Kabigting, and C. A. Dasanu, "Immunotherapy for Melanoma: Current Status and Perspectives," *Journal of Immunotherapy*, vol. 33, pp. 570–590, July 2010.
- [75] A. M. Rothschilds and K. D. Wittrup, "What, Why, Where, and When: Bringing Timing to Immuno-Oncology," *Trends in Immunology*, vol. 40, pp. 12–21, Jan. 2019.
- [76] W. W. Overwijk and N. P. Restifo, "B16 as a Mouse Model for Human Melanoma," *Current Protocols in Immunology*, vol. 39, Oct. 2000.
- [77] A. N. McCray, K. E. Ugen, K. Muthumani, J. Kim, D. B. Weiner, and R. Heller, "Complete Regression of Established Subcutaneous B16 Murine Melanoma Tumors after Delivery of an HIV-1 Vpr-Expressing Plasmid by in Vivo Electroporation," *Molecular Therapy*, vol. 14, pp. 647–655, Nov. 2006.
- [78] V. Bobek, K. Kolostova, D. Pinterova, G. Kacprzak, J. Adamiak, J. Kolodziej, M. Boubelik, M. Kubecova, and R. M. Hoffman, "A clinically relevant, syngeneic model of spontaneous, highly metastatic B16 mouse melanoma," *Anticancer Research*, vol. 30, pp. 4799–4803, Dec. 2010.
- [79] R. L. Siegel, K. D. Miller, and A. Jemal, "Cancer statistics, 2019," *CA: A Cancer Journal for Clinicians*, vol. 69, pp. 7–34, Jan. 2019.
- [80] J. Kleeff, M. Korc, M. Apte, C. La Vecchia, C. D. Johnson, A. V. Biankin, R. E. Neale, M. Tempero, D. A. Tuveson, R. H. Hruban, and J. P. Neoptolemos, "Pancreatic cancer," *Nature Reviews Disease Primers*, vol. 2, p. 16022, Dec. 2016.

- [81] R. E. Royal, C. Levy, K. Turner, A. Mathur, M. Hughes, U. S. Kammula, R. M. Sherry, S. L. Topalian, J. C. Yang, I. Lowy, and S. A. Rosenberg, “Phase 2 Trial of Single Agent Ipilimumab (Anti-CTLA-4) for Locally Advanced or Metastatic Pancreatic Adenocarcinoma;” *Journal of Immunotherapy*, vol. 33, pp. 828–833, Oct. 2010.
- [82] J. R. Brahmer, S. S. Tykodi, L. Q. Chow, W.-J. Hwu, S. L. Topalian, P. Hwu, C. G. Drake, L. H. Camacho, J. Kauh, K. Odunsi, H. C. Pitot, O. Hamid, S. Bhatia, R. Martins, K. Eaton, S. Chen, T. M. Salay, S. Alaparthi, J. F. Grosso, A. J. Korman, S. M. Parker, S. Agrawal, S. M. Goldberg, D. M. Pardoll, A. Gupta, and J. M. Wigginton, “Safety and Activity of Anti-PD-L1 Antibody in Patients with Advanced Cancer,” *New England Journal of Medicine*, vol. 366, pp. 2455–2465, June 2012.
- [83] D. Kabacaoglu, K. J. Cicielski, D. A. Ruess, and H. Algül, “Immune Checkpoint Inhibition for Pancreatic Ductal Adenocarcinoma: Current Limitations and Future Options,” *Frontiers in Immunology*, vol. 9, p. 1878, Aug. 2018.
- [84] I. Poschke, M. Faryna, F. Bergmann, M. Flossdorf, C. Lauenstein, J. Hermes, U. Hinz, T. Hank, R. Ehrenberg, M. Volkmar, M. Loewer, H. Glimm, T. Hackert, M. R. Sprick, T. Höfer, A. Trumpp, N. Halama, J. C. Hassel, O. Strobel, M. Büchler, U. Sahin, and R. Offringa, “Identification of a tumor-reactive T-cell repertoire in the immune infiltrate of patients with resectable pancreatic ductal adenocarcinoma,” *OncoImmunology*, vol. 5, p. e1240859, Dec. 2016.
- [85] L. Norton, R. Simon, H. D. Brereton, and A. E. Bogden, “Predicting the course of Gompertzian growth,” *Nature*, vol. 264, pp. 542–545, Dec. 1976.
- [86] V. Kuznetsov, I. Makalkin, M. Taylor, and A. Perelson, “Nonlinear dynamics of immunogenic tumors: Parameter estimation and global bifurcation analysis,” *Bulletin of Mathematical Biology*, vol. 56, pp. 295–321, Mar. 1994.
- [87] V. Kuznetsov and G. Knott, “Modeling tumor regrowth and immunotherapy,” *Mathematical and Computer Modelling*, vol. 33, pp. 1275–1287, June 2001.
- [88] M. Villasana and A. Radunskaya, “A delay differential equation model for tumor growth,” *Journal of Mathematical Biology*, vol. 47, pp. 270–294, Aug. 2003.
- [89] L. G. de Pillis, A. E. Radunskaya, and C. L. Wiseman, “A Validated Mathematical Model of Cell-Mediated Immune Response to Tumor Growth,” *Cancer Research*, vol. 65, pp. 7950–7958, Sept. 2005.
- [90] S. Bunimovich-Mendrazitsky, E. Shochat, and L. Stone, “Mathematical Model of BCG Immunotherapy in Superficial Bladder Cancer,” *Bulletin of Mathematical Biology*, vol. 69, pp. 1847–1870, Aug. 2007.

- [91] N. Kronik, Y. Kogan, V. Vainstein, and Z. Agur, "Improving alloreactive CTL immunotherapy for malignant gliomas using a simulation model of their interactive dynamics," *Cancer Immunology, Immunotherapy*, vol. 57, pp. 425–439, Mar. 2008.
- [92] M. Robertson-Tessi, A. El-Kareh, and A. Goriely, "A mathematical model of tumor-immune interactions," *Journal of Theoretical Biology*, vol. 294, pp. 56–73, Feb. 2012.
- [93] F. Nani and H. Freedman, "A mathematical model of cancer treatment by immunotherapy," *Mathematical Biosciences*, vol. 163, pp. 159–199, Feb. 2000.
- [94] C. Kelly, S. Cox, and H. Byrne, "Macrophage-tumour interactions: In vivo dynamics," *Discrete and Continuous Dynamical Systems - Series B*, vol. 4, pp. 81–98, Nov. 2003.
- [95] R. J. De Boer, P. Hogeweg, H. F. Dullens, R. A. De Weger, and W. Den Otter, "Macrophage T lymphocyte interactions in the anti-tumor immune response: a mathematical model.," *Journal of immunology (Baltimore, Md. : 1950)*, vol. 134, pp. 2748–2758, Apr. 1985.
- [96] R. Eftimie, J. L. Bramson, and D. J. D. Earn, "Interactions Between the Immune System and Cancer: A Brief Review of Non-spatial Mathematical Models," *Bulletin of Mathematical Biology*, vol. 73, pp. 2–32, Jan. 2011.
- [97] K. Peskov, I. Azarov, L. Chu, V. Voronova, Y. Kosinsky, and G. Helmlinger, "Quantitative Mechanistic Modeling in Support of Pharmacological Therapeutics Development in Immuno-Oncology," *Frontiers in Immunology*, vol. 10, p. 924, Apr. 2019.
- [98] M. Stroh, D. Carlile, C.-C. Li, J. Wagg, B. Ribba, S. Ramanujan, J. Jin, J. Xu, J.-E. Charoin, Z.-X. Xhu, P. Morcos, J. Davis, and A. Phipps, "Challenges and Opportunities for Quantitative Clinical Pharmacology in Cancer Immunotherapy: Something Old, Something New, Something Borrowed, and Something Blue: Something Old, Something New, Something Borrowed, and Something Blue," *CPT: Pharmacometrics & Systems Pharmacology*, vol. 4, pp. 495–497, Sept. 2015.
- [99] S. Nayak, O. Sander, N. Al-Huniti, D. de Alwis, A. Chain, M. Chenel, S. Sunkaraneni, S. Agrawal, N. Gupta, and S. A. Visser, "Getting Innovative Therapies Faster to Patients at the Right Dose: Impact of Quantitative Pharmacology Towards First Registration and Expanding Therapeutic Use," *Clinical Pharmacology & Therapeutics*, vol. 103, pp. 378–383, Mar. 2018.
- [100] A. Lindauer, C. Valiathan, K. Mehta, V. Sriram, R. de Greef, J. Elassaiss-Schaap, and D. de Alwis, "Translational Pharmacokinetic/Pharmacodynamic Modeling of Tumor Growth Inhibition Supports Dose-Range Selection of the Anti-PD-1 Antibody Pembrolizumab: Translational Pharmacokinetic/Pharmacodynamic Modeling," *CPT: Pharmacometrics & Systems Pharmacology*, vol. 6, pp. 11–20, Jan. 2017.

- [101] R. de Greef, J. Elassaiss-Schaap, M. Chatterjee, D. Turner, M. Ahamadi, M. Forman, D. Cutler, D. de Alwis, A. Kondic, and J. Stone, “Pembrolizumab: Role of Modeling and Simulation in Bringing a Novel Immunotherapy to Patients With Melanoma: Modeling and Simulation of Pembrolizumab,” *CPT: Pharmacometrics & Systems Pharmacology*, vol. 6, pp. 5–7, Jan. 2017.
- [102] R. J. De Boer, D. Homann, and A. S. Perelson, “Different Dynamics of CD4<sup>+</sup> and CD8<sup>+</sup> T Cell Responses During and After Acute Lymphocytic Choriomeningitis Virus Infection,” *The Journal of Immunology*, vol. 171, pp. 3928–3935, Oct. 2003.
- [103] C. L. Althaus, V. V. Ganusov, and R. J. De Boer, “Dynamics of CD8<sup>+</sup> T Cell Responses during Acute and Chronic Lymphocytic Choriomeningitis Virus Infection,” *The Journal of Immunology*, vol. 179, pp. 2944–2951, Sept. 2007.
- [104] D. Le, J. D. Miller, and V. V. Ganusov, “Mathematical modeling provides kinetic details of the human immune response to vaccination,” *Frontiers in Cellular and Infection Microbiology*, vol. 4, Jan. 2015.
- [105] M. Gabel, N. S. Baumann, A. Oxenius, and F. Graw, “Investigating the Dynamics of MCMV-Specific CD8<sup>+</sup> T Cell Responses in Individual Hosts,” *Frontiers in Immunology*, vol. 10, p. 1358, June 2019.
- [106] R. Frank, M. Gabel, K. Heiss, A.-K. Mueller, and F. Graw, “Varying Immunizations With Plasmodium Radiation-Attenuated Sporozoites Alter Tissue-Specific CD8<sup>+</sup> T Cell Dynamics,” *Frontiers in Immunology*, vol. 9, p. 1137, May 2018.
- [107] E. D. Hawkins, M. L. Turner, M. R. Dowling, C. van Gend, and P. D. Hodgkin, “A model of immune regulation as a consequence of randomized lymphocyte division and death times,” *Proceedings of the National Academy of Sciences*, vol. 104, pp. 5032–5037, Mar. 2007.
- [108] J. M. Marchingo, A. Kan, R. M. Sutherland, K. R. Duffy, C. J. Wellard, G. T. Belz, A. M. Lew, M. R. Dowling, S. Heinzl, and P. D. Hodgkin, “Antigen affinity, costimulation, and cytokine inputs sum linearly to amplify T cell expansion,” *Science*, vol. 346, pp. 1123–1127, Nov. 2014.
- [109] S. Heinzl, T. Binh Giang, A. Kan, J. M. Marchingo, B. K. Lye, L. M. Corcoran, and P. D. Hodgkin, “A Myc-dependent division timer complements a cell-death timer to regulate T cell and B cell responses,” *Nature Immunology*, vol. 18, pp. 96–103, Jan. 2017.
- [110] J. M. Marchingo, G. Prevedello, A. Kan, S. Heinzl, P. D. Hodgkin, and K. R. Duffy, “T-cell stimuli independently sum to regulate an inherited clonal division fate,” *Nature Communications*, vol. 7, p. 13540, Dec. 2016.
- [111] R. J. De Boer and A. S. Perelson, “Quantifying T lymphocyte turnover,” *Journal of Theoretical Biology*, vol. 327, pp. 45–87, June 2013.

- [112] L. Kretschmer, M. Flossdorf, J. Mir, Y.-L. Cho, M. Plambeck, I. Treise, A. Toska, S. Heinzel, M. Schiemann, D. H. Busch, and V. R. Buchholz, “Differential expansion of T central memory precursor and effector subsets is regulated by division speed,” *Nature Communications*, vol. 11, p. 113, Dec. 2020.
- [113] S. Hross and J. Hasenauer, “Analysis of CFSE time-series data using division-, age- and label-structured population models,” *Bioinformatics*, vol. 32, pp. 2321–2329, Aug. 2016.
- [114] T. Luzyanina, D. Roose, T. Schenkel, M. Sester, S. Ehl, A. Meyerhans, and G. Bocharov, “Numerical modelling of label-structured cell population growth using CFSE distribution data,” *Theoretical Biology and Medical Modelling*, vol. 4, no. 1, p. 26, 2007.
- [115] V. R. Buchholz, M. Flossdorf, I. Hensel, L. Kretschmer, B. Weissbrich, P. Graf, A. Verschoor, M. Schiemann, T. Hofer, and D. H. Busch, “Disparate Individual Fates Compose Robust CD8+ T Cell Immunity,” *Science*, vol. 340, pp. 630–635, May 2013.
- [116] A. Reynaldi, N. L. Smith, T. E. Schlub, C. Tabillas, V. Venturi, B. D. Rudd, and M. P. Davenport, “Fate mapping reveals the age structure of the peripheral T cell compartment,” *Proceedings of the National Academy of Sciences*, vol. 116, pp. 3974–3981, Mar. 2019.
- [117] J. Oyler-Yaniv, A. Oyler-Yaniv, M. Shakiba, N. K. Min, Y.-H. Chen, S.-y. Cheng, O. Krichevsky, N. Altan-Bonnet, and G. Altan-Bonnet, “Catch and Release of Cytokines Mediated by Tumor Phosphatidylserine Converts Transient Exposure into Long-Lived Inflammation,” *Molecular Cell*, vol. 66, pp. 635–647.e7, June 2017.
- [118] G. Voisinne, B. G. Nixon, A. Melbinger, G. Gasteiger, M. Vergassola, and G. Altan-Bonnet, “T Cells Integrate Local and Global Cues to Discriminate between Structurally Similar Antigens,” *Cell Reports*, vol. 11, pp. 1208–1219, May 2015.
- [119] Becton, Dickinson & Company, *FlowJo<sup>TM</sup> Software [Proliferation] Version 10*. Becton, Dickinson & Company, Becton, USA, 2019.
- [120] R Core Team, *R: A Language and Environment for Statistical Computing*. R Foundation for Statistical Computing, Vienna, Austria, 2014.
- [121] D. P. Doane, “Aesthetic Frequency Classifications,” *The American Statistician*, vol. 30, pp. 181–183, Nov. 1976.
- [122] P. Revy, M. Sospedra, B. Barbour, and A. Trautmann, “Functional antigen-independent synapses formed between T cells and dendritic cells,” *Nature Immunology*, vol. 2, no. 10, pp. 925–931, 2001.
- [123] A. V. Gett and P. D. Hodgkin, “A cellular calculus for signal integration by T cells,” *Nature Immunology*, vol. 1, no. 3, pp. 239–244, 2000.

- [124] G. Bocharov, J. Quiel, T. Luzyanina, H. Alon, E. Chiglintsev, V. Chereshev, M. Meier-Schellersheim, W. E. Paul, and Z. Grossman, “Feedback regulation of proliferation vs. differentiation rates explains the dependence of CD4 T-cell expansion on precursor number,” *Proceedings of the National Academy of Sciences of the United States of America*, vol. 108, pp. 3318–3323, Feb. 2011.
- [125] R. J. De Boer and A. S. Perelson, “Estimating division and death rates from CFSE data,” *Journal of Computational and Applied Mathematics*, vol. 184, pp. 140–164, Dec. 2005.
- [126] M. R. Dowling, A. Kan, S. Heinzl, J. H. S. Zhou, J. M. Marchingo, C. J. Wellard, J. F. Markham, and P. D. Hodgkin, “Stretched cell cycle model for proliferating lymphocytes,” *Proceedings of the National Academy of Sciences*, vol. 111, pp. 6377–6382, Apr. 2014.
- [127] J. A. Smith and L. Martin, “Do cells cycle?,” *Proceedings of the National Academy of Sciences of the United States of America*, vol. 70, pp. 1263–1267, Apr. 1973.
- [128] R. J. De Boer, V. V. Ganusov, D. Milutinović, P. D. Hodgkin, and A. S. Perelson, “Estimating Lymphocyte Division and Death Rates from CFSE Data,” *Bulletin of Mathematical Biology*, vol. 68, pp. 1011–1031, July 2006.
- [129] V. V. Ganusov, S. S. Pilyugin, R. J. de Boer, K. Murali-Krishna, R. Ahmed, and R. Antia, “Quantifying cell turnover using CFSE data,” *Journal of Immunological Methods*, vol. 298, pp. 183–200, Mar. 2005.
- [130] H. Y. Lee and A. S. Perelson, “Modeling T Cell Proliferation and Death in Vitro Based on Labeling Data: Generalizations of the Smith–Martin Cell Cycle Model,” *Bulletin of Mathematical Biology*, vol. 70, pp. 21–44, Jan. 2008.
- [131] V. G. Subramanian, K. R. Duffy, M. L. Turner, and P. D. Hodgkin, “Determining the expected variability of immune responses using the cyton model,” *Journal of Mathematical Biology*, vol. 56, pp. 861–892, June 2008.
- [132] K. León, J. Faro, and J. Carneiro, “A general mathematical framework to model generation structure in a population of asynchronously dividing cells,” *Journal of Theoretical Biology*, vol. 229, pp. 455–476, Aug. 2004.
- [133] A. Matiašová, J. Sevc, J. Mikeš, R. Jendželovský, Z. Daxnerová, and P. Fedoročko, “Flow cytometric determination of 5-bromo-2'-deoxyuridine pharmacokinetics in blood serum after intraperitoneal administration to rats and mice,” *Histochemistry and cell biology*, vol. 142, pp. 703–712, Dec. 2014.
- [134] R. M. Sutherland, S. L. Londrigan, J. L. Brady, E. M. Carrington, J. M. Marchingo, S. Heinzl, P. D. Hodgkin, K. L. Graham, T. W. Kay, Y. Zhan, and A. M. Lew, “Cognate antigen engagement on parenchymal cells stimulates CD8+ T cell proliferation in situ,” *Nature Communications*, vol. 8, p. 14809, Apr. 2017.

- [135] H. Yoon, T. S. Kim, and T. J. Braciale, “The cell cycle time of CD8+ T cells responding in vivo is controlled by the type of antigenic stimulus.,” *PloS one*, vol. 5, p. e15423, Nov. 2010.
- [136] R. Mercado, S. Vijh, S. E. Allen, K. Kerksiek, I. M. Pilip, and E. G. Pamer, “Early Programming of T Cell Populations Responding to Bacterial Infection,” *The Journal of Immunology*, vol. 165, pp. 6833–6839, Dec. 2000.
- [137] H. X. Chao, R. I. Fakhreddin, H. K. Shimerov, K. M. Kedziora, R. J. Kumar, J. Perez, J. C. Limas, G. D. Grant, J. G. Cook, G. P. Gupta, and J. E. Purvis, “Evidence that the human cell cycle is a series of uncoupled, memoryless phases.,” *Molecular systems biology*, vol. 15, p. e8604, Mar. 2019.
- [138] S. S. Kang, J. Herz, J. V. Kim, D. Nayak, P. Stewart-Hutchinson, M. L. Dustin, and D. B. McGavern, “Migration of cytotoxic lymphocytes in cell cycle permits local MHC I-dependent control of division at sites of viral infection,” *The Journal of Experimental Medicine*, vol. 208, pp. 747–759, Apr. 2011.
- [139] J. C. Becker, M. H. Andersen, D. Schrama, and P. Thor Straten, “Immune-suppressive properties of the tumor microenvironment.,” *Cancer immunology, immunotherapy : CII*, vol. 62, pp. 1137–1148, July 2013.
- [140] D. Hanahan and L. M. Coussens, “Accessories to the crime: functions of cells recruited to the tumor microenvironment.,” *Cancer cell*, vol. 21, pp. 309–322, Mar. 2012.
- [141] F. Fröhlich, C. Loos, and J. Hasenauer, “Scalable Inference of Ordinary Differential Equation Models of Biochemical Processes,” in *Gene Regulatory Networks* (G. Sanguinetti and V. A. Huynh-Thu, eds.), vol. 1883, pp. 385–422, New York, NY: Springer New York, 2019.
- [142] T. Hastie, R. Tibshirani, and J. Friedman, *The Elements of Statistical Learning*. Springer Series in Statistics, New York, NY: Springer New York, 2009.
- [143] C. Kreutz, A. Raue, and J. Timmer, “Likelihood based observability analysis and confidence intervals for predictions of dynamic models,” *BMC Systems Biology*, vol. 6, no. 1, p. 120, 2012.
- [144] L. N. Hwang, Z. Yu, D. C. Palmer, and N. P. Restifo, “The in vivo expansion rate of properly stimulated transferred CD8+ T cells exceeds that of an aggressively growing mouse tumor.,” *Cancer research*, vol. 66, pp. 1132–1138, Jan. 2006.
- [145] V. V. Ganusov, “Discriminating between different pathways of memory CD8+ T cell differentiation.,” *Journal of immunology (Baltimore, Md. : 1950)*, vol. 179, pp. 5006–5013, Oct. 2007.

- [146] T. R. Mempel, S. E. Henrickson, and U. H. Von Andrian, “T-cell priming by dendritic cells in lymph nodes occurs in three distinct phases.,” *Nature*, vol. 427, pp. 154–159, Jan. 2004.
- [147] J. R. Maxwell, J. D. Campbell, C. H. Kim, and A. T. Vella, “CD40 activation boosts T cell immunity in vivo by enhancing T cell clonal expansion and delaying peripheral T cell deletion,” *Journal of Immunology (Baltimore, Md.: 1950)*, vol. 162, pp. 2024–2034, Feb. 1999.
- [148] P. A. Baars, L. M. Ribeiro do Couto, J. H. W. Leusen, B. Hooibrink, T. W. Kuijpers, S. M. A. Lens, and R. A. W. van Lier, “Cytolytic Mechanisms and Expression of Activation-Regulating Receptors on Effector-Type CD8<sup>+</sup> CD45ra<sup>+</sup> CD27<sup>-</sup> Human T Cells,” *The Journal of Immunology*, vol. 165, pp. 1910–1917, Aug. 2000.
- [149] H. Tomiyama, H. Takata, T. Matsuda, and M. Takiguchi, “Phenotypic classification of human CD8<sup>+</sup> T cells reflecting their function: inverse correlation between quantitative expression of CD27 and cytotoxic effector function,” *European Journal of Immunology*, vol. 34, pp. 999–1010, Apr. 2004.
- [150] A. Xia, Y. Zhang, J. Xu, T. Yin, and X.-J. Lu, “T Cell Dysfunction in Cancer Immunity and Immunotherapy,” *Frontiers in Immunology*, vol. 10, p. 1719, July 2019.
- [151] N. R. Maimela, S. Liu, and Y. Zhang, “Fates of CD8<sup>+</sup> T cells in Tumor Microenvironment,” *Computational and Structural Biotechnology Journal*, vol. 17, pp. 1–13, 2019.
- [152] E. D. Hawkins, M. Hommel, M. L. Turner, F. L. Battye, J. F. Markham, and P. D. Hodgkin, “Measuring lymphocyte proliferation, survival and differentiation using CFSE time-series data,” *Nature Protocols*, vol. 2, pp. 2057–2067, Sept. 2007.
- [153] J. D. Peske, E. D. Thompson, L. Gemta, R. A. Baylis, Y.-X. Fu, and V. H. Engelhard, “Effector lymphocyte-induced lymph node-like vasculature enables naive T-cell entry into tumours and enhanced anti-tumour immunity,” *Nature Communications*, vol. 6, p. 7114, May 2015.
- [154] V. H. Engelhard, A. B. Rodriguez, I. S. Mauldin, A. N. Woods, J. D. Peske, and C. L. Slingluff, “Immune Cell Infiltration and Tertiary Lymphoid Structures as Determinants of Antitumor Immunity,” *The Journal of Immunology*, vol. 200, pp. 432–442, Jan. 2018.
- [155] A. B. Rodriguez, J. D. Peske, and V. H. Engelhard, “Identification and Characterization of Tertiary Lymphoid Structures in Murine Melanoma,” in *Tertiary Lymphoid Structures* (M.-C. Dieu-Nosjean, ed.), vol. 1845, pp. 241–257, New York, NY: Springer New York, 2018.

- [156] D. J. Campbell and E. C. Butcher, “Rapid Acquisition of Tissue-specific Homing Phenotypes by CD4<sup>+</sup> T Cells Activated in Cutaneous or Mucosal Lymphoid Tissues,” *The Journal of Experimental Medicine*, vol. 195, pp. 135–141, Jan. 2002.
- [157] H. Sigmundsdottir and E. C. Butcher, “Environmental cues, dendritic cells and the programming of tissue-selective lymphocyte trafficking,” *Nature Immunology*, vol. 9, pp. 981–987, Sept. 2008.
- [158] L. J. Picker, J. R. Treer, B. Ferguson-Darnell, P. A. Collins, P. R. Bergstresser, and L. W. Terstappen, “Control of lymphocyte recirculation in man. II. Differential regulation of the cutaneous lymphocyte-associated antigen, a tissue-selective homing receptor for skin-homing T cells,” *Journal of Immunology (Baltimore, Md.: 1950)*, vol. 150, pp. 1122–1136, Feb. 1993.
- [159] E. D. Thompson, H. L. Enriquez, Y.-X. Fu, and V. H. Engelhard, “Tumor masses support naive T cell infiltration, activation, and differentiation into effectors,” *The Journal of Experimental Medicine*, vol. 207, pp. 1791–1804, Aug. 2010.
- [160] D. Schrama, P. thor Straten, W. H. Fischer, A. D. McLellan, E.-B. Bröcker, R. A. Reisfeld, and J. C. Becker, “Targeting of Lymphotoxin- $\alpha$  to the Tumor Elicits an Efficient Immune Response Associated with Induction of Peripheral Lymphoid-like Tissue,” *Immunity*, vol. 14, pp. 111–121, Feb. 2001.
- [161] A. Brand, K. Singer, G. E. Koehl, M. Kolitzus, G. Schoenhammer, A. Thiel, C. Matos, C. Bruss, S. Klobuch, K. Peter, M. Kastenberger, C. Bogdan, U. Schleicher, A. Mackensen, E. Ullrich, S. Fichtner-Feigl, R. Kesselring, M. Mack, U. Ritter, M. Schmid, C. Blank, K. Dettmer, P. J. Oefner, P. Hoffmann, S. Walenta, E. K. Geissler, J. Pouyssegur, A. Villunger, A. Steven, B. Seliger, S. Schreml, S. Haferkamp, E. Kohl, S. Karrer, M. Berneburg, W. Herr, W. Mueller-Klieser, K. Renner, and M. Kreutz, “LDHA-Associated Lactic Acid Production Blunts Tumor Immunosurveillance by T and NK Cells,” *Cell Metabolism*, vol. 24, pp. 657–671, Nov. 2016.
- [162] H. Xia, W. Wang, J. Crespo, I. Kryczek, W. Li, S. Wei, Z. Bian, T. Maj, M. He, R. J. Liu, Y. He, R. Rattan, A. Munkarah, J.-L. Guan, and W. Zou, “Suppression of FIP200 and autophagy by tumor-derived lactate promotes naïve T cell apoptosis and affects tumor immunity,” *Science Immunology*, vol. 2, p. eaan4631, Nov. 2017.
- [163] O. Nakano, M. Sato, Y. Naito, K. Suzuki, S. Orikasa, M. Aizawa, Y. Suzuki, I. Shintaku, H. Nagura, and H. Ohtani, “Proliferative activity of intratumoral CD8(+) T-lymphocytes as a prognostic factor in human renal cell carcinoma: clinicopathologic demonstration of antitumor immunity,” *Cancer Research*, vol. 61, pp. 5132–5136, July 2001.
- [164] P. Wang, B. Huang, Y. Gao, J. Yang, Z. Liang, N. Zhang, X. Fu, and L. Li, “CD103 + CD8 + T lymphocytes in non-small cell lung cancer are phenotypically and functionally primed to respond to PD-1 blockade,” *Cellular Immunology*, vol. 325, pp. 48–55, Mar. 2018.

- [165] Q. Song, F. Shi, M. Adair, H. Chang, X. Guan, Y. Zhao, Y. Li, G. Wu, and J. Wu, "Cell Counts, rather than Proportion, of CD8/PD-1 Tumor-Infiltrating Lymphocytes in a Tumor Microenvironment Associated with Pathological Characteristics of Chinese Invasive Ductal Breast Cancer," *Journal of Immunology Research*, vol. 2019, p. 8505021, 2019.
- [166] D. H. Munn and V. Bronte, "Immune suppressive mechanisms in the tumor microenvironment," *Current Opinion in Immunology*, vol. 39, pp. 1–6, Apr. 2016.
- [167] K. G. Anderson, I. M. Stromnes, and P. D. Greenberg, "Obstacles Posed by the Tumor Microenvironment to T cell Activity: A Case for Synergistic Therapies," *Cancer Cell*, vol. 31, pp. 311–325, Mar. 2017.
- [168] R. G. Uzzo, P. Rayman, V. Kolenko, P. E. Clark, T. Bloom, A. M. Ward, L. Molto, C. Tannenbaum, L. J. Worford, R. Bukowski, R. Tubbs, E. D. Hsi, N. H. Bander, A. C. Novick, and J. H. Finke, "Mechanisms of apoptosis in T cells from patients with renal cell carcinoma.," *Clinical cancer research : an official journal of the American Association for Cancer Research*, vol. 5, pp. 1219–1229, May 1999.
- [169] B. Lu and O. J. Finn, "T-cell death and cancer immune tolerance," *Cell Death & Differentiation*, vol. 15, pp. 70–79, Jan. 2008.
- [170] M. H. Spitzer, Y. Carmi, N. E. Reticker-Flynn, S. S. Kwek, D. Madhireddy, M. M. Martins, P. F. Gherardini, T. R. Prestwood, J. Chabon, S. C. Bendall, L. Fong, G. P. Nolan, and E. G. Engleman, "Systemic Immunity Is Required for Effective Cancer Immunotherapy," *Cell*, vol. 168, pp. 487–502.e15, Jan. 2017.
- [171] A. J. Ozga, F. Moalli, J. Abe, J. Swoger, J. Sharpe, D. Zehn, M. Kreutzfeldt, D. Merkler, J. Ripoll, and J. V. Stein, "pMHC affinity controls duration of CD8+ T cell-DC interactions and imprints timing of effector differentiation versus expansion," *The Journal of Experimental Medicine*, vol. 213, no. 12, pp. 2811–2829, 2016.
- [172] D. Zehn, S. Y. Lee, and M. J. Bevan, "Complete but curtailed T-cell response to very low-affinity antigen.," *Nature*, vol. 458, pp. 211–214, Mar. 2009.
- [173] S. Hugues, L. Fetler, L. Bonifaz, J. Helft, F. Amblard, and S. Amigorena, "Distinct T cell dynamics in lymph nodes during the induction of tolerance and immunity," *Nature Immunology*, vol. 5, pp. 1235–1242, Dec. 2004.
- [174] S. R. Schwab and J. G. Cyster, "Finding a way out: lymphocyte egress from lymphoid organs.," *Nature Immunology*, vol. 8, pp. 1295–1301, Dec. 2007.

---

## Acknowledgments

---

My sincere thanks to Michael Floßdorf for his ongoing competent supervision through which I learned a lot and for his support and guidance when planning the projects with our collaboration partners. Thank you for always finding the time to discuss problems, for helping me with advancing my projects and the opportunity to visit summer schools.

I am very grateful to Thomas Höfer for his advice, scientific insight and support throughout the years and for his encouragement in difficult times. I also very much appreciate the opportunities he gave me to meet other scientists at summer schools through which I could broaden my horizon.

I am very thankful to my collaboration partners Lena Kranz, Isabel Poschke and Mustafa Diken who planned and conducted the experiments with us. I would like to thank Lena Kranz, Isabel Poschke and Daniel Baumann for discussions and for patiently answering all my questions regarding experimental procedures and the biological background. I've learned a lot through this. I would also like to thank Susann Wendler, Aaron Ehrenfried, Daria Jaeger and Daniel Baumann, who were involved in the experiments.

I would like to thank Ursula Kummer for her willingness to assume the role of thesis referee on short notice and for accepting the role of chairperson of the examining committee. I am also grateful to Ralf Bartenschlager for being part of my thesis advisory committee and giving valuable advice. I would, furthermore, like to thank Frederik Graw and Hedda Wardemann for being part of the examining committee.

I am very thankful to Diana Best and Nick Kepper for their professional and patient support when dealing with bureaucratic and technical challenges.

Many thanks go to my office colleagues (Jonas, Lena, Atefeh, Verena, Melania and Nasrin) for many fruitful discussions, help and encouragement.

I want to express my deep gratitude to my family and to András for the continuing understanding and support, when I would even have lost patience with myself. Thank you for proof reading and correcting.

Last not least I'd like to thank all my friends who bore with me through difficult times, kept a smiling face, and helped me stay afloat.



---

Supplementary information to the solution of ordinary differential  
equations for birth models

---

### A.1. Solving an ordinary differential equation for a birth model with a time dependent proliferation rate

Consider the following differential equation for a birth model where the proliferation rate  $k$  changes in time:

$$\begin{aligned} \frac{d}{dt}G_0(t) &= -k(t)G_0(t) \\ \frac{d}{dt}G_1(t) &= 2k(t)G_0(t) - k(t)G_1(t) \\ \frac{d}{dt}G_2(t) &= 2k(t)G_1(t) - k(t)G_2(t) \\ &\dots \end{aligned}$$

Here,  $G_i(t)$  is the number of cells which divided  $i$  times. We want to derive a solution for  $G_i(t)$ , with the initial conditions  $G_0(0) = G_0$  and  $G_i(0) = 0 \forall i \in \mathbb{N}^*$ .  $G_0(0)$  is the initial number of undivided cells.

We write the indefinite integral of  $k(t)$  as  $F_k(t)$  with  $\frac{d}{dt}F_k(t) = k(t)$ . We furthermore define  $K(t) := \left(\int_0^t k(t') dt'\right)$ . For the expression  $K(t)$  it thus follows

$$\frac{d}{dt}K(t) = \frac{d}{dt} \left( \int_0^t k(t') dt' \right) = \frac{d}{dt} (F_k(t) - F_k(0)) = \frac{d}{dt} F_k(t) = k(t). \quad (\text{A.1})$$

In the following we would like to show that

$$G_n(t) = \frac{2^n G_0}{n!} K(t)^n e^{-K(t)} \quad (\text{A.2})$$

by employing a mathematical induction.

**Show that the statement holds for  $n = 0$**

The solution for  $G_0(t)$  is

$$G_0(t) = b_0 e^{-K(t)}, \quad (\text{A.3})$$

where  $b_0$  has to be defined by initial conditions.

We show this by calculating

$$\frac{d}{dt} G_0(t) = b_0 (-k(t)) e^{-K(t)} = -b_0 k(t) e^{-K(t)} \stackrel{(\text{A.3})}{=} -k(t) G_0(t).$$

Determine  $b_0$  by plugging in initial conditions:

$$G_0(0) = b_0 e^{-K(0)} \stackrel{!}{=} G_0,$$

so  $b_0 = G_0$  and we obtain:

$$G_0(t) = G_0 e^{-K(t)}. \quad (\text{A.4})$$

Our statement is true for  $n = 0$ .

### Induction step

The induction hypothesis is

$$G_n(t) = \frac{2^n G_0}{n!} K(t)^n e^{-K(t)} \quad (\text{A.5})$$

and under this assumption we show that

$$G_{n+1}(t) = \frac{2^{n+1} G_0}{(n+1)!} K(t)^{n+1} e^{-K(t)} \quad (\text{A.6})$$

can solve

$$\frac{d}{dt} G_{n+1}(t) = 2k(t) G_n(t) - k(t) G_{n+1}(t). \quad (\text{A.7})$$

We calculate

$$\begin{aligned} \frac{d}{dt} G_{n+1}(t) &\stackrel{(\text{A.6})}{=} \frac{2^{n+1} G_0}{(n+1)!} \left( (n+1) K^n(t) k(t) e^{-K(t)} - k(t) K(t)^{n+1} e^{-K(t)} \right) \\ &= 2k(t) \frac{2^n G_0}{n!} K^n e^{-K(t)} - k(t) \frac{2^{n+1} G_0}{(n+1)!} K^{n+1}(t) e^{-K(t)} \\ &= 2k(t) G_n(t) - k(t) G_{n+1}(t) \end{aligned}$$

and see that (A.6) solves the equation, if (A.5) is true.

## A.2. Solving an ordinary differential equation for birth models with a source term

To gain an intuition how a continuous influx of undivided cell changes the dynamics and in how far a death rate in all organs could be compensated by an influx, we calculated the solution to the following simplified model.

Assume a cell proliferation with exponential waiting times with a general death rate  $d$  and a proliferation rate  $k$

$$\begin{aligned}
 \frac{d}{dt} src(t) &= -d \cdot src(t) \\
 \frac{d}{dt} G_0(t) &= src(t) - (k + d) \cdot G_0(t) \\
 \frac{d}{dt} G_1(t) &= 2k \cdot G_0(t) - (k + d) \cdot G_1(t) \\
 \frac{d}{dt} G_2(t) &= 2k \cdot G_1(t) - (k + d) \cdot G_2(t) \\
 &\dots,
 \end{aligned} \tag{A.8}$$

where the  $src$  is the influx of undivided cells from an outside compartment and  $G_i(t)$  is the number of cells which divided  $i$  times. We want to derive a solution for  $G_i(t)$  with the initial conditions  $src(0) = src_0$  and  $G_i(0) = 0 \forall i \in \mathbb{N}_0$ .  $src_0$  is the initial influx of undivided cells.

In all basic model structures in this work, we have no death rates. In these cases, by introducing a constant influx term (i.e.  $src = const.$ ), we implicitly assume a compartment outside, which is either very large or steadily replenished, such that it can continuously provide the same number of cells at all times. If we assume that the compartment is very large a death rate should not change the influx dynamics. If we think of it in terms of a replenished compartment the introduction of a death rate for the source term, as is done in (A.8), makes sense. As the solution of (A.8) is neat and provides an intuition for this model, it is presented here.

The first equation in eq. A.8 yields

$$src(t) = src_0 \cdot e^{-dt}. \tag{A.9}$$

In the following we show that

$$G_n(t) = \frac{2^n src_0}{k} e^{-dt} \left( 1 - \sum_{i=0}^n \frac{(kt)^i}{i!} e^{-kt} \right), \tag{A.10}$$

with mathematical induction.

This solution means that all generations  $G_n(t)$  scale with  $e^{-dt}$ , which can be compensated by  $src_0$  at single time points. This is not the case anymore if we have no death rate in the source term. We can, furthermore, see that the second term in the bracket is a cumulative Poisson distribution ranging from 0 to  $n$ .

**Show that the statement holds for  $n = 0$**

To solve

$$\frac{d}{dt}G_0(t) = src(t) - (k + d)G_0(t) = src_0e^{-dt} - (k + d)G_0(t) \quad (\text{A.11})$$

use variation of parameters. The solution of the homogeneous equation  $\dot{G}_0(t) = -(k + d)G_0(t)$  is  $G_0(t) = b_0 \cdot e^{-(k+d)t}$  and to solve the inhomogeneous equation we use the Ansatz:

$$G_0(t) = b_0(t)e^{-(k+d)t} \quad (\text{A.12})$$

with its derivative

$$\begin{aligned} \frac{d}{dt}G_0(t) &= -b_0(t)(k + d)e^{-(k+d)t} + \frac{d}{dt}(b_0(t))e^{-(k+d)t} \\ &\stackrel{(\text{A.12})}{=} -(k + d)G_0(t) + \frac{d}{dt}(b_0(t))e^{-(k+d)t} \end{aligned} \quad (\text{A.13})$$

Now equate (A.11) and (A.13)

$$-(k + d)G_0(t) + \frac{d}{dt}(b_0(t))e^{-(k+d)t} = src_0e^{-dt} - (k + d)G_0(t)$$

and we obtain

$$\frac{d}{dt}b_0(t) = src_0e^{kt}.$$

A general solution for  $b_0(t)$  is then

$$b_0(t) = src_0 \int e^{kt'} dt' = \frac{src_0}{k} e^{kt} + b_{0,0}, \quad (\text{A.14})$$

where  $b_{0,0}$  is a constant which has to be determined by the initial condition. Now insert (A.14) in (A.12) and obtain:

$$G_0(t) = \left( \frac{src_0}{k} e^{kt} + b_{0,0} \right) e^{-(k+d)t}. \quad (\text{A.15})$$

For  $G_0(0) \stackrel{!}{=} 0$  we obtain

$$b_{0,0} = -\frac{src_0}{k}. \quad (\text{A.16})$$

Inserting (A.16) into (A.15), we have

$$G_0(t) = \frac{src_0}{k} e^{-dt} \left( 1 - e^{-kt} \right),$$

with which we showed (A.10) for  $n = 0$ .

### Induction step

Assuming that (A.10) holds, we have to show that

$$G_{n+1}(t) = \frac{2^{n+1}src_0}{k} e^{-dt} \left( 1 - \sum_{i=0}^{n+1} \frac{(kt)^i}{i!} e^{-kt} \right). \quad (\text{A.17})$$

solves

$$\frac{d}{dt} G_{n+1}(t) = 2k \cdot G_n(t) - (k+d) \cdot G_{n+1}(t). \quad (\text{A.18})$$

The derivative of (A.17) is calculated:

$$\begin{aligned} \frac{d}{dt} G_{n+1}(t) &= (-d) \frac{2^{n+1}src_0}{k} e^{-dt} \left( 1 - \sum_{i=0}^{n+1} \frac{(kt)^i}{i!} e^{-kt} \right) \\ &+ \frac{2^{n+1}src_0}{k} e^{-dt} \left( -\frac{(n+1)k^{n+1}t^n}{(n+1)!} e^{-kt} - (-k) \frac{(kt)^{n+1}}{(n+1)!} e^{-kt} \right. \\ &- \frac{nk^n t^{n-1}}{n!} e^{-kt} - (-k) \frac{(kt)^n}{n!} e^{-kt} \dots - \frac{k}{1!} e^{-kt} - (-k) \frac{kt}{1!} e^{-kt} \\ &\left. - (-k) \frac{1}{0!} e^{-kt} + k - k \right). \end{aligned}$$

The expression in the first line simplifies to  $-d \cdot G_{n+1}(t)$ . In the case of the remaining expressions we add a  $+k - k$  inside of the brackets. Then we summarize all terms with the multiplicative factor of  $(-k)$  in front and the extra  $-k$  and obtain  $-k \cdot G_{n+1}(t)$  and are left with

$$\begin{aligned} \frac{d}{dt} G_{n+1}(t) &= -d \cdot G_{n+1}(t) - k \cdot G_{n+1}(t) \\ &+ \frac{2^{n+1}src_0}{k} e^{-dt} \left( -\frac{k^{n+1}t^n}{n!} e^{-kt} - \frac{k^n t^{n-1}}{(n-1)!} e^{-kt} \dots - k e^{-kt} + k \right). \end{aligned} \quad (\text{A.19})$$

Taking  $k$  out of the brackets we have:

$$\begin{aligned} \frac{d}{dt} G_{n+1}(t) &= -d \cdot G_{n+1}(t) - k \cdot G_{n+1}(t) \\ &+ 2k \frac{2^n src_0}{k} e^{-dt} \left( -\frac{(kt)^n}{n!} e^{-kt} - \frac{(kt)^{n-1}}{(n-1)!} e^{-kt} \dots - e^{-kt} + 1 \right) \end{aligned} \quad (\text{A.20})$$

and by using (A.10) we have

$$\frac{d}{dt} G_{n+1}(t) = -(k+d) \cdot G_{n+1}(t) + 2k \cdot G_n(t). \quad (\text{A.21})$$



---

Supplementary information to the melanoma experiments and models

---

### B.1. Supplementary figures to the data

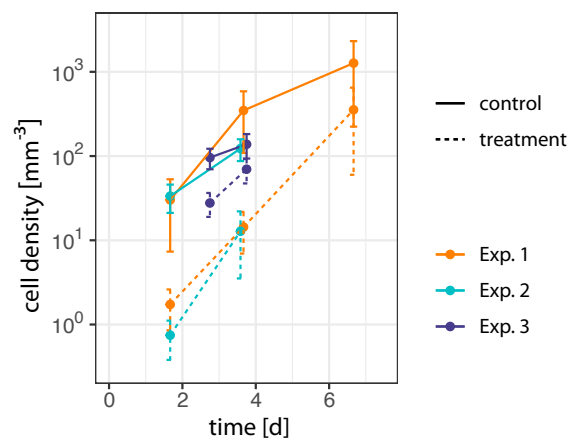


**Figure B.1** : OT-I T cell density in the tumor. The density of OT-I T cells is smaller in the anti-CD40 treatment setting

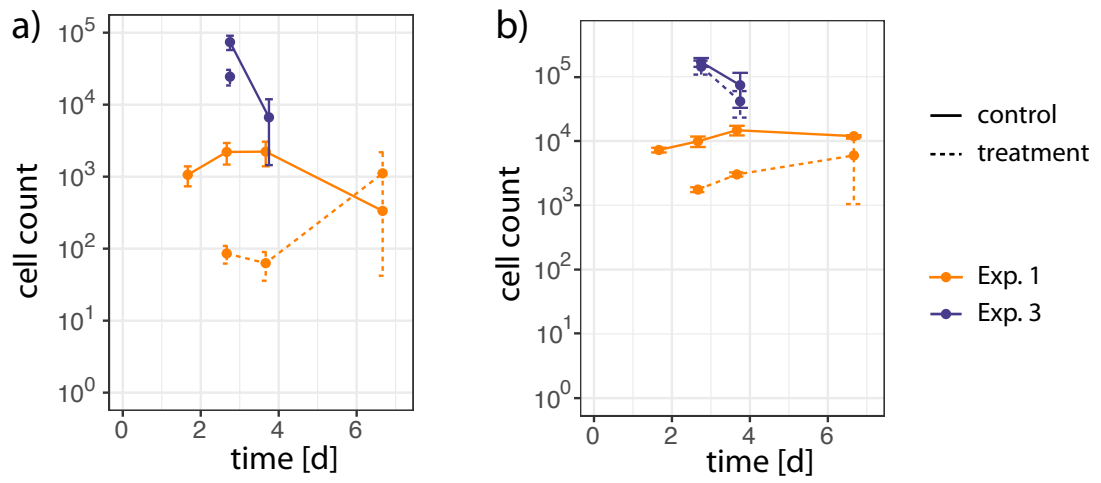


**Figure B.2** : Number of undivided cells in the a) tumor and b) blood for the time-resolved (Exp. 1) and the proliferation-resolved (Exp. 3) experiment: anti-CD40 treatment (dashed) and control (solid).

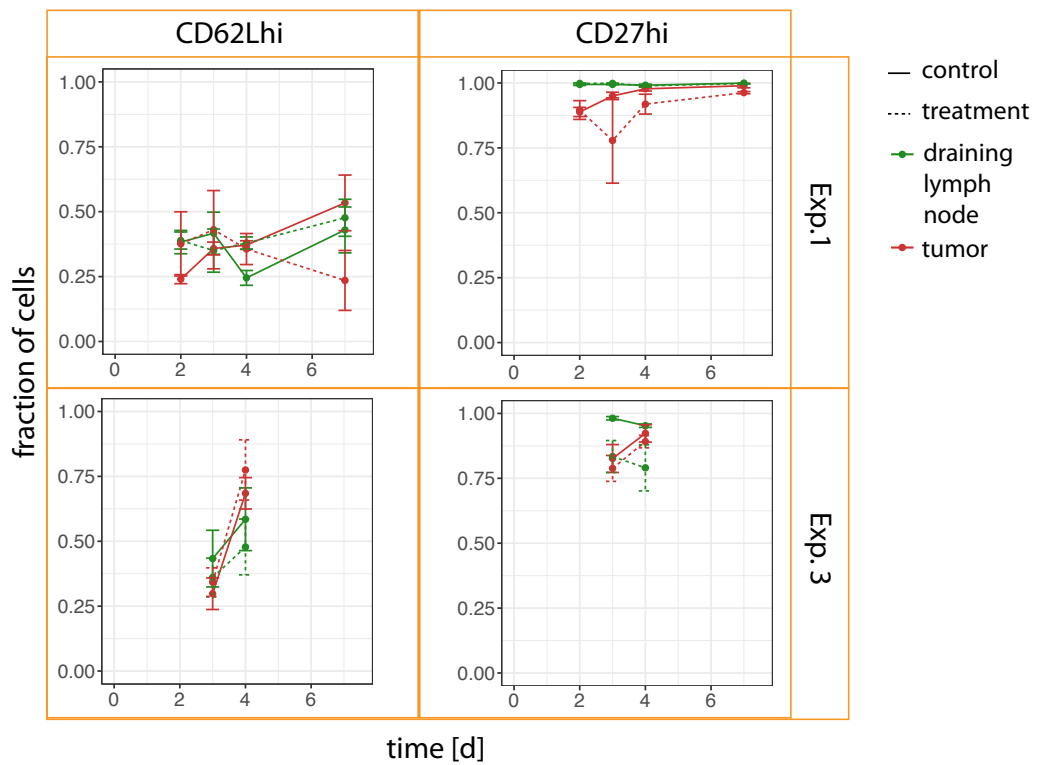


**Figure B.3** : Fraction of CD62Lhi(left column) and CD27hi(right column) cells in the draining lymph node (green) and tumor (red) for both the time-resolved experiment (Exp.1, upper lane) and the proliferation-resolved experiment (Exp.3, lower lane).

## B.2. Differential equations and observable functions of the mathematical model

### B.2.1. Time-resolved model

**Differential equations for the time-resolved model** Differential equations used to describe the dynamics of proliferating cells in the draining lymph node:

$$\begin{aligned}
 \dot{Inakt}_{dLN} &= -act \cdot Inakt_{dLN} + source \\
 \\
 \dot{Akt0}_{dLN} &= act \cdot Inakt_{dLN} - p_{dLN} \cdot Akt0_{dLN} \\
 \dot{Akt1}_{dLN} &= 2p_{dLN} \cdot Akt0_{dLN} - (p_{dLN} + e_{dLN}) \cdot Akt1_{dLN} \\
 \dot{Akt2}_{dLN} &= 2p_{dLN} \cdot Akt1_{dLN} - (p_{dLN} + e_{dLN}) \cdot Akt2_{dLN} \\
 &\dots \\
 \dot{Akt4}_{dLN} &= 2p_{dLN} \cdot Akt3_{dLN} - (e_{dLN}) \cdot Akt4_{dLN} \\
 \\
 \dot{p}_{dLN} &= -\alpha \cdot p_{dLN} \\
 \dot{e}_{dLN} &= \beta \cdot e_{dLN} \cdot (1 - e_{dLN}/e_{dLN,max}). \tag{B.1}
 \end{aligned}$$

Here,  $AktX_{dLN}$  is representing the “activated T cell in generation X in the draining lymph node”.  $Inakt_{dLN}$  stands for the inactive undivided cells. The division stops after generation 4. The last two lines are determining the time dependency of the proliferation  $p_{dLN}$  and the egress  $e_{dLN}$ , such that the proliferation decays exponentially with time and the egress grows logistically in time. The initial values are 0, but for the rates ( $p_{dLN,0}$  and  $e_{dLN,0}$ ).

Differential equations governing the proliferating cells in the tumor:

$$\begin{aligned}
 \dot{Akt1}_{T,1} &= e_{dLN} \cdot Akt1_{dLN} - p_T \cdot Akt1_{T,1}; \\
 \dot{Akt2}_{T,1} &= 2p_T \cdot Akt1_{T,1} - p_T \cdot Akt2_{T,1} \\
 \dot{Akt3}_{T,1} &= 2p_T \cdot Akt2_{T,1} \\
 \\
 \dot{Akt2}_{T,2} &= e_{dLN} \cdot Akt2_{dLN} - p_T \cdot Akt2_{T,2}; \\
 \dot{Akt3}_{T,2} &= 2p_T \cdot Akt2_{T,2} - p_T \cdot Akt3_{T,2} \\
 \dot{Akt4}_{T,2} &= 2p_T \cdot Akt3_{T,2} \\
 &\dots \\
 \dot{Akt4}_{T,4} &= e_{dLN} \cdot Akt4_{dLN} - p_T \cdot Akt4_{T,4}; \\
 \dot{Akt5}_{T,4} &= 2p_T \cdot Akt4_{T,4} - p_T \cdot Akt5_{T,4} \\
 \dot{Akt6}_{T,4} &= 2p_T \cdot Akt5_{T,4}. \tag{B.2}
 \end{aligned}$$

Here,  $AktX_{T,Y}$  is representing the ‘‘activated T cell in generation X in the tumor, which entered the tumor in generation Y’’. With this we can keep track of the history of the cell, i.e. at which generation it entered the tumor and ascertain that it divides only twice more. In contrast to the draining lymph node, in the tumor there is no equation for undivided cells  $Inakt_T$ , as this is a parameter and not a state.

**Observable for the time-resolved model** The set of observable functions  $g$  comprises the following quantities of interest: absolute cell number in draining lymph node ( $Abs_{dLN}$ ) and tumor ( $Abs_T$ ), mean number of division for the generations 1 to 4 or 5 for draining lymph node and tumor ( $MDiv_{dLN,5+}$  or  $MDiv_{dLN,6+}$  and  $MDiv_{T,5+}$  or  $MDiv_{T,6+}$ ) and the fraction of cells in generation 0 ( $Rel_{dLN,0}$  and  $Rel_{T,0}$ ) and generations 5+ or 6+ ( $Rel_{dLN,5+}$  or  $Rel_{dLN,6+}$  and  $Rel_{T,5+}$  or  $Rel_{T,6+}$ ). Note in the following that the mean number of divisions is normalized by cells from generation 1 to 4 or 5, which are also the generations contributing to the numerator. Here, we note the observable function for the measurement days 4 and 7, where we could obtain the fractions of cells in the generation 0 to 4. The equations are analogous for the case, where we have the fractions for the generations 0 to 5.

$$\begin{aligned}
 Abs_{dLN} &= Inakt_{dLN} + Akt0_{dLN} \dots Akt4_{dLN} \\
 MDiv_{dLN,5+} &= \frac{Akt1_{dLN} + 2 \cdot Akt2_{dLN} + 3 \cdot Akt3_{dLN} + 4 \cdot Akt4_{dLN}}{Akt1_{dLN} + Akt2_{dLN} + Akt3_{dLN} + Akt4_{dLN}} \\
 Rel_{dLN,0} &= \frac{Inakt_{dLN} + Akt0_{dLN}}{Abs_{dLN}} \\
 Rel_{dLN,5+} &= 0
 \end{aligned} \tag{B.3}$$

$$\begin{aligned}
 Abs_T &= Inakt_T + Akt1_{T,1} + Akt2_{T,1} \dots Akt4_{T,4} + Akt5_{T,4} + Akt6_{T,4} \\
 MDiv_{T,5+} &= \frac{Akt1_{T,1} + 2(Akt2_{T,1} + Akt2_{T,2}) + \dots + 4(Akt4_{T,2} + Akt4_{T,3} + Akt4_{T,4})}{Abs_T - (Inakt_T + Akt5_{T,3} + Akt5_{T,4} + Akt6_{T,4})} \\
 Rel_{T,0} &= \frac{Inakt_T}{Abs_T} \\
 Rel_{T,5+} &= \frac{Akt5_{T,3} + Akt5_{T,4} + Akt6_{T,4}}{Abs_T}
 \end{aligned} \tag{B.4}$$

In summary, for each measurement time point we have  $2 \cdot 8$  observables (treatment and control) and in total we have four measurement time points, which gives us 64 observables. From this we have to subtract three, as we do not have information on the cell division profiles in the tumor on day two for the treatment setting, i.e. we do not have  $MDiv_{T,5+}$ ,  $Rel_{T,0}$  and  $Rel_{T,5+}$  such that we are left with 61 observables.

### B.2.2. Proliferation-resolved model

**Differential equations for the proliferation-resolved model** Differential equations governing the proliferation of BrdU- cells in the draining lymph node:

$$\begin{aligned}
 \dot{Inakt}_{dLN,B-} &= -act \cdot Inakt_{dLN,B-} + source \\
 \dot{Akt0}_{dLN,G1,B-} &= act \cdot Inakt_{dLN,B-} - p_{G1,dLN} \cdot Akt0_{dLN,G1,B-} \\
 \dot{Akt0}_{dLN,S,B-} &= p_{G1,dLN} \cdot Akt0_{dLN,G1,B-} - p_S \cdot Akt0_{dLN,S,B-} \\
 \dot{Akt1}_{dLN,G1,B-} &= 2p_S \cdot Akt0_{dLN,S,B-} - (p_{G1,dLN} + e_{dLN}) \cdot Akt1_{dLN,G1,B-} \\
 \dot{Akt1}_{dLN,S,B-} &= p_{G1,dLN} \cdot Akt1_{dLN,G1,B-} - (p_S + e_{dLN}) \cdot Akt1_{dLN,S,B-} \\
 &\dots \\
 \dot{Akt6+}_{dLN,G1,B-} &= 2p_S \cdot (Akt5_{dLN,S,B-} + Akt6+_{dLN,S,B-}) - (p_{G1,dLN} + e_{dLN}) \cdot Akt6+_{dLN,G1,B-} \\
 \dot{Akt6+}_{dLN,S,B-} &= p_{G1,dLN} \cdot Akt6+_{dLN,G1,B-} - (p_S - e_{dLN}) \cdot Akt6+_{dLN,S,B-} \\
 \dot{p}_{G1,dLN} &= -\alpha \cdot p_{G1,dLN}.
 \end{aligned} \tag{B.5}$$

Here,  $AktX_{dLN,Y,B-}$  is representing the “activated T cell in generation X in the draining lymph node in cell cycle phase Y, which is BrdU-”.  $G_1$  stands for the  $G_1$  phase and  $S$  for the combination of the phases S,  $G_2$  and M. The BrdU+ cell dynamics are governed by analogous equations. Initially all states (BrdU+ and BrdU-) are zero and all states with BrdU+ remain zero until the time point of BrdU administration. At the time point of BrdU injection all BrdU- cells in our  $S$  phase ( $AktX_{dLN,S,B-}$ ) become BrdU+ ( $AktX_{dLN,S,B+}$ ), such that their numbers are transferred from the former compartment to the latter and the proliferation continues. As a consequence, we do not have inactive BrdU+ cells ( $Inakt_{dLN,B+}$ ) and active undivided BrdU+ cells in the  $G_1$  phase ( $Akt0_{dLN,G1,B+}$ ), as there is no prior state, for which BrdU- cells can turn BrdU+ and can enter into these compartments. Thus, compared to the equations governing the dynamics of the BrdU- cells (B.5), the equations for the BrdU+ cells lack the first two equations and the third equation lacks the input from the activated undivided cells in  $G_1$ . In generation 6+ the equations are written such that the proliferation continues and cells alternate between the  $G_1$  and our  $S$  phase. The last line is determining the time dependency of the proliferation  $p_{G1,dLN}$  and has the initial value  $p_{G1,dLN,0}$ .

Differential equations governing the proliferation of BrdU- cells in the tumor:

$$\begin{aligned}
 \dot{Akt}1_{T,G1,B-} &= -p_{G1,T} \cdot Akt1_{T,G1,B-} + e_{dLN} \cdot Akt1_{dLN,G1,B-} \\
 \dot{Akt}1_{T,S,B-} &= p_{G1,T} \cdot Akt1_{T,G1,B-} - p_S \cdot Akt1_{T,S,B-} + e_{dLN} \cdot Akt1_{dLN,S,B-} \\
 \\ 
 \dot{Akt}2_{T,G1,B-} &= 2p_S \cdot Akt1_{T,S,B-} - p_{G1,T} \cdot Akt2_{T,G1,B-} + e_{dLN} \cdot Akt2_{dLN,G1,B-} \\
 \dot{Akt}2_{T,S,B-} &= p_{G1,T} \cdot Akt2_{T,G1,B-} - p_S \cdot Akt2_{T,S,B-} + e_{dLN} \cdot Akt2_{dLN,S,B-} \\
 &\dots \\
 \dot{Akt}6_{T,G1,B-} &= 2p_S (Akt5_{T,S,B-} + Akt6_{T,S,B-}) - p_{G1,T} \cdot Akt6_{T,G1,B-} \\
 &\quad + e_{dLN} \cdot Akt6_{dLN,G1,B-} \\
 \dot{Akt}6_{T,S,B-} &= p_{G1,T} \cdot Akt6_{T,G1,B-} - p_S \cdot Akt6_{T,S,B-} + e_{dLN} \cdot Akt6_{dLN,S,B-} \quad (B.6)
 \end{aligned}$$

As opposed to the draining lymph node there are no undivided cells  $Inakt_T$ , as this is a parameter and not a state and stays constant over time. Cells from generation  $X$  and phase  $Y$  can enter from the draining lymph node ( $AktX_{dLN,Y}$ ) into the corresponding tumor state ( $AktX_{T,Y}$ ) with rate  $e_{dLN}$ . The rest works analogously to the draining lymph node.

**Observables for the proliferation-resolved model** The set of observable functions  $g$  comprises the following quantities of interest: absolute cell number in draining lymph node ( $Abs_{dLN}$ ) and tumor ( $Abs_T$ ) and, if available, the fraction of BrdU+ and BrdU- cells for each generation from 0 to 5+ or 6+ in the draining lymph node ( $Rel_{dLN,0,B-}$  and  $Rel_{dLN,0,B+}$  to  $Rel_{dLN,5+,B-}$  or  $Rel_{dLN,6+,B-}$  and  $Rel_{dLN,5+,B+}$  or  $Rel_{dLN,6+,B+}$ ) and the tumor (analogous observables as for the draining lymph node). As the information comprised in the fractions is not independent, the last fraction is not used for the fit and if two or more fractions sum up to  $\leq 2\%$ , all of these are not used for the fit and the respective observable functions are omitted accordingly. If only one fraction is omitted (in this example:  $Rel_{dLN,5+,B+}$ ), for the draining lymph node we would obtain:

$$\begin{aligned}
 Abs_{dLN} &= Inakt_{dLN,B-} + Akt0_{dLN,G1,B-} + Akt0_{dLN,S,B-} \dots Akt6_{+dLN,S,B-} \\
 &\quad + Akt0_{dLN,S,B+} + Akt1_{dLN,G1,B+} \dots Akt6_{+dLN,S,B+} \\
 Rel_{dLN,0,B-} &= \frac{Inakt_{dLN,B-} + Akt0_{dLN,G1,B-} + Akt0_{dLN,S,B-}}{Abs_{dLN}} \\
 Rel_{dLN,0,B+} &= \frac{Akt0_{dLN,S,B+}}{Abs_{dLN}}
 \end{aligned}$$

$$\begin{aligned}
 Rel_{dLN,1,B-} &= \frac{Akt1_{dLN,G1,B-} + Akt1_{dLN,S,B-}}{Abs_{dLN}} \\
 Rel_{dLN,1,B+} &= \frac{Akt1_{dLN,G1,B+} + Akt1_{dLN,S,B+}}{Abs_{dLN}} \\
 &\dots \\
 Rel_{dLN,5+,B-} &= \frac{Akt5_{dLN,G1,B-} + Akt5_{dLN,S,B-} + Akt6_{dLN,G1,B-} + Akt6_{dLN,S,B-}}{Abs_{dLN}}.
 \end{aligned}$$

If the information on the fraction of BrdU+/- cells in different generations is available in the tumor data, the analogous observable equations can be applied. The only exception is the undivided fraction of cells, where we do not distinguish between BrdU+/- . Here, we use the combined fraction  $Rel_{T,0}$  instead, since we assume all these cells to be inactive. Although the real state of these cells is not quite clear (see section 3.2.1), at least the number of BrdU+ cells in this fraction is negligible.

If the fractions of cells in different generations are not identifiable even when BrdU+ and BrdU- cells are combined, the absolute cell numbers  $Abs_T$  and the total fraction of all BrdU+ cells  $Rel_{T,all,B+}$  are used as observables. If the combined BrdU+ and BrdU- fraction of cells for each generation is available, these can be used as observables and we obtain

$$\begin{aligned}
 Abs_T &= Inakt_T + Akt1_{T,G1} + Akt1_{T,G2M} \dots + Akt6_{+T,S} \\
 &\quad Akt1_{T,G1,B+} + Akt1_{T,G2M,B+} \dots Akt6_{+T,S,B+} \\
 Rel_{T,all,B+} &= \frac{Akt1_{T,G1,B+} + Akt1_{T,G2M,B+} \dots Akt6_{+T,S,B+}}{Abs_T} \\
 Rel_{T,0} &= \frac{Inakt_T}{Abs_T} \\
 Rel_{T,1} &= \frac{Akt1_{T,G1,B-} + Akt1_{T,S,B-} + Akt1_{T,G1,B+} + Akt1_{T,S,B+}}{Abs_T} \\
 &\dots \\
 Rel_{T,4} &= \frac{Akt4_{T,G1,B-} + Akt4_{T,S,B-} + Akt4_{T,G1,B+} + Akt4_{T,S,B+}}{Abs_T},
 \end{aligned}$$

where we again omit the last fraction ( $Rel_{T,5+}$ ).

**Number of Observables** In total we have 79 observables.

For the fit to the treatment and control data on day 3: 2 observables from the absolute cell numbers, 13 observables for the BrdU+ and BrdU- fractions of cells in the generations 0 to 6+ of the draining lymph node, 5 observables for the BrdU+/- combined fractions of cells in the generations 0 to 5+ of the tumor and one for fitting the total fraction of BrdU+ cells in the tumor. This gives us 21 observables and if we combine the ones from the treatment and control we obtain 42 in total.

For the fit to the control data on day 4 we have 2 observables from the absolute cell numbers, 11 observables for the BrdU+ and BrdU- fractions of cells in the generations 0 to 5+ of the draining lymph node, 9 observables for the BrdU+ and BrdU- fractions of cells in the generations 1 to 5+ of the tumor and one from the the undivided number of cells in the tumor. This leaves us with 23 observables.

For the fit to the treatment data on day 4 we have 2 observables from the absolute cell numbers, 11 observables for the BrdU+ and BrdU- fractions of cells in the generations 0 to 5+ of the draining lymph node, none for the cell division profile in the tumor and one for fitting the total fraction of BrdU+ cells in the tumor. This leaves us with 14 observables.

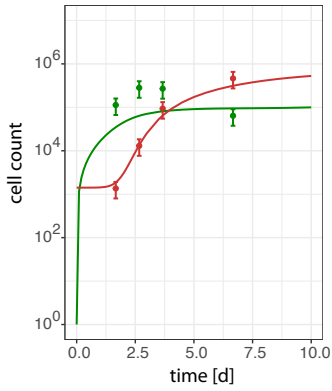
### **B.3. Best model fits with different observables**

The best minimal model was found by conducting a model selection with a fit to the mean number of divisions for the time-resolved experiment (section 3.2.4) and a direct fit to the cell division profile for the proliferation-resolved experiment (section 3.2.5). Here, in Figs. B.4 and B.5, we show results for the best minimal models fitted to observables, which are swapped between the two experiments. The similarity of the results show the robustness of the fits: For the time-resolved experiment compare Tab. 3.3 and Tab. B.1 and for the proliferation-resolved experiment compare Tab. 3.4 and Tab. B.2.

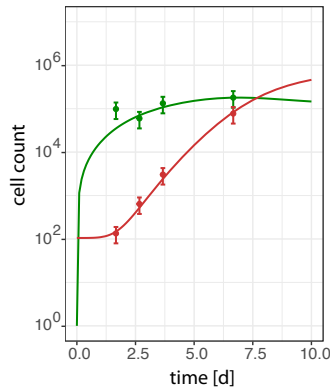
B.3. Best model fits with different observables

Fit to absolute cell numbers

a) Control

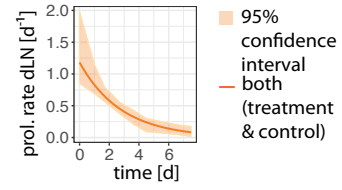


b) Anti-CD40 treatment

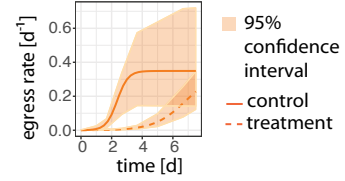


Estimated rates

c) Proliferation rate



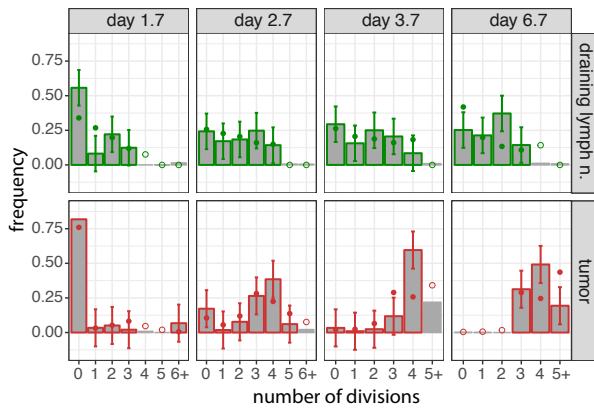
d) Egress rate



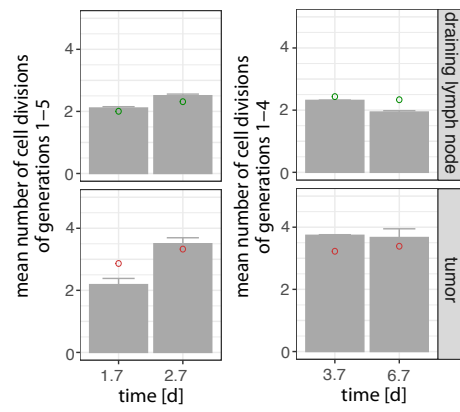
Fit to proliferation data



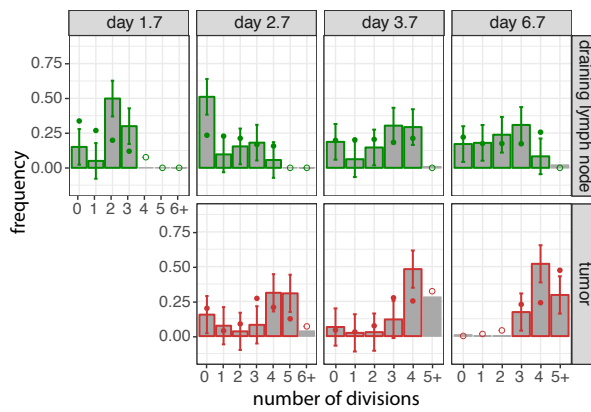
e) Cell division profile (control)



f) Mean number of cell divisions (control)



g) Cell division profile



h) Mean number of cell divisions

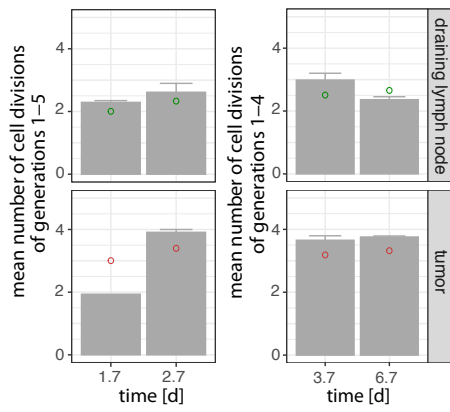


**Figure B.4 (previous page):** Fit of the best minimal model to the data of the time-resolved experiment using the cell division profiles as observables. a) & b) Fit to the absolute cell numbers in the draining lymph node (green) and tumor (red) for the a) control and b) anti-CD40 treatment. c) Estimated proliferation rate in the draining lymph node, which is the same for control and treatment. Filled area indicates the 95% confidence interval. d) Estimated egress rate for the control (solid) and treatment (dashed). Filled area indicates the 95% confidence interval. e) - h) Fit (dots) and prediction (circles) of the proliferation data. Only the color-bordered bars are used for fitting. e) Fitted and predicted cell division profiles<sup>1</sup> and f) predicted mean number of divisions of the control. g) & h) Analogous plots for the treatment setting. Experimental data: Lena Kranz and Mustafa Diken.

**Table B.1.:** Estimated rates for the BMM, time-resolved experiment, fit to cell division profile

Parameter	Control	CD40
source	11000 cells/d	"
activation	6.7 1/d	"
$p_{dLN,0}$ *	1.2 1/d	"
$\alpha^*$	0.35 1/d	"
$e_{dLN,0}$ **	0.0005 1/d	"
$\beta^{**}$	2.8 1/d	0.97 1/d
$e_{dLN,max}$ **	0.35 1/d	"
$p_T$	3.3 1/d	"
Undivided cells, tumor	1400 cells	100 cells
$sd_{abs}$	0.41	"
$sd_{Gen,dLN}$	0.13	"
$sd_{Gen,T}$	0.13	"

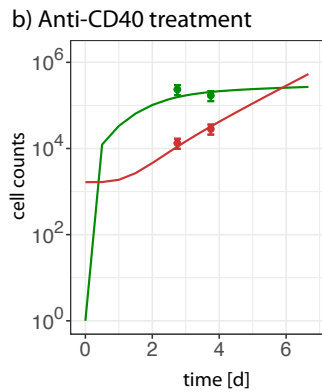
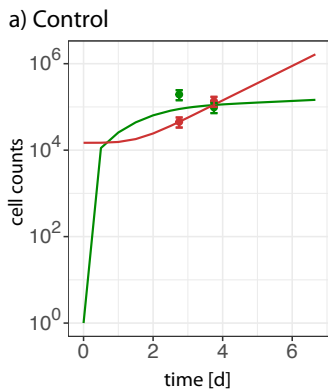
\* see eq.(3.1)

---

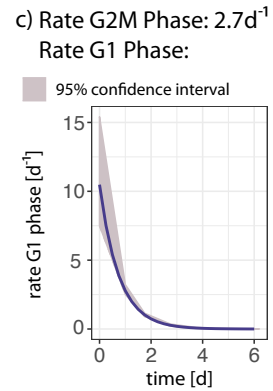
<sup>1</sup>For each cell division profile we fit all fractions but one. If the sum of more than one fraction is  $\leq 2\%$ , these are not used for fitting instead.

B.3. Best model fits with different observables

Fit to absolute cell numbers



Proliferation rate



Fit to proliferation data

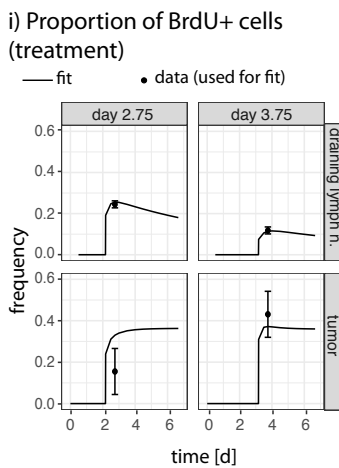
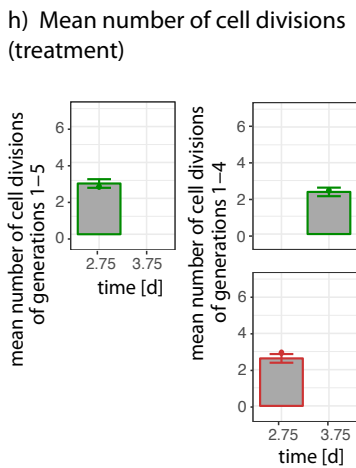
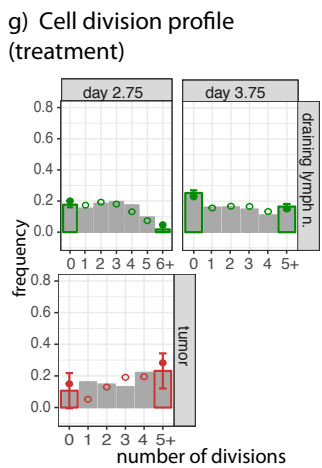
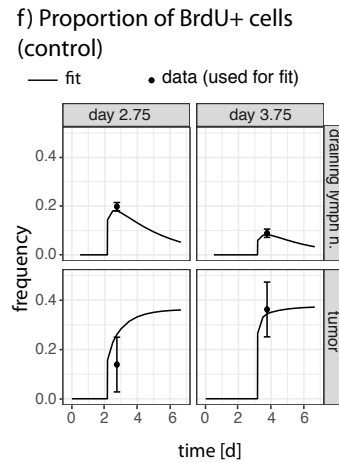
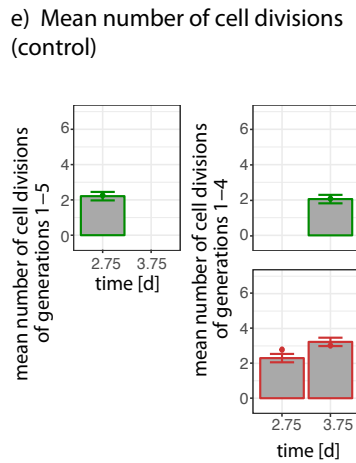
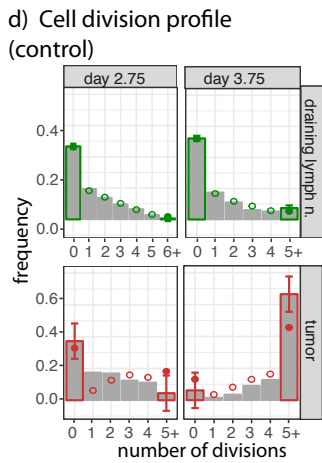


**Figure B.5 (previous page):** Fit of the best minimal model to the data of the proliferation-resolved experiment using the mean number of divisions as observables. a)& b) Fit to the absolute cell numbers in draining lymph node (green) and tumor (red) for the a) control and b) anti-CD40 treatment. c) Estimated proliferation rate in the draining lymph node, which is the same for control and treatment. Filled area indicates the 95% confidence interval. d) - i) Fit to the proliferation data. Only the color-bordered bars are used for fitting. d) Fitted (dots) and predicted (circles) cell division profiles for the control setting. e) Fitted (dots) mean number of divisions for the control. f) Fitted (solid line) total fraction of BrdU+ cells for the control setting. g) - i) Analogous plots for the treatment setting. Experimental data: Lena Kranz and Mustafa Diken.

**Table B.2.:** Estimated rates for the BMM, proliferation resolved experiment, fit to mean number of divisions

Parameter	Control	CD40
source	21000 cells/d	"
activation	1.1 1/d	4.1 1/d
$p_{G1,dLN,0}^*$	12 1/d	"
$\alpha^*$	1.4 1/d	"
$p_S$	2.6 1/d	"
$e_{dLN}$	0.28 1/d	0.034 1/d
$p_{G1,T}$	1.9 1/d	"
Undivided cells, tumor	15000 cells	1700 cells
$sd_{abs}$	0.26	"
$sd_{MDiv}$	0.24	"
$sd_{Gen,dLN}$	0.017	"
$sd_{Gen,T}$	0.11	"

\* see eq.(3.1) \*\*see eq.(3.2)

---

Supplementary information to the pancreatic ductal adenocarcinoma  
experiments and models

---

### C.1. Supplementary figures to the data

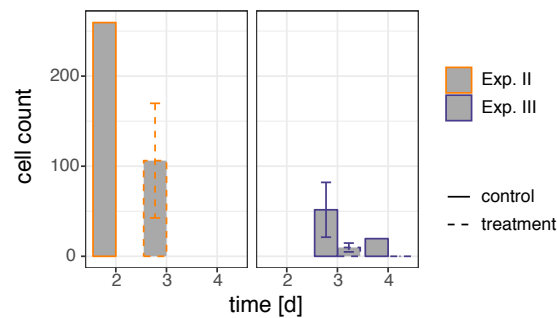


**Figure C.1 :** Absolute number of undivided cells in the blood in the second (left) and third (right) PDAC experiment

### C.2. Differential equations and observable functions of the mathematical model

Differential equations used to describe the dynamics of proliferating cells in the draining lymph node of PDAC experiments are the same as the equations for the time-resolved melanoma experiment, see section B.2.1 and eqn. (B.1). We use the same abbreviations for the parameters and variables. The only difference to the equations for the time-resolved experiment is that the cells continue to divide beyond the fourth division: The

model of the second pancreatic experiment describes an ongoing division and the model for the third pancreatic experiment includes a division stop in the sixth generation.

For the second pancreatic experiment this means that the last line describing the dividing cells would be

$$\dot{Akt4}_{dLN} = 2p_{dLN} \cdot Akt3_{dLN} - e_{dLN} \cdot Akt4_{dLN} + p_{dLN} * Akt4_{dLN} \quad (C.1)$$

indicating a continued proliferation after the fourth division (further generations do not need to be calculated, as we can only resolve 4 generations in the data). The equations for the proliferation in the tumor for the second experiment are analogous and only differ in so far as we have an ingress into this compartment. The corresponding last line would be

$$\dot{Akt4}_T = 2p_{dLN} \cdot Akt3_T + e_{dLN} \cdot Akt4_{dLN} + p_{dLN} \cdot Akt4_T. \quad (C.2)$$

For the third pancreatic cancer experiment the last line in the draining lymph node is

$$\dot{Akt6}_{dLN} = 2p_{dLN} \cdot Akt5_{dLN} - e_{dLN} \cdot Akt6_{dLN} \quad (C.3)$$

meaning that the proliferation stops in the sixth generation. The equations for the proliferation in the tumor are analogous and only differ in so far as we have an ingress into this compartment. The corresponding last line would be

$$\dot{Akt6}_T = 2p_{dLN} \cdot Akt5_T - e_{dLN} \cdot Akt6_{dLN}. \quad (C.4)$$

**Observable functions** We have an analogous set of observable functions as for the time-resolved melanoma experiment, see section B.2.1 and eqn. (B.3). The only differences are that the mean number of division has contributions from generation 1 to 3 ( $MDiv_{dLN,4+}$ ) for the second experiment and 1 to 5 ( $MDiv_{dLN,6+}$ ) for the third experiment, and that the fraction of cells in the last generation ( $Rel_{dLN,4+}$  and  $Rel_{dLN,6+}$ ) are not equal to zero.

Observable function for the second experiment:

$$\begin{aligned} Abs_{dLN} &= Inakt_{dLN} + Akt0_{dLN} \dots Akt4_{dLN} & (C.5) \\ MDiv_{dLN,4+} &= \frac{Akt1_{dLN} + 2 \cdot Akt2_{dLN} + 3 \cdot Akt3_{dLN}}{Akt1_{dLN} + Akt2_{dLN} + Akt3_{dLN}} \\ Rel_{dLN,0} &= \frac{Inakt_{dLN} + Akt0_{dLN}}{Abs_{dLN}} \\ Rel_{dLN,4+} &= \frac{Akt4_{dLN}}{Abs_{dLN}}. \end{aligned}$$

Observable function for the third experiment:

$$\begin{aligned}
 Abs_{dLN} &= Inakt_{dLN} + Akt0_{dLN} \dots Akt6_{dLN} & (C.6) \\
 MDiv_{dLN,6+} &= \frac{Akt1_{dLN} + 2 \cdot Akt2_{dLN} \dots + 5 \cdot Akt5_{dLN}}{Akt1_{dLN} + Akt2_{dLN} + \dots Akt5_{dLN}} \\
 Rel_{dLN,0} &= \frac{Inakt_{dLN} + Akt0_{dLN}}{Abs_{dLN}} \\
 Rel_{dLN,6+} &= \frac{Akt6_{dLN}}{Abs_{dLN}}.
 \end{aligned}$$

In the tumor compartment we have an additional difference to the observable functions of the melanoma experiment. Here, we don't have a parameter describing the number of undivided cells such that the model predicts no cells for the corresponding observable. In consequence, the observable is disregarded, see section 4.2.1.

Observable function for the second experiment:

$$\begin{aligned}
 Abs_T &= Akt1_T + \dots + Akt4_T & (C.7) \\
 MDiv_{T,4+} &= \frac{Akt1_T + 2 \cdot Akt2_T + 3 \cdot Akt3_T}{Akt1_T + Akt2_T + Akt3_T} \\
 Rel_{T,4+} &= \frac{Akt4_T}{Abs_T}.
 \end{aligned}$$

Observable function for the third experiment:

$$\begin{aligned}
 Abs_T &= Akt1_T + \dots + Akt6_T & (C.8) \\
 MDiv_{T,6+} &= \frac{Akt1_T + 2 \cdot Akt2_T \dots + 5 \cdot Akt5_T}{Akt1_T + Akt2_T + \dots Akt5_T} \\
 Rel_{T,6+} &= \frac{Akt6_T}{Abs_T}.
 \end{aligned}$$

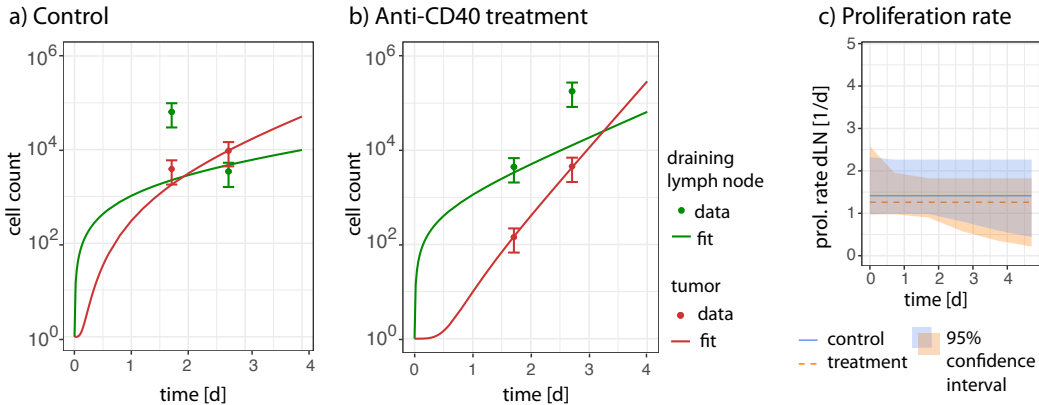
In summary, for each measurement time point in both experiments we have  $2 \cdot 7$  observables (treatment and control) and in total we have two measurement time points, which gives us 28 observables. From this we have to subtract 2 in the second experiment, as we do not have any information on the cell division profiles in the tumor on day two for the treatment setting, i.e. we do not have  $MDiv_{T,4+}$  and  $Rel_{T,4+}$ , and we are left with 26 observables. In the third experiment, we do not have any information on the cell division profiles in the tumor on day three for the control setting and day four for the treatment setting, i.e. we do not have  $MDiv_{T,6+}$  and  $Rel_{T,6+}$ , and we are left with 24 observables.

### C.3. Alternatives to the best model fits

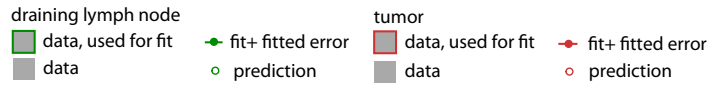
**Fit of full model to the data of the second PDAC experiment** The fit to the data of the second experiment is challenging and different model options could not be distinguished properly, such that in our best minimal model all parameters are the same for

the treatment and the control. Here, we present the fit of the full model (Fig. C.3), where all parameters can be different but for the source term and the errors, as we assume that they are not influenced by the treatment. In this way, we show how well a model with the given basic model structure can in principle approximate the data and illustrate which part of the data is still difficult to explain as is discussed in section 4.2.3.

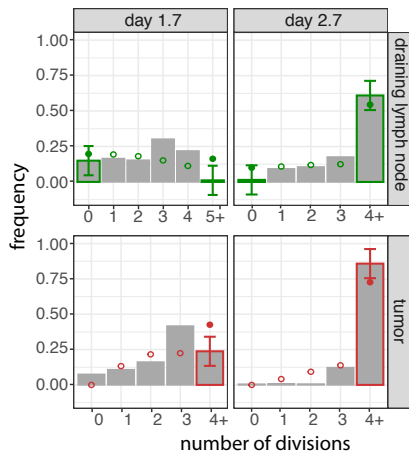
Fit to absolute cell numbers



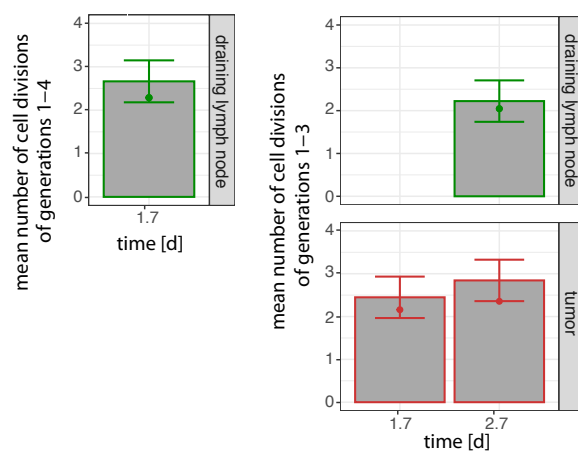
Fit to proliferation data



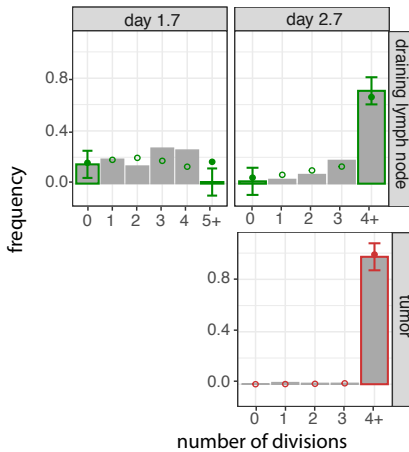
d) Cell division profile (control)



e) Mean number of cell divisions (control)



f) Cell division profile (treatment)



g) Mean number of cell divisions (treatment)

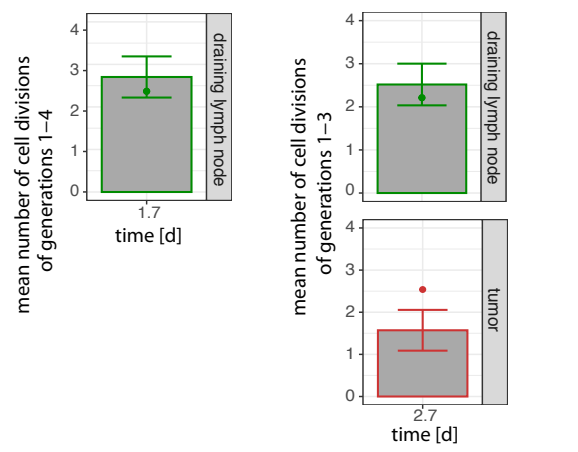


**Figure C.2 (previous page):** Fit of full model to the data of the second experiment. a) & b) Fit to the absolute cell numbers in the draining lymph node (green) and tumor (red) for the a) control and b) anti-CD40 treatment. c) Estimated proliferation rate in the draining lymph node. Filled area indicates the 95% confidence interval. d)-g) Fit (dots) and prediction (circles) of the proliferation data. Only the color-bordered bars are used for fitting. d) Fitted and predicted cell division profiles and e) fitted mean number of divisions for the control. f) & g) Analogous plots for the treatment setting. Experimental data: Susann Wendler.

**Table C.1.:** Estimated rates for the full model, second PDAC experiment

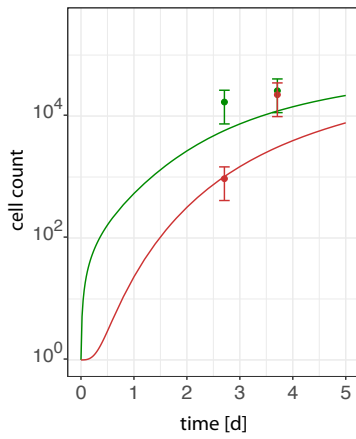
Parameter	Control	CD40
source	650 cells/d	"
activation	31 1/d	7.8 1/d
$p_{dLN}^*$	1.4 1/d	1.3 1/d
$\alpha^*$	0 1/d	0 1/d
$e_{dLN}$	1 1/d	0.02 1/d
$p_T$	1 1/d	3.2 1/d
$sd_{abs}$	0.53	"
$sd_{MDiv}$	0.48	"
$sd_{Gen}$	0.10	"

\* see eq.(3.1)

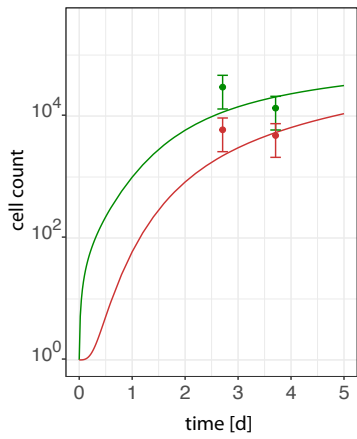
**Fit of best minimal model to changed observables of the third PDAC experiment** In section 4.2.4, we ask whether the fit is robust under a change of observables. A direct fit to the cell division profiles, see Fig. C.3, instead of the mean number of divisions yields similar results, compare Tab. C.2 and Tab. 4.4.

Fit to absolute cell numbers

a) Control

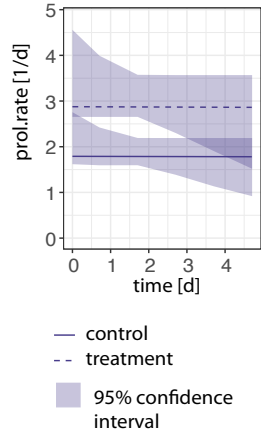


b) Anti-CD40 treatment



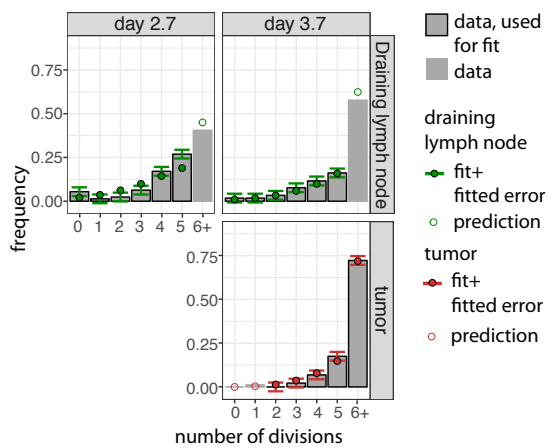
Estimated rates

c) Proliferation rates

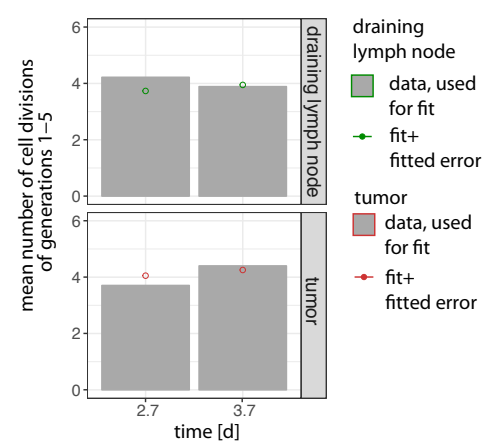


Fit to proliferation data

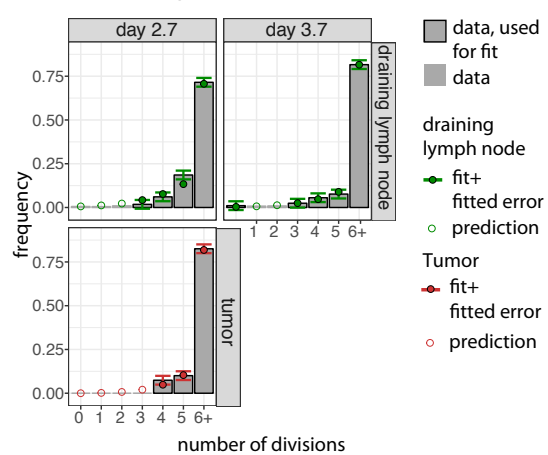
d) Cell division profile (control)



e) Mean number of cell divisions (control)



f) Cell division profile (treatment)



g) Mean number of cell divisions (treatment)

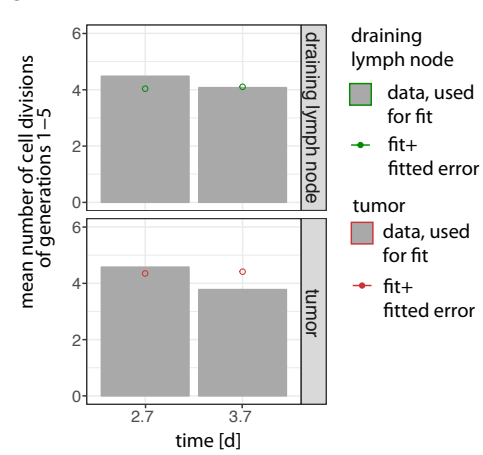


**Figure C.3 (previous page):** Fit of the best minimal model to the data of the third experiment using the cell division profiles as observables. a) & b) Fit to the absolute cell numbers in the draining lymph node and tumor: a) control b) anti-CD40 treatment. c) Estimated proliferation rate in the draining lymph node, which is the same for control and treatment. Filled area indicates 95% confidence interval. d) - g) Fit (dots) and predictions (circles) of the proliferation data. Only the color-bordered bars are used for fitting. d) Fitted and predicted cell division profiles <sup>1</sup> and e) fitted mean number of divisions for the control. f) & g) Analogous plots for the treatment setting. Experimental data: Susann Wendler and Aaron Rodriguez Ehrenfried.

**Table C.2.:** Estimated rates for the BMM, third PDAC experiment, fit to cell division profile

Parameter	Control	CD40
source	200 cells/d	"
activation	370 1/d	"
$p_{dLN}^*$	1.8 1/d	2.9 1/d
$\alpha^*$	0.001 1/d	"
$e_{dLN}$	0.1 1/d	"
$p_T$	1.8 1/d	3.3 1/d
$sd_{abs}$	0.56	"
$sd_{Gen}$	0.025	"

\* see eq.(3.1)

---

<sup>1</sup>For each cell division profile we fit all fractions but one. If the sum of more than one fraction is  $\leq 2\%$ , these are not used for fitting instead.

### Table of abbreviations

AIC	Akaike information criterion
APC	antigen presenting cell
BMM	best minimal model
BrdU	Bromodeoxyuridine
CFSE	carboxyfluorescein succinimidyl ester
CI	confidence interval
CV	coefficient of variation
negLL	negative loglikelihood
ODE	ordinary differential equation
PDAC	pancreatic ductal adenocarcinoma
S1PR1	sphingosine 1-phosphate receptor type 1
TCR	T cell receptor